Summer 8-2018

Inverse Design of Three-Dimensional Frequency Selective Structures and Metamaterials using Multi-Objective Lazy Ant Colony Optimization

Danny Zhu
danny.z.zhu@gmail.com

Recommended Citation

Zhu, Danny, "Inverse Design of Three-Dimensional Frequency Selective Structures and Metamaterials using Multi-Objective Lazy Ant Colony Optimization" (2018).

The Pennsylvania State University

The Graduate School

College of Engineering

INVERSE DESIGN OF THREE-DIMENSIONAL FREQUENCY SELECTIVE STRUCTURES AND METAMATERIALS USING MULTI-OBJECTIVE LAZY ANT COLONY OPTIMIZATION

A Dissertation in

Electrical Engineering

by

Danny Z. Zhu

Submitted in Partial Fulfillment
of the Requirements
for the Degree of

Doctor of Philosophy

August 2018

The dissertation of Danny Z. Zhu was reviewed and approved[1] by the following:

Douglas H. Werner
Professor of Electrical Engineering
Dissertation Adviser
Chair of Committee

Pingjuan L. Werner
Professor of Electrical Engineering

Ram M. Narayanan
Professor of Electrical Engineering

Michael T. Lanagan
Professor of Engineering Science and Mechanics

Kultegin Aydin
Professor of Electrical Engineering
Head of the Department of Electrical Engineering

---

[1] Signatures are on file in the Graduate School.

Abstract

With the rise of big data and the "internet of things," wireless signals permeate today's environment more than ever before. As the demand for information and security continues to expand, the need for filtering a crowded signal space will become increasingly important. Although existing devices can achieve this with additional components, such as in-line filters and low noise amplifiers, these approaches introduce additional bulk, cost and complexity. An alternative, low-cost solution to filtering these signals can be achieved through the use of Frequency Selective Surfaces (FSSs), which are commonly used in antennas, polarizers, radomes, and intelligent architecture. FSSs typically consist of a doubly-periodic array of unit cells, which acts as a spatial electromagnetic filter that selectively rejects or transmits electromagnetic waves, based on the unit cell's geometry and material properties. Unlike traditional analog filters, spatial filters must also account for the polarization and incidence angle of signals; thus, an ideal FSS maintains a given frequency response for all polarizations and incidence angles. Traditional FSS designs have ranged from planar structures with canonical shapes to miniaturized and multi-layer designs using fractals and other space-filling geometries. More recently, FSS research has expanded into three-dimensional (3D) designs, which have demonstrated enhanced fields of view over traditional planar and multi-layer designs. To date, nearly all FSSs still suffer from significant shifts in resonant frequencies or onset of grating lobes at incidence angles beyond 60 degrees in one or more polarizations. Additionally, while recent advances in additive manufacturing techniques have made fully 3D FSS designs increasingly popular, design tools to exploit these fabrication methods to develop FSSs with ultra-wide Fields of View (FOV) do not currently exist. In this dissertation, a Multi-Objective Lazy Ant Colony Optimization (MOLACO) scheme will be introduced and applied to the problem of 3D FSS design for extreme FOVs. The versatility of this algorithm will further be demonstrated through application to the design of meander line antennas, optical antennas, and phase-gradient metasurfaces.

Table of Contents

List of Tables

List of Figures

List of Abbreviations

3D	Three Dimensional
ABS	Acrylonitrile Butadiene Styrene
ACO	Ant Colony Optimization
AMC	Artificial Magnetic Conductor
AR	Axial Ratio
CP	Circularly Polarized
C-RAM	Carbon-based Radar Absorbing Material
DED	Directed Energy Deposition
DLP	Digital Light Processing
DMLS	Direct Metal Laser Sintering
EBAM	Electron Beam Additive Manufacturing
FBW	Fractional Bandwidth
FDM	Fused Deposition Modeling
FEBID	Focused Electron Beam Induced Deposition
FFF	Fused Filament Fabrication
FNDS	Fast Non-Dominated Sort
FSS	Frequency Selective Surface
FWHM	Full Width Half Max
GA	Genetic Algorithm
GRL	Gated Reflect Line
HPBW	Half Power Beam Width
LP	Linearly Polarized
MCAA	Multi Criterion Ant Algorithm
MGA	Macro Genetic Algorithm
MLA	Meander Line Antenna
MMAS	Max Min Ant System
MOAQ	Multi-Objective Ant-Q
MOACO	Multi-Objective Ant Colony Optimization
MOLACO	Multi-Objective Lazy Ant Colony Optimization
MPL	Membrane Projection Lithography
MWIR	Mid-Wave Infrared
NSGA	Non-dominated Sorting Genetic Algorithm
NZIM	Near Zero Index Material
PCR	Polarization Conversion Ratio
PCS	Polarization Converting Surface
PEC	Perfect Electric Conductor
PFEBI	Periodic Finite Element Boundary Integrals
PJP	Polymer Jetting Printing
PLA	Polylactic Acid
PMMA	Polymethylmethacrylate
PSO	Particle Swarm Optimization
PSS	Polarization Selective Surface

PVA	Polyvinyl Alcohol
PVDC	Polyvinylidene Chloride
RAM	Random Access Memory
RF	Radio Frequency
SEM	Scanning Electron Microscope
SLA	Stereolithography
SLM	Selective Laser Melting
SLS	Selective Laser Sintering
SRR	Split Ring Resonator
TE	Transverse Electric
TM	Transverse Magnetic
TSP	Traveling Salesman Problem
UV	Ultra Violet

Acknowledgement

This journey could not have been possible without the inspiration, examples, and encouragement given to me by my family, professors, and colleagues. When I was in grade school, my grandfather quoted Thomas Edison to me, saying “Genius is one percent inspiration, and ninety-nine percent perspiration.” Having heard and seen all that he has achieved and continues to accomplish, it was easy to see that he is my one percent. He showed me the reason “why,” while my parents taught me “how.” Our very first learning experiences start by example, and I am fortunate my parents taught me right from wrong, and to be punctual, responsible, and hard working. Throughout my research, I also found myself surrounded by remarkable professors and colleagues, whose mentorship and discussions enabled me to develop the tools I needed to succeed. While the inspiration and examples before me helped to forge a foundation for success, sometimes there are no examples to draw from and we must learn through failure, as is often the case with original research. It was in these moments that Saerom gave me a glimmer of hope to light the path through the darkness. Her continued support and encouragement gave me the strength I needed to succeed.

Chapter 1

Introduction

1.1 Background

Frequency Selective Surfaces (FSSs) are passive structures consisting of doubly periodic unit cells that collectively behave as a spatial electromagnetic filter. Unit cell shapes can take on many forms but are typically represented by conductive elements arranged in in such a way as to introduce some resonant or anti-resonant behavior as a result of mutual electromagnetic coupling, cavitation, or other phenomena. Typical FSS applications can include enhancement of antenna performance, reduction in radar cross section, as well as filtering and absorption of waveforms. However, since incident waves propagating in free space can assume an infinite number of field configurations, an ideal FSS should be capable of consistently achieving a specific filtering response over a given range of operating frequencies, and more importantly, wide range of incidence angles. Common examples of planar geometries are given in Figure 1.1. To date, many FSSs have been proposed ranging from planar structures using combined and modified canonical shapes [1][2] to multi-layer cascaded designs [3]-[9] and most recently, three dimensional structures [10]. Although conventional planar designs using canonical shapes like those shown in perform well at normal and near-normal incidences (in some cases up to 50°), they can quickly be burdened by the onset of grating lobes or odd modes excited only by oblique incidences thereafter. Grating lobes are a form of backscattering that arises due to

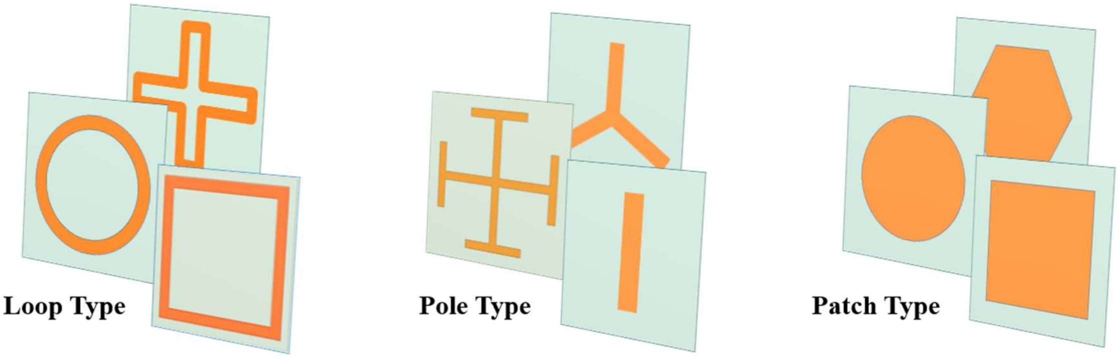

(a) (b) (c)

Figure 1.1. Canonical, planar FSS structures take on various forms, including (a) loop-type designs, (b) multi-legged pole type designs and (c) patch type designs. Combinations of these geometries also exit and provide various benefits.

constructive or destructive phase accumulation at oblique incidences, similar to improperly spaced elements of a phased array antenna. A diagram depicting the formation of grating lobes is shown in Figure 1.2. While grating lobes can be delayed by reducing unit cell sizes, this can prove troublesome for filters with a low target frequency and large operating

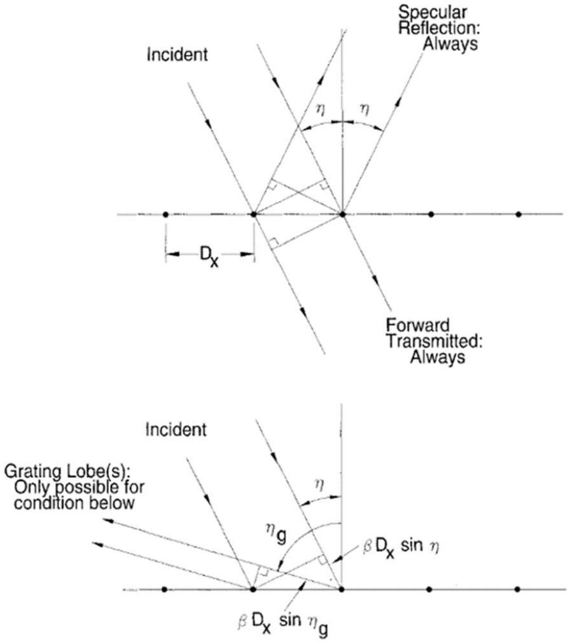

Figure 1.2. Example of formation of grating lobe at oblique incidences as a function of the unit cell periodicity, D_x. Figure reproduced from [1] with permission from Wiley & Sons.

band. For example, loop type FSSs resonate at a circumference length near λ [1]. Thus, as the target operating frequency becomes smaller, the unit cell size becomes larger, encouraging the onset of grating lobes at higher frequencies much earlier. To alleviate these issues, FSS unit cells are often miniaturized either through dielectric loading, effectively reducing the wavelength within the medium, or by modifying the geometry using a space-filling element, such as a fractal pattern [11]-[16] or meander line [17]-[24] as seen in Figure 1.3. At near normal incidences, these miniaturization techniques have proven to be quite effective; however, while the onset of grating lobes can be significantly delayed, odd modes are often still excited at oblique incidences.

Another technique to enhance FSS performance has been to cascade multiple planar designs. While this approach is often used to enhance bandwidth of designs by introducing additional resonances, in most cases, the final designs are often only as angularly stable as

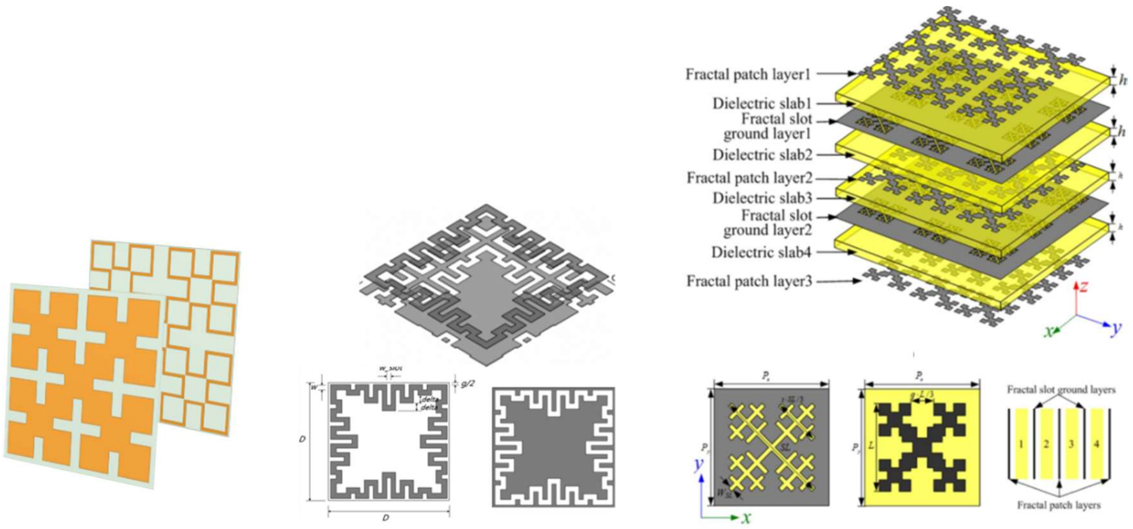

© 2010 IEEE © 2015 IEEE

(a) (b) (c)

Figure 1.3. Examples of miniaturized designs, including (a) planar Minkowski fractal patches and loops [11][13], (b) cascaded complementary meandering square loop [18] and (c) multi-layer fractal patterns [14].

their individual layers. In fact, the disadvantages of this approach can often outweigh the benefits. Multi-layer designs suffer from stringent registration requirements for layer alignment [25], and may be further limited by coupling between layers, which is sometimes solved by adding yet another layer, *i.e.* a coupling aperture as described in [3]. This can quickly result in a multi-stage design that is too bulky and cumbersome, with only marginal improvements in angular stability over planar designs. Examples of cascaded and multi-layer designs are shown in Figure 1.4.

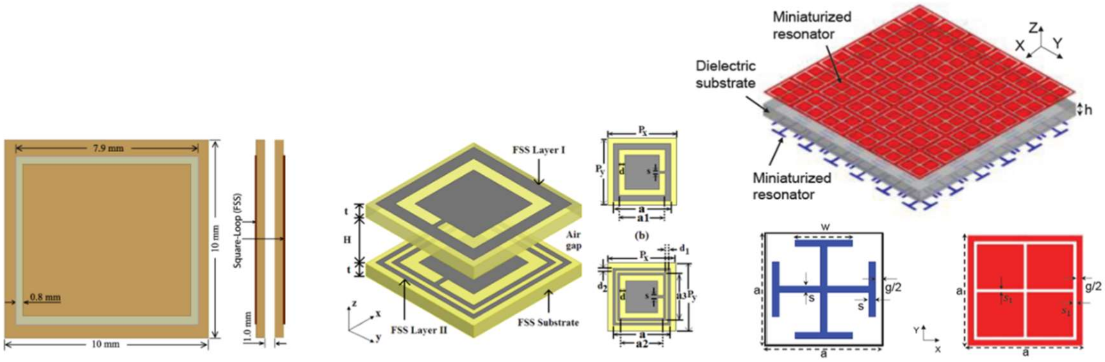

© 2015 IEEE
(a)

© 2016 IEEE
(b)

© 2016 IEEE
(c)

Figure 1.4. Examples of cascaded FSS designs, including (a) loaded square loops [6], (b) double loaded square loops [7] and (c) complementary dual-layer Jerusalem cross structure [8].

More recently, it has been shown that three-dimensional (3D) FSS designs can provide enhanced fields of view over planar and cascaded designs, often up to 60° for one or both polarizations. Among these include designs consisting of planar microstrip lines arranged to form 3D multi-mode cavities [26]-[29] and those consisting of individual symmetrically formed elements [30][33], shown in Figure 1.5. Recent improvements in additive manufacturing techniques enable printing of single solid structures, which can be metalized and arranged into two-dimensional arrays. These approaches can eliminate layer

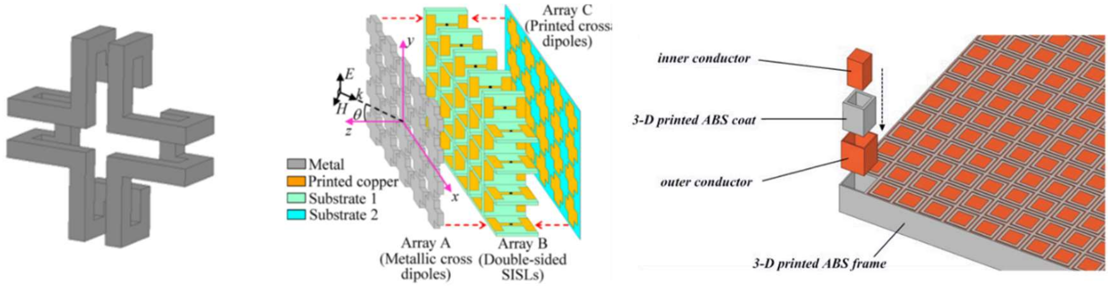

(a) (b) (c)

Figure 1.5. Example of 3D FSSs including a (a) folded loop [31], (b) multi-mode microstrip cavity [28], and (c) a loaded square waveguide array [33].

alignment issues introduced by cascaded designs, while capitalizing on miniaturization capabilities seen in fractal and meander-based FSS designs, at the expense of increased unit cell thickness. These fabrication techniques will be discussed further in Chapter 5.

While much work has been done to enhance Fields of View (FOV) for linearly polarized FSSs, far less work has been done to enhance the angular stability of FSSs for use with circularly polarized waves. Within this realm, three sub-categories have emerged, including Polarization Selective Surfaces (PSSs), Polarization Converting Surfaces (PCSs), and Circularly Polarized Frequency Selective Surfaces (CPFSSs). PSSs operate by discriminating between the handedness of incident waves, allowing transmission of either left/right handed polarizations and reflection of right/left polarized waves. Early innovations in PSS design included 3D trefoil knots [34] capable of separating left and right hand circularly polarized waves into forward and backward scattered components using their chiral geometry. Since then, other PSS designs have been introduced, including cascaded Multi-Layer Meander Line [35] and 3D Pierrot cell structures [36] that achieved 3dB Axial Ratio (AR) FOVs of up to 20°.

In addition to filtering handedness of circularly polarized waves, PCSs or polarizers have also been developed to convert incident waveforms to and from linear, elliptical or circular polarizations. This can be achieved by modifying the incident wave's magnitude and phase [37], using geometric chirality to rotate the polarization angle of incident waves [38], or using multiple layers to engineer a 90° phase difference between orthogonal polarizations [39]-[41]. When applied to conformal antenna geometries, this can dramatically improve an antenna's AR FOV [37]. Non-conformal applications of existing polarizers have been able to function with FOVs between 25° [41] and 45° [42].

Finally, CPFSSs that behave like traditional FSSs while preserving the polarization state of circularly polarized waveforms have also been proposed. Among these designs, an all-dielectric multi-layer surface optimized for millimeter wave applications demonstrated a 30° FOV [43]. More recently, an FSS-backed CP reflectarray and metallo-dielectric diplexer was introduced in [44] and [45]. In the case of the diplexer, the design consisted of a double-sided planar FSS with square loops of different dimensions that reflected and transmitted circularly polarized Ku- and Ka-band waves with a 3dB AR with up to 60° FOV. Examples of these designs are shown in Figure 1.6.

(a) (b) (c)

Figure 1.6. Examples unit cell geometries used in a (a) CPFSS diplexer [45], (b) chiral U-shaped PSS [38], and (c) Multi-Layer Meander Line PSS [35].

1.2 Motivation

Thus far, an overview of existing linear and circular polarized FSS designs have been presented. Over the years, designs have evolved from simple planar geometries to multi-layer structures and most recently, fully volumetric ones. Nonetheless, the vast majority of FSS designs to date are restricted to FOVs of 60° in one or both polarizations, and existing design methods have produced unit cells which are both electrically large and electrically thick, making application to conformal surfaces a challenge. While recent advancements in additive manufacturing techniques have inspired rapid prototyping of FSSs in a variety of polymers and metals, no design tools exist to leverage these manufacturing capabilities to surpass the polarization independence and angular stability of existing FSSs. Although traditional FSS engineers are likely to eschew such tools, preferring to focus on theoretical and analytical approaches in developing designs, wave interaction at oblique incidence on arbitrary 3D structures are not easily modeled at normal incidence, and even less so at oblique incidences. Additionally, research into 3D FSS designs are early enough in their nascence that having such a tool would provide valuable insight into benefits and drawbacks of fully 3D FSS designs. Once new innovative and unintuitive geometries are generated, they can be deconstructed and analyzed *ex post facto* to better understand their capabilities and further advance the state of the art. As such, this work aims to introduce a robust global optimization technique that can effectively search for ideal 3D FSS unit cell topologies that offer superior polarization independence and angular stability, while still maintaining an electrically thin and small profile, making them ideal for application to conformal surfaces.

1.3 Problem Formulation

The FSSs proposed in this dissertation are formed based on unit cells defined by the generalized pre-defined 3D wire grid shown in Figure 1.7, consisting of N_x by N_y by N_z PEC wire segments, and immersed in a homogeneous dielectric medium with relative permittivity ε_r. Under this formulation, unique 3D unit cell geometries can be formed via different combinations of PEC wire segments placed within the grid. Unit cells are arranged in a rectangular lattice and assumed to be infinitely periodic in the *x*- and *y*-directions, with incident waves impinging on them along the -*z* direction.

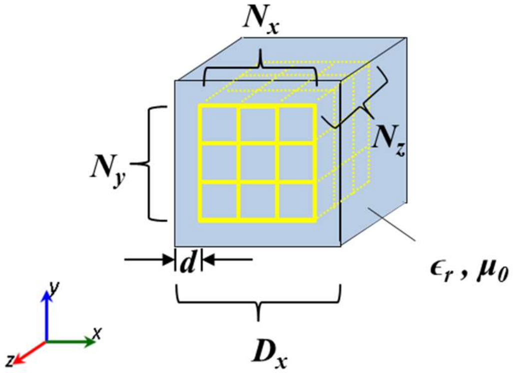

Figure 1.7. 3D FSS unit cell periodic in x and y, consisting of a pre-defined wire grid structure of $N_{xyz} = [N_x\ N_y\ N_z]$ wire segments with periodicity D_x, element to element spacing $2d$, permittivity ε_r and permeability μ_0.

In order to encourage polarization independence and angular stability, eight-fold geometric symmetry is imposed, implying $N_x = N_y$. Moreover, to prevent onset of grating lobes, a unit cell periodicity of $0.35\lambda_{max}$ is chosen, where λ_{max} represents the wavelength of the maximum operating frequency, and is considered the lowest frequency at which grating lobes are accepted at near-grazing incidence angles, according to [1]:

$$f_{g0} = \frac{nc}{D_x\left(\sin\eta + 1\right)} \tag{1}$$

where n is the diffraction order, c is the speed of light, D_x represents the unit cell periodicity and η is the angle of incidence. Based on the wire grid shown in Figure 1.7, this problem can be analyzed in the context of a combinatorial optimization or graph problem, where the interconnection of various nodes yields a unique solution.

Although nature-inspired evolutionary algorithm techniques such as Genetic Algorithms (GA) and Particle Swarm Optimization (PSO) have been employed in the past to design FSSs [46]-[49] and Artificial Magnetic Conductors (AMCs) [50][51], these structures were strictly planar in nature. Other 3D FSSs developed using GAs proved difficult to manufacture and only provided marginal fields of view [52]. In the next chapter, an overview of both GAs and PSO techniques will be given, along with an introduction to Ant Colony Optimization (ACO). The limitation of such approaches will be demonstrated and an improved optimization strategy, known as Multi-Objective Lazy Ant Colony Optimization (MOLACO) will be presented in Chapter 3. Simulated results will be presented in Chapter 4, demonstrating that MOLACO is well suited to the problem of both linearly and circularly polarized 3D FSS design for maximum angular stability and polarization independence. Chapter 5 explores existing additive manufacturing techniques that will be used to realize such designs, as well as methods and examples of dielectric characterization. Prototype optimized unit cells are manufactured and comparisons are made between measured and simulated results. Chapter 6 will provide examples of alternative applications of the MOLACO algorithm in antenna and metamaterial design, with a summary of key contributions and future work outlined in Chapter 7, including:

- The MOLACO algorithm and its unique features, including:
    - Modeling of lazy ants using phantom termination segments
    - Population-based adaptation based on masking or meander operators
    - Generalized graph representation for application to a variety of problems
    - A tandem Macro-GA technique that enables large-scale combinatorial optimization, *in situ* parameter optimization, or auto-adaptive colonies
    - Multi-Ant modeling for problems requiring enhanced degrees of freedom
    - Pareto-locus based search mechanism for generating libraries of unit cells for metamaterial design
- Polarization independent linear and circularly polarized 3D FSSs with wide FOVs
- Impedance matched meandered dipoles in a Near Zero Index Metamaterial (NZIM)
- 3D metallodielectric optical metamaterials in the Mid-Wave Infrared (MWIR) regime, which directly resulted in:
    - Discovery of ***highly transmissive metallodielectric*** structures with wide FOVs that cannot be achieved by planar metallodielectric structures alone
    - Demonstration of anomalous refraction of incident light using a phase-gradient metasurface supercell
    - Development and application of strategies to mitigate inter-element coupling effects among inhomogeneous supercells

Chapter 2

Optimization Algorithms in FSS Design

2.1 Genetic Algorithms

The GA is a global optimization algorithm which uses principles of evolution to form designs each generation. Solutions are encoded into a string of bits, also referred to as a chromosome, according to the number of states each component can take on. In this case, since the proposed FSS designs are generalized into a pre-defined 3D wire grid, each wire element (or gene) can assume one of two states, and the bit string is of binary form (zero for absent and one for present). Once an encoding structure has been determined, a pre-determined population size of randomly arranged chromosomes are initialized. At each iteration, chromosomes are decoded to generate their associated FSS structure, which is then evaluated using a full wave solver and assigned a fitness value according to some objective.

Once all chromosomes have been assigned fitness values, the mating process begins by choosing parent chromosomes, which is usually accomplished by roulette or tournament selection. Some GAs also enforce elitism, where only solutions with the best performance are used to form the following generation. In either case, once a set of parents has been selected, the next generation of chromosomes are formed by combining genetic information between parent chromosomes to form offspring chromosomes. This process is known as crossover and can occur in multiple ways, including uniform crossover, where all genes are equally likely of being exchanged, or single and multiple point crossover, where sets of gene information are divided at specific points and exchanged. An example of selection, single-point crossover and mutation are shown in Figure 2.1.

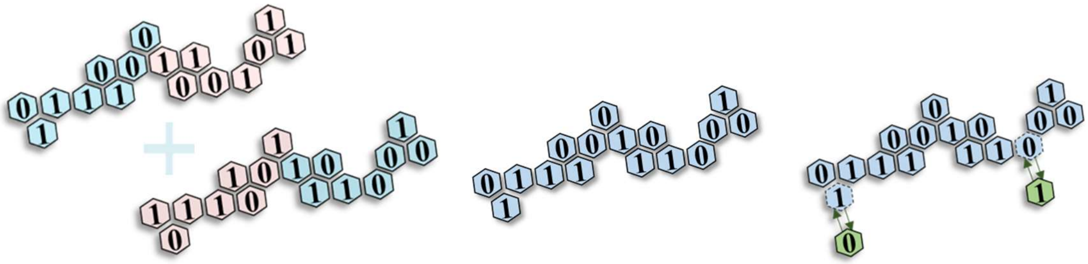

(a) (b) (c)

Figure 2.1. Example of (a) selection, (b) single-point crossover and (c) mutation of a chromosome in a GA optimization.

This process is repeated until a new generation of chromosomes is formed, and the process repeats itself until pre-determined termination conditions are met. A simplified overview of the entire process is outlined in Figure 2.2.

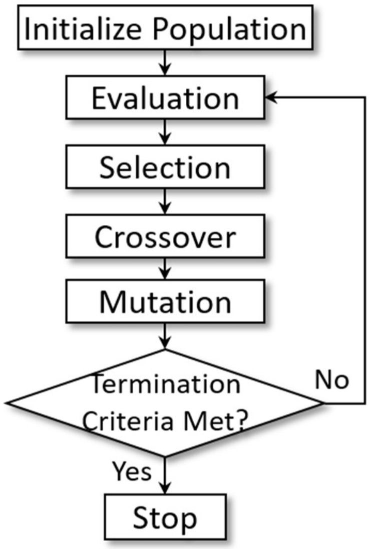

Figure 2.2. Flowchart of a typical GA procedure.

2.2 Particle Swarm Optimization

PSO belongs to the swarm intelligence family of evolutionary algorithms and is based on social behaviors of flocks of birds, schools of fish and swarms of insects [53]. For a problem with n parameters, each solution is represented by a particle in an n-dimensional space, which changes velocity based on its own performance and the holistic performance of the swarm. Particle motion is confined according to the boundary conditions set for each parameter. At each iteration, the location of the particle, and hence its associated design parameters, are updated according to a velocity, which changes according to three parameters: inertial weight, cognitive rate and social rates. The cognitive rate represents the influence of the particle's historical best solution, and hence its likelihood for individual exploration, whereas the social rate is a measure of how likely the particle is to follow the best solution found by the swarm thus far.

In electromagnetics, PSO has had applications in both antenna synthesis and FSS design [46][47]. PSO was preferred over the GA for FSS design in [46], since it is considerably less complex, has fewer parameters to adjust and requires only one operation every iteration: adjustment of particle velocity. Genovisi *et al.* further suggest that solutions generated by PSO are capable of performing multiple searches independently, whereas in GA implementations, all solutions are influenced according to the best chromosomes. In [46], multi-layer FSS design is achieved using a discrete binary implementation of PSO, which was introduced in [54] to replace the velocity parameter with a probability instead. This encoding methodology is identical to the GA, where the FSS is described by a set of binary parameters which determine whether metal or dielectric is present at each point. Early applications of GAs in planar FSS design were seen in [48], but only considered performance at normal incidence, with later attempts made in an all-dielectric 3D FSS design, in which FOV was also considered [52].

Although several fast and efficient forms of GA and PSO exist, their application in the problem of 3D FSS design is undesirable for two main reasons. First, the solution space grows exponentially with the dimensionality of the wire grid, resulting in a massive number of bits and a near infinite number of unique combinations. Second, having wire segments simultaneously independently activated or deactivated results in a high probability of generating fractured designs, as shown in Figure 2.3:

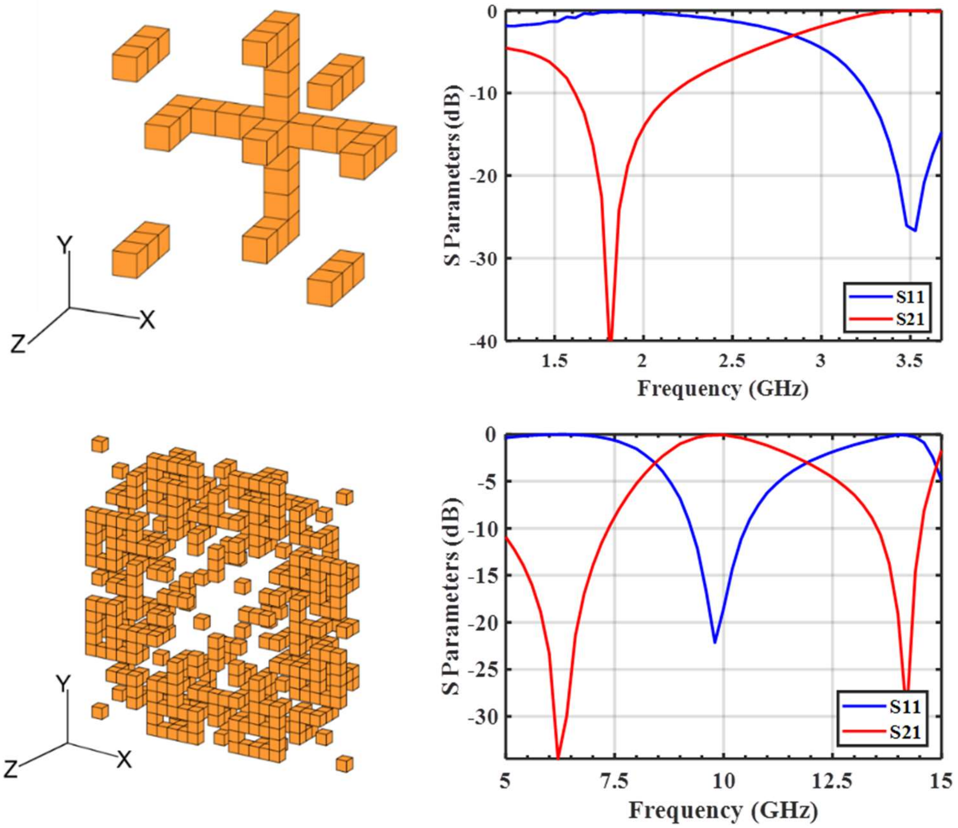

Figure 2.3. Examples of fractured 3D FSS geometries generated using a binary-encoded GA (left) and associated frequency responses at normal incidence (right).

In some cases, coupling between fractured components can introduce additional resonances, which can be desirable in applications requiring multi-pole responses. On the other hand, fractured designs remain difficult to manufacture, as wire segments or conductive particles remain floating within the medium, which can interfere with desired filtering responses by introducing unwanted coupling or scattering properties, especially at oblique incidences. While some of this can be mitigated by forcing adjacent segments to be connected, there is no guarantee that islands of wire segments do not form, since both GA and PSO approaches allow every wire segment of the design to be individually switched on or off. Additionally, forcibly shunting these fragments by either removing them or connecting them to their nearest neighbors fundamentally changes the geometry and overrides the evolutionary mechanism of the GA. As a result, it is desirable to find a combinatorial optimization method that is capable of generating contiguous structures. One alternative to the GA and discrete PSO that can do this is Ant Colony Optimization (ACO).

2.3 Ant Colony Optimization

2.3.1 Ant System

Several variations of ACO exist, including the original Ant System [55][56], the Max Min Ant System [57] and Multi-Objective Ant Colony Optimization [58]-[60]. In the past, these algorithms have been applied in designing planar Meander Line Antennas (MLAs) [61]-[64], corrugated filters [65] and linear antenna arrays [66]; however, this work represents the first known application of ACO in generating 3D FSS unit cells. ACO belongs to the swarm-intelligence family of nature-inspired optimization algorithms and is based on ant colonies' ability to collectively forage for food via an indirect communication method known as stigmergy. Stigmergic collaboration occurs between ants when they communicate with one another by modifying their local environment. This is best understood by considering the "double bridge experiment" performed on Argentine ants in [67], where two paths of different lengths are placed between an ant colony and a food source. Initially, since no pheromone concentrations exist nearby, ants randomly pick a path to travel in their forage. As they proceed along the path, they begin depositing pheromones. Future ants are able to detect nearby pheromones and become more likely to follow paths that have higher pheromone concentrations. Over time, the ants converge to almost exclusively using the shorter path, which has become saturated with pheromones, since early ants utilizing this path were able to reach the food source and return to the colony faster.

Based on empirical data gathered in [67], Goss *et al.* developed a mathematical model that described the likelihood for an ant to pick a particular direction, which served as the basis for modeling the stochastic decision-making process by ants in the first Ant Colony System [55][56]. All feasible paths available to an ant traversing an orthogonal 3D lattice are shown in Figure 2.4. Each direction has an associated probability, P_1 to P_6.

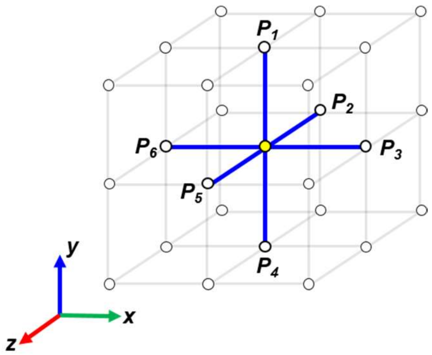

Figure 2.4. 3D segment selection for volumetric FSS design.

The corresponding mathematical model used to calculate the probabilities associated with each direction of travel is:

$$p_{xyz}^{k}(t) = \frac{\left[\tau_{xyz}(t)\right]^{\alpha}\left[\eta_{xyz}\right]^{\beta}}{\sum_{\{xyz\}\in N^{k}}\left[\tau_{xyz}(t)\right]^{\alpha}\left[\eta_{xyz}\right]^{\beta}} \tag{2}$$

Equation (2) represents the probability that ant *k* will select wire segment *xyz* with pheromone concentration τ_{xyz}(t) at time interval *t*. In general, η_{xyz} is a problem-specific parameter which represents heuristic information about segment *xyz*, while α and β correspond to the weights of the pheromone and heuristic information respectively. Since no known information about the value of selecting an arbitrary wire segment *xyz* is known ahead of time, only pheromone concentrations are considered and therefore $\alpha = 1$ and $\beta = 0$ for this application. The probability that an ant will occupy segment *xyz* is then given by the total pheromone concentration of segment *xyz* as compared to the cumulative pheromones available at all non-traveled *xyz* segments local to the *k*-th ant's neighborhood, N_k. If no segments are available in the neighborhood, the ant stops moving. At each iteration, the pheromones are then updated according to:

$$\tau_{xyz}(t+1) = \left(1-\rho\right)\tau_{xyz}(t) + \Delta\tau_{xyz} \tag{3}$$

where ρ represents the rate of pheromone evaporation and the change in pheromone $\Delta\tau_{xyz}$ traditionally varies according to the total pheromone contribution from m ants that have previously traversed segment *xyz*:

$$\Delta \tau_{xyz} = \sum_{k=1}^{m} \Delta \tau_{xyz}^{k} \tag{4}$$

The pheromone concentration is directly proportional to the solution fitness, *F*, according to a scaling factor, *Q*:

$$\Delta \tau_{xyz}^{k} = QF \tag{5}$$

This helps to scale the fitness to be of the same order as initial pheromone concentrations. One important mechanism to prevent ants from stagnating on a particular path is the evaporation of pheromones over time shown in (3). Nonetheless, if the number of ants traversing a particular trail far exceeds the rate of evaporation, a significant imbalance still occurs between segments with very large pheromone concentrations versus those that have completely decayed. This can quickly result in ants exclusively using well-traveled paths and no longer exploring new directions, leading to premature convergence to a sub-optimal solution. A summary of the traditional ACO procedure is given in Figure 2.5:

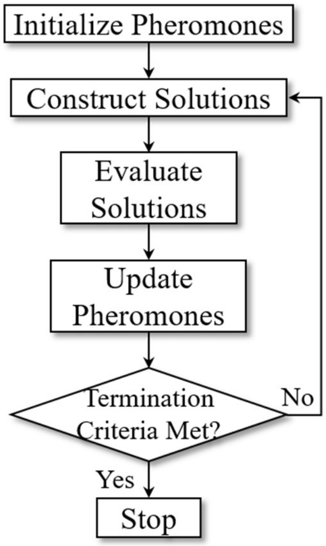

Figure 2.5. Ant Colony Optimization flowchart.

2.3.2 Max Min Ant System

The Max-Min Ant System (MMAS) introduced in [57] made two major changes to the traditional Ant Colony System. First, an elitist approach to pheromone updates was implemented whereby the aggregate pheromone concentration in (3) is instead replaced by only the best performing ant, $\Delta\tau_{xyz}^{best}$. Additionally, a constraint on the minimum and maximum pheromone concentration of all segments is enforced, such that no segment's pheromone concentration will decay to zero, and likewise, no segment's pheromone concentration could accumulate to infinity. This serves to balance the exploration versus exploitation aspect of the algorithm, guaranteeing that a minimum probability exists for exploring new directions, while further reducing likelihood of stagnation by making sure that no particular path overly dominates others. Studies performed in [57] demonstrated that MMAS performance was almost always superior when compared to seven other ACO variants in the Traveling Salesman Problem (TSP).

To illustrate the effect of introducing pheromone limits, surface contours of segment selection probabilities for an ant foraging in 3D space with five possible directions to choose from are shown in Figure 2.6. Since trails adjacent to the ant's location can take on a range of pheromone concentrations, depending on the fitness values associated with each, the probability of selecting a segment is shown for the two extreme cases: when ant k is in a neighborhood, N^k, of segments with minimum pheromone concentrations (τ_{min}), and a neighborhood with maximum pheromone concentrations (τ_{max}). Additionally, a range of pheromone levels for segment *xyz* are expressed using weighted values for the minimum and maximum pheromone limits, according to:

$$p_{xyz}^{k} = \frac{[\tau_1]_{xyz}^{\lambda_1}[\tau_2]_{xyz}^{\lambda_2}}{\sum_{\{xyz\}\in N^k}[\tau_1]_{xyz}^{\lambda_1}[\tau_2]_{xyz}^{\lambda_2}} \tag{6}$$

where $\tau_1 = \tau_{min}$, $\tau_2 = \tau_{max}$ and $\lambda_1 = 1 - \lambda_2$. The calculations are extended for a variety of dynamic ranges of maximum to minimum pheromone limits. It can be seen that for $\tau_{min} = \tau_{max}$, there is a constant 20% probability of selecting a particular segment, since this condition implies all pheromone concentrations must remain the same. The same probability occurs if a segment with minimum pheromone concentration (*i.e.,* $\lambda_2 = 0$) is surrounded by a neighborhood of minimum pheromones (left), and if a segment with maximum pheromone concentration (*i.e.,* $\lambda_2 = 1$) is surrounded by a neighborhood of maximum pheromones (right).

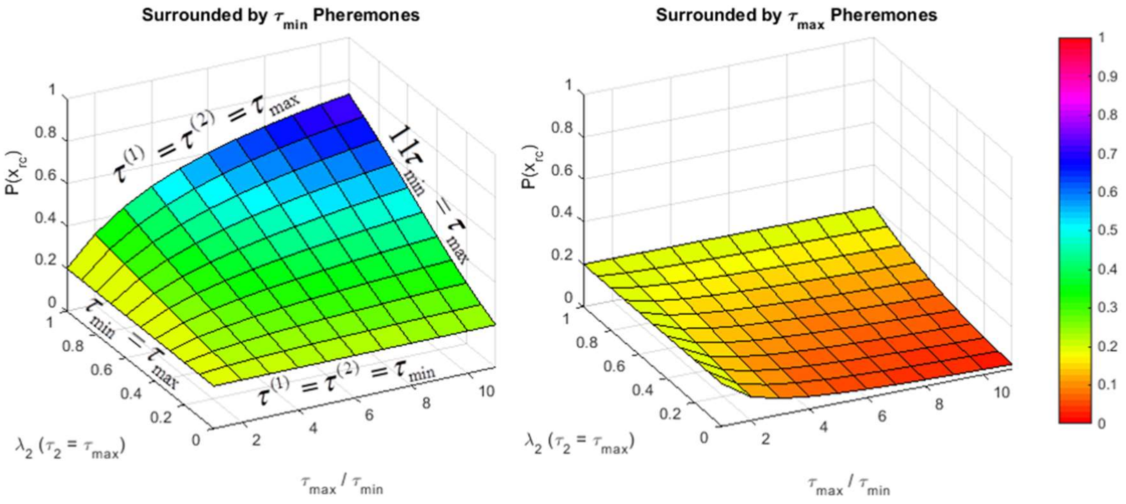

Figure 2.6. Probability surface for selecting a particular segment based on the dynamic range of τ_{max} / τ_{max}, when in a neighborhood of segments with minimum (left) and maximum (right) pheromone concentrations.

2.3.3 Multi-Criterion Ant Algorithm

Unlike single-objective optimization algorithms, multi-objective optimization techniques offer an effective way to identify a set of optimal designs by exploiting trade-offs between each objective as opposed to combining several performance metrics into a single fitness value with arbitrary weights. Each of the designs in the optimal set, also known as a Pareto set, can be considered as a result of a single objective optimization using a different weighting scheme. With regard to FSS design, although there are no known trade-offs between filter performance, angular stability and polarization independence, it is possible to exploit the inherent trade-off between stop and pass band performance to form a Pareto-optimal or non-dominated set of solutions. Solutions are considered non-dominated when they match or outperform all other solutions with respect to every objective. The key difference in multi-objective ACO algorithms is in the handling of pheromone information. Construction of ant trails and evaporation of pheromones continues to occur in the same way as traditional ACO.

Early implementations of ACO to multi-objective combinatorial optimization problems were limited to problems in which objectives could be prioritized by importance as in Multiple Objective Ant-Q (MOAQ) [58]. In MOAQ, each objective is assigned an ant colony and optimizations are sequentially performed starting with the most important objective. Within each colony, non-dominated solutions' pheromones are incrementally reinforced, whereas dominated solutions' pheromones are incrementally depleted. The updated pheromones are then used to generate designs in the subsequent colony. This process repeats until the algorithm converges on a set of only non-dominated solutions.

A more generalized multiple colony approach to a bi-objective optimization was proposed by Iredi *et al.* in [59], where no assumptions are made on objective importance. Unlike MOAQ, objectives are not assigned to individual colonies and pheromone data is individually maintained for each colony and objective. The segment selection probabilities are based on a maximally dispersed set of weights, λ, for each objective, which varies with ant k, $k \in [1, K]$, according to:

$$p_{xyz}^{k} = \frac{\tau_{xyz}^{\lambda} \cdot \tau_{xyz}'^{(1-\lambda)}}{\sum\limits_{\{xyz\} \in N^{k}} \tau_{xyz}^{\lambda} \cdot \tau_{xyz}'^{(1-\lambda)}} \tag{7}$$

where τ_{xyz} and τ'_{xyz} represent the pheromone data at wire segment *xyz* for each objective, and the set of maximally dispersed weight vectors are described by $\lambda = (k-1) / (K-1)$. Thus, for the first ant, $\lambda = 0$ and only the first objective is used to determine the ant's trail, whereas for the K-th ant, only pheromone information from the second objective applies. In the objective space, this approach allows each colony to explicitly explore a different region of the Pareto set, based on various trade-offs between the two objectives' pheromone data. Within each colony, a local non-dominated set of solutions is formed, representing the best ant trails generated by that colony at a particular generation. These solutions are then combined to form a global Pareto-set, and ant trails for each solution are evenly distributed across colonies to update their pheromones. This process is repeated until the maximum number of generations has been reached.

2.3.4 Limitations in FSS Design

Thus far, an overview of GA and PSO have been provided, with references to applications in FSS design, and an in-depth review of the current state of the art in ACO has been presented. While ACO solves the problem of isolated wire segments resulting in fractured designs, traditional ACO methods are inherently designed to be space-filling; that is, the meander travels indefinitely between nodes, never visiting a node twice and terminating only when it becomes trapped. Although traditional implementations of ACO are ideal for problems like the TSP and in the design of MLAs, they offer few advantages in FSS design. While some amount of space-filling is desirable for unit cell miniaturization, a completely space-filled unit cell would result in a solid Perfect Electric Conductor (PEC) block and offer no filtering value. Furthermore, since solution construction continues until boundary conditions are met, even when segments are correctly combined to form an optimal design, additional segments will continue to populate resulting in an "over-meandered" design, as shown in Figure 2.7. As a result, geometries consisting only of a subset of segments of fully meandered geometries are inaccessible in the solution space. Although over-meandered designs can appear to perform well at normal incidences, discontinuities are often formed as a result of unexpected coupling behaviors, which are further manifested at large angles of incidence.

Unfortunately, intelligently changing the meander rules and mitigating this effect requires either *a priori* knowledge about the effect that an arbitrary 3D convolution has on a given filtering response, which is difficult to predict, or requires multiple function evaluations at each meander-iteration of the current structure's fitness meander-iteration of the current structure’s fitness, introducing additional requirements to an already computationally burdensome problem. Therefore, since it is unrealistic to guide the meander in a desirable direction, two novel improvements to traditional ACO implementations are introduced in the next section to intelligently constrain the meander: adaptive colony masking and the use of lazy ants.

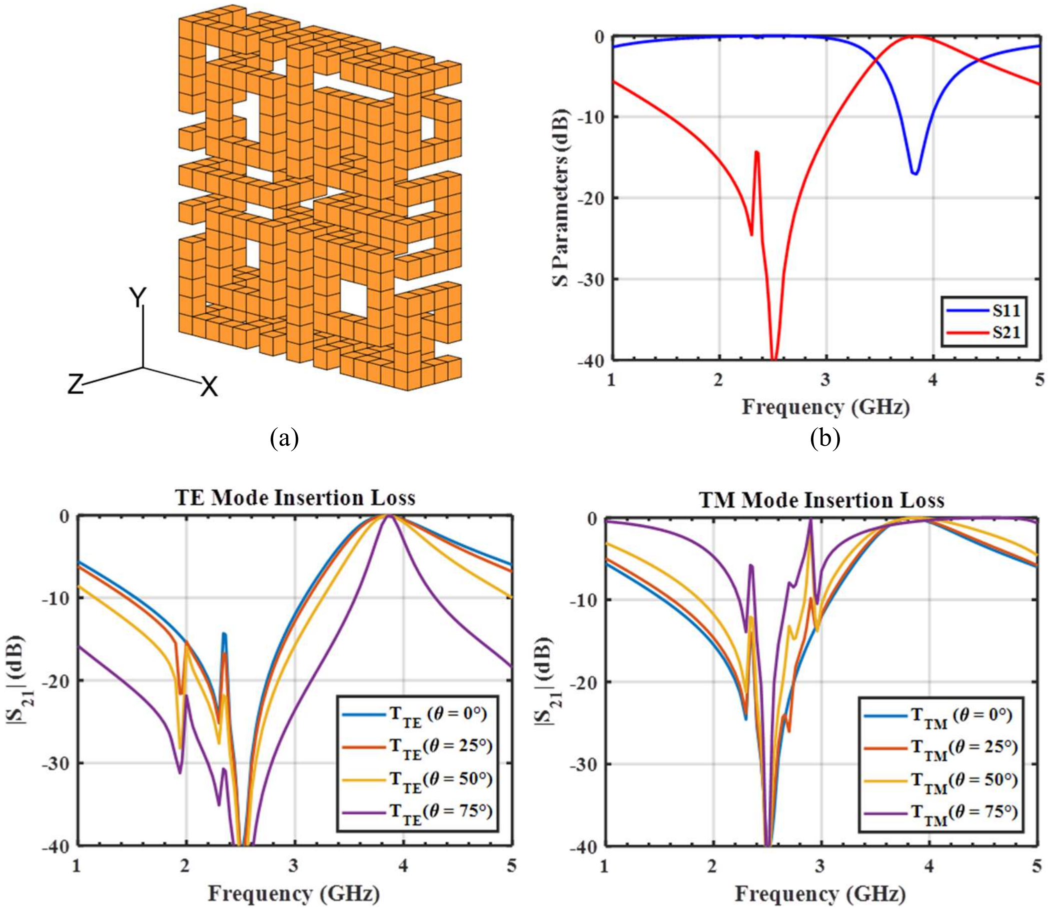

(a) (b)

(c) (d)

Figure 2.7. Example of a (a) space-filled, “over-meandered” design generated by traditional ACO methods, (b) corresponding frequency response at normal incidence as well as (c) TE and (d) TM responses at oblique incidences.

Chapter 3

Multi-Objective Lazy Ant Colony Optimization

3.1 Overview

Lazy ants represent a significant portion of an ant colony's population [68] and have been shown to be a key component of sustainability in ant colonies with respect to task allocation [69]. In addition, recent research in swarm intelligence suggests that lazy ants play key roles in exploration and sensing [70]. These concepts are heavily leveraged in MOLACO to increase the diversity of solutions generated in traditional ACO schemes by intelligently constraining space-filling meanders. Since meandering occurs until boundary conditions are met, colony masking works by simply applying constrained boundary conditions, whereas lazy ants introduce a probability of termination to the ant's decision-making process. MOLACO operates under the same framework as MO-ACO and MMAS, while leveraging high performance computing to parallelize both colonies and ants to quickly and efficiently converge to a Pareto-optimal set of 3D FSS designs.

The algorithm begins by initializing pheromones to their maximum values and defining a discrete set of n colony "masks," as shown in Figure 3.1. Masks are defined by restricting access to certain nodes and choosing start points such that canonical shapes (*i.e.* square and circular loops as well as principal and diagonal crosses) will most likely be formed. Each colony is divided into sub-populations of K^n ants that meander according to the boundaries established by these masks, with node selection probabilities proportional

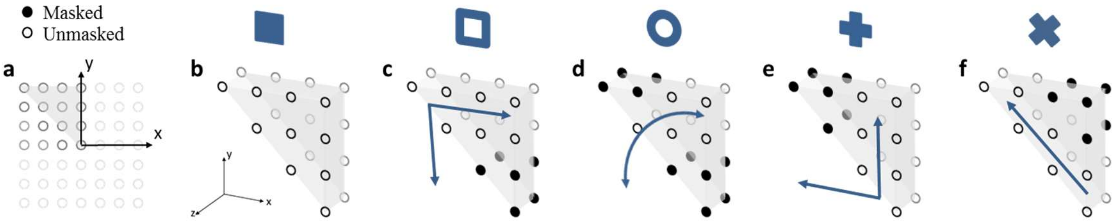

Figure 3.1. Illustration of (a) front view of a pre-defined wire grid with $N_{xyz} = [6\ 6\ 1]$, (b) isometric view of 1/8 of unit cell geometry (unmasked), and masked unit cell geometries corresponding to (c) square loop, (d) circular loop, (e) principal cross and (f) diagonal cross. Shaded circles represent restricted nodes, and arrows represent unmasked and therefore traversable regions, which result in the corresponding FSS geometries shown above after applying 8-fold symmetry. In the unmasked case (b), all nodes can be traversed and any fully-meandered design can be realized. © 2017 IEEE.

to the best fitness of each objective thus far. Additionally, each ant terminates their movement according to a unique fatigue profile described by an Endurance Factor, EF^k, which is discussed later. If the solutions have already been previously generated, results are retrieved from the archive. Otherwise, unique geometries undergo an 8-fold symmetry operation, are evaluated using an external solver, and assigned a fitness value. While any solver can be used with MOLACO, since FSSs are doubly infinitely periodic structures, a custom full wave solver based on Periodic Finite Element Boundary Integrals (PFEBI) is employed, which offers a fast and accurate way to perform full-wave simulations by taking advantage of Floquet boundary conditions. Once all solutions have been calculated, the archive is updated and new solutions are sorted according to Pareto-optimality using a Fast Non-Dominated Sorting (FNDS) routine [71]. The best Pareto set is then used to update the pheromone matrices for each colony by mask and objective. Finally, objective weights are updated by generation according to a maximally dispersed weight, λ_q, [60] and the process is repeated until termination criteria are met. An overview of the complete algorithm is given in Figure 3.2. The remaining sections in this chapter will introduce fitness criteria for a variety of FSS types, adaptive colony masking, phantom termination segments and provide a comparison of diversity between MOLACO and traditional ACO algorithms. Finally, advanced capabilities including multi-ant modeling, graph generalization, and tandem operation with a GA will be introduced.

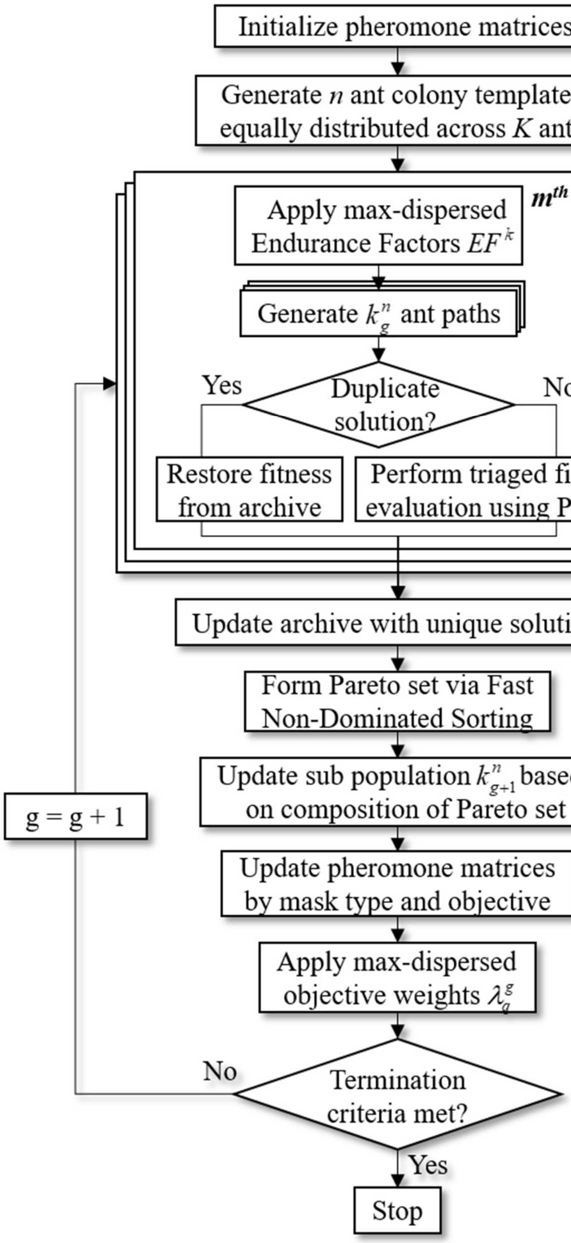

Figure 3.2. Proposed Multi-Objective Lazy Ant Colony Optimization flowchart, incorporating key elements of MMAS and MCAA. © 2017 IEEE.

3.2 Fitness Evaluation

For any optimization algorithm to be successful, development and implementation of a robust fitness function is critical and begins with understanding the dynamics of the problem. An ideal fitness function is fast, efficient and accurately classifies all designs in the solution space. The PFEBI approach combines Finite Element Method (FEM) with Method of Moments (MoM), offering a fast and accurate way to evaluate S Parameters over a broad range of frequencies. Based on the numerically solved reflection and transmission characteristics of the structure, a quantitative measure of an ideal arbitrary FSS design can be assigned based on a desired stop/pass filter response in the following domains:

- Specified pass/stop frequencies and bandwidths
- Multiple incidence angles from normal to oblique
- Both TE and TM incident polarization states

This inherently requires sampling of multiple frequencies and incidence angles for each polarization; thus, for f frequency points of interest, m incidence angles, and two polarization states, at least $2 \cdot m \cdot f$ function evaluations are required per design. This cannot be avoided without sacrificing performance in one or more domains.

One approach to minimizing the computation time is by choosing reasonable values for N_x, N_y and N_z to balance the number of mesh elements (directly proportional to the number of wire segments and therefore the duration of a function evaluation) with the total number of feasible segment combinations. If the values of N_x, N_y and N_z are too small, function evaluations will be rapid, but few solutions will exist in the design space to meet the specified criteria. If N_x, N_y and N_z are too large, the time required to perform the optimization will exponentially grow. Even for a reasonably sized geometry, a large design space is still expected, with only a fraction of solutions that satisfy the desired bandwidth, field of view and polarization independence. Therefore, it is equally important to perform function evaluations only when necessary, which can be achieved by maintaining an archive of previous solutions, and intelligently triaging function evaluations.

Since angular stability can only be achieved if filtering performance is consistent across a continuous range of incidence angles, it is not necessary to evaluate designs at oblique incidences if they do not exhibit stability at smaller angles. Because the design space is large, and few ideal solutions are expected, triaging function evaluations in this manner drastically reduces computation time spent, quickly separating weaker designs from better ones, while investing more time on designs that show potential. For example, if a design does not yield any TE or TM bandwidth for an angle θ_n, the bandwidths at angle θ_{n+1} are not evaluated. However, as long as the design achieves some non-zero bandwidth at θ_n, the next angle, θ_{n+1}, will be evaluated. In this manner, designs are only rewarded for progressively better performance, which provides a gradient to the fitness surface to guide the optimization algorithm's search. Finally, maintaining an archive of unique solutions allows fitness values to be restored from the archive if duplicate geometries are generated, rather than entirely re-evaluating them. This is particularly useful for smaller values of N_x, N_y and N_z, where duplicate geometries are more likely.

While these strategies undoubtedly improve algorithm efficiency, accounting for all of these parameters implies a fitness function in the form of a weighted sum, and special care must be taken not to bias it according to angle, polarization or band. Since a large number of terms and no *a priori* knowledge of their associated weights is known, a multi-objective approach provides an effective method to explore the various weights associated with each term. A summary of the optimization strategy is illustrated in Figure 3.3.

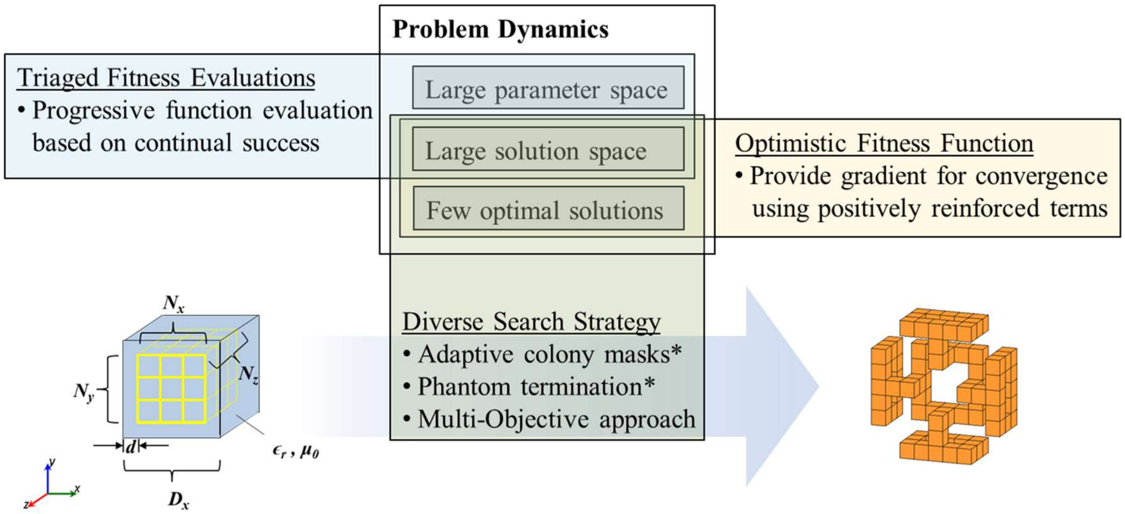

Figure 3.3. Optimization strategy for a generalized FSS unit cell based on a pre-defined three-dimensional wire grid immersed in a homogeneous non-magnetic dielectric. Using these techniques, a set of Pareto-optimal solutions can be quickly and efficiently found. Key differences from traditional ACO implementations are denoted with an asterisk (*) and discussed further in Sections 3.3 and 3.4.

Finally, although the fitness function is used to assign a metric of performance to a single design, this value must be considered in the context of other solutions within the design space. For a large solution space in which ideal solutions are expected to be few and far in between, an optimistic approach to fitness evaluation must be applied, where some gradient between the worst performing designs and the best performing designs is formed as time prevails to provide the optimization algorithm with a non-random search direction. Since few good solutions exist, fitness terms should describe how well designs perform, rather than how poorly they perform, as bad performing designs are abundant, and will do little to guide the search toward good designs.

3.3 Adaptive Colony Masking

An unconstrained design generated by ACO initially arbitrarily meanders within the confines of the pre-defined wire grid. As a result, designs can take on a variety of forms and shapes, as shown in Figure 3.4.

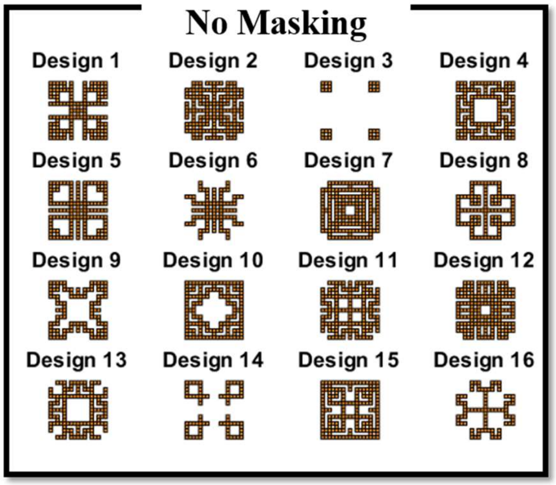

Figure 3.4. Example of FSS unit cell geometries generated without masks.

For a given generation of ants, the geometries explored are largely dependent on the start point of the ants, and the boundary conditions of the colony. These two parameters have a significant impact on the final geometry of each design and while it is not possible to intelligently control the meander in a meaningful way, it is possible to confine the meander to a pre-defined shape. In this section, fully meandered designs confined to select canonical shapes (*i.e.* square and circular loops as well as principal and diagonal cross type designs) are generated within a colony of 64 ants, as seen in Figure 3.5. In each of these cases, the designs generated generally satisfy the intended geometry type of the associated mask. Thus, by employing masking, it is possible to emulate multiple instances of traditional ACO simultaneously, each representing a unique colony based on boundaries established by each mask type. As will be seen later, this approach contributes to enhanced diversity of solutions generated by MOLACO.

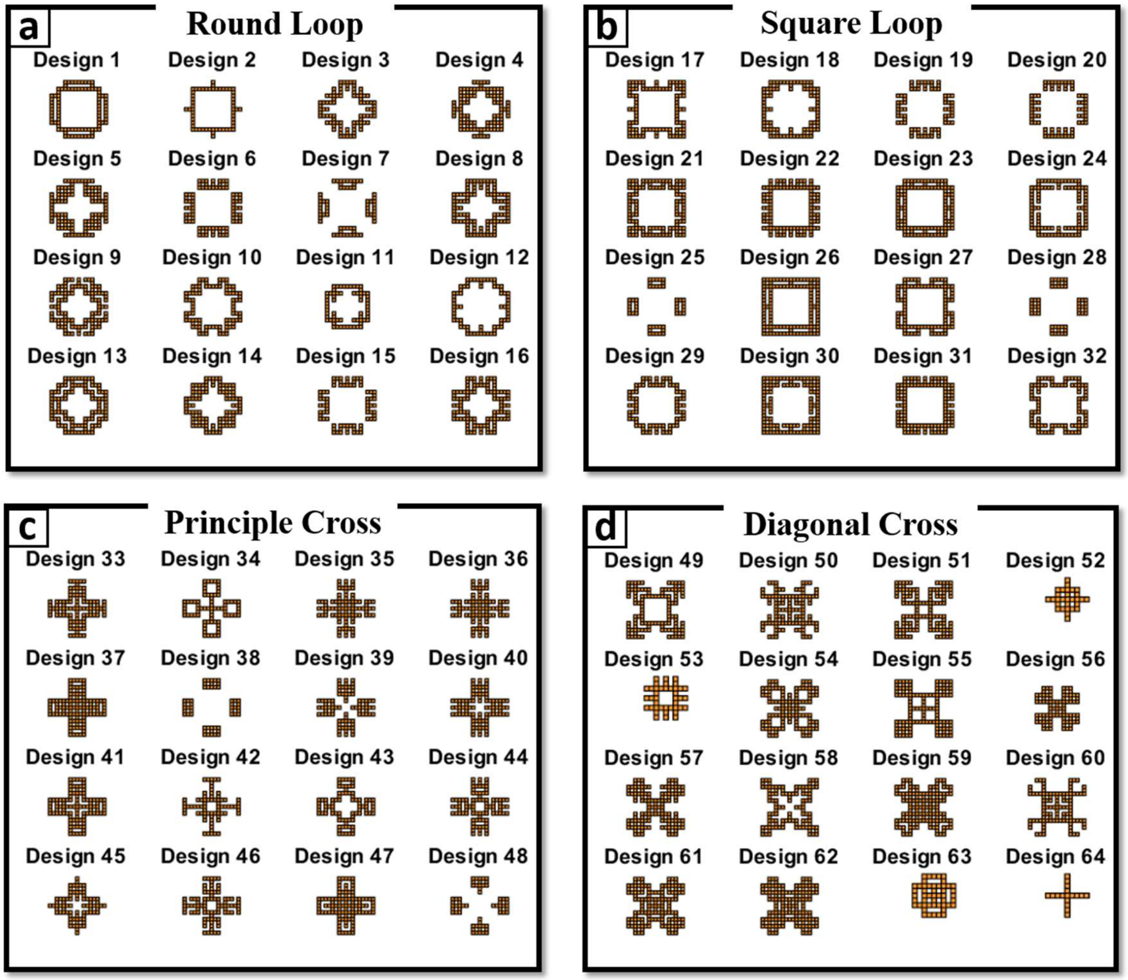

Figure 3.5. Examples of FSS unit cell geometries using mask based on canonical shapes, including (a) round loops, (b) square loops, (c) principle crosses and (d) diagonal crosses.

The challenge with this approach is choosing the appropriate mask without *a priori* knowledge that a given geometry is ideal for a specified filtering response. Furthermore, since colony masking alone is fundamentally no different than running multiple optimizations with different colony sizes and picking the best results from the set, an adaptive population-based masking strategy is used. Using this approach, the number of ants assigned to a given mask increases if the designs outperform other masks and decreases otherwise. This is similar to the evolutionary strategy suggested in [72], in which the population adapts proportionately to the number of solutions in the current Pareto set. This method allows the best Pareto solutions to be exploited across all colonies and is preferred, however, an alternate strategy to encourage de-centralized exploration can also be employed. For example, a z-score metric can be applied, where at each iteration, the average performance of each mask is expressed in terms of standard deviations from the overall average performance of the entire colony. Sub-populations for the next iteration are then adjusted proportionally based on the calculated z-scores.

With the introduction of masks, pheromone management becomes slightly more complex, since pheromone trails for one mask are not applicable to another, due to mismatched boundary conditions. Therefore, for each colony, it is necessary to maintain one set of pheromone data for each mask, as well as each objective. Furthermore, since assigning a single mask to a colony would preclude colonies from collaborating, and hence offer no advantages to multiple single colony optimizations with different boundary conditions, multiple masks are used in each colony and assigned sub-population sizes. At the start of the algorithm, all masks are equally populated with sub-population sizes updated at each generation. The best-ever Pareto-optimal ant trails for each mask type are then used to update the pheromones data for their respective masks within each colony. To encourage continued exploration, a minimum sub population size is enforced, such that no mask is ever completely eliminated from a generation.

While the proposed masks take on the form of different templates from which geometries are generated, in the most general sense, these masks represent geometric operators. In other words, while a meander is stochastically generated by the underlying ACO mechanism, some operation must be performed on the meander to generate the final geometry, and different operations performed on the same meander will yield different geometries and therefore different performances. Thus, it is also possible to adapt by a set of operator types and not just masks. Examples of these operations can include symmetry, fractalization and rotation among others.

3.4 Phantom Termination Segment

While adaptive colony masking by selectively applying start points and boundary conditions encourages exploration of different design geometries, it still does not address the issue of a “runaway” meander. Therefore, the concept of a phantom termination segment is introduced. At a given vertex within the pre-defined 3D wire grid, an ant has up to five available directions along each principle axis (x, y, and z) that it can travel to next, since backtracking from the direction of arrival is not allowed. The phantom termination segment essentially gives the ant a sixth option: cease travel altogether. An illustration of this behavior is shown in Figure 3.6.

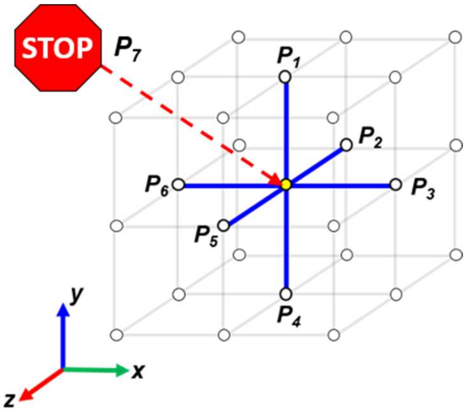

Figure 3.6. In addition to the standard probabilities ($P_1 - P_6$) associated with each available path direction, a new probability, P_7, is assigned to a phantom termination segment, which determines the likelihood the ant is lazy and remains in place.

The phantom termination segment can be implemented in several manners: it can serve as a constant probability of termination, or progressively increase, making termination more likely as meander length increases, similar to fatigue. Since termination probability is independent of solution fitness, the termination pheromone is maintained separately from the regular pheromones, and not subject to the constraints imposed by MMAS. This is easily done by using complex notation to represent pheromones, where the real component represents the likelihood of traveling a particular direction, and the imaginary component represents the likelihood of termination. To further enhance diversity, a maximally dispersed fatigue profile is proposed, similar to the objective weighting scheme used in equation (6), ensuring each ant within a colony experiences a different fatigue. However, both objectives and fatigue profile cannot be simultaneously maximally dispersed within each colony in this manner. This is because doing so would unfairly bias searches by causing designs where one objective is weighted to be fully meandered, and those in the other to be fully truncated. Instead, the objective weighting scheme is adjusted to be maximally dispersed by generation [60], which achieves a similar effect of directed searches at each generation.

The selected fatigue profile must ensure that truncation does not occur until a minimum number of segments have been populated, and truncation is guaranteed by the time the maximum number of segments is exhausted. One appropriate model can be described by:

$$Fatigue = \left({}^{l}\!/_{L} \right)^{EF} \exp(\nu) \tag{8}$$

where *l* represents the current number of segments traversed and *L* represents the maximum number of segments feasible. A good approximation to *L* can be made based on the mask applied, since *L* can never exceed the total number of segments confined by the mask. The Endurance Factor (*EF*) is a measure of how many segments an ant can travel before being exhausted, whereas *v* is a measure of the maximum termination pheromone that can be accumulated. The larger *v* is, the faster the imaginary pheromone count increases. Similarly, *EF* controls the rate at which fatigue sets in; the lower it is, the sooner fatigue sets in. Since the pheromone concentrations at each segment vary in an unpredictable manner, but have a finite limit based on MMAS, the fatigue profile in Figure 3.7 is plotted according to the best and worst-case scenarios. This demonstrates the range of feasible termination probabilities experienced by the ant, when in a neighborhood of maximum ($\tau_{max} = 0.5$) and minimum ($\tau_{min} = 0.1$) pheromone concentrations.

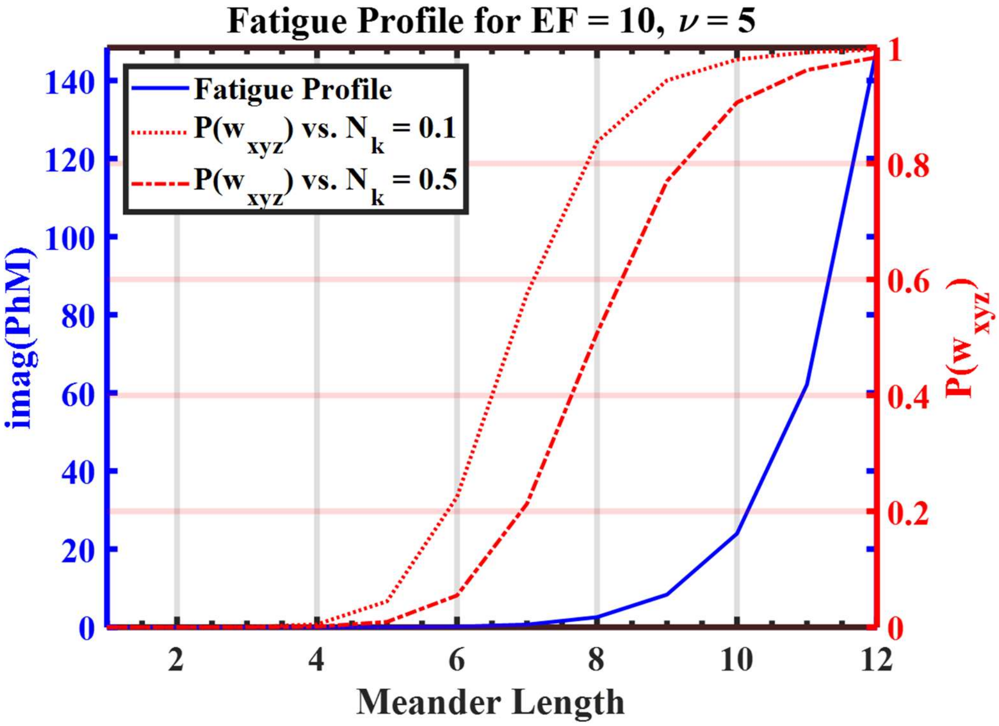

Figure 3.7. Fatigue profile using an Endurance Factor (*EF*) of 10 and Fatigue Factor (*FF*), $\nu = 5$, normalized to a geometry of $N_{xyz} = [4\ 4\ 1]$ with maximum meander length of $L = 12$ segments. The left axis represents the magnitude of the imaginary pheromone concentration, and the right axis corresponds to the probability that termination will occur for the given imaginary pheromone concentration as compared to a neighborhood of maximum pheromones (dash-dotted line) and minimum pheromones (dotted line). © 2017 IEEE.

In order to maximally disperse fatigue profiles within a colony, *EF* is varied by ant across each mask's sub population, resulting in a variety of ants who are very lazy, terminating almost immediately, as well as those which are hyperactive and only terminate after exhausting all meander options. As a result, a thorough investigation of the search space is performed at each iteration, for each mask, including both space-filling and non-space filling designs.

3.5 Comparison with Traditional ACO

For a wire grid dimension of $N_{xyz} = [4\ 4\ 1]$ using four colonies and a population size of 192 ants over 40 generations, a comparison of the total number of unique ant trails generated using both MOLACO methods versus nominal ACO with uniform (u) and dispersed (d) fatigue profiles is given in Table 3-1. Regardless of method, it is evident that all approaches unique to MOLACO offer access to designs that are not feasible in traditional ACO implementations. Furthermore, Figure 3.8 shows that a dispersed fatigue profile offers superior diversity in the generation of unique ant trails and accumulates unique solutions more rapidly. With regard to masking, the initial population size is equally distributed across five masks (circular loop, square loop, principle cross, diagonal cross and no mask). For this reason, masking takes longer to accumulate unique solutions since fewer members of the population are available to construct solutions per mask. Additionally, although the number of new unique solutions generated via masking appears relatively small, this is expected since a small wire grid dimension is used and masking serves only to further reduce the number of accessible wire segments. Thus, while masking is capable of achieving unique designs by directing meanders in different shapes, it comes at the cost of fewer possible designs overall requiring either a larger population base or more iterations to fully reach its potential. Since unmasked colonies are able to access more trails than masked ones, the population distribution is initialized with 50% of the population committed to unmasked design, and the rest equally distributed among other mask types.

Table 3-1. Comparison of Unique Ant Trails generated by MOLACO vs. Traditional ACO.

Method	Unique Trails	% New Designs
nominal	1,086[1]	-
masked	981	16.8%
lazy(u)	1,603	79.6%
lazy(d)	2,047	126.3%
both(u)	1,419	74.6%
both(d)	1,697	101.7%

[1] The total number of unique fully-meandered solutions for this geometry is 1,376, based on brute force exploration.

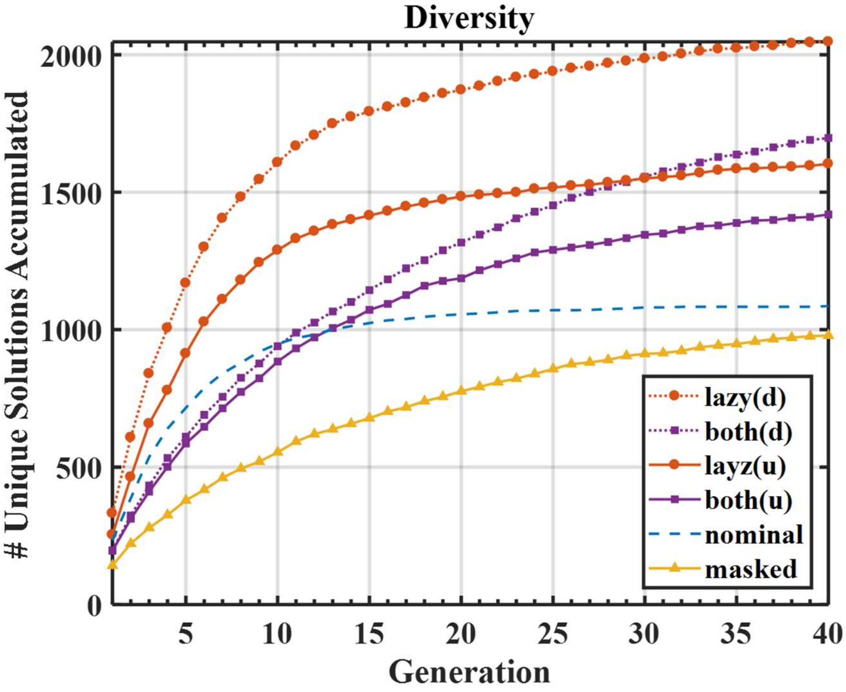

Figure 3.8. Comparison of solution diversity accumulated by MOLACO methods versus traditional ACO. © 2017 IEEE.

With the exception of masking on its own, a closer examination of the population members by meander length shown in Figure 3.9 confirms a marked increase in designs that are not fully meandered, validating that both colony masking and phantom termination segments make MOLACO a suitable contiguous combinatorial optimization algorithm for 3D FSS design, as well as other applications, including data mining, routing problems and topology optimization. In the next section, a generalized implementation of MOLACO will be shown, in which the capability to represent arbitrary network topologies will be demonstrated.

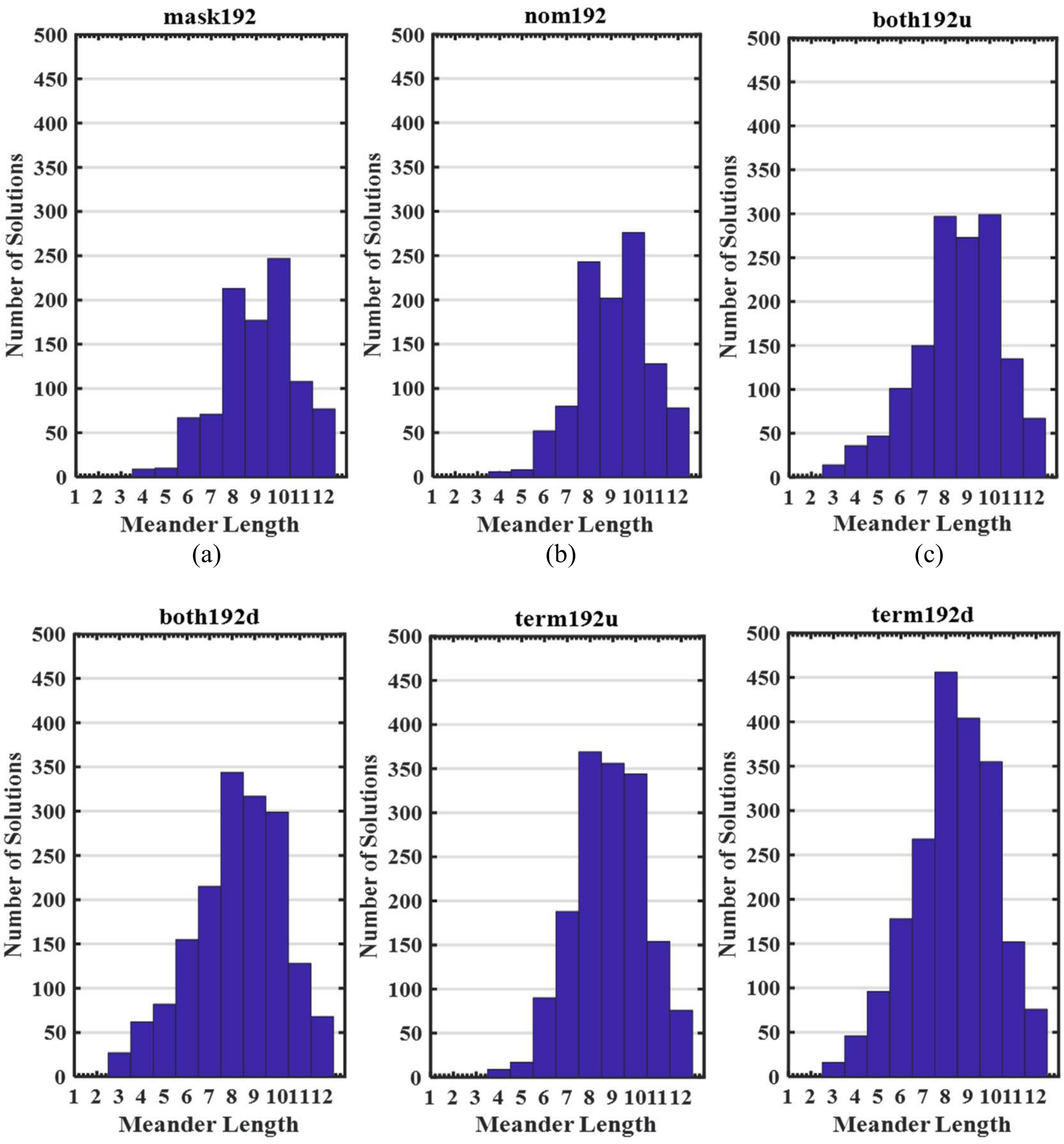

(a) (b) (c) (d) (e) (f)

Figure 3.9. Final population distributions according to meander length after 40 generations of population 192 for an N = [4 4 1] grid size, arranged in order of least to most unique solutions for various MOLACO methods, including (a) masking, (b) traditional ACO, (c) masking and uniform fatigue profiles, (d) masking and dispersed fatigue profiles, (e) uniform fatigue profile and (f) dispersed fatigue profiles. © 2018 IEEE.

3.6 Generalized MOLACO

In addition to the population-adaptive colony masks, and phantom termination segments, a wide variety of additional enhancements are made to the MOLACO algorithm. Perhaps the most important enhancement is generalization of the meander space to an arbitrary graph representation. In traditional applications of ACO, where the topology of physical devices is optimized, users typically establish a pre-defined uniform meander grid, which contains some spatial relationship suited to the design space of the problem. As a result, feasible designs are dictated by the selected value for grid spacing and exploring other grid spacing options would require multiple additional optimizations, which quickly become time consuming and cumbersome to manage. However, by abstractly defining the relationships between nodes on a meander grid, and disassociating them with fixed, spatial coordinates, it is possible to apply the algorithm to a variety of new problems, and also define custom grid transformations.

Although MOLACO was originally designed for the problem of 3D FSS design, a generalized version of MOLACO provides a robust and versatile tool for optimizing network structures for a wide variety of problem sets, including artificial intelligence, routing problems, and topology optimization to name a few. Whereas the FSS variant of the algorithm concentrated on physical representations using a square grid graph network, the generalized MOLACO algorithm is capable of optimizing graph paths of arbitrary N-dimensional graph topologies, which can be useful in problems where relationships are more important than physical geometries. Examples of some of these arbitrary network topologies are given in Figure 3.10. In general, graphs can take on a uniform grid graph, an arbitrary graph, or even an image-based graph. A uniform grid graph is useful for optimization of physical structures and can be manipulated to conform to any coordinate system. Although the grid graph in Figure 3.10(a) is visualized according to a cartesian coordinate system, nodes can just as easily be mapped to a cylindrical, spherical or other arbitrary system, allowing for optimization of geometries on conformal surfaces. Arbitrary graphs can characterize problems where non-spatial relationships are important; examples of this include analysis of computer network architectures, or social networks to evaluate network centric metrics such as degree, centrality and so forth. Image-based graphs showcase a creative way of applying graph networks and has potential applications in image processing.

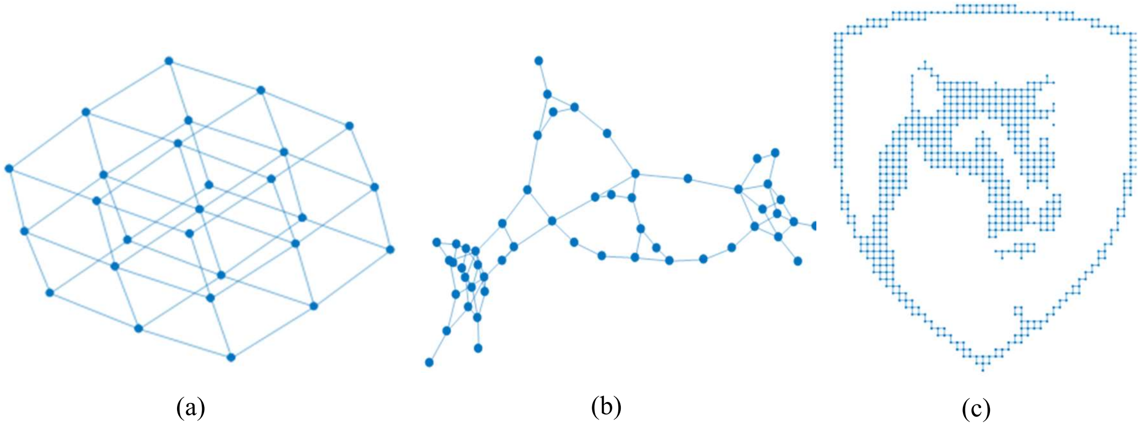
(a) (b) (c)

Figure 3.10. Examples of (a) grid graph, ideal for problems where spatial geometries are being optimized, (b) arbitrary graphs where non-physical relationships may be more important and (c) image-based graphs.

By representing the relationships of the meander grid in graph form, the MOLACO algorithm becomes generalized and the problems it can be applied to are left entirely to the user's imagination. In this way, the MOLACO algorithm is only as limited as the solver it is paired to, and the physical limitations set forth by manufacturing processes. This enhancement will be instrumental in writing custom applications of MOLACO to a variety of problems, including 3D FSS design, optical antenna design, metamaterial optimization and impedance matching of meandering dipoles embedded in a NZIM.

3.7 Multi Ant Modeling

Another valuable enhancement of the MOLACO algorithm is the introduction of the multi-ant modeling capability. Thus far, the proposed design methodology has entailed the use of single ant trails across several colonies using a multi-objective approach, with each colony divided into sub-populations according to mask type. Although one of the primary motivations for using ACO (as opposed to GA) was to generate contiguous geometries according to the foraging behavior of a single ant, in some cases non-contiguous designs can provide benefits, including additional coupling behaviors and resonances. While GA approaches result in designs that are highly fractured, the same benefits can be achieved in a controlled manner through the use of multiple ants. This can be done by defining a “super cell” template which is composed of a pre-defined subset of independently meandering ants.

While each ant forages independently on its own, fitness values are assigned based on the collective behavior of all of the ants. Just as each segment of a single ant trail was uniformly assigned the same pheromone values with respect to each objective previously, in this case, each trail of the supercell is assigned the same pheromone values with respect to each objective, however, the pheromones are stored separately so that each element’s foraging mechanic is independent of the others. Additionally, since each ant is considered a mask, and an ant from each mask collectively constitutes the super cell, sub-populations for each mask must remain equal, and population-based adaptation cannot be used. Examples of these types of structures are shown in Figure 3.11.

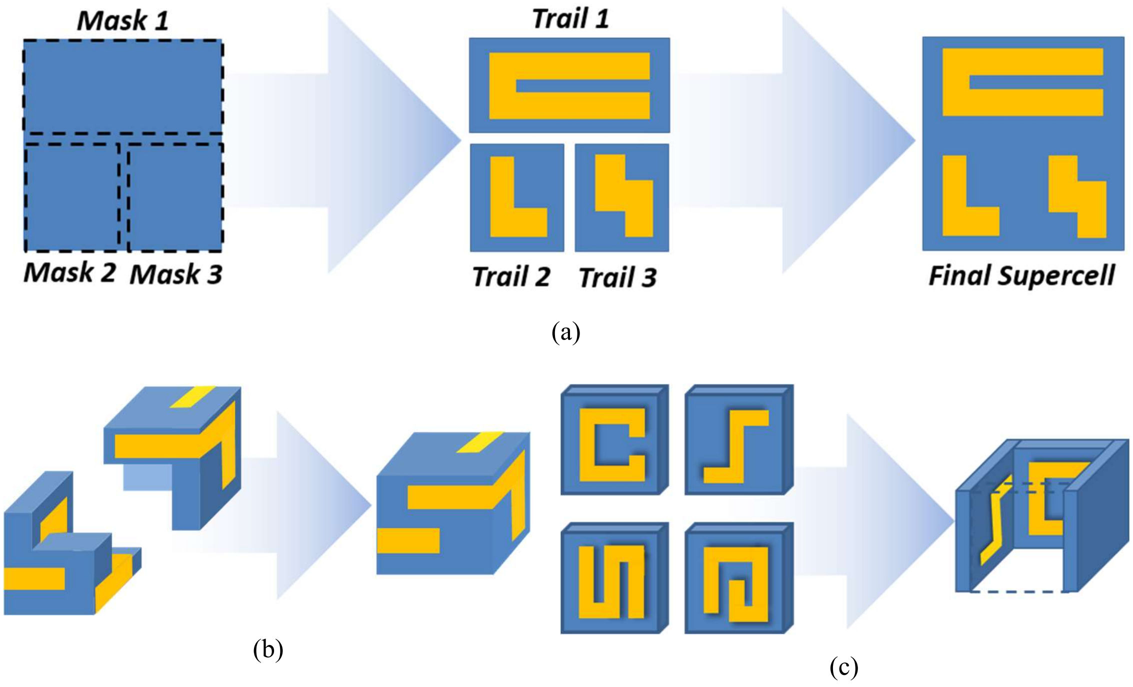

(a)

(b)

(c)

Figure 3.11. Examples of multi-ant modeling, including (a) masking methodology, trail generation and formation of supercell for a co-planar geometry, as well as (b) three-dimensional puzzle piece and (c) card house geometries.

3.8 GA-MOLACO

In addition to the advancements highlighted thus far, since MOLACO is inherently a combinatorial optimization scheme, the problems it will be used to solve are naturally suited towards pairing with a GA. Although the GA was initially avoided for the problem of 3D FSS design, due to generation of non-contiguous solutions, it can be intelligently paired with MOLACO to leverage the global exploration capabilities of the GA to perform in-situ parameter optimization, while still generating contiguous designs. Although previous works with traditional ACO algorithms have employed GAs with applications in computational biology [73], and topology optimization [74], these works pre-date the introduction of MOLACO, and placed the algorithms in series, with the latter acting as a local optimizer. The proposed implementation of GA is done in tandem with MOLACO, transforming it into an auto-adaptive scheme, offering even greater search diversity, and enabling both large-scale combinatorial optimization problems as well as *in situ* parameter optimization. This pairing is referred to as a "Macro" GA (MGA), since the chromosomes

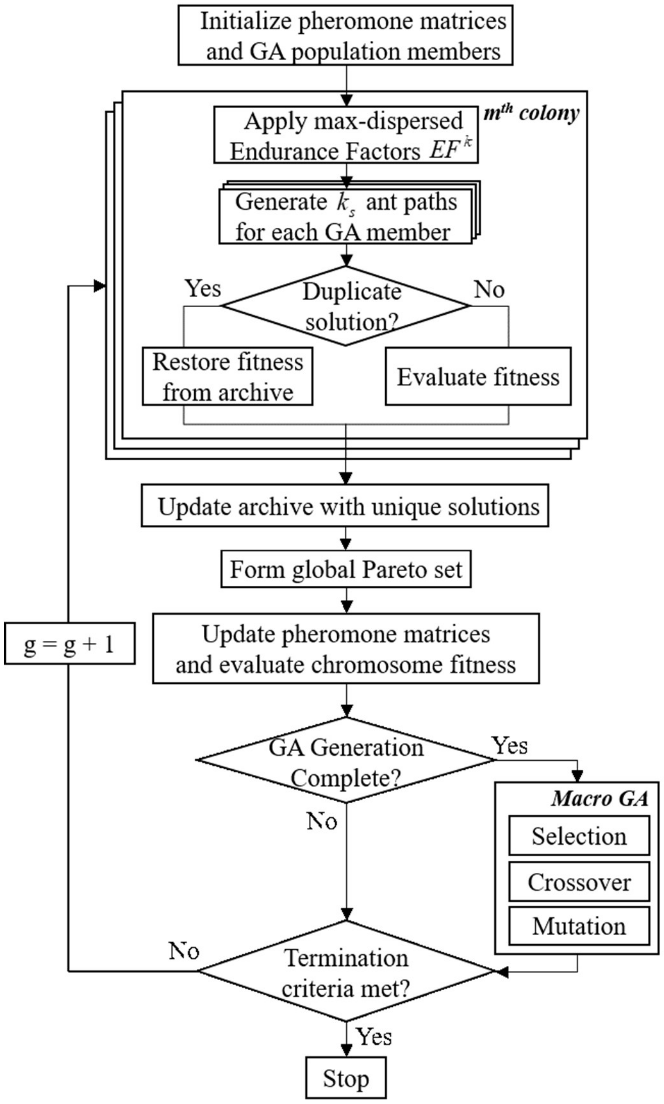

Figure 3.12. Flowchart of a Macro-GA driven MOLACO algorithm.

represent traits associated with an entire population of designs, versus an individual design under traditional GA implementations. The entire procedure is outlined in Figure 3.12. Although a given binary GA bit string still represents a chromosome, and each bit still represents a gene, the LACO variations can be considered alleles, or variants of those genes, forming a more complete analogy of evolution. In this way, the MGA is responsible for higher level evolution of the chromosomes and genes, whereas the LACO optimizes subsets of the populations exhibiting the traits described by those genes. An example of this is illustrated in Figure 3.13. Whereas traditional binary GA genes can occupy two states that collectively result in a single design, for a given set of genes, the MGA can take on as many designs as are accessible in the design space via MOLACO. The contiguous geometries generated by MOLACO are sampled based on a pre-determined sample size

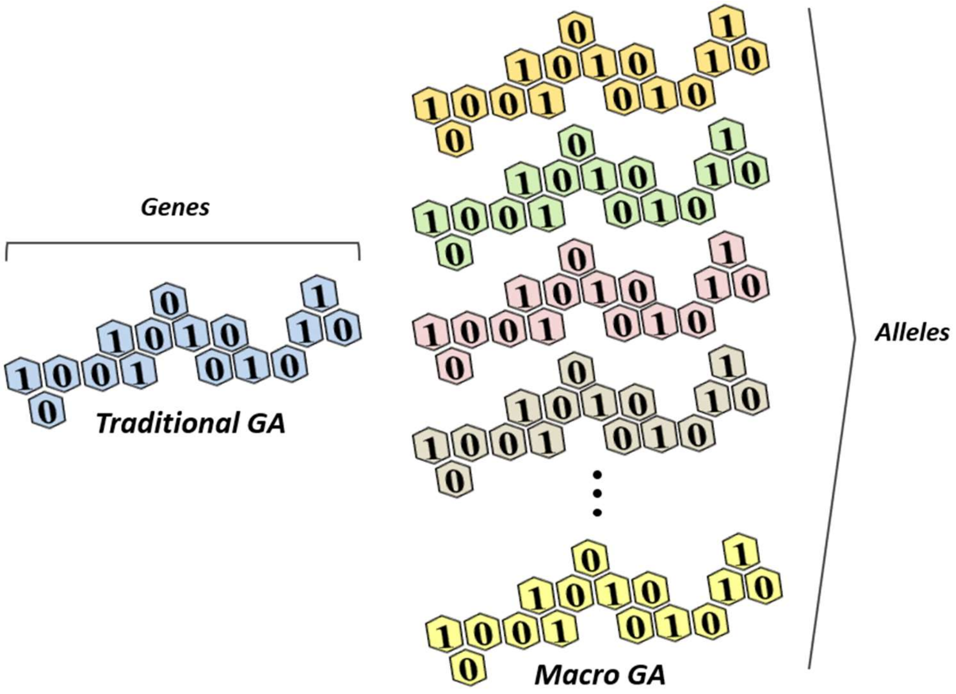

Figure 3.13. Comparison of traditional GA genes, resulting in a single design, and MOLACO-based variations of MGA genes, resulting in a sample size of designs.

and can be considered as alleles, or variations of these genes.

Since single chromosomes essentially represent a sub-population of designs, it is necessary to define a sufficiently large sample size to represent each chromosome. As an example, consider six ant colonies, each with a population of 768 ants, parallelized with an MGA population of 72, and a sample size of 64 (i.e. 64 ants explore the design space of 72 chromosomes every generation). This means that each colony will perform a distributed search of 12 members of the MGA population per LACO generation, and a MGA generation will be complete every six colonies. Since all six colonies are executed in parallel, the number of MOLACO generations coincides with the number of MGA generations. Alternatively, it is also possible to "straddle" MGA generations across MOLACO generations, such that the ratio of MOLACO generations to MGA generations is an integer greater than one. However, sample and colony sizes must be carefully selected, as it is not possible for a MGA generation to end in the middle of a MOLACO generation, since the next MGA generation must be evolved from the previous one. Thus, the number of MGA generations can never exceed the number of MOLACO generations.

To maximize the diversity of colony types explored each generation, and prevent premature convergence due to genetic drift, a non-elitist GA with roulette selection is used. When placed in tandem with MOLACO, it behaves the same as multiple MOLACO searches performed for a variety of colony types that adapt and evolve according to the metrics recorded by the MGA. Thus, whereas MOLACO offers population-based adaptation for a limited set of user-defined topologies, the MGA adaptively searches for a solution in a design space augmented by a factor of 2^N, where N is the number of bits encoded by the MGA. Moreover, in the proposed implementation, the required fitness values of each design used by MOLACO are shared with MGA, and therefore no additional function evaluations are needed. The key distinction is in the way the fitnesses are interpreted; while MOLACO uses the individual fitness values of the best ant paths to determine its pheromone concentrations, the MGA is concerned with the overall performance of the sub-population. Therefore, the MGA chromosome maintains a distribution of fitness values, whose performance can be characterized by the best Pareto set of each distribution, and the hypervolume of the distribution's Pareto set is used as the MGA's fitness to evolve its solutions.

Since the MGA chromosomes and their corresponding sub-populations are constantly evolving, it is computationally inefficient to maintain unique sets of pheromones for each chromosome and instead, pheromones are maintained only by objective and colony. While it is possible for the exact same geometry to have two different fitness values if their MGA chromosomes differ, and pheromones accumulated under one chromosome may not be desirable under a different one, this effect is normalized by the pheromone evaporation mechanism. The resulting modification takes advantage of the GA's effectiveness in global searching, while retaining the advantages of MOLACO's contiguous designs, further expanding the range of manufacturable designs explored.

As alluded to earlier, implementation of the MGA in tandem with MOLACO opens up the design space for large-scale combinatorial optimization problems, as well as *in situ* parameter optimization, which were both not possible under traditional ACO implementations. Combinatorial optimization problems with a large number of variables are computationally intensive for a population-adaptive approach, due to the large number of pheromones that need to be stored, as well as the minimum sub-population required for each combination. While the population-adaptive approach requires a fixed number of combinations to be searched with varying population sizes, the MGA relies on a fixed sample size, with the combinations evolving over time. While the population-adaptive approach was capable of searching a fixed set of masks, or operators, the large number of variables enabled through MGA allows them to also be used as design parameters. Just as in a traditional GA, chromosomes can now be used to optimize trace thickness, lattice constant, number of meanders, deposition angle, or any combination thereof. For each of these traits, a variety of geometries is searched using MOLACO, and over time, traits evolve via selection, mating, crossover and mutation in the usual manner.

Chapter 4

3D FSS Optimization Using MOLACO

4.1 Optimization Parameters

In this chapter, the versatility and efficiency of MOLACO will be demonstrated through optimization of multiple types of 3D FSSs using various wire grid sizes and operating frequencies. All MOLACO simulations are performed using either four 12-core processors operating in parallel, each with 48 GB of RAM, or 24-core processors between 64 GB and 256 GB of RAM. Top designs in each Pareto set with respect to polarization and incidence angle are shown and comparisons will be made to conventional single, multi-layer and 3D designs. Results will show that MOLACO is well-suited for the problem of 3D FSS design and capable of generating innovative and unintuitive FSS unit cell geometries that surpass the performance of traditional designs. The optimization parameters used are given in Table 4-1:

Table 4-1. Summary of MOLACO parameters.

Parameter	Description	Value
N	Number of colonies	4
P	Population Size	192
Q	Fitness scaling factor	0.1
ρ	Pheromone evaporation rate	0.05
τ_{min}	Minimum pheromone concentration	0.1
τ_{max}	Maximum pheromone concentration	0.5
FBW_d	Desired fractional bandwidth percentage	0.2
n_{freqs}	Number of frequency samples per band	10
n_θ	Number of incidence angles sampled	4

4.2 Single-Pole, Single-Zero FSS Designs

In the first application of MOLACO, design of single-pole, single-zero 3D FSSs for polarization and angle independence is addressed. For a given FSS design, complex reflection and transmission coefficients can be computed and the corresponding fitness values for each frequency band (stop or pass) can be formulated by accumulating the squares of the average squared TE and TM normalized bandwidth at each incidence angle according to:

$$F_{band} = \sum_{n=1}^{m} \left[\frac{1}{2} \left(FBW_{TE}^{2}(\theta_n) + FBW_{TM}^{2}(\theta_n) \right) \right]^2 \tag{9}$$

where $0 < \mathrm{FBW}_{\mathrm{TE/TM}}(\theta_n) < 1$ represents the fractional bandwidth (normalized to the desired fractional bandwidth) inclusive of the target frequency, f_0, for incidence angle θ_n and TE/TM polarizations according to:

$$FBW_{TE/TM} = \begin{Bmatrix} \dfrac{f_{\max} - f_{\min}}{f_0} & f_{\min} < f_0 < f_{\max} \\ 0 & otherwise \end{Bmatrix} \tag{10}$$

where angle dependence is assumed and f_{min} and f_{max} are determined based on the following goals: for a stop band, an adequate rejection band is defined as a continuous range over which $|S_{21}| <$ -10dB, whereas an adequate pass band corresponds to $|S_{21}| >$ -3dB. Since a large number of terms are included in the summation, each term is squared to further emphasize flaws or strengths of each design. The set of terms in equation (9) is required for each band of interest. In this problem, a minimum of two bands (stop and pass) are considered. Even with a few sample points in each band, over a large solution space, this quickly becomes computationally expensive. For this reason, the triaged fitness evaluation described in Section 3.2 is applied.

A series of three MOLACO simulations are performed for various wire grid resolutions ($N_{xy} = \{4, 6, 8\}$ and $N_z = 1$), a 20% target bandwidth and 75° FOV. In each case, a population size of 192 is used over 60 generations. The corresponding convergence plots are shown in Figure 4.1 with the best Pareto sets for each optimization given in Figure 4.2 by mask type. While the coarse wire grid converges as early as 1 hour and 38 minutes, a slight increase in degrees of freedom yields a significantly better set of solutions within 10 hours and 26 minutes, while the largest grid size offers the most diverse set of solutions with comparable stop band performance and slightly better pass band performance at the cost of additional computation time (up to 9 days and 5 hours). It is worthwhile to note that each wire segment is meshed with two elements to guarantee solver accuracy, however a quadratic reduction in convergence time can be achieved for singly meshed wires. Nevertheless, it is apparent that each Pareto front contains a diverse set of solutions, from which an engineer can select a suitable design, and that better solutions are generated with larger wire grid dimensions. This is expected, since increasing wire grid resolution increases the ants' degree of freedom. Thus, engineers can choose to quickly generate unique coarsely meshed 3D FSS topologies and re-tune the design dimensions *ex post facto,* using commercial tools of their choice, or allow the algorithm to produce a more accurate solution at the cost of finer meander features (and therefore a more precise manufacturing process), and added computation time. In the following section, a variety

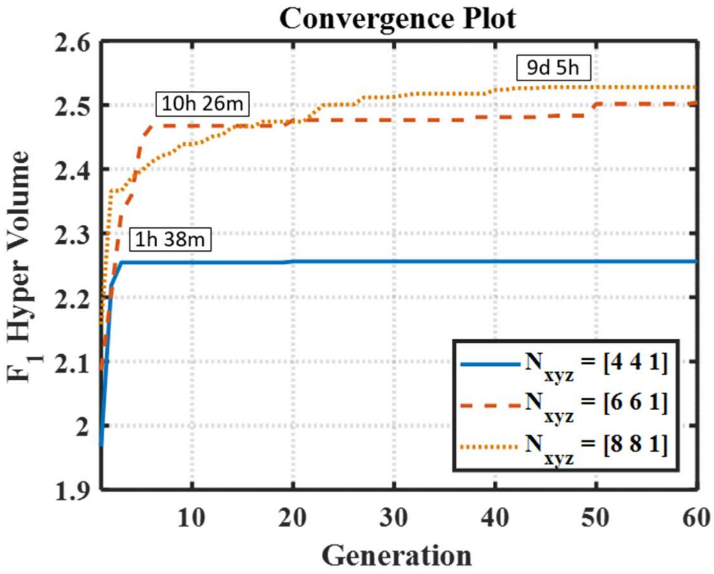

Figure 4.1. Comparison of bi-objective hyper volume of best Pareto set at each generation, clearly demonstrating that this application of MOLACO favors a higher resolution (i.e. more degrees of freedom) in geometry, as expected. © 2017 IEEE.

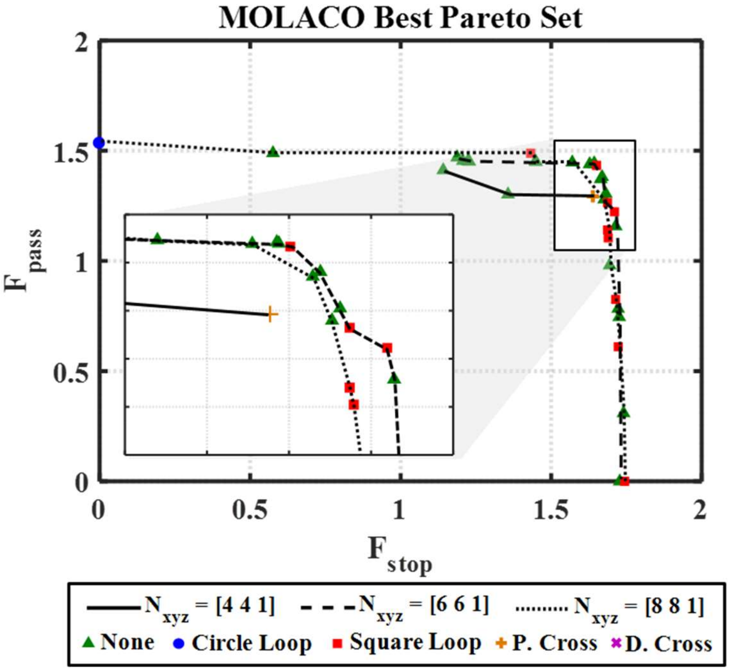

Figure 4.2. Comparison of Pareto set compositions for various MOLACO trials using different resolutions and frequency values, showing that a dispersed colony profile allows for better exploration of the Pareto front. © 2017 IEEE.

of solutions are selected from each Pareto set and examined in more detail.

Since it is not readily apparent what frequency responses are attainable for a given wire grid resolution, the formation of a Pareto set exploiting trade-offs between stop and pass band performance allows for more careful selection of solutions that satisfy design goals to varying degrees. For a coarse wire-grid resolution of N_{xyz} = [4 4 1], the optimal design is shown in Figure 4.3(a) with a thickness of 6.51 mm (~λ/12 at 4 GHz). The S parameters at normal incidence are plotted based on simulations in both PFEBI and HFSS, indicating excellent agreement, with the highlighted region corresponding to a common bandwidth region over which both TE and TM waves satisfy the -10dB stop and -3dB pass criteria for incidence angles up to 80°. Furthermore, contour lines representing these goals are generated as a function of frequency and incidence angle using HFSS and overlaid on a contour map generated by PFEBI demonstrating the relationship between frequency and incidence angle for TE and TM polarizations in Figure 4.3(b) and (c) respectively. From these graphs, it can be seen that the proposed FSS possesses a stop band centered about 2.496 GHz, and a pass band centered at 3.55 GHz. While the stop-band is only 0.16% away from the target frequency, the pass band falls short with an 11.25% deviation from the desired pass frequency. This is a fundamental limitation imposed by the wire grid dimension, allowing few permutations that support a pass band closer to 4 GHz, which will be resolved in the following examples.

Additionally, it should be noted that the design resembles a loaded 3D convoluted Jerusalem cross. This is an important distinction that explains the discontinuity at 3 GHz, as seen in Figure 4.3(c), which is referred to as a “bent-mode.” This mode is excited at oblique incidences where no potential difference exists between opposite ends of a dipole, causing current to flow instead from one leg of the dipole to an orthogonal leg of the dipole [1]. While separating the dipoles eliminates this discontinuity, it also introduces registration issues between the dipoles and disrupts the angular stability of both bands for polarizations in the plane of incidence. Although it is possible for anomalous resonances to manifest in the proposed geometries, decision makers can intelligently select designs to suit their needs from the optimized Pareto set such that any existing discontinuities occur outside the bands of interest, and can therefore be disregarded, as is the case here.

Finally, it can be seen that the onset of grating lobes is delayed, even at near-grazing incidence angles. This is expected since the unit cell periodicity is constrained according to equation (1) in all designs. Finally, like all FSS designs, this one exhibits an unavoidable variation in bandwidth with respect to incidence angle. This phenomenon occurs as a result of the wave impedance in TE and TM modes varying in opposite manners [75][76] and becomes even more pronounced at near-grazing incidence. While some degree of variation is expected, angular stability about the center frequency ensures the formation of a common fractional bandwidth, providing a 6.8% -10dB stop bandwidth and a 7% -3dB pass bandwidth.

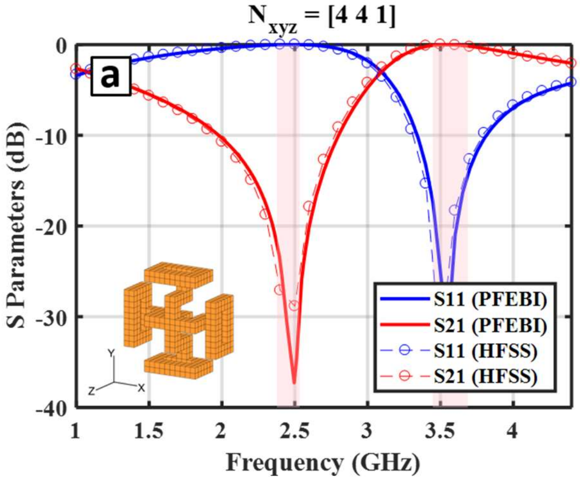

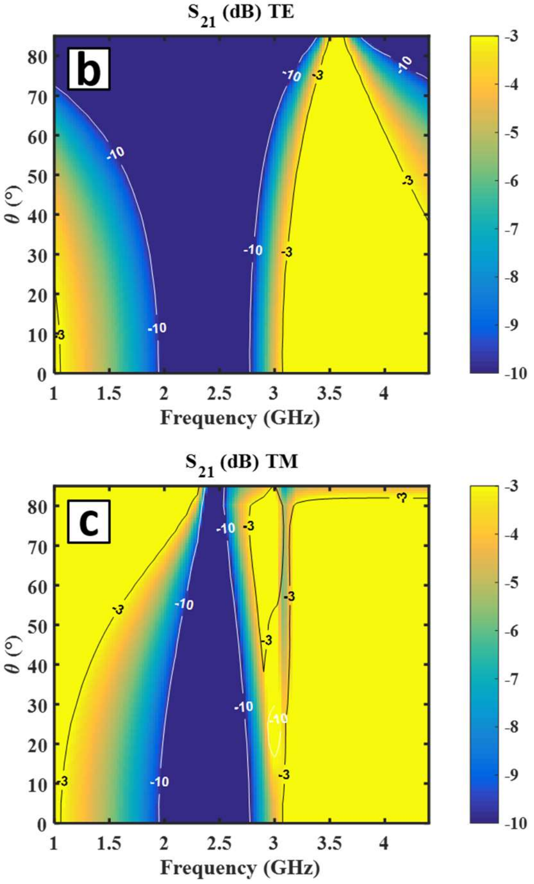

Figure 4.3. A 3D loaded Jerusalem cross generated by MOLACO simulation using N_{xyz} = [4 4 1]. Shown above are the (a) *S* parameters at normal incidence with 3D FSS unit cell geometry (inset) and highlighted regions corresponding to a 6.8% -10 dB common fractional stop bandwidth and a 7% -3dB common fractional pass bandwidth at 80°, and |S21| associated with the (b) TE and (c) TM modes for various incidence angles. PFEBI results are shown in color, with contour lines validated in HFSS corresponding to the -10dB (white line) and -3dB (black line) goals for stop and pass bands, respectively. The discontinuity near 3 GHz occurs due to excitation of a bent-mode, which is common in cross type structures [1], and acceptable since it occurs outside the frequency bands of interest. © 2017 IEEE.

In the next example, a higher wire grid resolution of N_{xyz} = [6 6 1] is used. The best design selected is shown in Figure 4.4 and also belongs to the cross family of FSS structures as evident from the bent-mode discontinuity at 3.2 GHz. This design is 4.773 mm (~λ/16 at 4GHz) thick and has a stop band centered about 2.445 GHz and pass band centered around 3.856 GHz, representing a 2.2% and 3.6% deviation from the desired target frequency respectively. In practice, small shifts in center frequencies are not a major concern, as the frequency response can easily be adjusted by further tuning the dimensions of the wire segments. In this case, a 7.16% -10dB fractional stop bandwidth and a 11.67%

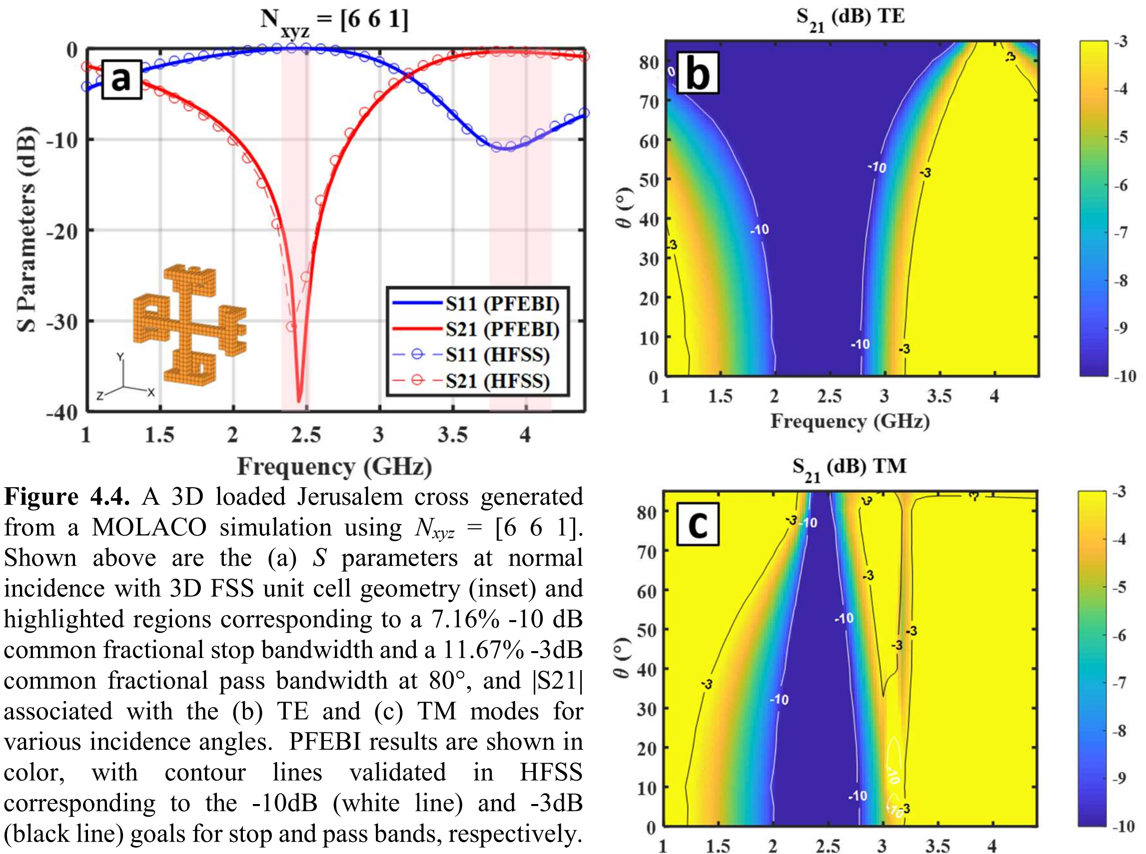

Figure 4.4. A 3D loaded Jerusalem cross generated from a MOLACO simulation using N_{xyz} = [6 6 1]. Shown above are the (a) *S* parameters at normal incidence with 3D FSS unit cell geometry (inset) and highlighted regions corresponding to a 7.16% -10 dB common fractional stop bandwidth and a 11.67% -3dB common fractional pass bandwidth at 80°, and |S21| associated with the (b) TE and (c) TM modes for various incidence angles. PFEBI results are shown in color, with contour lines validated in HFSS corresponding to the -10dB (white line) and -3dB (black line) goals for stop and pass bands, respectively. Similar to the previous example, this design is chosen such that the anomalous resonance occurs outside the frequency bands of interest near 3.2 GHz. © 2017 IEEE.

-3dB fractional pass bandwidth common to both TE and TM polarizations are formed, inclusive of the respective target operating frequencies, and further tuning is not necessary.

Finally, a very fine wire-grid resolution with *Nxyz* = [8 8 1] is considered. To demonstrate the additional degrees of freedom provided by a higher wire grid resolution, a square loop type geometry is chosen in this case. The design is shown in Figure 4.5, and is approximately 3.77 mm (~λ/20 at 4 GHz) thick. At normal incidence, a stop band exists at 2.445 GHz (2.2% shift from desired), with the pass band centered about 3.9 GHz (2.5% shift from desired). At near-grazing incidences, a 9.69% common -10dB fractional stop

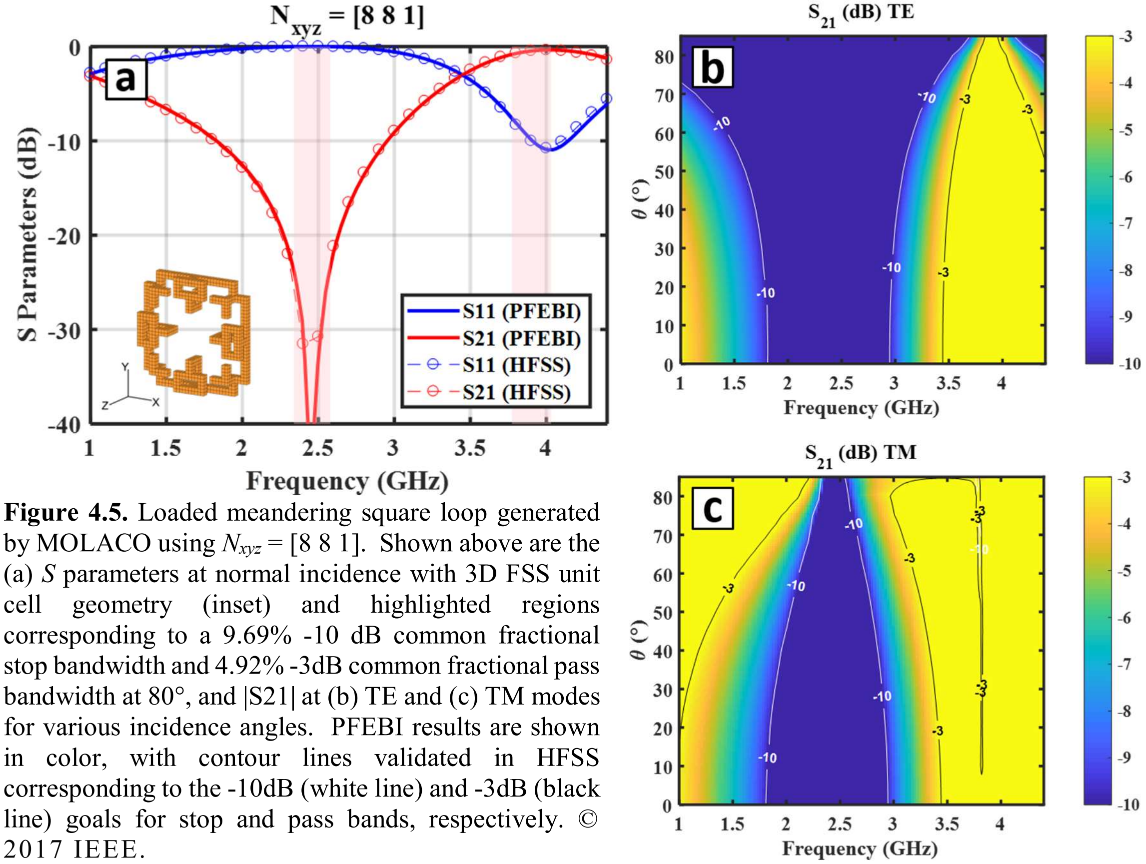

Figure 4.5. Loaded meandering square loop generated by MOLACO using N_{xyz} = [8 8 1]. Shown above are the (a) *S* parameters at normal incidence with 3D FSS unit cell geometry (inset) and highlighted regions corresponding to a 9.69% -10 dB common fractional stop bandwidth and 4.92% -3dB common fractional pass bandwidth at 80°, and |S21| at (b) TE and (c) TM modes for various incidence angles. PFEBI results are shown in color, with contour lines validated in HFSS corresponding to the -10dB (white line) and -3dB (black line) goals for stop and pass bands, respectively. © 2017 IEEE.

bandwidth and a 4.92% common -3dB fractional pass bandwidth are achieved for angles of incidence up to 80°. Although a narrow discontinuity exists near 3.8 GHz in the TM mode of operation, the choice of design ensures that it is below the target frequency of 4 GHz. However, if this is too close to the operating frequency, an alternative design can be selected from the solution set.

A summary of the best designs generated by MOLACO from Figure 4.3-Figure 4.5 as compared to conventional 2D and 3D FSS designs is given in Table 4-2 on the basis of polarization independence and field of view. It is evident that the proposed designs demonstrate superiority over conventional FSS designs, which are either polarization dependent, or suffer from instability and degradation beyond 60° in the form of significant shifts in frequency, onset of grating lobes or coupling and excitation of odd modes. In the next section, design of 3D CP FSSs will be addressed using the same formulation, with special consideration given to reflected and transmitted phase, such that incident circularly polarized waveforms are filtered while maintaining their polarization handedness.

Table 4-2. Comparison of 3D FSS designs generated by MOLACO to existing FSS designs in literature.

Ref	TE/TM	FOV	f_0	FBW_0	D_x/λ_0	h/λ_0	V/λ_0^3	ε_r
Figure 4.3	TE/TM	80°	2.5	6.8%	0.199	0.054	1.4e-3	2.78
Figure 4.4	TE/TM	80°	2.45	7.16%	0.195	0.039	1.5e-3	2.78
Figure 4.5	TE/TM	80°	2.45	9.69%	0.195	0.031	1.2e-3	2.78
[24]	TE/TM	60°	2.44	4.2%	0.05	0.013	3.25e-5	2.65
[4]	TE/TM	60°	8.8	39.9%	0.235	0.049	2.7e-3	4.3
[7]	TE	60°	5.5	54%	0.202	0.117	4.8e-3	4.4
[27]	TE	60°	10.5	4.8%	0.318	0.170	1.72e-2	11.2
[6]	TE/TM	45°	10.2	47.3%	0.34	-	-	2.2
[31]	TE/TM	45°	2.5	14%	0.3	0.075	6.7e-3	-
[11]	TE/TM	45°	7.3	10%	0.146	<0.01	1.037e-4	3
[3]	TE/TM	40°	11.9	8%	0.138	0.138	2.83e-2	10.2
[13]	TE/TM	30°	4.51	47%	0.241	0.024	1.4e-3	4.4

4.3 Circularly Polarized FSS Designs

In the previous section, linearly polarized 3D FSSs were optimized with exceptional FOVs along TE and TM polarizations, without regard to the reflected or transmitted phase introduced by the filter. As a result, these designs are not suitable for applications requiring Circularly Polarized (CP) frequencies to be filtered while maintaining their polarization integrity or handedness. However, CP waves provide many advantages over linearly polarized waves, and are often used in radar and satellite communications due to their resilience against Faraday rotation in the ionosphere as well as attenuation as a result of precipitation. Furthermore, unlike linearly polarized waves, CP antennas do not have strict alignment requirements in order to achieve full transmission of a signal, which makes it an attractive alternative to linear polarization. However, in order to maintain conditions for circular polarization, two orthogonal electric field components of a propagating signal must possess the same amplitude and be 90° out of phase. The leading component is rotated towards the lagging component to form the handedness, which is dictated by the direction of rotation as observed in the direction of propagation. Thus, CP waves are typically characterized as Left Hand Circularly Polarized (LHCP) for Counter Clockwise (CCW) rotation or Right Hand Circularly Polarized (RHCP) for Clockwise (CW) rotation. The quality of a circularly polarized signal is typically measured by the ratio of the major to the minor axis, which is known as the Axial Ratio (AR), and is usually expressed in decibels (dB). Typically, a 3 dB AR is a common metric for acceptable deviation from the ideal case, and corresponds to a phase difference of ±20° between field components as shown in Figure 4.6:

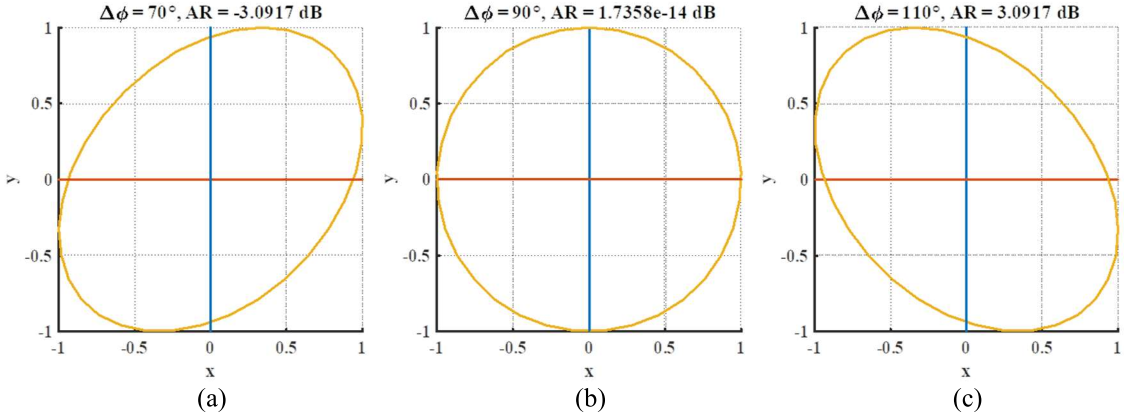

(a) (b) (c)

Figure 4.6. Locus of Electric Field for (a) -3dB, (b) 0 dB and (c) +3dB ARs.

The generalized AR is defined in [71] as:

$$AR = \pm 20\log 10\left(\frac{OA}{OB}\right) \tag{11}$$

$$OA = \left[\frac{1}{2}\left\{\left(E_{x0}^{+}\right)^{2} + \left(E_{y0}^{+}\right)^{2} + \left[\left(E_{x0}^{+}\right)^{4} + \left(E_{y0}^{+}\right)^{4} + 2\left(E_{x0}^{+}\right)^{2}\left(E_{y0}^{+}\right)^{2}\cos\left(2\Delta\phi\right)\right]\right\}^{1/2}\right]^{1/2} \tag{12}$$

$$OB = \left[\frac{1}{2}\left\{\left(E_{x0}^{+}\right)^{2} + \left(E_{y0}^{+}\right)^{2} - \left[\left(E_{x0}^{+}\right)^{4} + \left(E_{y0}^{+}\right)^{4} + 2\left(E_{x0}^{+}\right)^{2}\left(E_{y0}^{+}\right)^{2}\cos\left(2\Delta\phi\right)\right]\right\}^{1/2}\right]^{1/2} \tag{13}$$

where $E_{y0}^{+} = |\Gamma_{TE}|$, $E_{x0}^{+} = |\Gamma_{TM}|$, and $\Delta\phi = \frac{\pi}{2} + (\phi_{TE} - \phi_{TM})$.

Using the calculated TE and TM responses as orthogonal components of the reflected or transmitted wave, the reflected or transmitted AR can be calculated using equation (11), assuming an incident CP waveform. Thus, for near-equal high reflection magnitudes, optimized by the fitness terms in equation (9), large phase variations $\Delta\phi < 70°$ or $\Delta\phi > 110°$ between the reflected wave in TE and TM polarizations will result in the reflected wave becoming elliptically polarized with an AR greater than 3 dB. Since 0 < |AR| < ∞, the worst-case AR over the most stable regions (in which there exists a common TE and TM response) are calculated for each incidence angle and scaled according to:

$$\overline{AR}_{\max} = \begin{cases} \left(\dfrac{3dB}{AR_{\max}}\right)^{2} & AR >= 3dB \\ 1 & AR < 3dB \end{cases} \tag{14}$$

The resulting term in equation (14) augments the fitness function in equation (9) according to the same triaged fitness construct. This ensures that values meeting an AR goal of 3 dB are scaled to unity to prevent the fitness function from diverging to infinity and significantly dominating rest of the fitness function, while still providing a gradient for the optimization algorithm to traverse throughout its search. Thus, the fitness will accrue proportional to the quality of the design's AR within the bands of interest, and the same search technique can be applied to the problem of CP 3D FSS Design.

In this application, impinging waves are assumed to be Right Hand Circularly Polarized (RHCP), and an additional AR term described by equation (14) is included in the fitness formulation to generate electrically small and thin 3D CPFSS designs with 3dB AR FOVs in excess of 80°. Since a clear performance benefit from increasing the wire grid dimensions beyond N_{xyz} = [4 4 1] was apparent from the previous section, the coarse grid size is omitted from consideration, and only N_{xyz} = [6 6 1] and N_{xyz} = [8 8 1] are considered. A plot of the convergence behavior in both resolutions are given in Figure 4.7. The best Pareto set of each optimization will be examined with respect to both stop and pass bands, as well as reflected and transmitted AR.

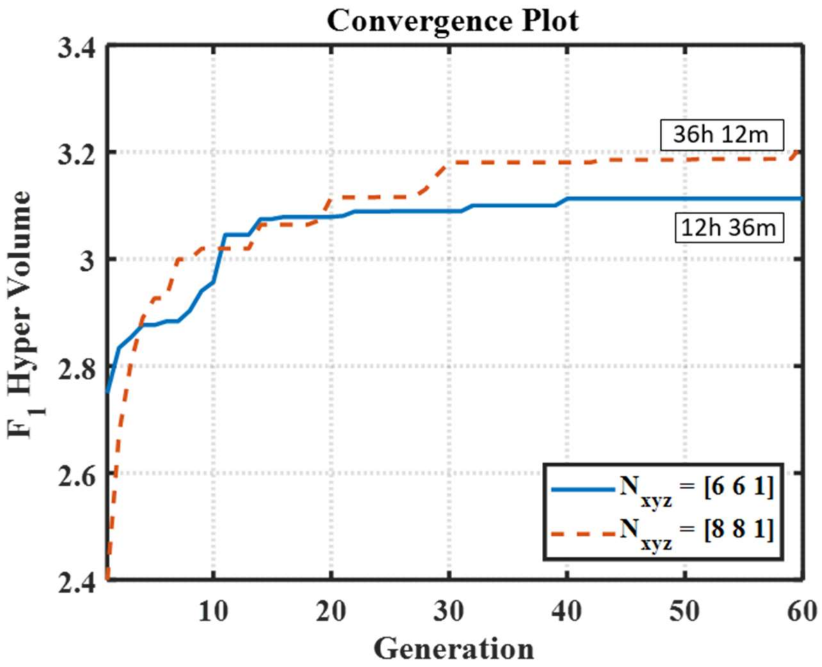

Figure 4.7. Convergence behavior according to a hypervolume metric of 3D CP FSS optimization for designs with wire grid sizes of N_{xyz} = [6 6 1] and N_{xyz} = [8 8 1].

The first Pareto-optimal design is selected from the N_{xyz} = [6 6 1] Pareto set in Figure 4.8 and shown above in the inset of Figure 4.9(a) with periodicity 13.6 mm and thickness 2.73 mm. A comparison of the *S* Parameters at normal incidence in both PFEBI and HFSS are given, with highlighted regions representing 3dB AR bandwidths stable up to 80° of 5.25% across a -10 dB stop band and 4.84% over a 3dB pass band. The 3dB AR stop band is centered about 4.01 GHz, corresponding to a 0.3% deviation from the target frequency of 4 GHz, whereas the pass band is centered about 6.6 GHz respectively resulting in a 5.71% deviation from 7 GHz. The TM and TE polarized transmission coefficients are shown in decibels in Figure 4.10(a)-(b), with the AR as a function of both frequency and incidence angle are shown in Figure 4.10(c)-(d) below. While the stop-band deviation is well within acceptable 3dB AR bandwidth, the pass-band does not include the target frequency, despite having a frequency nearby which is quite stable for large angles of incidence.

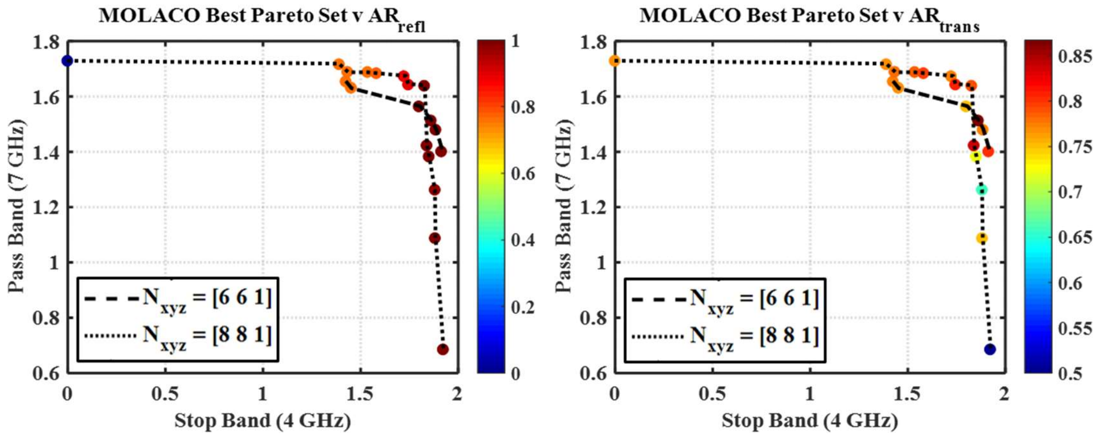

(a) (b)

Figure 4.8. Best Pareto set for each grid size with respect to (a) reflected AR and (b) transmitted AR fitnesses.

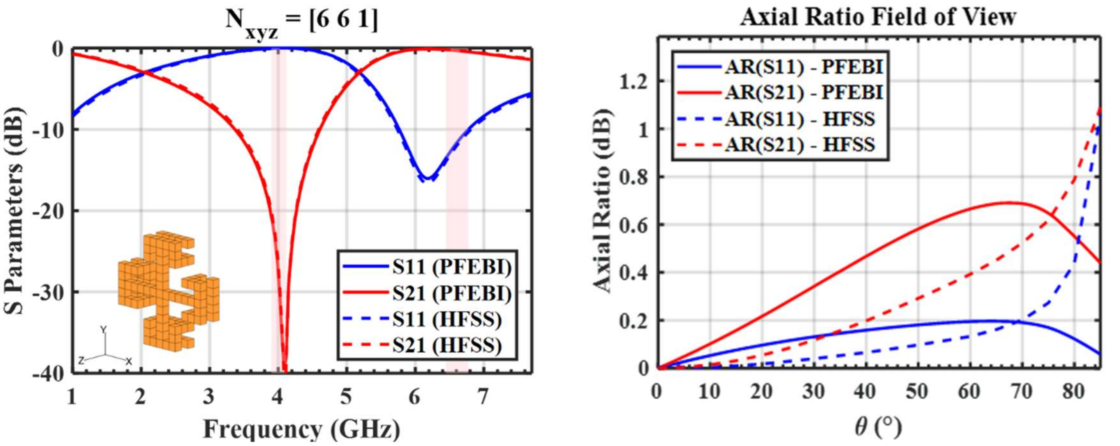

(a) (b)

Figure 4.9. Comparison of (a) S Parameters and (b) Axial Ratio Field of View for 3D CPFSS geometry (inset) using PFEBI and HFSS.

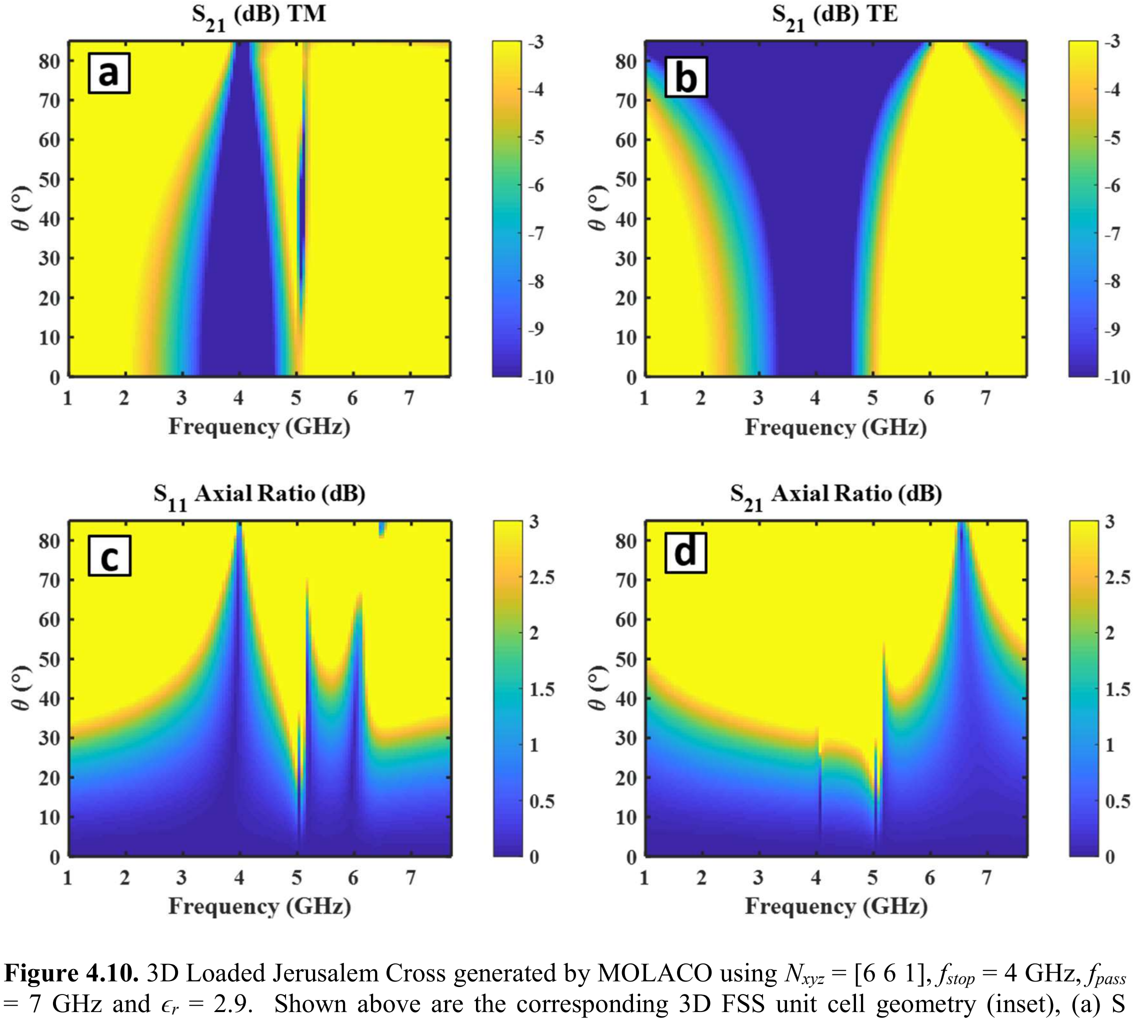

Figure 4.10. 3D Loaded Jerusalem Cross generated by MOLACO using N_{xyz} = [6 6 1], f_{stop} = 4 GHz, f_{pass} = 7 GHz and ϵ_r = 2.9. Shown above are the corresponding 3D FSS unit cell geometry (inset), (a) S Parameters at normal incidence with highlighted regions corresponding to the 3dB AR bandwidth for (b) $|S_{11}|$ and (c) $|S_{21}|$ over various incidence angles. At 80 degrees, a 5.25% 3dB reflected AR and 4.84% 3dB transmitted AR bandwidths are achieved for an incident RHCP wave.

The second design chosen has the same periodicity and thickness as the previous design, since the wire-grid dimensions have not changed. The normal incidence frequency response is given in Figure 4.11(a), alongside its AR FOV in Figure 4.11(b). This design has a shared 3dB AR bandwidth of 5.6% across a -10 dB stop band and 6.5% over a 3dB pass band for incidence angles up to 80°. Similar to the previous design, the TM and TE polarized S_{21} Parameters and reflected and transmitted ARs are given in Figure 4.12(a)-(d). In this case, the opposite problem occurs, where the 3dB AR stop band is centered about 4.3 GHz, corresponding to a 7.5% deviation from the target frequency, and the pass band is centered about 7.11 GHz respectively resulting in a 1.57% deviation. While the pass-band deviation is well within acceptable 3dB AR bandwidth, the pass-band does not include the target frequency, most likely due to discretization of design features. In the next example, the wire grid size is increased to N_{xyz} = [8 8 1].

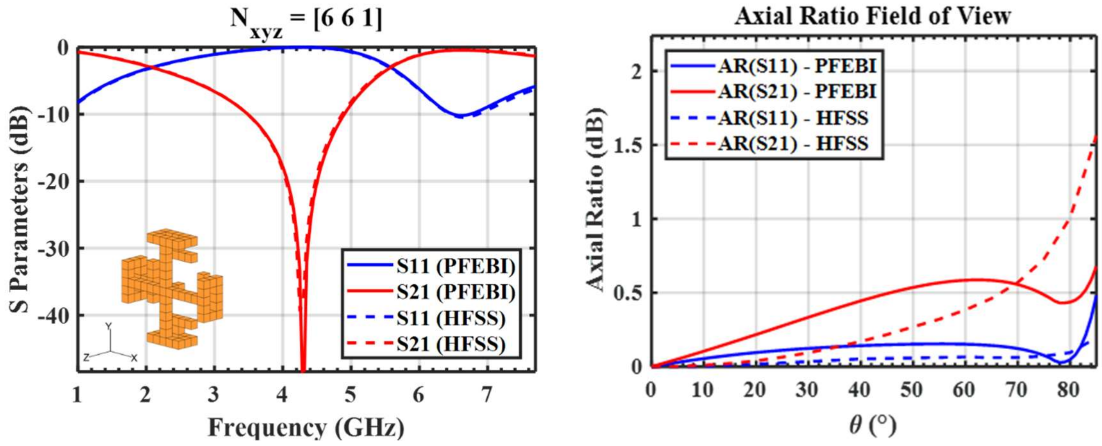

(a) (b)

Figure 4.11. Comparison of (a) S Parameters and (b) Axial Ratio Field of View for 3D CPFSS geometry (inset) using PFEBI and HFSS.

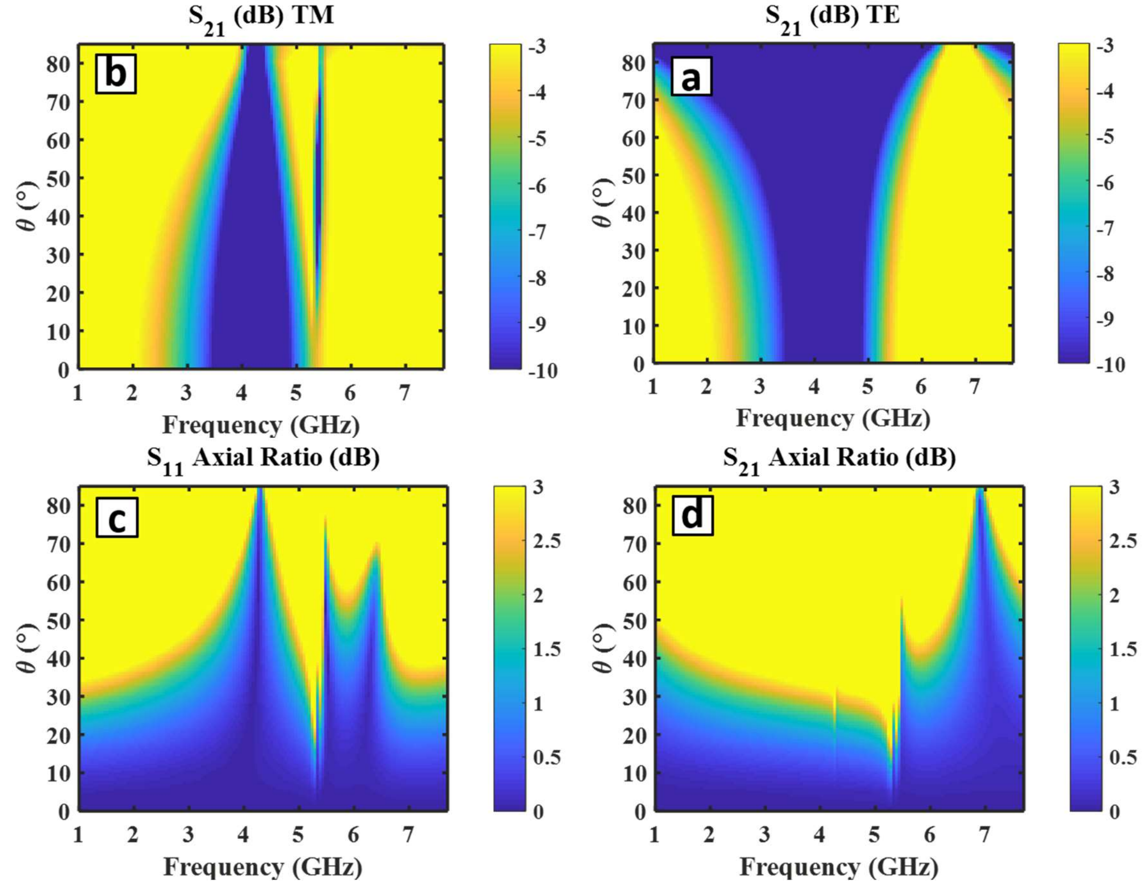

Figure 4.12. 3D Loaded Jerusalem Cross generated by MOLACO using N_{xyz} = [6 6 1], f_{stop} = 4 GHz, f_{pass} = 7 GHz and ϵ_r = 2.9. Shown above are the corresponding 3D FSS unit cell geometry (inset), (a) S Parameters at normal incidence with highlighted regions corresponding to the 3dB AR bandwidth for (b) $|S_{11}|$ and (c) $|S_{21}|$ over various incidence angles. At 80 degrees, a 5.6% 3dB reflected AR and 6.5% 3dB transmitted AR bandwidths are achieved for an incident RHCP wave.

For a grid dimension of N_{xyz} = [8 8 1] wire segments, two designs are presented with similar performance. In these optimizations, the target frequencies are selected to be f_{stop} = 3 GHz and f_{pass} = 6 GHz to demonstrate scalability. Based on the lattice constant selected according to Eq. (1), the dimensions of these designs are slightly smaller at 15.9 mm^2 x 2.51 mm. A comparison of the PFEBI and HFSS calculated S parameters of this design at normal incidence are shown in Figure 4.13(a), with highlighted regions corresponding to 3dB AR bandwidths of 8% and 4.67% over which both TE and TM responses maintain a -10dB rejection and -3dB transmission at 3 GHz and 6 GHz respectively, for incidence angles beyond 80°. The AR FOV is given in Figure 4.13(b) demonstrating a 3dB AR is maintained for incidence angles between 75° and 80°. The contour plots in Figure 4.14(a)-(b) show the TM and TE response of the structure with respect to frequency and incidence angle, whereas Figure 4.14(c)-(d) illustrate the AR of the reflected and transmitted waves respectively as a function of both incidence angle and frequency, which line up consistently with the stop and pass bands. As in the linearly polarized 3D FSS case, the higher resolution wire grid provides a more precise optimized design, which is able to achieve the target stop and pass frequencies with much less deviation, at the cost of a more precise manufacturing process.

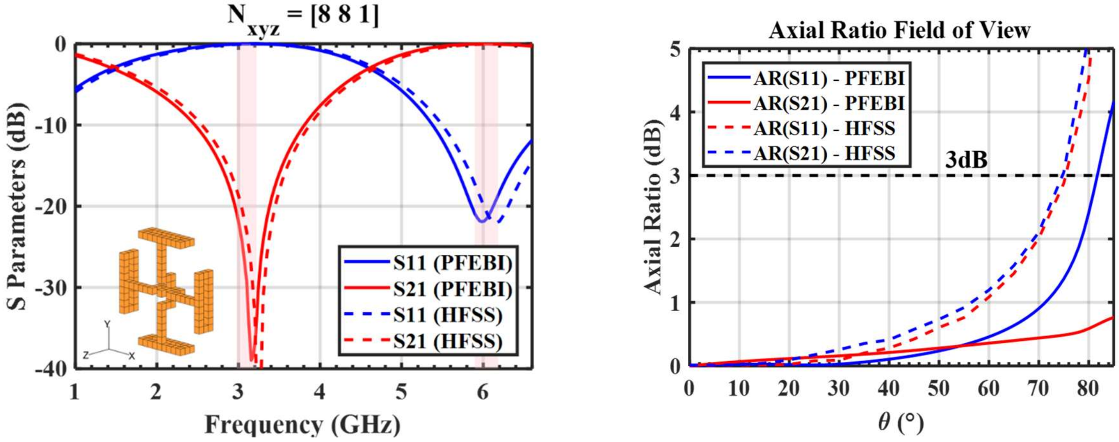

(a) (b)

Figure 4.13. Comparison of (a) S Parameters and (b) Axial Ratio Field of View for 3D CPFSS geometry (inset) using PFEBI and HFSS.

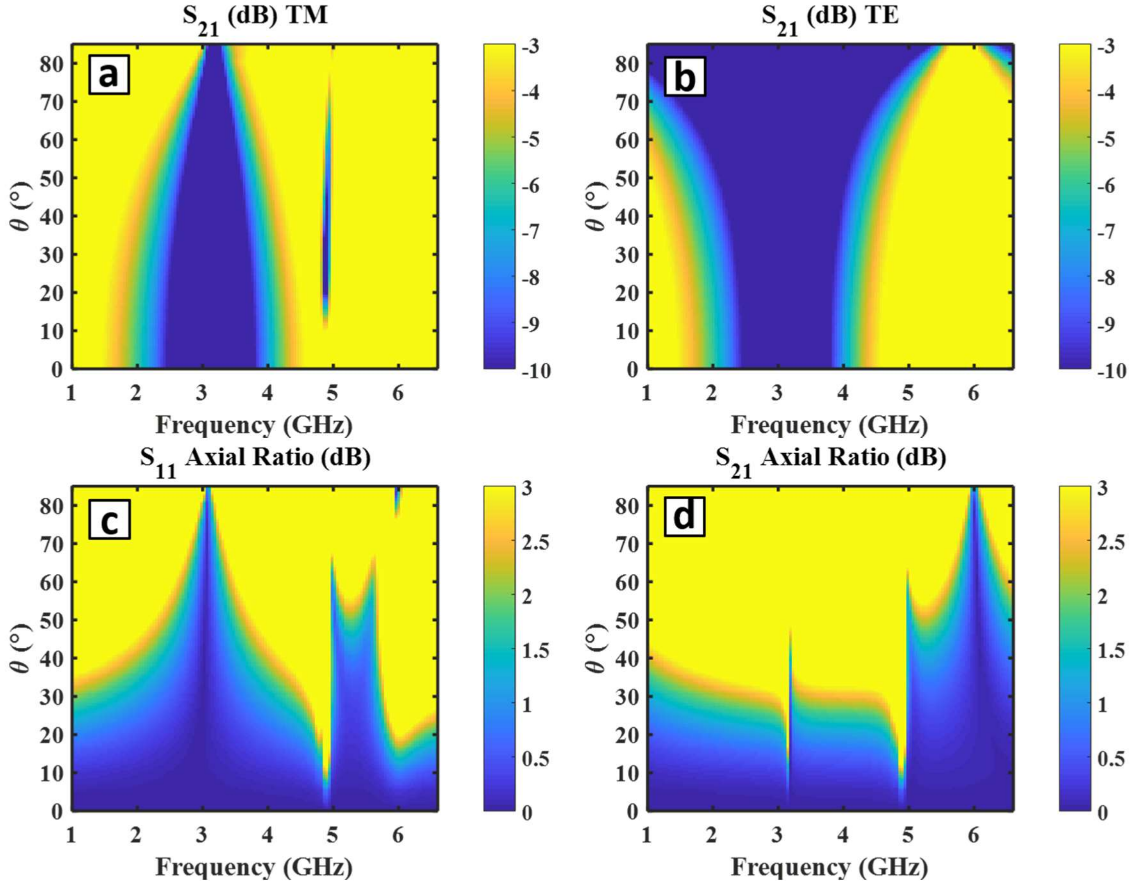

Figure 4.14. 3D Loaded Jerusalem Cross generated by MOLACO using N_{xyz} = [8 8 1], f_{stop} = 3 GHz, f_{pass} = 6 GHz and ϵ_r = 2.9. Shown above are the corresponding 3D FSS unit cell geometry (inset), (a) S Parameters at normal incidence with highlighted regions corresponding to the 3dB AR bandwidth for (b) $|S_{11}|$ and (c) $|S_{21}|$ over various incidence angles. At 80 degrees, an 8% 3dB reflected AR and 4.67% 3dB transmitted AR bandwidths are achieved for an incident RHCP wave.

The geometry of the second design and its associated *S* Parameters and AR FOV are given in Figure 4.15(a)-(b). This design has a 3dB AR bandwidth of 8% with greater than -10 dB rejection in the stop band, and a slightly larger transmission band of 5.67% with less than 3dB AR and greater than 3dB transmission. The TE and TM transmission, as well as reflected and transmitted ARs with respect to frequency and incidence angle are given in Figure 4.16(a)-(d). In both the N_{xyz} = [8 8 1] designs, the target frequency responses are satisfied and no further enhancement in resolution is necessary.

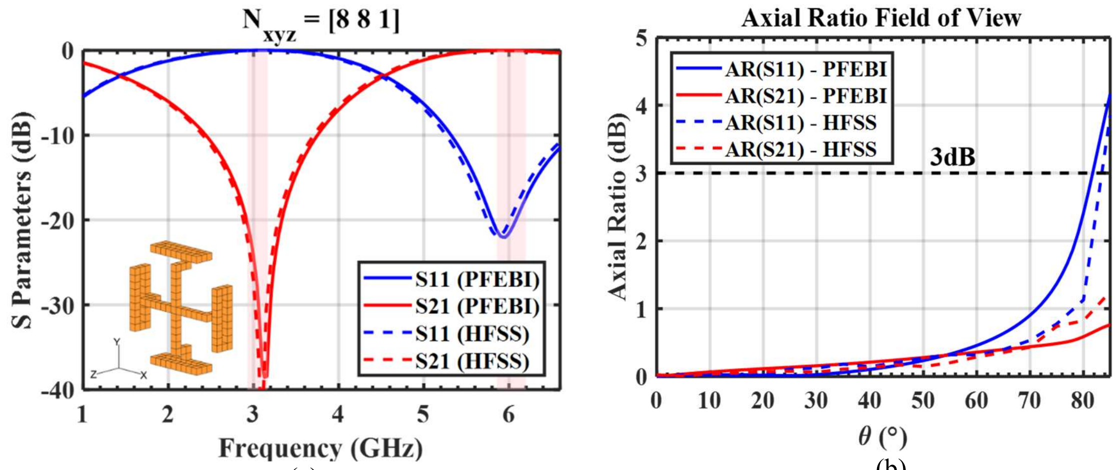

(a)

(b)

Figure 4.15. Comparison of (a) S Parameters and (b) Axial Ratio Field of View for 3D CPFSS geometry (inset) using PFEBI and HFSS.

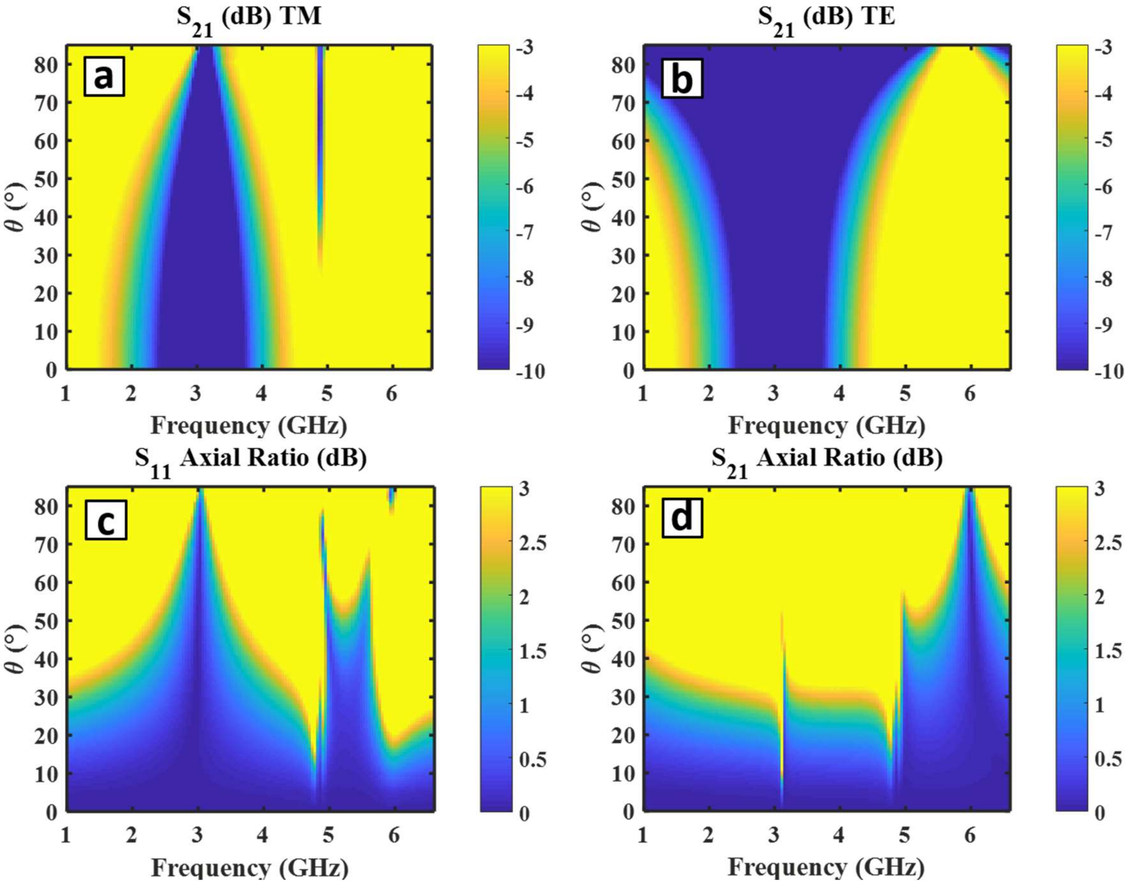

Figure 4.16. 3D Loaded Jerusalem Cross generated by MOLACO using N_{xyz} = [8 8 1], f_{stop} = 3 GHz, f_{pass} = 6 GHz and ϵ_r = 2.9. Shown above are the corresponding 3D FSS unit cell geometry (inset), (a) S Parameters at normal incidence with highlighted regions corresponding to the 3dB AR bandwidth for (b) $|S_{11}|$ and (c) $|S_{21}|$ over various incidence angles. At 80 degrees, a 8% 3dB reflected AR and 4.67% 3dB transmitted AR bandwidths are achieved for an incident RHCP wave.

A closer inspection of the phase behavior across the target frequencies for both designs is given in Figure 4.17, which shows that the phases of the reflected and transmitted waves in both polarizations are nearly identical over a wide range of incidence angles. Thus, although a RHCP waveform was initially assumed, the polarization of any incident waveform is maintained, since the phase for both components of the waveform are equally advanced or delayed. In each design, the degradation in reflected AR beyond 3dB is consistent with a phase discrepancy of over 20° between reflected TE and TM components for near-grazing incidences. It should also be noted that slight frequency shifts in stop and pass band inherently affect the magnitude of the reflected or transmitted waveforms and compound the quality of the AR. Minor discrepancies in AR FOV plots between PFEBI and HFSS can be attributed to the adaptive meshing of HFSS, whereas the PFEBI solver is limited to a finite mesh size. Thus, some amount of inaccuracy is expected if the structure is not meshed fine enough. Furthermore, sharp edges and corners of PEC structures, where field singularities may exist can also be problematic for fixed cuboidal mesh elements. Therefore, although PFEBI allows for rapid evaluation of structures and is ideal for optimization, its advantage in speed is balanced at the cost of accuracy.

A comparison of the thickness (h/λ), periodicity (D_x/λ) and angular stability of the final proposed design with existing designs in literature is presented in Table 4-3. Although the proposed design is a CPFSS, PCS and PSS designs are also included for context. Among designs that demonstrate wide FOVs, the 3D convoluted CPFSS offers superior angular stability, while maintaining an electrically small and thin profile, making it ideal for lightweight and conformal applications.

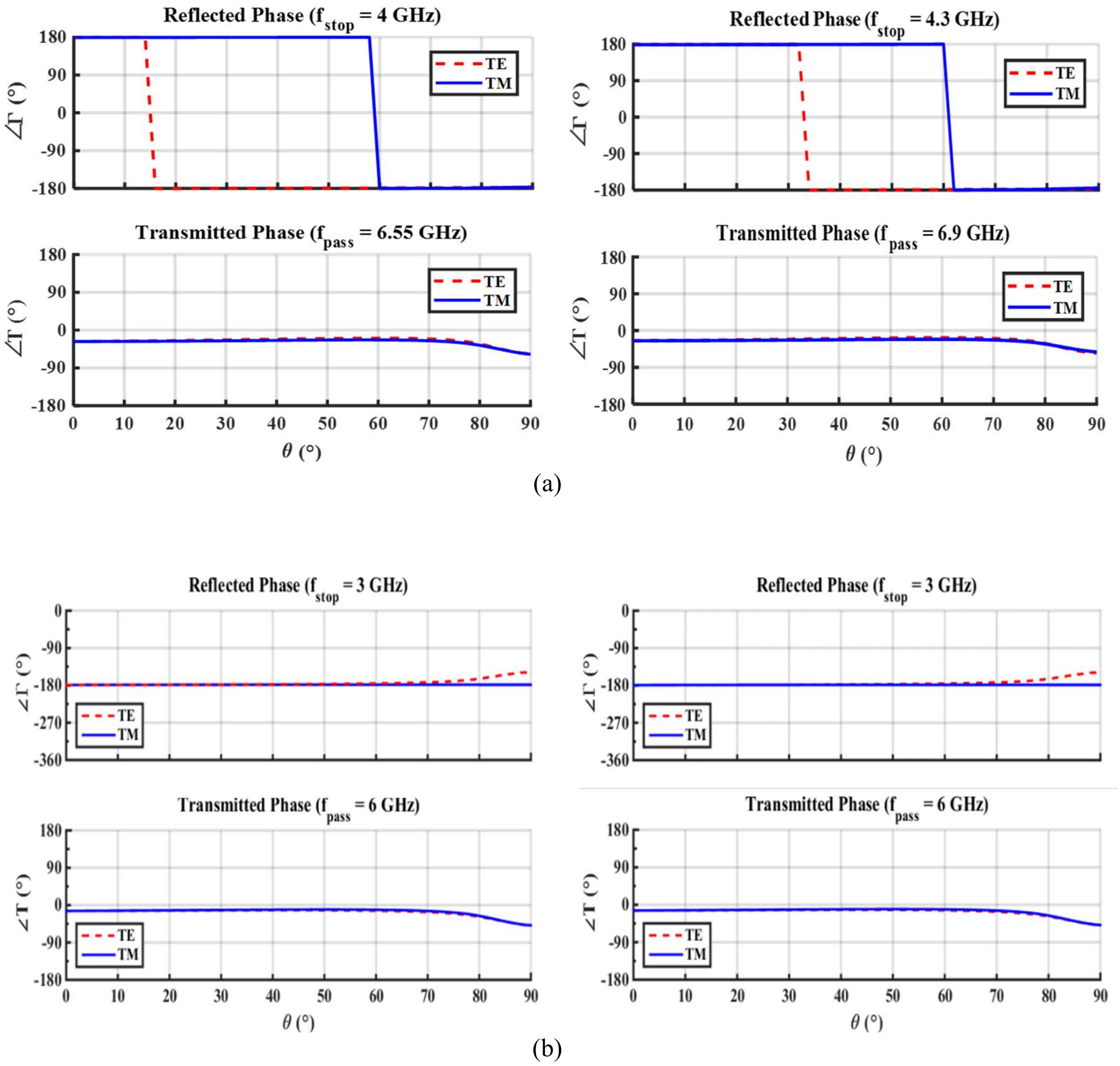

(a)

(b)

Figure 4.17. Comparison of TE and TM phase introduced by the 3D CPFSSs shown in (a) Figures 4.9, 4.11, and (b) Figures 4.13, 4.15 at the reflected (top) and transmitted (bottom) frequencies. Since reflected and transmitted phase values are nearly identical for a wide range of incidence angles, the polarization of incident and transmitted waveforms is preserved.

Table 4-3. Comparison of 3D CPFSS designs generated by MOLACO to existing designs in Literature.

Ref	Geometry	h/λ*	D_x/λ*	Field of View (°)
Figure 4.15	3D Convoluted CPFSS	0.025	0.159	80
[45]	Dual Layer CPFSS Diplexer	0.49	0.75	60
[42]	Wideband Mini-Element PCS	0.18	0.15	45
[43]	Multilayer Dielectric CPFSS	0.77	-	30
[39]	Multilayer Gradual Polarizer	0.24	0.3	25
[36]	Pierrot Cell PSS	1.46	0.47	20
[35]	Multi-Layer Meander CPSS	0.67	0.20	20
[44]	FSS-Backed CP Reflectarray	0.14	0.37	-
[41]	Linear to Circular JC PCS	0.095	0.33	-
[38]	Chiral Metamaterial Polarizer	0.026	0.26	-

*For designs with multiple operating bands, the lowest center frequency is used to compute the thickness and periodicity along the shortest dimension.

In this Chapter, a variety of linearly and circularly polarized 3D FSSs with wide FOVs have been optimized and validated in simulation. In the following Chapter, an overview of additive manufacturing, metallization and characterization techniques are reviewed and applied to fabricate the proposed 3D unit cell structures. Prototype S-band unit cells are initially optimized, and characterized in a waveguide, with a C-band design re-optimized for full-scale fabrication of a finite array. Comparisons of simulated and measured results are provided in both cases.

Chapter 5

Fabrication and Characterization of 3D FSS Arrays

5.1 Additive Manufacturing Techniques

5.1.1 Polymers

Several methods exist for rapid prototyping of polymers including Fused Deposition Modeling (FDM, also known as Fused Filament Fabrication or FFF), PolyJet Printing (PJP), Stereolithography (SLA), Digital Light Processing (DLP) and Selective Laser Sintering (SLS). In FDM and FFF methods, a plastic filament is heated and fed through a computer numerically controlled print head. The print head is usually automated by G-code, which instructs the extruder to heat up, and moves the print head in a pattern corresponding to the desired shape, and cool down the extruder. Depending on the geometry of the design, additional support structures may need to be included in the print, which can be made out of a separate material within the same print. In some cases, a Polyvinyl Alcohol (PVA) material can be used, which has the advantage of being water soluble and therefore easier to separate from the part itself. Although FDM printers are relatively inexpensive, the print quality is inferior to other technologies currently available. FDM-printed geometries are coarse in resolution and must often be scaled accordingly to compensate for expansion of materials in the final print. Even after fine tuning sizes, surface roughness on the order of several hundred microns typically manifests due to the layering process, which is unavoidable, but can be mitigated via an additional smoothing process, such as an acetone-based vapor bath, if using Acrylonitrile Butadiene Styrene (ABS) plastic, or by placing the part in a tumbling medium.

From an electrical design perspective, use of FDM-printed polymers as insulators or dielectrics can be challenging because some printers do not allow 100% filling of the part, which can impact the effective medium properties. However, if the volume fraction of the material can be determined, an effective medium can be calculated using a mixing model. In some cases, this can be useful for applications such as Gradient Index (GRIN) lenses [77][78], since it is possible to mix materials to form a range of dielectric properties. Aside from these challenges, PLA and ABS polymers that are FDM-printed generally have well-behaved electrical properties that can be readily found in literature [79].

An alternative to FDM is SLA and DLP, which both bolster improved strength and resolution, although only one material can be used to print both objects and support structures within the same process. In both SLA and DLP printing, layers of liquid photopolymers are rapidly cured using a UV laser, while the build platform is raised or lowered, allowing multiple layers of hardened resin to form a shape. The difference between the two methods is how the laser illuminates the build platform; SLA prints offer finer features as a continuous wave laser traces out each layer, while DLP prints tend to have a more “stepped” appearance, illuminating an entire layer with light that is digitized into pixels. As a result, DLP retains an advantage in speed, at the cost of resolution. In either case, resulting prints are homogeneous and often UV cured again for improved rigidity. In some cases, additional smoothing to remove surface roughness where support structures were removed is necessary.

Two additional printing techniques which offer even finer resolution are SLS and PJP, which are currently only available commercially and industrially, due to their size, cost and complexity. Instead of using a filament or liquid, SLS fuses material in powdered form to create fully 3D objects, while PJP is a mixed-material printing technique that is capable of combining a variety of resins to achieve a wide range of color, transparency and stiffness. These resins are fed into multiple print heads, which control the mixture ratios and cures the resin as each layer is deposited. Since layers are deposited and cured mechanically, PJP is slower than SLA and DLP techniques, but is capable of forming layers on the scale of tens of microns and uses a wax-like substance to support free-standing structures, which can be water blasted out of the part following production. Alternatively, SLS prints rest on a bed of powdered material and therefore do not require any support structures, however, resulting prints do have an inherent roughness associated with the sintered powder and resolutions are not quite as smooth as PJP. For industrial quantity prints, SLS offers a competitive edge in efficiency by maximizing build volume and material usage by omitting support structures. Although SLA, DLP, SLS and PJP all offer improved resolution over FDM methods, photo polymers tend to be more lossy than traditional thermoplastics, potentially limiting their usefulness as substrates.

Despite the wide range of strengths and weaknesses associated with each printing technology, all of these methods allow for rapid, low-cost manufacturing of exotic structures, which were previously difficult to realize. Continued advances in 3D printing have found increasingly more applications in electrical engineering, whether in prototyping antennas or printing FSS arrays. Although it is also possible to take advantage of the electrical characteristics of these polymers, dielectrics alone are usually not sufficient for most electronic applications, and some conductive surface is needed to feed, couple, transport and channel radiated energy. In the following section, an overview of current metal printing technologies is reviewed.

5.1.2 Metals

Recent advances in additive manufacturing have paved the way for metal printing via three major methods: powder bed fusion, binder jetting and metal deposition. In powder bed fusion, techniques such as Selective Laser Melting (SLM) or Direct Metal Laser Sintering (DMLS) are used to fuse together metallic powders to form layers. Alternatively, binder jetting methods combine powdered metal using an adhesive, which is later removed by sintering the final design in a kiln. Finally, metal deposition techniques include Directed Energy Deposition (DED) and Electron Beam Additive Manufacturing (EBAM), which slowly release metal powder and fuse it together with a laser beam. While each of these techniques produce high quality results, 3D printing in metal is far more expensive than with plastics, and most available metal printing materials have low conductivities, with the exception of aluminum. An alternative to expensive metal and fully 3D printing techniques using both metals and polymers is via conductive plating of 3D printed polymers. One key consideration for this approach, especially in the context of RF design is the effective skin depth resulting from the plating technique, which is based on the plating material and the frequency of operation. At higher frequencies, some plating methods may not accumulate enough layers onto the polymer, resulting in lossy performance. The effective skin depth of a conductor that is well below its plasma frequency is given by:

$$\delta = \sqrt{\frac{2\rho}{\omega\mu}} \tag{15}$$

where ρ is the bulk resistivity of the conductor, ω is the angular frequency and μ is the permeability of the material. In the next section, a sample unit cell design is given and three conductive plating techniques are explored, including conductive painting, electroless chemical painting, and electroplating.

5.2 Prototype Unit Cell

First, a unit cell optimized in the S-band is chosen as a proof of concept to balance manufacturability of fine features with overall unit cell size. The geometry of the proposed design and its performance are given in Figure 5.1 below:

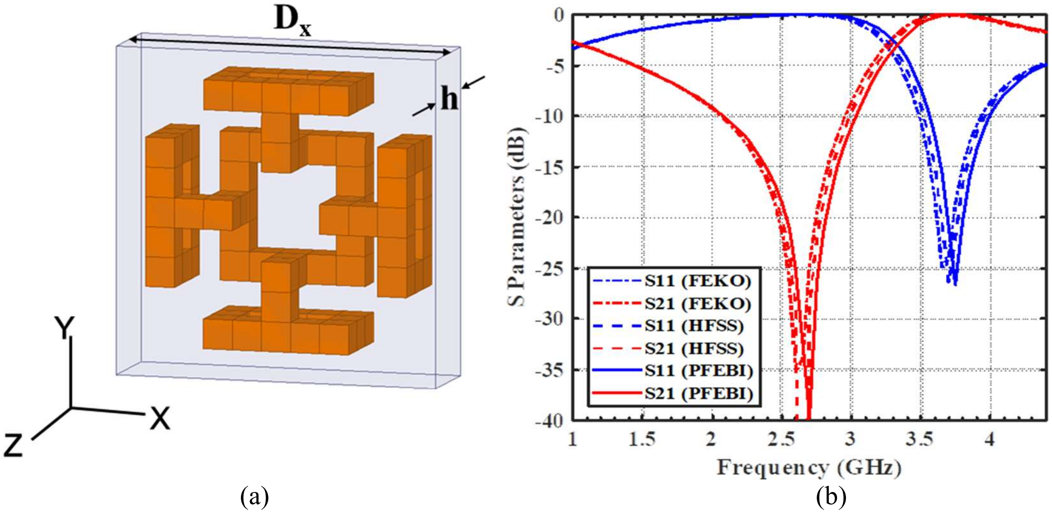

(a) (b)

Figure 5.1. HFSS model of (a) S-band 3D FSS unit cell design consisting of uniform PEC cubes of 2.17 mm^3 immersed in a homogeneous dielectric of permittivity $\varepsilon_r = 2.9$, with periodicity $D_x = 23.9$ mm, h = 6.51 mm and (b) corresponding S Parameter performance.

Since 3D printing in metal is expensive (the proposed unit cell would cost approximately $22 per unit cell manufactured in aluminum from a commercial vendor), a more cost-effective alternative is metallization of 3D printed plastics in the form of painting, electroplating and chemical plating. In addition to being a low-cost alternative to mixed dielectric/metal or full-metal prints, this approach also results in significant weight savings, while maintaining comparable performance metrics [80]. In the next section, metallization of 3D FSS unit cells printed out of a Vera White Plus photopolymer using a Stratasys Objet260 Connex3 is explored.

5.2.1 Conductive Paint

There are many commercially available options for conductive paint ranging from carbon-based paints, to copper, nickel, and silver. Although manufacturer data with the bulk resistivity of the material is published and available, it is difficult to determine what is sufficient for the application without experimental characterization. In this section, MG Chemicals' Total Ground Carbon Conductive Coating (838AR-340G) and Super Shield Silver Conductive Coating (842AR-15ML) are explored. Both are acrylic-based paints that come in brush and spray form. The carbon-based paint has an advertised volume resistivity of 0.33 Ω·cm, whereas the silver print has a resistivity of 100 μΩ·cm (as compared to 1.59 μΩ·cm for pure silver). Three 3D FSS unit cells optimized by MOLACO are spray coated with carbon-based paint and hand-painted using silver print, as shown in Figure 5.2. Once the designs have cured, the resistance of the unit cells are measured using a Keithley 175 auto-ranging multimeter. The carbon-based 3D FSSs registered values ranging in the tens of kilo-ohms, whereas the silver painted unit cells consistently measured five orders of magnitude less at about 0.5 Ω load to load.

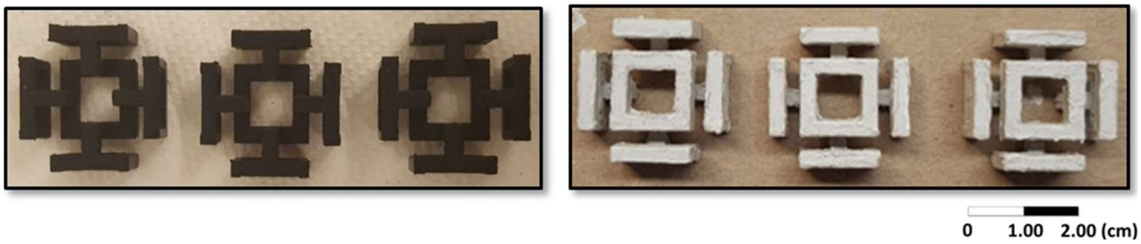

(a) (b)

Figure 5.2. Side by side view of 3D FSS unit cells coated with (a) carbon-based and (b) silver-based conductive paints.

5.2.2 Electroless Chemical Plating

Another technique explored during the fabrication of the 3D FSS array was electroless plating using an Electroless Copper Plating Kit from Caswell, Inc. After parts were 3D printed, they were cleaned and sealed using the carbon-based paint shown in the previous section, to ensure the materials were non-porous. Once the paint was cured, the FSSs underwent a three-step treatment process, where they were placed in a sensitizing solution for two minutes, followed by an activator solution for two minutes, and finally into a 1:1 mixture of a two-part electroless copper solution. In between each step, the unit cell is thoroughly rinsed with distilled water. Based on the published copper content of the solution, only 8 ml was needed per unit cell, however, to ensure the entire surface area of the unit cells were submerged in the beaker, 30 ml was used, and three unit cells were electroplated at the same time. The plating process lasted about an hour and is advertised to coat parts with a thin 5 μm film of copper. The final copper coated elements are shown in Figure 5.3. Although the coating appeared very uniform, initially elements had to be carefully handled to ensure none of copper was accidentally rubbed off. After carefully removing and drying the unit cells, the 3D FSSs were measured using the multimeter, yielding resistances between 4-6 Ω. Although copper plating clearly outperformed the carbon-based paint, it was still about an order of magnitude greater than the silver print.

Figure 5.3. Example 3D FSS unit cells coated with ~5µm of copper using an electroless copper solution.

5.2.3 Electroplating

The most involved metallization technique, electroplating is widely used in a variety of industries. This process works by applying a negative charge to a part which is immersed in a solution that contains positively charged ions of the metal that is to be plated. Once these charged particles bond to the substrate, they deposit into a thin layer, resulting in a metallized part. Key to this process is the ability to negatively charge the part; that is, it must be conductive enough to sustain a negative potential so that a current can form in the solution, applying the metal ions onto the substrate. A silver plating process was applied to a carbon-coated FSS, as well as an electroless copper plated FSS, as shown in Figure 5.4. The conductive carbon-based paint was not conductive enough to form a uniform layer of silver, although the process did reduce the resistance of the unit cell to between 4-6 kΩ—still over a thousand times higher than the electroless copper. However, since the copper was much more conductive, it was possible to plate it in Krohn's silver electroplating solution. On average, the resulting unit cell had the same resistance as a silver painted unit cell at around 0.5 Ω.

Figure 5.4. FSS samples after undergoing various plating processes, including carbon-based conductive painting and attempted silver plating (left), electroless copper plating (middle), and silver electroplating after electroless copper plating (right).

After the plating process, the unit cells must then be arranged in a rectangular lattice and immersed in a homogeneous dielectric. While modeling conductive elements within homogeneous dielectrics can be a straightforward affair, manufacturing them as such can be more challenging. Although mixed print methods using both dielectrics and metals are available, they are often expensive and some additive manufacturing techniques intentionally generate porous support structures to reduce weight and material cost. Furthermore, many dielectrics used in additive manufacturing can prove to be lossy, must be represented by complex mixture models, and can prove difficult to characterize. For these reasons, a low permittivity, low-loss encapsulant is selected to form the homogeneous FSS substrate. One encapsulant that is commonly used is Sylgard-184 with an advertised dielectric constant of $\varepsilon_r = 2.68$ at 100 kHz by Dow-Corning. Since the target frequency range of operation is much higher than this, the following section will demonstrate some techniques that can be used to characterize this encapsulant.

5.3 Material Characterization Techniques

5.3.1 Dielectric Characterization

Like most dielectric materials, Sylgard-184 is dispersive and the manufacturer provided data sheet only specifies the permittivity at 100 kHz. However, it is well known that dielectric properties of materials vary not only as a function of frequency, but also of temperature [81]. This is important since many of these techniques subject powdered or filament-formed materials well beyond glass transition temperatures to mold them into nearly any shape the user desires. The rise of additive manufacturing techniques in the development of passive, active and auxiliary electrical components have prompted the need for accurate characterization of commercially available materials used in such applications. Since dielectric loading is leveraged in the proposed fully 3D designs to help increase FOV and provide mechanical support to the unit cells, one important consideration in manufacturing prototypes will be the permittivity of the lattice supporting the finite array of unit cells. For the designs considered, in which unit cells are immersed in a homogeneous low-permittivity, low-loss dielectric, it will be necessary to characterize the medium used to ensure the permittivity is commensurate to the parameters of the material used in the optimization, and that the substrate is indeed low loss.

A variety of dielectric measurement techniques exist for a range of different sample media, including liquids, solids and semi-solids. Some of these techniques include, but are not limited to, the use of coaxial probes, waveguides, horn antennas, resonant cavities, microwave transmission lines [82] and ring resonators [83]. For the purposes of this study, two specific techniques will be discussed: the parallel plate method and the Hakki-Coleman dielectric resonator method. For a detailed review of other techniques, readers are referred to [84].

5.3.2 Thin-Film Capacitor Approach

In the parallel plate technique, a dielectric is placed between two conductors, forming a capacitor. The capacitance value can then simply be measured using an LCR meter, which yields a capacitance, *C*, and a dissipation factor, *D* (also referred to as the loss tangent or *tan δ*). Using the well-known equation for capacitance, it is possible to determine the permittivity of the dielectric given its dimensions:

$$C = \frac{\varepsilon_r \varepsilon_0 A}{d} \tag{16}$$

where *A* represents the surface area of the dielectric and *d* represents the thickness of the dielectric. This measurement technique is simple to perform and provides an effective approximation for material permittivity at low frequencies (*i.e.* < 1 GHz), however is susceptible to deviations in surface roughness resulting from manufacturing processes. For microwave characterization of these polymers, a second technique is necessary.

5.3.3 Hakki-Coleman Resonator Technique

The dielectric resonator method, first introduced by Hakki and Coleman in 1960 [85], relies on modeling the resonant modes of a cylindrical dielectric cavity to determine its corresponding resonant frequency. Thus, given the excitation mode and cylinder dimensions, it is possible to determine the dielectric constant at the resonant frequency.

For a given a cylinder with dielectric constant κ, permeability μ_0, length L and radius a, placed between two parallel conducting plates, the resonant structure in the TE_{0nl} mode is:

$$\alpha_n \frac{J_0(\alpha_n)}{J_1(\alpha_n)} = -\beta \frac{K_0(\beta_l)}{K_1(\beta_l)} \tag{17}$$

where $J_0(\alpha)$ and $J_1(\alpha)$ are the Bessel functions of the first kind of orders zero and one, and $K_0(\alpha)$ and $K_1(\alpha)$ are the modified Bessel functions of the second kind of orders zero and one, and α and β depend on the geometry of the cylinder [85]:

$$\alpha_n = \frac{2\pi a}{\lambda_0}\left[\kappa_1 - \left(\frac{c}{v_p}\right)^2\right]^{1/2} \tag{18}$$

$$\beta_l = \frac{2\pi a}{\lambda_0}\left[\left(\frac{c}{v_p}\right)^2 - 1\right]^{1/2} \tag{19}$$

where $c/v_p = l\lambda_0/2L$. Thus, given a mode excitation, l, there is a value β_l which exists in the set of solutions for the characteristic equation (2), and a corresponding value for α_n. Rearranging equation (18) to solve for dielectric constant, κ_l, yields:

$$\kappa_l = \left(\frac{\alpha_n \lambda_0}{2\pi a}\right)^2 + \left(\frac{l\lambda_0}{2L}\right)^2 \tag{20}$$

Finally, the resonant frequency can be determined using the relationship $f_0 = c/\lambda_0$ where c is the speed of light. Furthermore, it can be shown that the loss tangent is inversely proportional to the quality factor (defined as the ratio of energy stored to energy dissipated), Q_0, of the dielectric resonator:

$$\tan\delta \approx \frac{1}{Q_0} \tag{21}$$

For a detailed derivation of the material loss tangent using this method, the reader is referred to Appendix II of [83]. This application will consider the TE_{011} mode, which is the dominant mode for many ceramic resonators, and has been used extensively to measure dielectric properties of high-κ ceramics.

Unlike the parallel plate capacitor technique described in the previous section, variations in surface roughness using the cylindrical dielectric resonator are not as significant, since the size of the resonator is much greater than the deviations in roughness. However, the size of the dielectric resonator does plays a vital role in characterizability. For higher frequency measurements, the dimensions of the dielectric resonator become much smaller than the parallel plates used in the measurement appartus, making it considerably difficult to distinguish the difference between the noise floor and resonant peaks. While the Hakki-Coleman technique has been frequently applied to ceramics of small dimensions with a high degree of accuracy, polymer resonators inherently have a lower quality factor, exhibiting more loss and not retaining energy as efficiently. However, when the resonant mode is on the same order of magnitude as the noise floor (*i.e.* if the material is very lossy), this approach will not work.

In order to generate a sample of the proper size, a family of curves depicting the resonant TE_{011} mode cylindrical cavity resonances are generated analytically for a range of cylinder diameters and heights, assuming the permittivity of the cavity is approximately 2.68, as shown in Figure 5.5. From this family of curves, practical cylinder dimensions can be chosen corresponding to a cavity with a resonant frequency in the band of interest. In this case, an approximate cylinder height of *h* = 4 cm and diameter of *d* = 5.5 cm is chosen to balance sample size and allow for deviations in permittivity and dimension in the S-Band. A cylindrical shell with an inner diameter of *d* is then 3D printed so that a Sylgard-184 mold can be made. A 10:1 mixture of encapsulant to hardener is poured into the mold, degassed at 29 inHg to remove trapped air bubbles, and cured. The final sample shown in Figure 5.6 has a diameter of *d* = 5.69 cm and height of *h* = 3.45 cm.

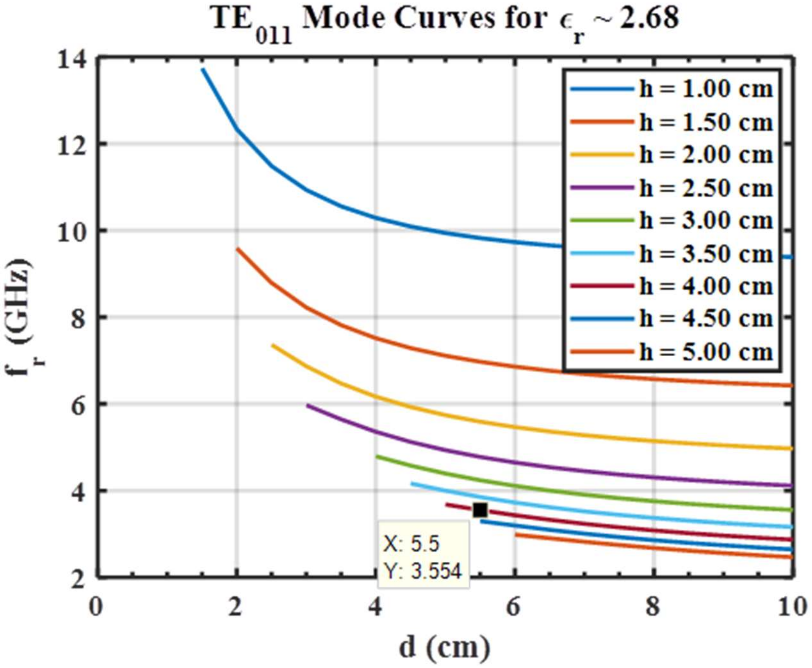

Figure 5.5. TE_{011} mode resonant frequencies for a cylindrical dielectric cavity as a function of height and diameter for an estimated permittivity of $\varepsilon_r = 2.68$ for Sylgard-184.

Figure 5.6. S-Band dielectric cylindrical cavity (left) formed using a 3D printed PLA cylindrical shell (right).

A two-port probe measurement of the cavity using an Agilent E8364B Network Analyzer is given in Figure 5.7 showing a clear resonant peak near 3.78 GHz, with a 3 dB bandwidth of 89.8 MHz, resulting in a permittivity of $\varepsilon_r = 2.78$ and loss tangent of $\tan\delta = 0.023$. Thus, the Sylgard-184 compound is minimally dispersive and the permittivity in the S-Band can be expected to vary up to 3% (between 2.68 and 2.78) from the manufacturer's

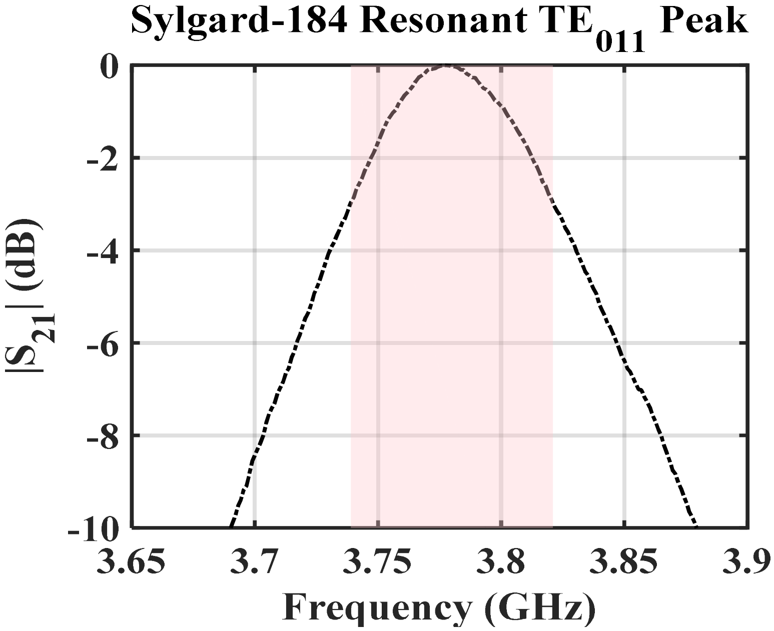

Figure 5.7. Measured TE$_{011}$ resonant peak (normalized) for the cylindrical Sylgard-184 dielectric resonator shown in Figure 5.6 with a 3dB bandwidth of 89.8 MHz (highlighted), corresponding to a permittivity of $\varepsilon_r = 2.7791$ and loss tangent of $\tan\delta = 0.023399$.

published data. Certainly, the permittivity of the sample is also a function of the proportions of mixing compounds used, as well as any imperfections in the molding which could affect the resonant frequency of the cavity, however, this characterization gives some confidence in the relative stability of the substrate permittivity in the band of interest.

5.3.4 Waveguide Measurement Technique

Another way to characterize materials is by measuring samples placed in a waveguide. First introduced by Nicolson and Ross [86], the waveguide measurement technique is based on a transmission line model and relies on accurate measurement of reflection magnitude and phase in order to characterize the complex permittivity of a material, using the following equations:

$$S_{11} = \frac{\left(1-T^2\right)\Gamma}{1-T^2\Gamma^2} \tag{22}$$

$$S_{21} = \frac{\left(1-\Gamma^2\right)T}{1-T^2\Gamma^2} \tag{23}$$

The complex reflection and transmission coefficients can be extracted from the measured S parameters according to equations (22) and (23), and the material parameters are calculated according to:

$$\Gamma = \frac{Z_L - Z_0}{Z_L + Z_0} = \frac{\sqrt{\mu_r / \varepsilon_r} - 1}{\sqrt{\mu_r / \varepsilon_r} + 1} \tag{24}$$

$$T = e^{-j\omega d\sqrt{\mu\varepsilon}} = e^{\frac{-j\omega d}{c}\sqrt{\mu_r \varepsilon_r}} \tag{25}$$

where d is the sample thickness. This method is applied to characterize three 3D printed photopolymers printed with dimensions 2.286 cm x 1.106 cm x 1.265 cm for a WR-90 waveguide, as shown in Figure 5.8. The faces of the samples that coincide with the waveguide are coated with conductive paint and pressed into a sample holder with a WR-90 cross section, and the S Parameters are measured. The average X-band material parameters are given in Figure 5.9, and is used to model 3D printed structures in simulations, which is useful for rapidly prototyped test fixtures and sample holders. Although the loss is relatively higher than most commercial dielectrics ($0.01 < \tan\delta < 0.02$), the permittivity is relatively stable in the X-band at approximately $\varepsilon_r = 2.8$.

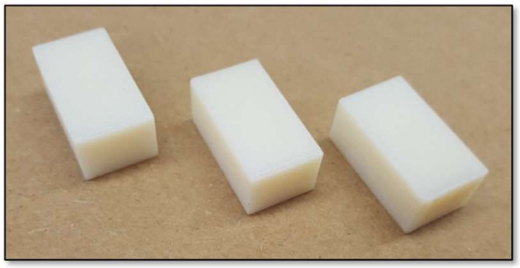

Figure 5.8. 3D printed samples of VeroWhitePlus for X-band characterization.

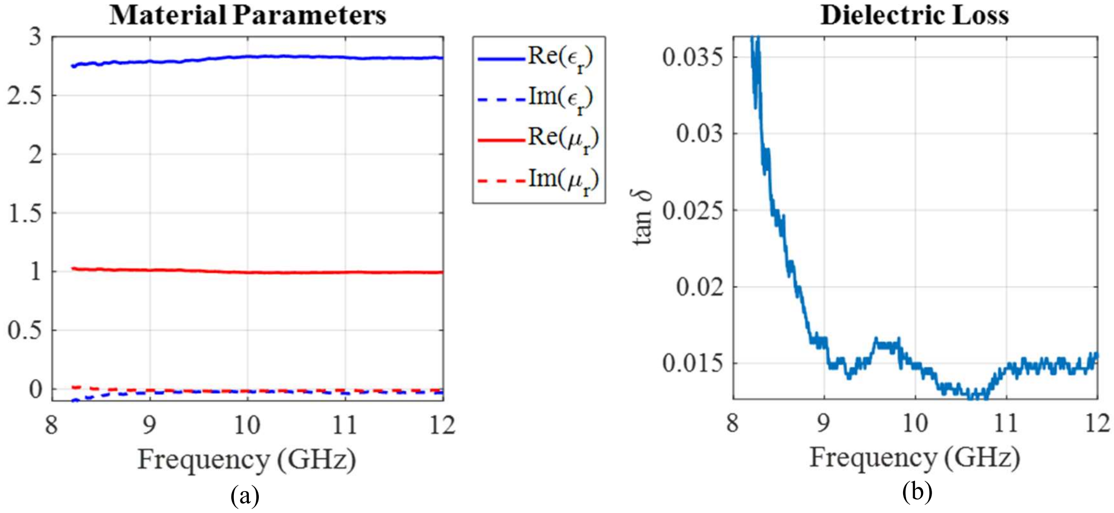

(a) (b)

Figure 5.9. Plot of (a) complex permittivity and permeability, and (b) average loss tangent based on three X-band sample measurements of VeroWhitePlus photopolymer.

5.4 Finite 3D FSS Sample Array

5.4.1 Waveguide Characterization

Prior to large-scale finite array testing, a small-scale sample array must be made to validate the manufacturing process. This is best done in a controlled environment, such as a waveguide. Under these conditions, FSS performance will vary from results optimized in free space as a result of several factors, including excitation of the dominant TE_{10} mode rather than by a TEM mode, the presence of a guided wavelength, finite arrangement of the array, non-uniform illumination and presence of a cutoff frequency. Although FSS performance in a waveguide is fundamentally different than in free space for these reasons, small-scale testing allows for a low-cost method to validate basic unit cell behavior, as well as quality of the fabrication and plating techniques for reproduction on a larger scale. Since the sample unit cell is resonant in the S-band, a WR-284 waveguide is selected for the waveguide test. The WR-284 waveguide has dimensions $a = 72.136$ mm, and $b = 34.036$ mm, which supports a three-element array for a periodicity of $D_x = 23.9$ mm.

The frequency response of a finite array of unit cells encapsulated in Sylgard-184 within a WR-284 waveguide is compared to the performance of an infinitely periodic array in free space and given in Figure 5.10(a). In the upper plot, the unit cell is arranged as optimized in free space, and also simulated with a lattice constant along the axis of polarization that is equivalent to the height of the waveguide. From here, it can be seen that the shift in frequency response predominantly comes from the fact that the effective lattice constant of the structure confined to a waveguide varies greatly from the free space model. In the lower plot of Figure 5.10(a), the unit cell array is confined to a standard WR-

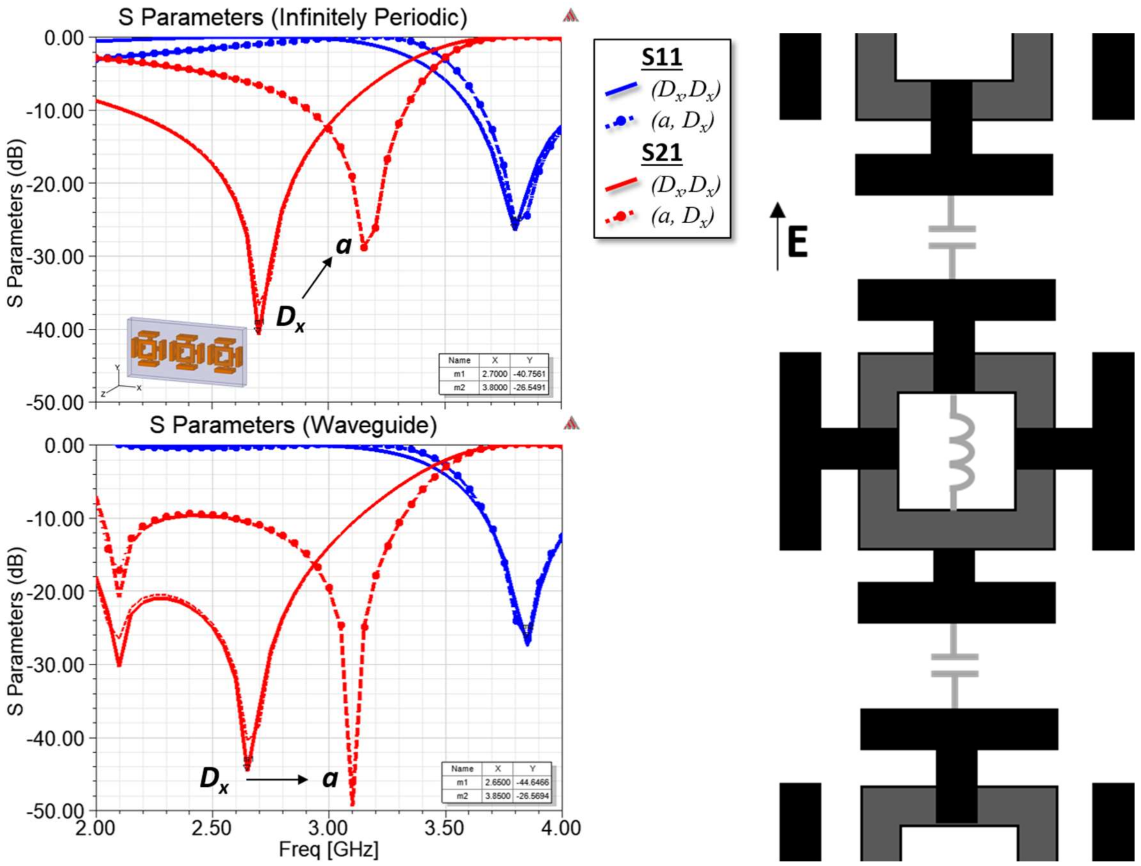

(a) (b)

Figure 5.10. Comparison of (a) *S* Parameters for a three-element 3D FSS array in free space (top), and confined to a WR-284 waveguide (bottom), for varying lattice constants in the axis of polarization. Change in periodicity affects capacitance according to (b) equivalent LC circuit of 3D Jerusalem cross at normal incidence.

284 waveguide, as well as a fictional waveguide with a height corresponding to the optimized lattice constant, which further confirms the change in behavior to this dimension. This can best be understood by considering the equivalent circuit model of a Jerusalem cross structure, shown in Figure 5.10(b). The end loads along the plane of polarization give rise to a capacitance, which decreases as the intercell spacing increases. The narrow dimension of the waveguide is approximately 1.42 times that of the free space design, which reduces the capacitance seen by the incident field. Since an LC circuit has a

resonance given by equation (26) below, it is evident that as capacitance decreases due to the increase in vertical periodicity, the resonant frequency increases.

$$f_0 = \frac{1}{\sqrt{LC}} \tag{26}$$

The fields of the waveguide are shown in Figure 5.11 at the center frequencies of the shifted stop band and pass band, validating the expected performance at normal incidence for TE polarization.

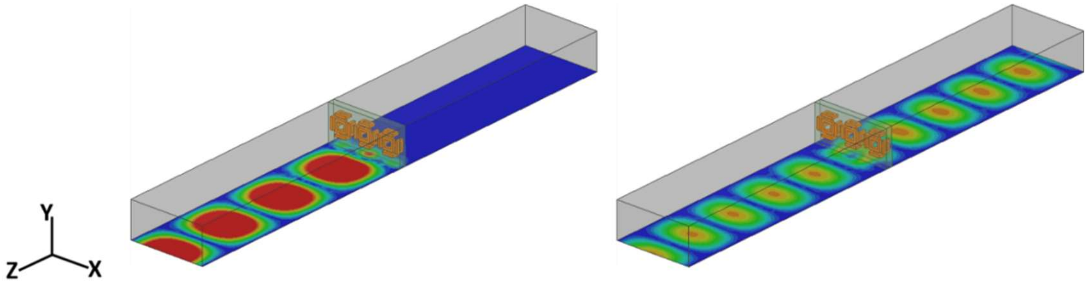

(a) (b)

Figure 5.11. HFSS simulation of a three-element 3D FSS array in a WR-284 waveguide depicting fields in the (a) stop band at 3.1 GHz and (b) pass band at 3.85 GHz.

5.4.2 FSS Sample Array Fabrication

With a basic understanding of unit cell performance in a WR-284 waveguide, a sample is fabricated for experimental validation of both the manufacturing method and functionality of the unit cell. To accomplish this, a two-part die is 3D printed in a Full Cure 720 material in the form of a WR-284 cross section, as shown in Figure 5.12. The die has three small guides with tapered edges coincident with the inner loops of the unit cell to help align the elements according to the proper periodicity, and is open-ended at the

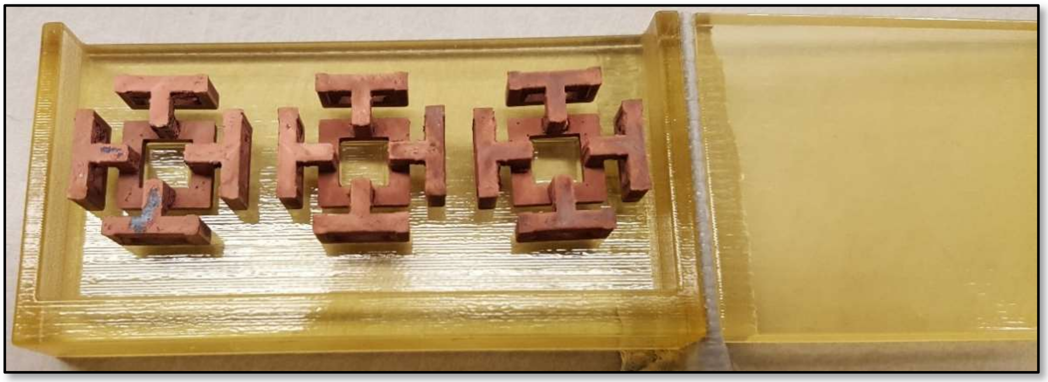

Figure 5.12. Electroless copper plated 3D FSS test sample placed in a two-piece 3D printed die.

top to allow the Sylgard-184 encapsulant to be poured in and de-gassed. Once the unit cells are aligned, the front and back pieces of the die are clamped together and sealed using duct tape. A 22 ml mixture of Sylgard-184 is mixed with a 10:1 ratio of encapsulant to hardener is made and placed in a hermetically sealed vacuum chamber. Next, the solution is de-gassed to a vacuum pressure of 29 inHg in order to remove all air bubbles. This process is shown in Figure 5.13 and repeated multiple times until little to no bubbles are formed during the vacuuming process. Once the mixture is adequately de-gassed, it is poured into the die and the de-gassing process is repeated once more with the sample die, as seen in Figure 5.14. This process ensures the encapsulant is as homogeneous as possible, and the permittivity of the substrate is not reduced as a result of excess air.

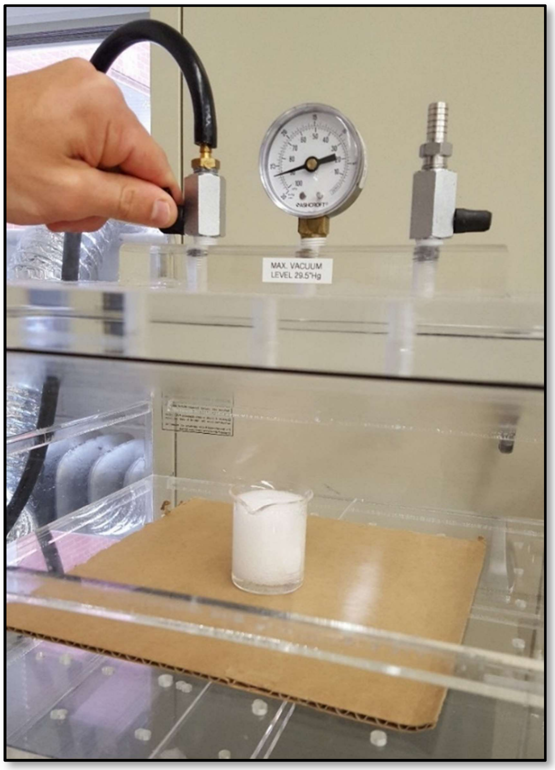

Figure 5.13. De-gassing of Sylgard-184 encapsulant using a vacuum chamber with an external air pump.

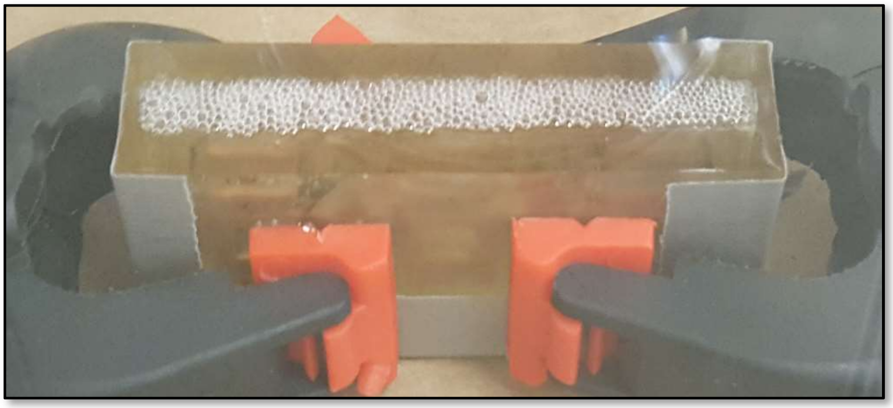

Figure 5.14. De-gassing of Sylgard-184 encapsulant from a two part die containing three FSS unit cells.

Once this process is complete, the encapsulant is left to cure for 48 hours, then baked for 30 minutes at 100° C to fully cure the sample, which is carefully separated from the die using a straight edge. The final waveguide sample is shown in Figure 5.15.

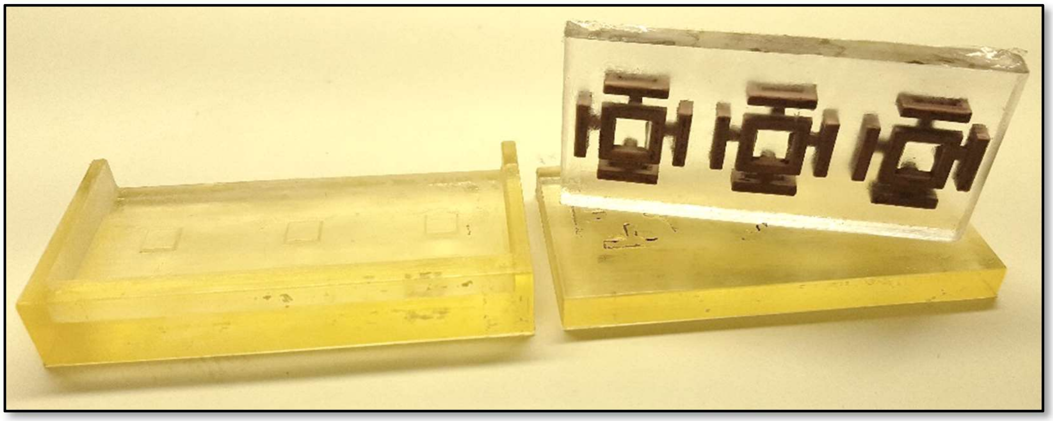

Figure 5.15. Cured 3D FSS waveguide sample, removed from 3D printed mold.

Two samples are made using the above method—one consisting of electroless copper plated unit cells, and the other consisting of silver painted unit cells. Next, a quarter inch CPRF adapter plate is custom machined out of aluminum to hold the test sample in place within the WR-284 waveguide, as shown in Figure 5.16.

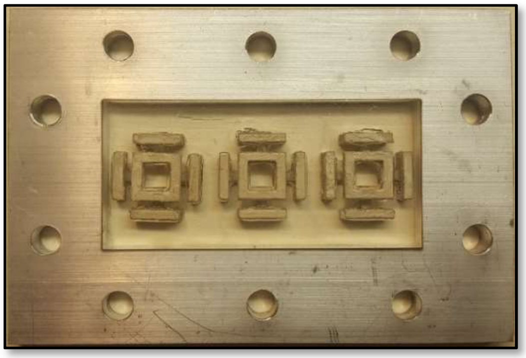

Figure 5.16. **S**ilver-plated 3D FSS test sample placed inside an aluminum machined WR-284 sample holder.

The experimental test apparatus used to measure the sample consists of a Keysight E5071C Network Analyzer, two Fairview Microwave SMA cables, SMA to WR-284 waveguide transitions, and two 10” straight sections of WR-284 waveguide manufactured by L3 Narda Advanced Technical Materials and is shown in Figure 5.17.

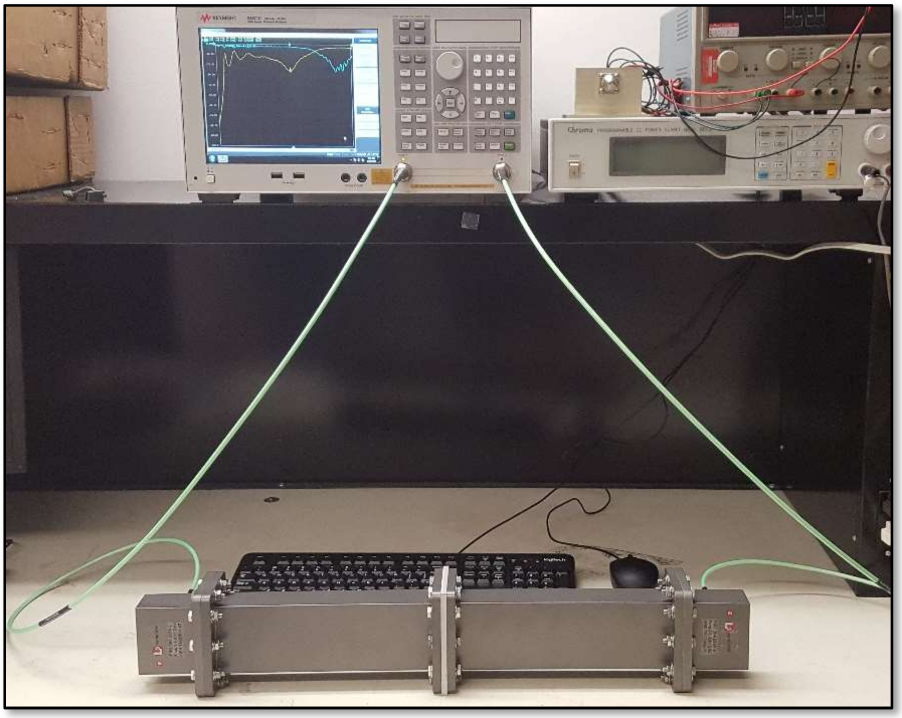

Figure 5.17. Experimental test setup of network analyzer, WR-284 waveguide and test sample.

A two-port calibration is performed using the network analyzer, and the sample holder is fastened between the 10” straight sections. The copper test sample was not conductive enough to resonate with a stop band in the waveguide, however, the silver-plated sample had excellent agreement with simulated results, and is shown in Figure 5.18. The measured waveguide results add confidence to both the performance of the unit cell and the fabrication method, which will next be used to fabricate a large-scale finite array for characterization in free space.

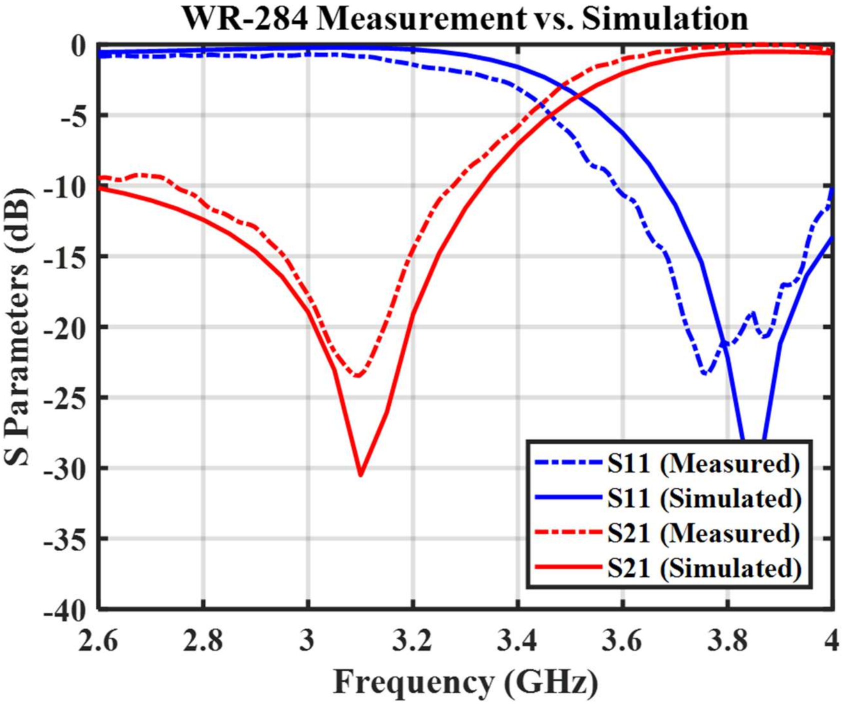

Figure 5.18. Comparison of simulated and measured results of a silver-plated 1x3 FSS array confined to a WR-284 waveguide.

5.4.3 Free Space Characterization

Several factors must be accounted for in the development of a free space test measurement, including the required horn offset to satisfy far field conditions, so that the array can be uniformly illuminated by a plane wave. While traditional FSS arrays are usually measured using a transmit and receive horn, the horns must be placed sufficiently far away to approximate a uniform plane wave effectively. Additionally, the Half Power Beamwidth (HPBW) of the horn will also dictate the dimensions of the finite array in order to ensure adequate illumination. In this application, since the performance of the FSS array at near-grazing incidence angles is of interest, the visible cross section of the array will be drastically reduced. Therefore, if the finite array is too small, energy will diffract around its edges, resulting in inaccurate measurements. In order to satisfy both far field conditions and uniform illumination of the array, an intractably large array is necessary. Alternatively, a focused beam measurement system can be utilized [87], which collimates the incident beam with a lens, focusing it to a particular spot size on the array. However, to reduce the physical size of the array, the 3D FSS elements are re-optimized for operation in the C-band, where the HPBW or Full Width Half Max (FWHM) for Compass Technology Group's focused beam measurement system is approximately between 4"-6" or approximately 10-15 cm, based on the Gaussian beam profile shown in Figure 5.19.

Since the visible cross section of the array reduces by nearly a factor of four at the most extreme incidence angle of interest, the array size along the axis of rotation must be lengthened by a factor of four. Based on equation (1), and the desired field of view, the unit cell size can be anywhere between 8.3 mm and 10.2 mm. However, as previously shown, a finer meander grid is more capable of resolving desired frequency responses. To maintain practical-sized elements that can be easily handled and post-processed during fabrication, the unit cell size is fixed to 12.5 mm, and 8 GHz is targeted as the pass band. The lattice structure holding the elements in place is chosen to be acrylic ($\varepsilon_r = 2.6$), with a Sylgard-527 superstrate ($\varepsilon_r = 2.85$) encapsulating the FSS element. A comparison of the frequency response of the re-optimized PFEBI unit cell and final HFSS unit cell designs are shown in Figure 5.20. While PFEBI results are optimized to approximate available sizes of fabrication materials, the HFSS results use the exact dimensions based on standard sizes of fabrication materials.

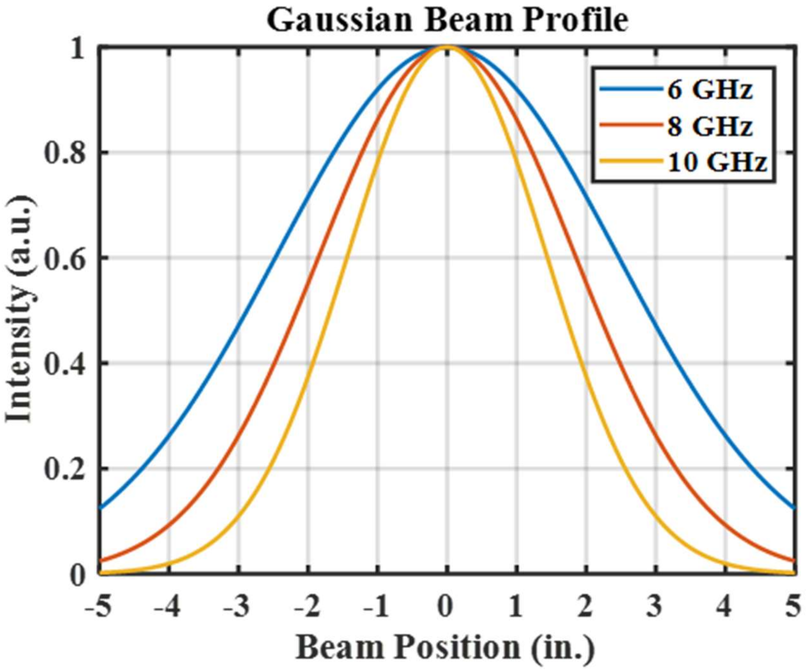

Figure 5.19. Approximate profile of Gaussian beam, showing a FWHM of approximately 3”-4” in lower X-band frequencies.

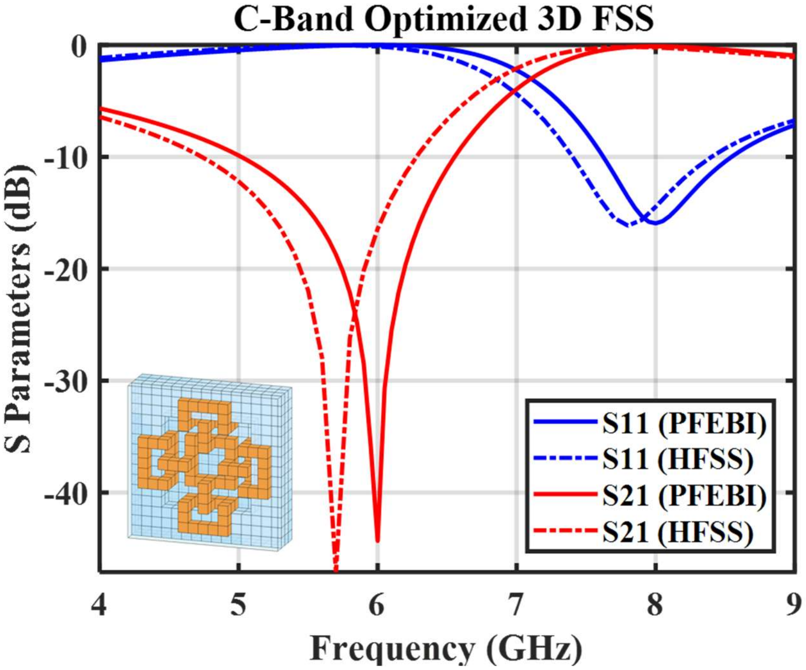

Figure 5.20. Frequency response of 3D FSS geometry (inset) re-optimized for upper C/lower X-band operation.

An initial batch of 3D FSSs is printed and plated. Due to the small size of the elements, the Objet260 Connex 3 is re-configured into a high-quality print mode, which supports a 16μm layer resolution. Since a large number of elements with small feature sizes must be produced, bulk post-processing methods are applied to minimize production time. This includes use of a SU706 soluble support material, which can be dissolved with a caustic soda solution. This is done using a PM Technologies CleanStation DT3 filled with 6 gallons of tap water. Approximately 400 g of NaOH crystals and 200 g of Sodium Metasilicate beads are added during a 20-minute agitation cycle to ensure adequate mixing. Since the parts are small and the agitation of the solution is forceful, hundreds of parts are submerged at a time in a container perforated with holes no larger than the elements. While this protects the parts from destructive collision, and prevents them from dispersing into the drain, it also results in longer exposure times to fully dissolve the support material, which tends to weaken the photopolymer. Parts are left in an agitation cycle for 30-45 minutes and then rinsed in cold water. Each element is allowed to air dry and inspected for leftover residue. Elements with excess residue buildup are cleaned with a precision blade and pressured air. Once all parts are cleaned and dry, they are ready to be painted using MG Chemicals 842AR Silver Conductive Coating aerosol paint.

Since it is difficult to consistently and uniformly coat individual parts in a static painting configuration, a miniature drum coating device is built using a small cylindrical bucket container approximately 8” in diameter. The inside of the drum is lined with silicone beads and fins formed from duct tape to help separate and tumble the parts. A hole is drilled at the bottom of the bucket, and a ¼” bolt is fastened through it, with the end of the bolt exposed outside of the bucket. The bolt acts as a bit and is fastened inside the collar of a power drill. Parts are placed into the barrel, and simultaneously tumbled and sprayed. In between coatings, parts stuck to the walls are gently removed using a paint brush. This process is repeated two to three times per batch, until all parts appear uniformly coated. Once this is done, unit cells are removed and left to air dry, as seen in Figure 5.21. A close-up of the unpainted and painted elements is given in Figure 5.22. After 24-48 hours, parts are briefly annealed in an oven to up to a temperature of 350-400 °F and allowed to air cool. This process ensures any leftover propellant is evaporated and allows the paint to better adhere to the surface of the element. After elements are cooled down at room temperature, each element is individually inspected and the end-to-end resistance is measured using a Keithley 175 auto ranging digital multimeter. The majority of elements registered a DC resistance between 0.3 Ω – 1 Ω. Of note, the internal resistance of the device is measured to be 0.1 Ω. After fabricating the C-band elements, dimensions of sample elements are measured with a Vernier caliper prior to and after metallization. These dimensions are depicted in Figure 5.23, and a summary of the simulated, printed and metallized dimensions of each element is shown in Table 5-1.

Figure 5.21. Photo of initial batch of 3D FSS elements after conductive painting.

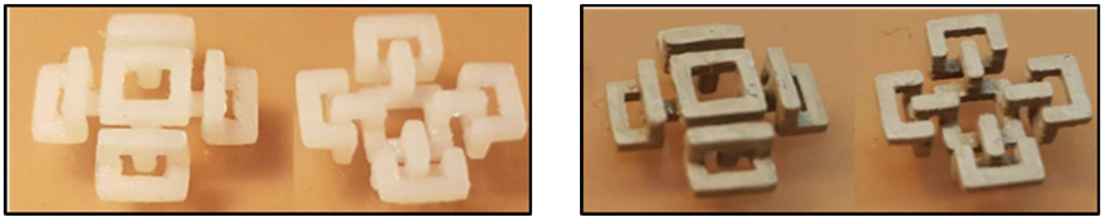

(a)

(b)

Figure 5.22. Close up views of (a) unpainted, and (b) conductively coated C-band 3D FSS elements.

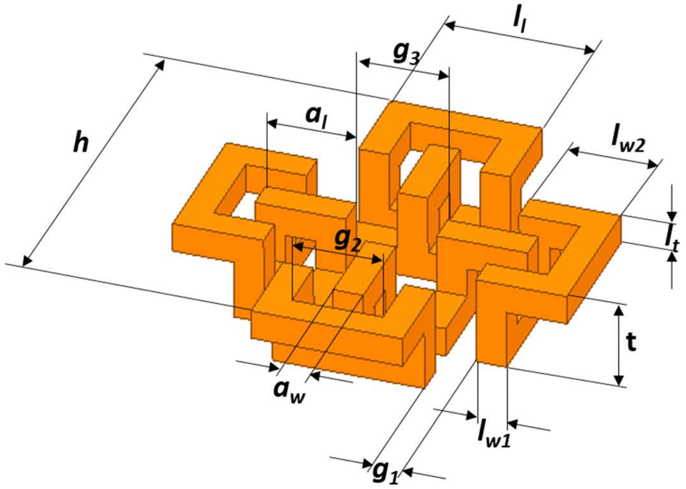

Figure 5.23. Close up of C-band 3D FSS element, with dimensions specified for arms (*a*), gaps (*g*), loads (*l*), height (*h*), and thickness (*t*).

Table 5-1. Comparison of C-band 3D FSS dimensions as simulated, printed, and metallized.

Parameter	Simulated (mm)	3D Printed (mm)	Metallized (mm)
l_1	4.167	4.25	4.32
l_{w1}	0.833	0.9	0.94
l_{w2}	2.5	2.45	2.56
l_t	0.833	0.83	0.89
a_w	0.833	0.92	0.95
a_l	2.5	2.52	2.68
g_1	0.833	0.78	0.75
g_2	2.5	2.37	2.3
g_3	2.5	2.43	2.36
h	10.83	10.95	11.07
t	2.5	2.46	2.5

Throughout this process, approximately 50% of the elements were destroyed during post-processing, having been weakened by the caustic soda solution, or experiencing external forces during various phases where handling was required. The points of failure always occurred at the joints of the element, where the main body consisting of the square loop is attached to the L-shaped loads. Anytime an element becomes caught or stuck to something, any force exerted would cause these joints to snap, rendering the element useless. As a result, the mechanical structure was re-designed to enhance robustness without drastically affecting the frequency response. This was done by importing the 3D model into SolidWorks and adding fillets to sharp edges. The updated model allowed the joints to withstand more torque and made it easier for paint to reach interior flat surfaces easier, by removing sharp corners in tight spaces which previously obscured them. A comparison of the geometries and frequency responses of the rigid and smoothed structures is given in Figure 5.24. In each case, the performance of the elements is consistent over large oblique incidence angles, allowing the previously metallized elements to still be used in the final array. Once again, before full construction, a sample of elements are tested in a waveguide setting, using a custom 3D printed sample holder, based on the VeroWhitePlus material characterized in Section 5.3.4. The faces of the sample holder coincident with the

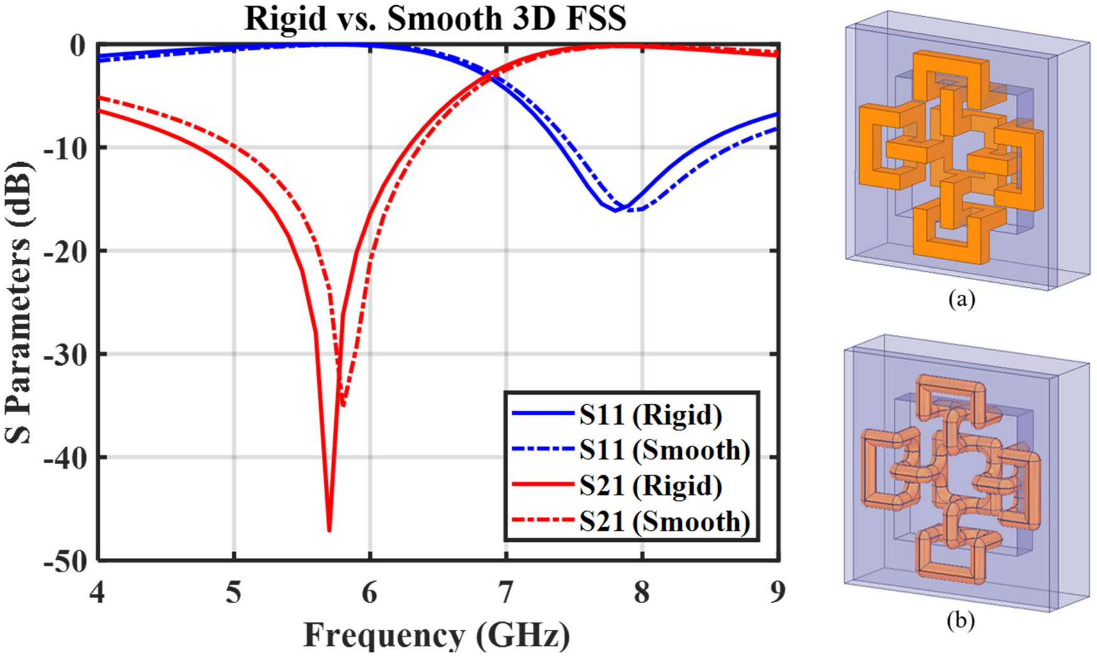

Figure 5.24. Comparison of HFSS frequency response of (a) rigid, and (b) smooth C-band FSS elements.

interior of the waveguide are brush coated with MG Chemicals 842AR Silver Conductive Coating as shown in Figure 5.25. A quick comparison of low conductivity simulation and smooth and rigid measurements in a WR-137 waveguide are given in Figure 5.26, using a bulk conductivity of $\sigma = 30{,}000$ S/m.

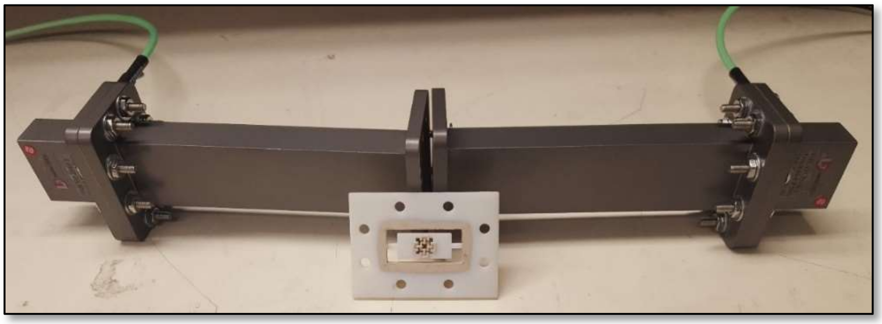

Figure 5.25. 3D printed WR-137 single element FSS sample holder, with waveguide mating regions painted with silver conductive paint.

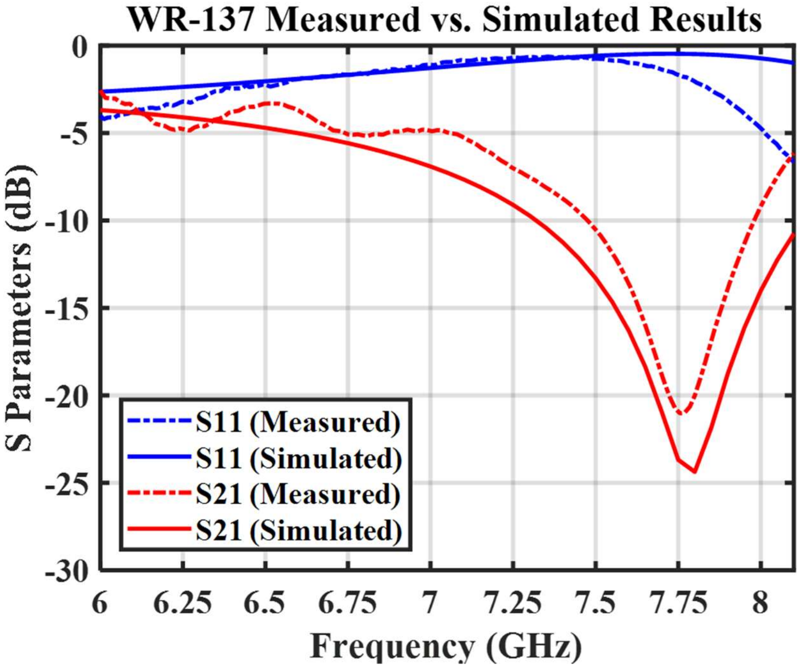

Figure 5.26. Sample measurement of smoothed FSS as compared to simulated waveguide model using finite conductivity. The divergence of the measured S11 parameter occurs as a result of approaching the cut-off frequency of the next higher order waveguide mode, which is suppressed in simulation.

Based on the finite conductivity used to fit the simulated results, the structure is re-simulated with a mixture of rigid and rounded elements in an infinitely periodic free space environment to ensure its performance is preserved. While additional loss is expected, the filtering response is minimally impacted at normal incidence, as shown in Figure 5.27, and -10 dB stop and -3 dB pass behaviors are consistent across oblique incidence angles up to 75°. While the additional loss is evident when measuring the DC resistance of each FSS element, it can be reduced by using higher quality plating methods, such as electroless silver [88]. Unfortunately, electroless silver plating solutions were not commercially available, and attempts to silver plate the painted elements dissolved the existing coat of conductive paint, due to the soluble nature of acrylic paints when immersed in liquid solutions for prolonged periods of time.

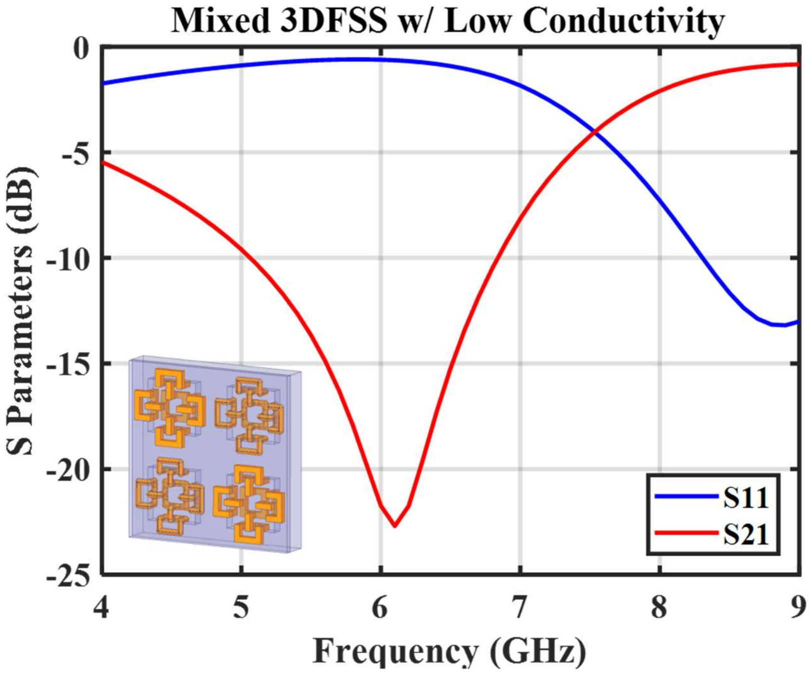

Figure 5.27. Frequency response of infinitely periodic FSS element in free space with finite conductivity.

Having validated the performance of the individual elements, the lattice of the FSS array is constructed out of a 12” x 24” x 1/16” PMMA sheet, precision cut using an Epilog Fusion M2 32 120W laser cutter to ensure accurate periodic spacing between elements, as shown in Figure 5.28. Since PMMA is susceptible to fracturing at hard corners, fillets are included near the edge of the pockets for added mechanical stability. A second PMMA sheet of the same thickness is chemically bonded to the back of the laser-cut sheet using solvent cement to form a 1/8” thick PMMA sheet with 1/16” element cavities. For an element periodicity of 12.5 mm, the chosen sample size contains 1,152 elements arranged in a 24 x 48 array. Once all 1,152 elements are 3D printed, cleaned, conductively coated, and individually measured, they are carefully placed into the PMMA frame according to their conductivity. To maximize performance, element placement is triaged based on the expected field concentrations from an incident gaussian beam, shown in Figure 5.29. Therefore, elements with the lowest measured resistance are placed near the center of the sample, whereas, less conductive elements are placed along the edges of the array, well outside of the FWHM beam waist of the incident Gaussian beam. Images of the lattice with all 1,152 elements embedded are shown in Figure 5.30.

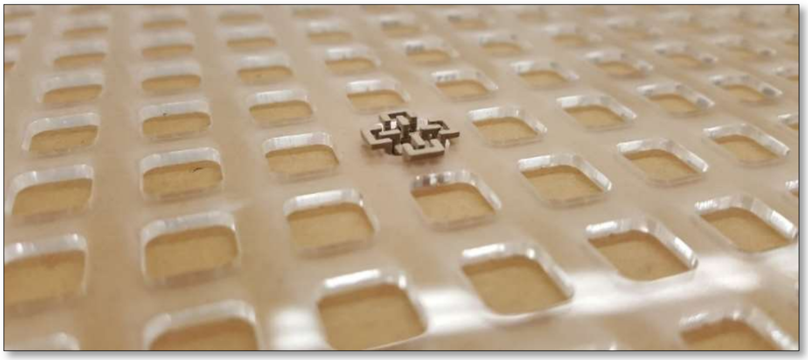

Figure 5.28. Close up view of single C-band 3D FSS element seated in an acrylic sheet with laser-cut pockets for precision alignment.

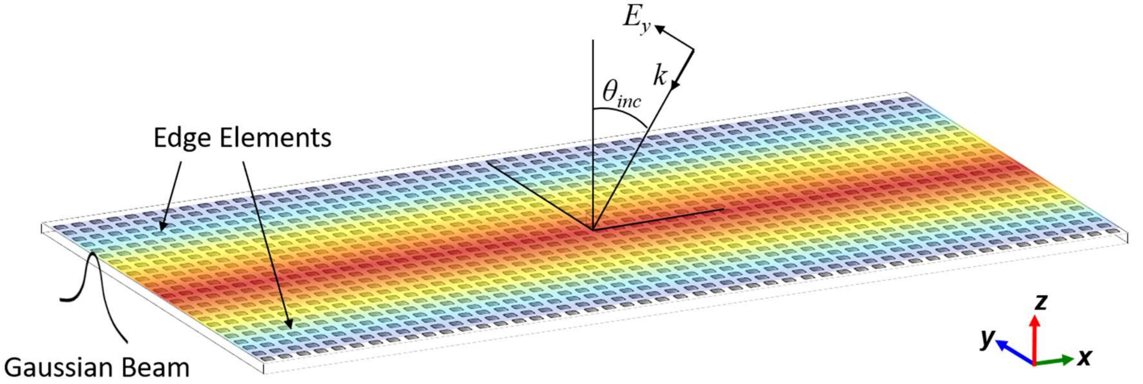

Figure 5.29. Illustration of incident gaussian beam exposure on finite FSS array sample along axis of rotation.

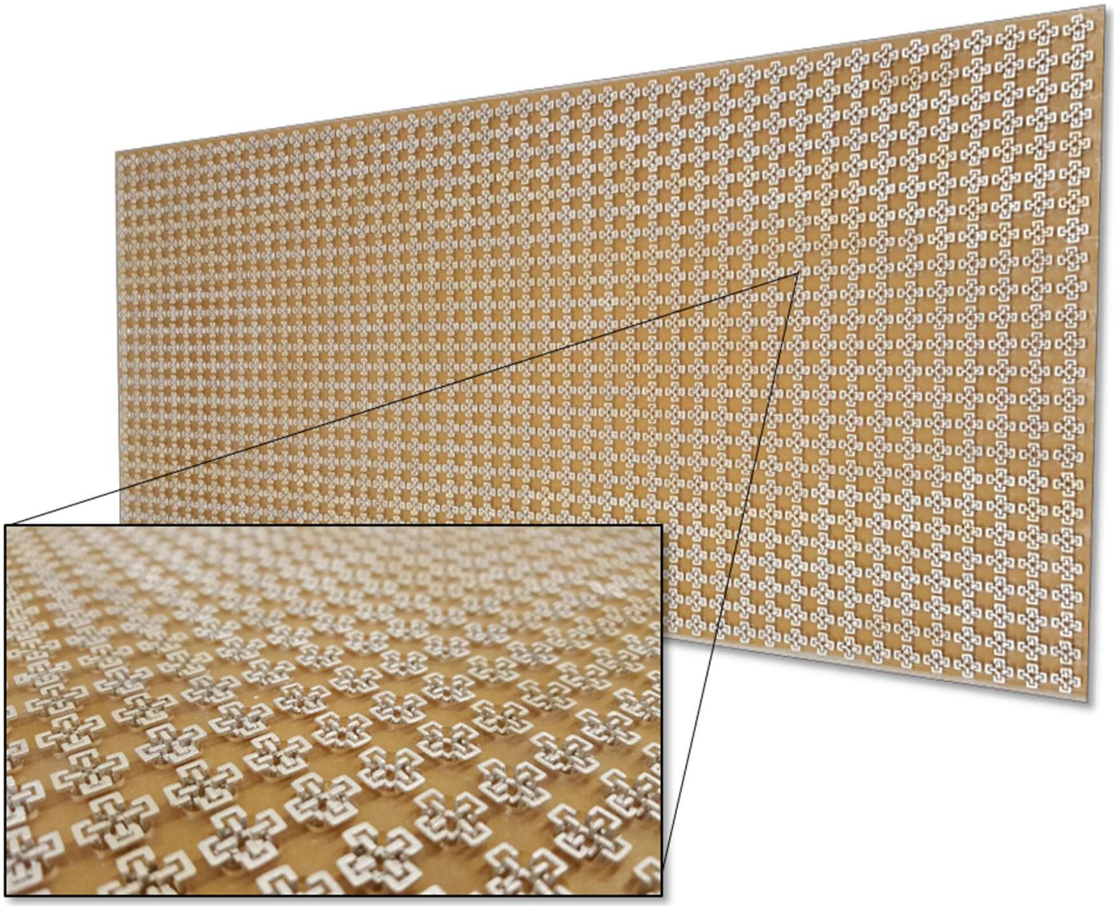

Figure 5.30. Finite array of 1,152 elements embedded in a two-ply 1/8" PMMA sheet with precision cavities cut.

Before proceeding to the final phase of fabrication, the full array is validated one more time at normal incidence in free space. To do this, the sample is centered between two 20 dB C-band standard gain horns, spaced approximately 11.5" apart. First, a two-port calibration is performed to account for mismatch and error introduced by the coaxial cables of each port. The cables are connected to WR-137 transitions, followed by a six-inch straight section, and finally the 20 dB C-band standard gain horn. Both horns are carefully aligned along all axes using a level and tee. The distance from the horn aperture to the plane of the sample is measured and used to perform a Gated Reflect Line (GRL) calibration via Keysight's N1500A Materials Measurement Suite software. Under this approach, two reference measurements are used: reflection from a PEC plate, and transmission without any samples in place. Based on time domain response of these measurements, calibration coefficients are internally calculated for the *S* Parameters to account for the error introduced by the free space between the horn aperture and sample on either side of the test setup. Once these measurements are taken, the finite FSS array is then placed between the two horns with the long dimension parallel to the incident field, as shown in Figure 5.31.

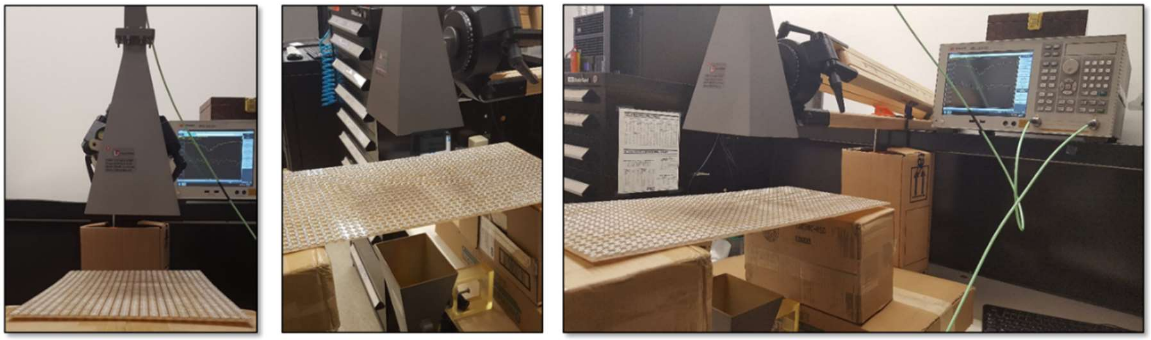

Figure 5.31. Normal incidence free space validation measurement setup for finite FSS array.

Of note, following the measurement, inspection of the horn setup revealed slight misalignment between the waveguide section and the horn, which is likely the cause of the low transmission levels. Nonetheless, a plot showing reference and sample measurements is given in Figure 5.32, showing a clear stop band near 7.8 GHz. While this frequency is higher than the expected stop frequency in an infinitely periodic simulation, these measurements provide a sufficient qualitative confirmation that the elements and array behave like a filter. Since the array is finite in nature, truncation effects may result in frequency shift of the array. Other possibilities include a significant deviation of the relative permittivity of the material from the average reported X-band values in the literature [89], and bowing at the center of the array, which can affect the effective lattice constant of the array. Nonetheless, a slightly higher resonant frequency is beneficial in the

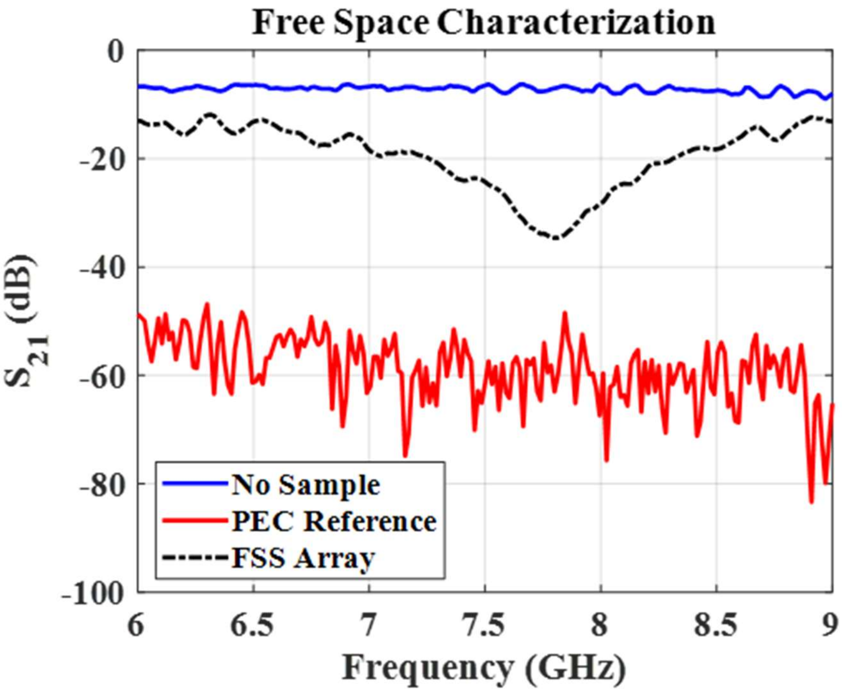

Figure 5.32. Normal incidence free space validation measurement setup for finite FSS array.

sense that the physical size of the FWHM of the gaussian beam will be smaller, meaning more energy can be focused on the finite array.

Following the free space validation of the array, the elements are potted using a Sylgard-527 elastomer, which has an advertised permittivity of $\varepsilon_r = 2.85$, to protect the elements and fix them in place. This encapsulant is preferred for elements with fine features, since the viscosity of Sylgard-527 is 465 cP, as opposed to Sylgard-184, which is approximately 3500 cP when mixed. Thus, the mixture can be de-gassed prior to encapsulation process, rather than during encapsulation, which is significant, since the size of the array is larger than the available vacuum chamber. The average amount of Sylgard-527 needed per unit cell is calculated to be approximately 0.18 ml, resulting in a total of 210 ml of a 1:1 silicon to hardener mixture needed. A wooden frame is constructed around the lattice, which is sealed with painter's tape and silicone caulking to prevent leakage and spillover, and the solution is carefully poured onto the lattice with the embedded FSS elements. Since encapsulation of the 3D FSS elements precisely to the front plane of the elements is challenging, and the elements are fragile, additional Sylgard-527 is used during the encapsulation, which forms a protective superstrate above the elements. The potted array is left to cure at room temperature, forming a solid gel superstrate above the PMMA lattice, as shown in Figure 5.33.

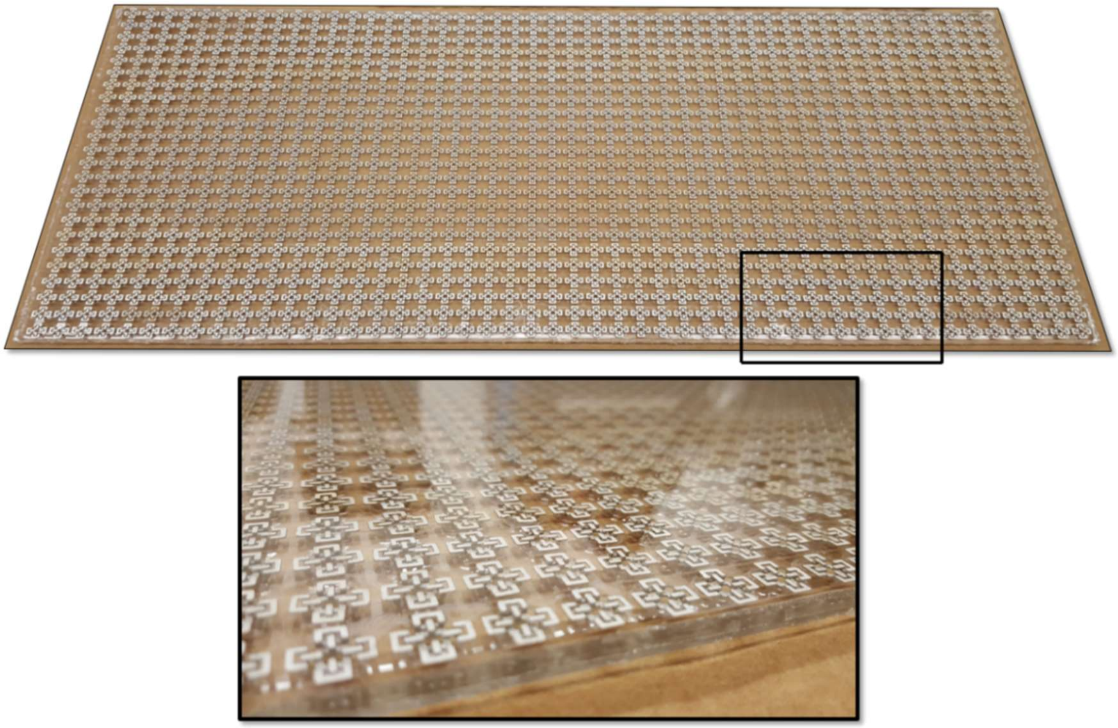

Figure 5.33. Overview and close-up of 24 x 48 finite 3D FSS array encapsulated in Sylgard-527.

Once potted, the FSS array is carefully separated from the wooden frame, and a thin sheet of Polyvinylidene Chloride (PVDC) is placed over the surface of the finite array with clear strips of tape covering the edges to protect the elements from debris. Before and after application of the PVDC, another free-space measurement of the finite FSS array is performed with a more precise calibration and measurement setup using pyramidal C-RAM absorbers, as pictured in Figure 5.34. Although the range of frequencies measured is limited to the operating range of the waveguide and horn, this serves as a final validation prior to broadband focused beam measurements across a wide range of incidence angles. A comparison of the frequency response of the FSS array with and without PVDC shows excellent agreement with simulated results, as seen in Figure 5.35. Finally, the completed

Figure 5.34. Free-space measurement setup of finite FSS array encapsulated in Sylgard-527.

sample is transported to Compass Technology Group in Alpharetta, GA and measured using their broadband focused beam measurement system for TE and TM performance across a wide range of oblique incidences. The entire apparatus is shown in Figure 5.36.

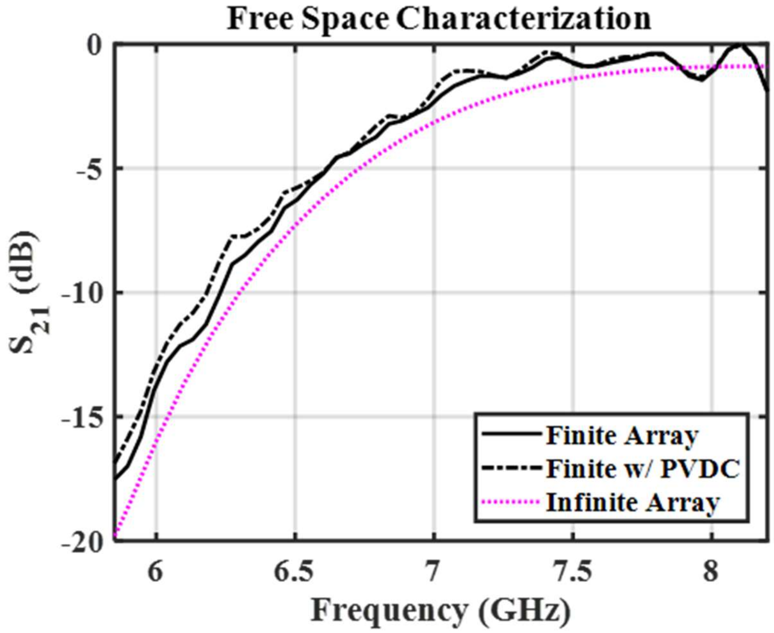

Figure 5.35. Comparison of free-space measured and simulated results using GRL-calibrated C-band 20 dB standard gain horns.

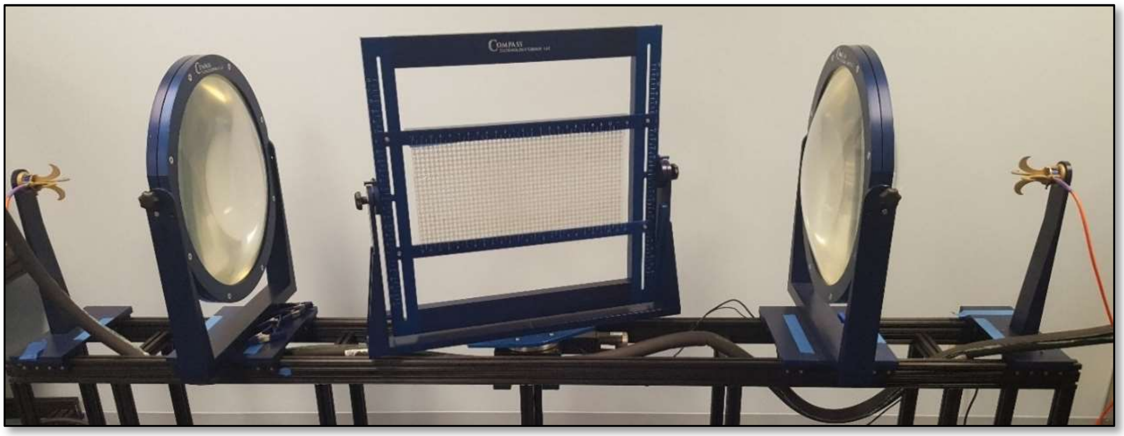

Figure 5.36. Compass Technology Group's broadband focused beam measurement system.

The focused beam measurement system consists of two broadband horn antennas and focusing lenses, placed on opposing ends of an automated sample rotation platform. The platform is actuated using a precision stepper motor, while the two-port measurement is performed using a Copper Mountain VNA, both of which are controlled by a computer with custom-developed data acquisition software. The horn antennas are configured to be co-polarized, and for each polarization (vertical and horizontal), reference measurements of the system are made by electronically rotating the empty sample holder from -80° to 80° in 1° increments. The regions above and below the sample are covered with conductive foil to minimize effects from diffracted energy, forming a baseline measurement of the total energy contained in the sample cross section. A total of 1801 frequency points are collected from 2 GHz to 20 GHz, and a 6 ns time gating, shown in Figure 5.37, is applied to the system to fully capture the resonant response of the structure, while omitting multipath effects introduced by the rest of the system. Once this is done, the process is repeated with the finite 3D FSS array fixed in the holder for both polarizations.

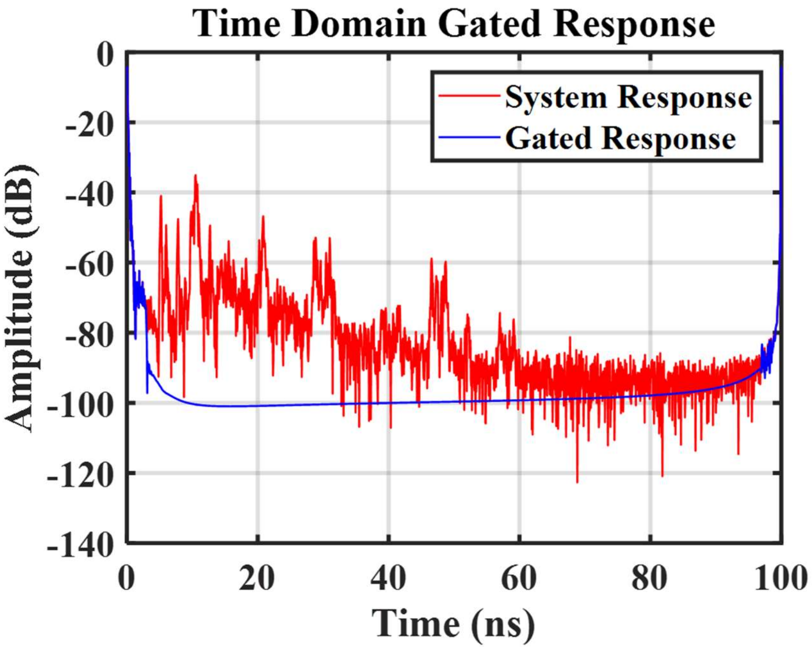

Figure 5.37. Time domain response of focused beam measurement system, with 6 ns time gating, and the sample reference plane normalized to 0 ns.

After the data is acquired, a response calibration [90] is performed by normalizing the sample measurements against the baseline ones for all frequencies and incidence angles. Although an isolation calibration can also be included, since only transmission was being considered, this was not necessary. In Figure 5.38, a comparison of simulated frequency responses of optimized and modified infinitely periodic elements is made against the finite fabricated array measurements. Although the structure was originally optimized using cubic elements for a stop band at 6 GHz and pass band at 8 GHz, modifications were made to the geometry for ease of fabrication, including fillets in the PMMA substrate and FSS geometry for mechanical stability and to mitigate shadowing during the metallization process. Furthermore, while simulations assumed the surface of the Sylgard-527 is level with the front face of the elements, more complex potting techniques would be required to accomplish this without trapping air bubbles in the array. In practice, however, full encapsulation of the element is desirable as it provides an additional protective layer to the elements. Thus, an additional shift in frequency occurs as a result of excess encapsulant used during fabrication, raising the effective permittivity of the structure.

Of note, the peak transmission at normal incidence is only 0.67 dB down from the baseline, indicating minimal loss in the structure. This loss is a direct result of the finite conductivity of the conductive paint, as well as the impedance mismatch and intrinsic loss of the Sylgard-527 and PMMA substrates. While this loss results in a slight reduction in bandwidth, a 6.25% -10 dB stop, and 8.26% 3 dB pass bandwidth still exist at 5.6 GHz and 7.75 GHz respectively, for incidence angles up to ±72°, which are shown in Figure 5.39. Closer examination of the minimum and maximum transmissions across these bands also shows a minimal deviation of ±35 MHz in the stop band, and ±100 MHz in the pass band as a function of incidence angle. These marginal deviations can be attributed to slight fluctuations in lattice constants due to misaligned or slightly deformed elements, and non-uniformities in their conductive coatings. Furthermore, while the bent-mode phenomena can clearly be observed near 6.6 GHz in the TM orientation, the effect is largely diminished due to the finite conductivity of the silver paint.

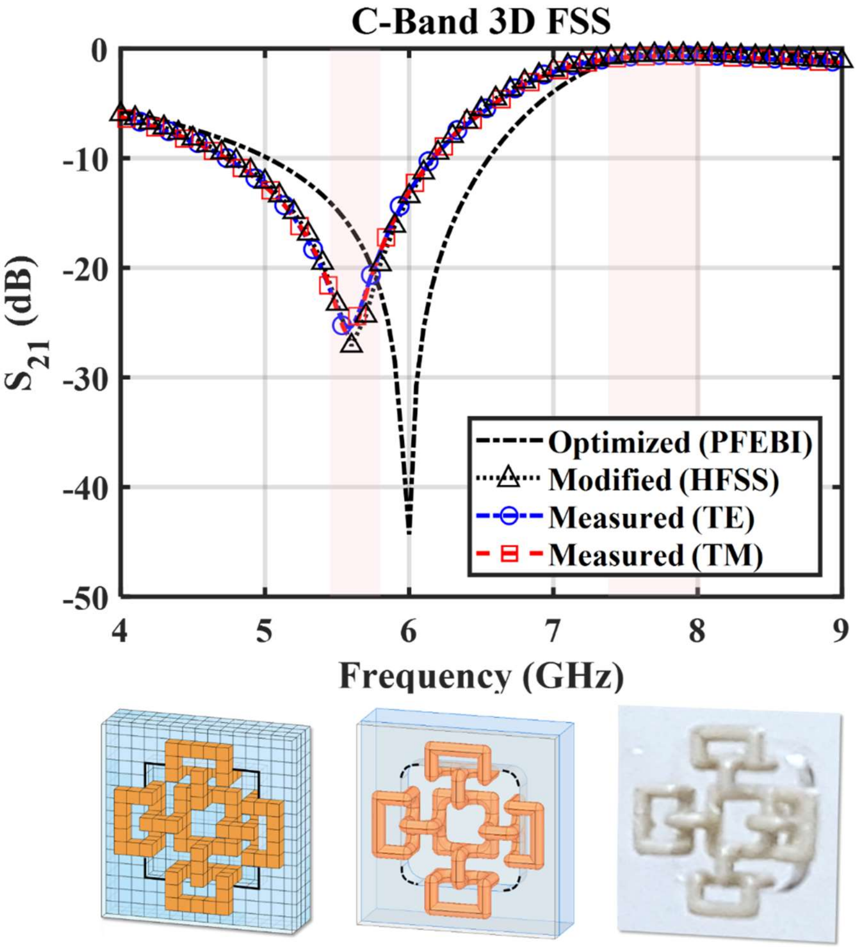

Optimized (PFEBI)
Cubic PEC Elements
w/ Lossless Substrate

Modified (HFSS)
Filleted Elements w/
Finite Conductivity, Loss

Fabricated (Finite Array)
Filleted Finite Conductivity
w/ Sylgard-527 Superstrate

Figure 5.38. Comparison of frequency response of infinitely periodic optimized (PFEBI) and modified (HFSS) elements, to the TE and TM measured results of a fabricated finite array at normal incidence. Highlighted regions correspond to a 6.25% -10 dB stop and 8.26% 3 dB pass bandwidths centered about 5.6 GHz and 7.75 GHz.

Beyond incidence angles of ±72°, edge diffraction from the finite length of the array is introduced. This effect can clearly be seen in the measurement of the sample, based on the divergence of the color map near 6.5 GHz in Figure 5.39 at extreme incidence angles for TE polarization, indicating a slightly overcalibrated response. Upon closer inspection of the calibrated transmission data (excluding the sample) in Figure 5.40, it is evident that an additional 0.3-0.8 dB of insertion loss is accumulated per degree beyond ±72°, as the metal sample holder begins to obstruct the beam waist of the focused Gaussian beam. In

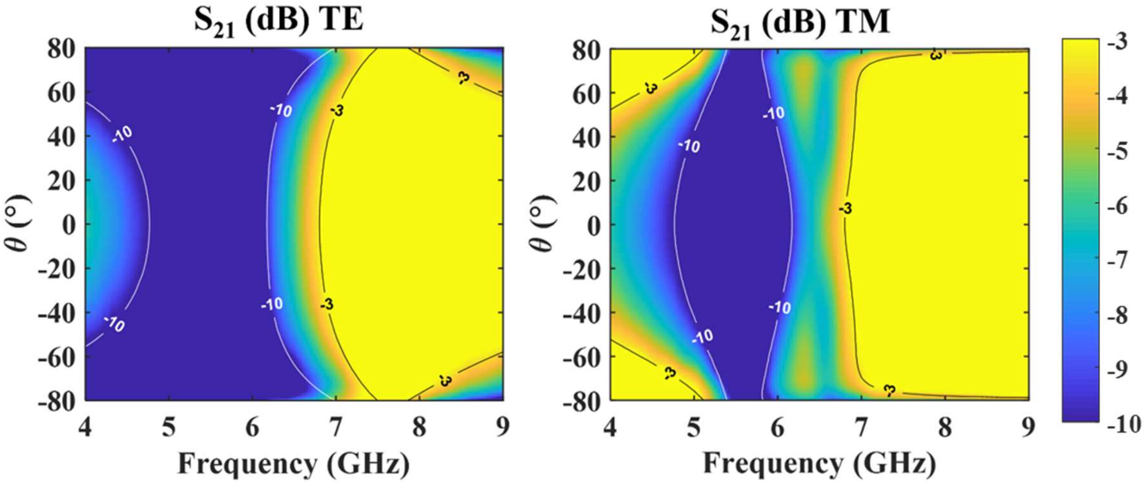

(a)

(b)

Figure 5.39. Comparison of focused beam measured transmission data (color map) versus -3 dB and -10 dB transmission levels of infinitely periodic 3D FSS array simulated in HFSS (contour lines) as a function of frequency and incidence angle for (a) TE, and (b) TM polarizations.

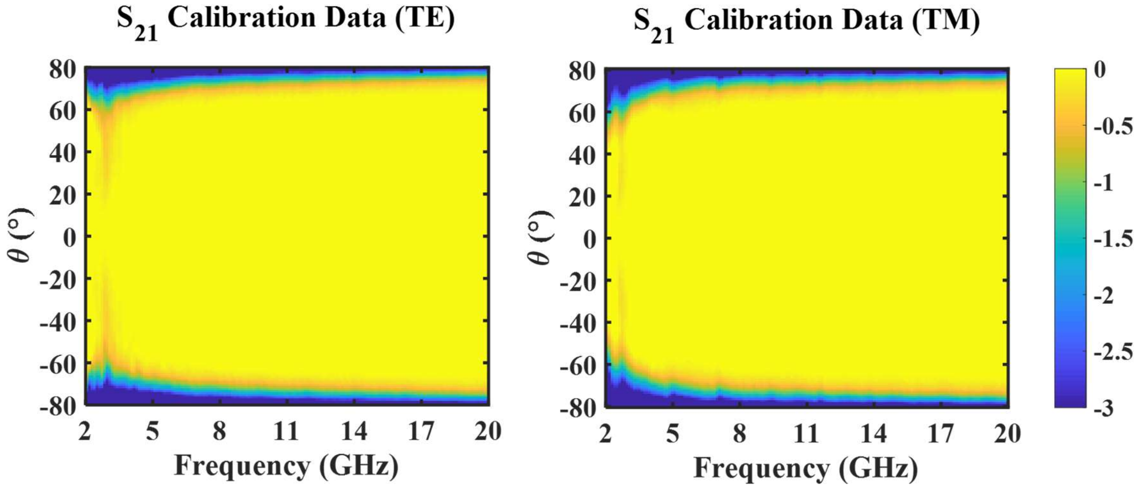

(a)

(b)

Figure 5.40. Calibrated broadband transmission data from 2-20 GHz as a function incidence angle for (a) TE and (b) TM polarizations, indicating the limitation of the focused beam measurement system at incidence angles beyond ±72°.

order to mitigate this, a dielectric sample holder can be used or the sample can be scaled to a higher frequency band, thereby reducing the cross section of the beam waist. Unfortunately, no dielectric sample holder was available, and fabrication at X-band via available additive manufacturing methods is very challenging due to the fragile nature of the fabricated elements.

Overall, the additive manufacturing and metallization of the optimized 3D FSS elements resulted in a low-loss, low-cost, and light weight finite array. Although the conductive paint used had a finite conductivity, this served to mitigate additional resonances in the structure, and suggest that it can also be considered as a loss mechanism in FSS absorber design. Furthermore, although a PMMA substrate was used in this case, in practice, the PMMA is not required and is only used here to provide a rigid mechanical structure. In fact, homogeneous encapsulation of the elements in Sylgard-527 would allow for lower loss and slightly improved angular stability. Additionally, since the elements are also electrically thin, measuring between $\lambda/20$ to $\lambda/15$ in thickness, application of these structures to conformal surfaces with radii of curvature greater than a wavelength is also possible, due to the pliable nature of the Sylgard-527 encapsulant. An added benefit of using this encapsulant is that damaged sections of the array are easily repaired, since sections of the Sylgard can easily be cut away, replaced, and re-potted to itself, forming a homogenous structure when cured again.

Chapter 6

Alternative Applications of MOLACO

6.1 Optimization of Meander Line Antennas

Although originally developed for the problem of 3D FSS design for wide fields of view, advancements made to the MOLACO algorithm including graph generalization, multi-ant modeling and tandem optimization with an MGA make it well-suited for a variety of other problems in electromagnetics. This includes simple problems, such as impedance matching of MLAs, to more challenging problems, including the design of optical antennas and metamaterial supercells in the MWIR regime, to name a few. Each of the examples given here has different problem dynamics and leverages a variety of solvers, further showing the versatility of the MOLACO algorithm.

In the first example, impedance matching of a planar array of dipole elements radiating at 2 GHz and embedded in a NZIM, is addressed. The NZIM acts as a lens to allow the radiators to form a flat main beam with a beamwidth of 30° and is previously optimized in COMSOL to have material tensors of $\varepsilon_x = \mu_x = 0.5351$, $\varepsilon_y = \mu_y = 0.4312$, and $\varepsilon_z = \mu_z = 0.9599$. To avoid grating lobes, the desired periodicity of the antenna element is chosen to be less than 0.5λ [75]. However, the presence of the NZIM and small size of the element makes it difficult to match a linear dipole to a 50 Ω feed. One common application of traditional ACO optimizers has been to miniaturize MLAs, which has proven to be quite effective. However, in this case, rather than miniaturization, we seek to impedance match the input by meandering the dipole arms. While traditional ACO approaches would require several space-filled optimizations of various grid sizes to achieve an ideal solution, MOLACO is capable of performing this in a single optimization, due to its ability to span a diverse set of solutions using lazy ants and masking. In order to solve this problem, the MOLACO optimizer is paired with the same full wave PFEBI tool used in FSS design, which is configured for radiation instead of scattering problems. Once the input impedance of the antenna element in an infinite environment is optimized using PFEBI, designs are validated in both infinite and finite array environments with HFSS, and an analysis of radiation pattern and impedance of each element in the planar array is performed.

Three colonies are used, each with a population size of 360 ants searching antenna geometries per generation. Furthermore, each colony is sub-divided into three mask types: geometries based on two-fold symmetry (Mask 1), 180° rotational symmetry (Mask 2) and four-fold symmetry (Mask 3). Since a symmetric radiation pattern is desired, the search space is chosen to be a 5x11 meander grid, with the feed point in the bottom center of the grid. Specifying a mask for the grid determines which nodes can be traversed, and which ones can represent start points. This allows all meander designs explored during the optimization to be forced to originate from the chosen feed point. Furthermore, a simple Gaussian fitness function centered around the desired real and imaginary impedance values are used as the two objectives:

$$F_{Dipole} = e^{-(Z-\mu)^2/2\sigma^2} \tag{27}$$

where μ = 50 Ω and σ = 55 Ω for the real impedance, and μ = 0 Ω and σ = 500 Ω for the imaginary impedance, since the reactive component spans a larger range of impedance values, which ensures the maximum fitness is assigned to a design with $Z_{in} = 50\ \Omega$, shown in Figure 6.1. From Figure 6.2(a), it can be seen that four-fold symmetric designs are heavily concentrated near the maximum values of both objectives. Additionally, due to the efficiency and speed of the PFEBI solver, the resulting approach rapidly converges on several solutions in as little as 45 minutes as shown in Figure 6.2(b). The best designs from

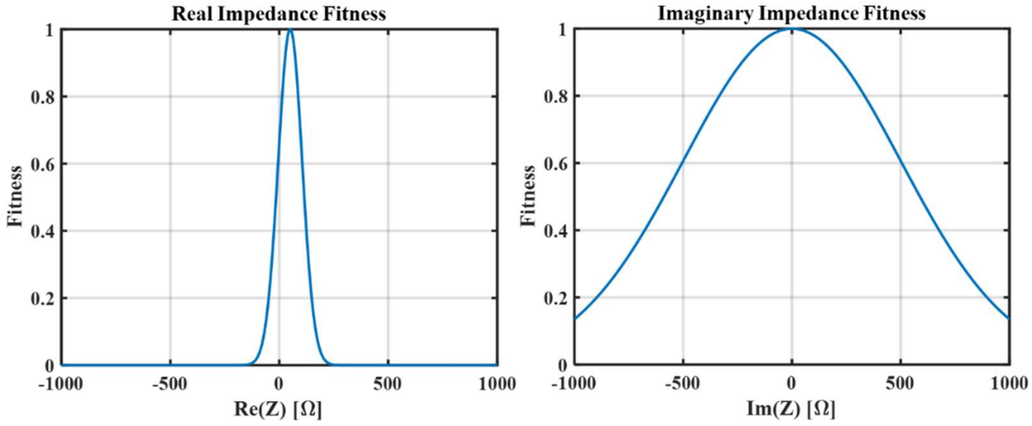

(a) (b)

Figure 6.1. Plots of Gaussian fitness distribution of (a) real and (b) imaginary impedances.

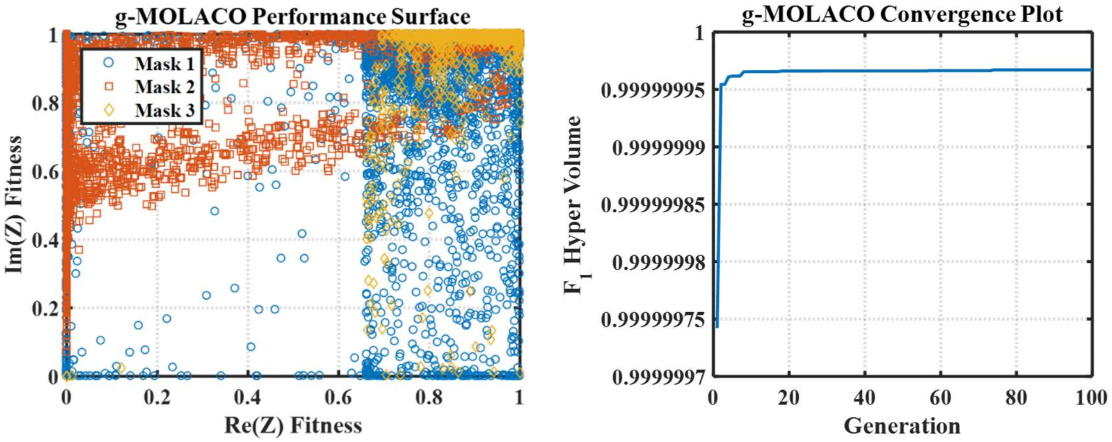

(a) (b)

Figure 6.2. Plots of (a) performance surface as a function of fitness and mask type, and (b) convergence of best Pareto set hypervolume.

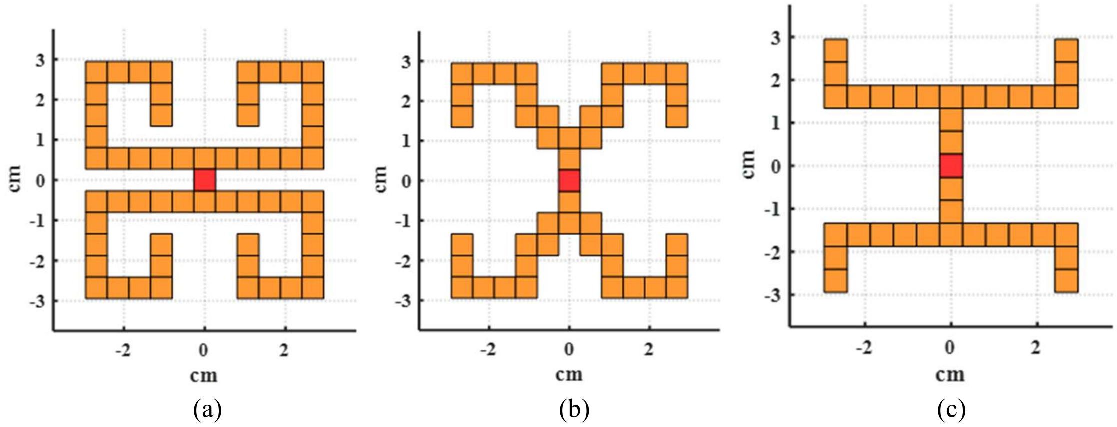

(a) (b) (c)

Figure 6.3. Geometries of select Pareto-optimal designs based on four-fold symmetry, where orange elements represent PEC and red elements represent the feed point. Input impedances of the designs in an infinite environment are (a) 29.56 – j 0.009 Ω, (b) 50.16 – j 2.68 Ω, and (c) 45.21 – j 0.025 Ω.

the Pareto set are selected and shown in Figure 6.3 above, all of which are four-fold symmetric. As a basis of comparison, both an infinite array and 7x7 planar array of 0.4λ dipoles are simulated in HFSS, and their corresponding input impedances are plotted in Figure 6.4. The dashed lines provide a frame of reference for the desired real (50 Ω) and imaginary (0 Ω) values. While the real impedance is relatively close to 50 Ω, the imaginary component is highly capacitive in both infinite and finite cases. Further analysis of the element pattern shows a null at broadside with grating lobes in both principle planes and a peak gain of 8 dB, as seen in Figure 6.5. Finally, examination of the input impedances of each element of a planar 7x7 array given in Figure 6.6 shows a large fluctuation of impedance values across elements, with up to 78.2 Ω variance in the real component and over 135.6 Ω in the imaginary component.

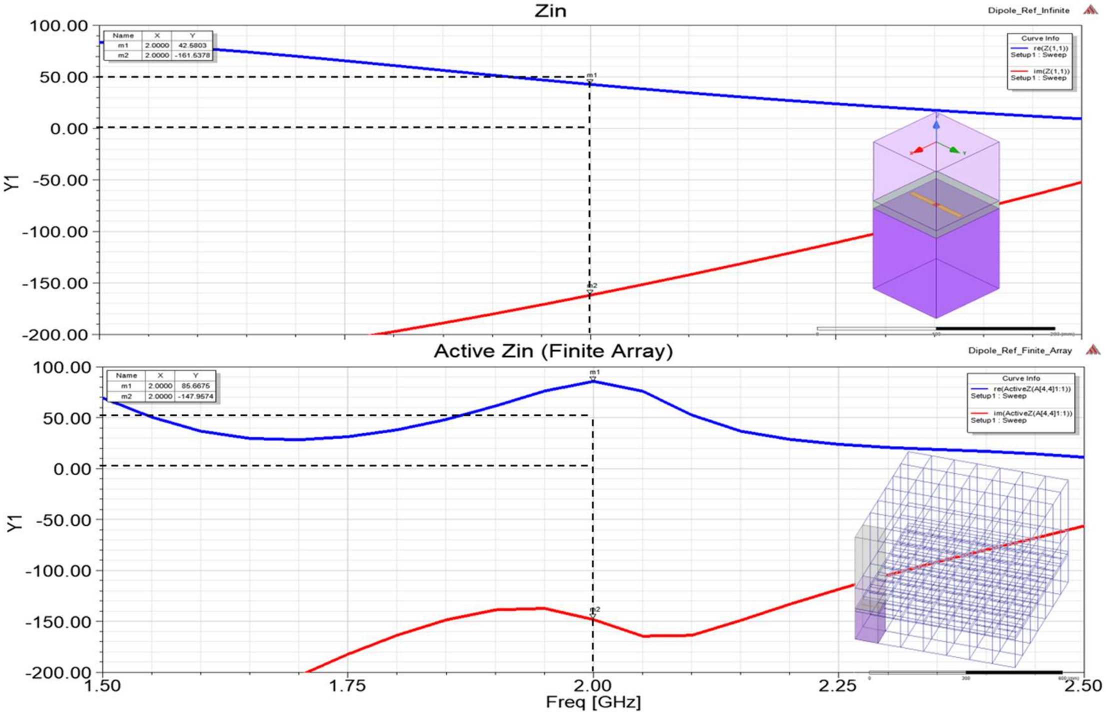

Figure 6.4. Input impedance of infinite array (top) and 7x7 planar array (bottom) of 0.4λ dipoles. Real impedance is shown in blue and imaginary impedance is shown in red, with the dashed line showing target values at 2 GHz.

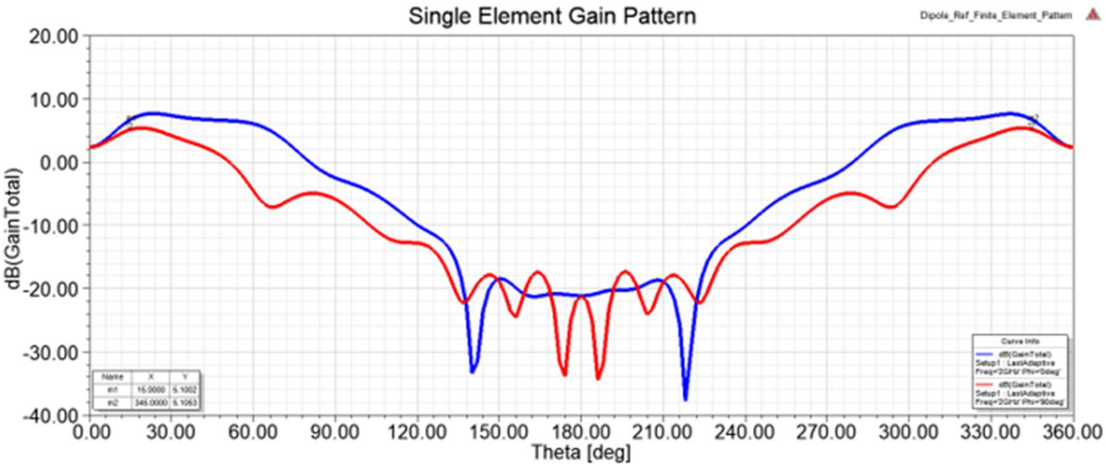

Figure 6.5. Single element pattern of a 0.4λ dipole embedded in an NZIM at 2 GHz.

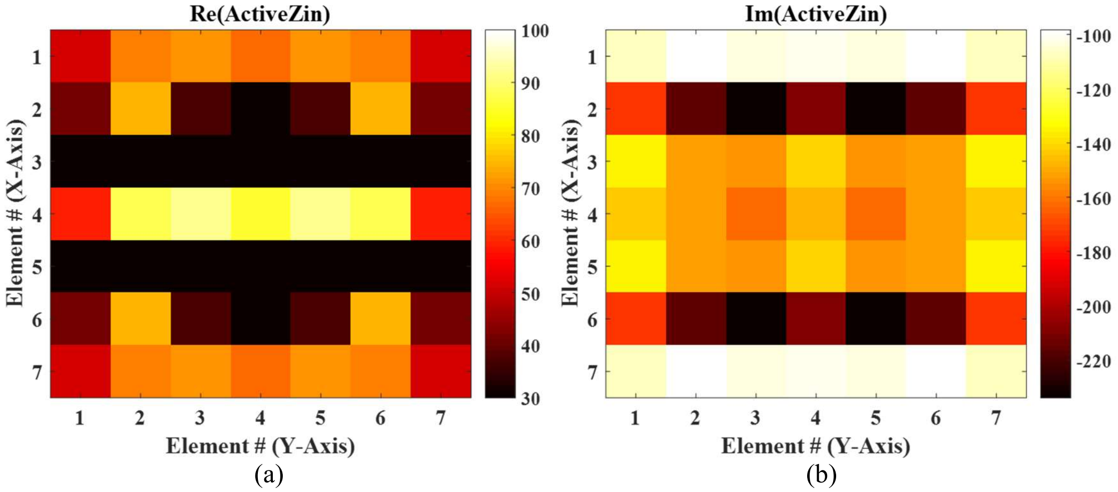

Figure 6.6. Comparison of (a) real and (b) imaginary input impedances of 7x7 planar array.

A similar analysis of the first optimized antenna geometry is presented in Figure 6.7-Figure 6.9. It can be seen that the impedance values are much closer and consistent with the desired values in both infinite and finite array cases, and a very flat beam exists in the H-plane up to 30° with less than 1 dB fluctuation of the main beam in the E-plane, and side lobe levels are 10 dB down from the main beam. Moreover, the range of real and imaginary impedance values is much more uniform with only 56.4 Ω fluctuation of the real component and 62.7 Ω fluctuation of the imaginary component, which is mostly inductive.

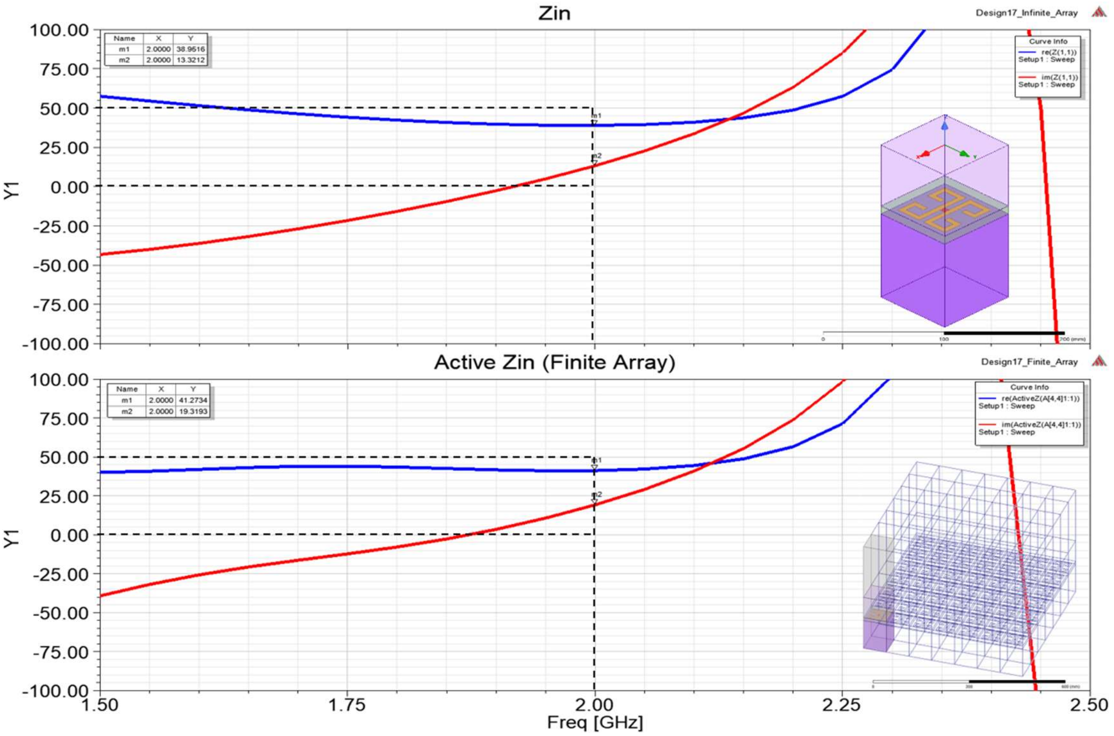

Figure 6.7. Input impedance of infinite array (top) and 7x7 planar array (bottom) of antenna elements with the geometry shown in Figure 6.3(a). Real impedance is shown in blue and imaginary impedance is shown in red, with the dashed line showing target values at 2 GHz.

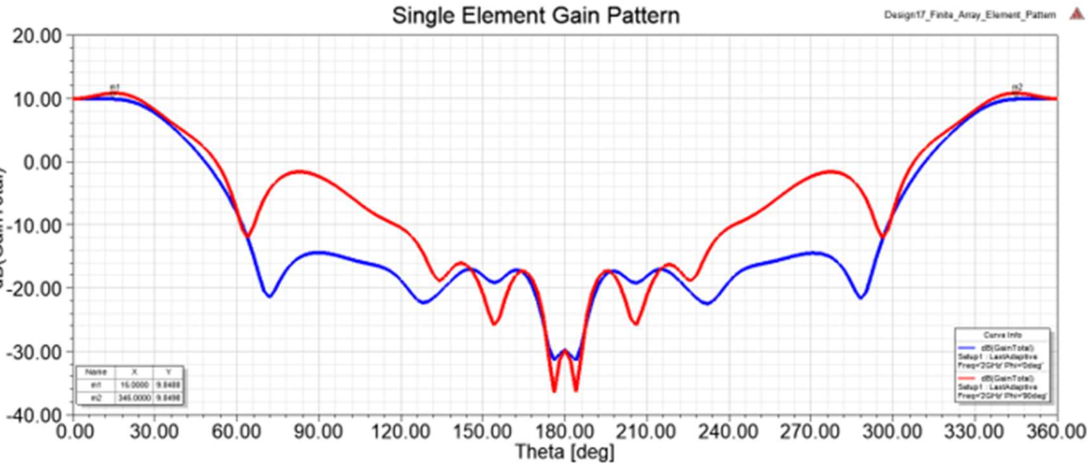

Figure 6.8. Single element pattern of antenna geometry shown in Figure 6.3(a) embedded in an NZIM at 2 GHz.

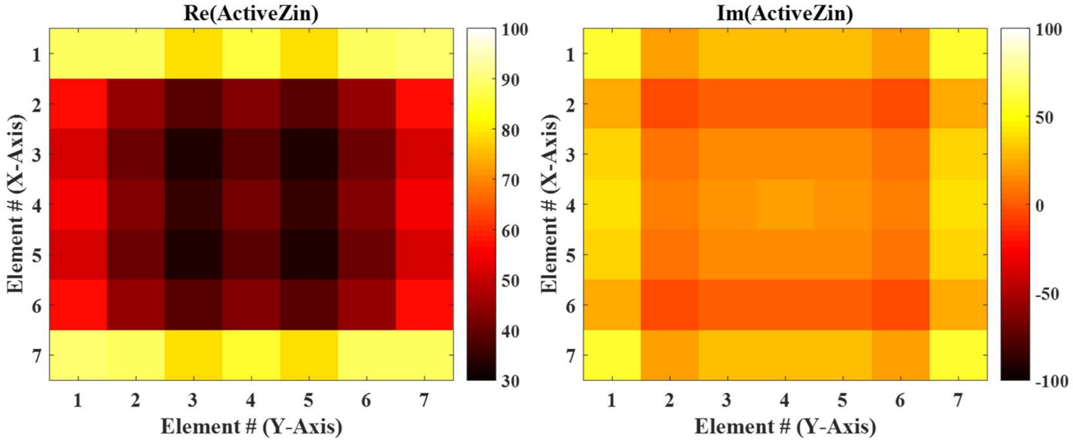

(a) (b)

Figure 6.9. Comparison of (a) real and (b) imaginary input impedances of 7x7 planar array for geometry shown in Figure 6.3(a).

Details of the second optimized design are given in Figure 6.10-Figure 6.12, featuring a slightly higher real impedance near 78.8 Ω. Although the main beam is flatter than the previous design in the E-plane, it tapers off more quickly in the H-plane, although side lobe levels still remain 10 dB down from the main beam. However, the element impedances are less uniform with real impedance values having a variance of 112.5 Ω, and imaginary impedance values fluctuating as much as 121.7 Ω across both capacitive and inductive reactances, which can make matching networks more complicated to implement.

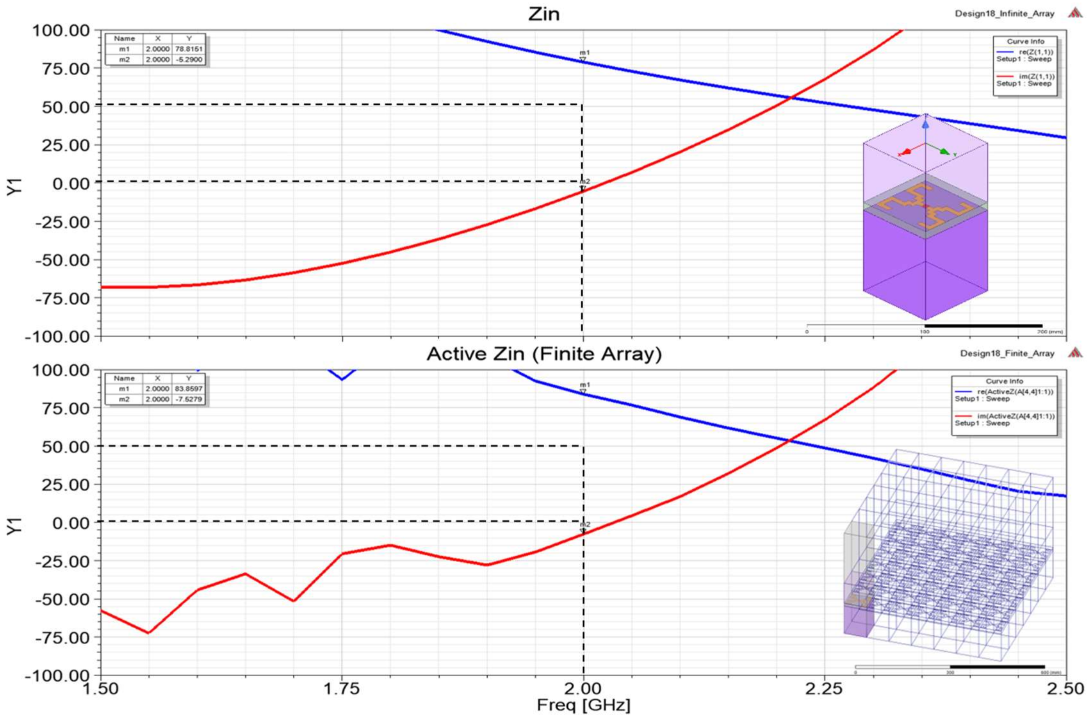

Figure 6.10. Input impedance of infinite array (top) and 7x7 planar array (bottom) of of antenna elements with the geometry shown in Figure 6.3(b). Real impedance is shown in blue and imaginary impedance is shown in red, with the dashed line showing target values at 2 GHz.

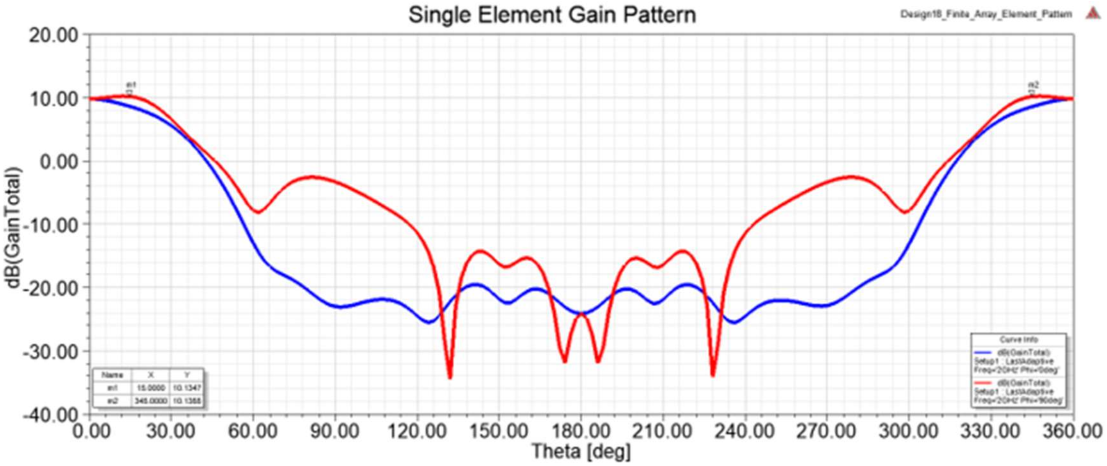

Figure 6.11. Single element pattern of antenna geometry shown in Figure 6.3(b) embedded in an NZIM at 2 GHz.

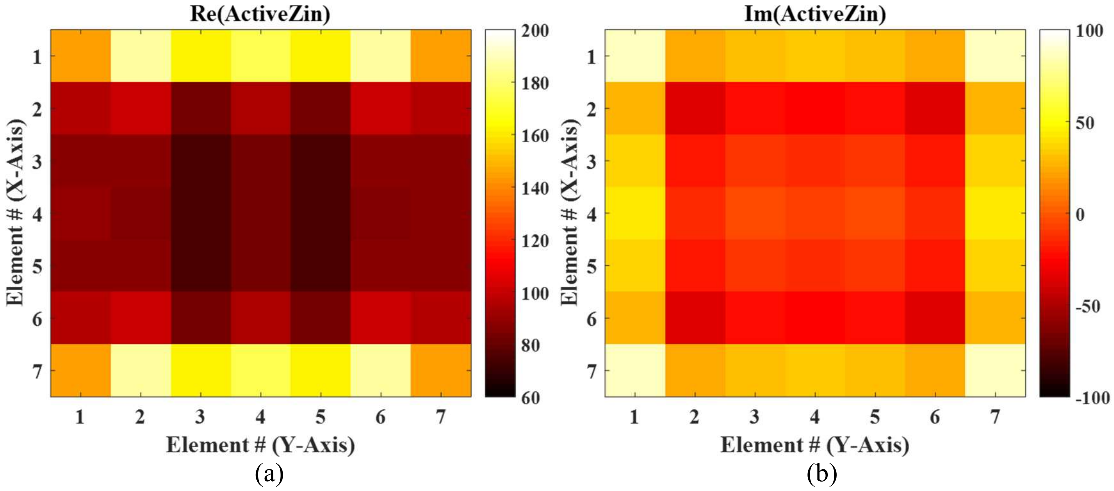

(a) (b)

Figure 6.12. Comparison of (a) real and (b) imaginary input impedances of 7x7 planar array for geometry shown in Figure 6.3(b).

Finally, the results of the last optimized design are given in Figure 6.13-Figure 6.15. The real component is nearly perfectly matched with an impedance of 48.38 Ω, and a slightly inductive imaginary component of 27 Ω. The main beam of the single element pattern is remarkably flat up to 30°, with less than 1 dB fluctuation, and a much more uniform distribution of impedance values exists in the planar array, with real impedances varying as little as 44.4 Ω, and the imaginary component varying up to 71.6 Ω, but entirely inductive. While the overall gain at broadside is 9.4 dB, which is 0.5 dB lower than the other optimized designs, the side lobe levels are 15 dB down from the main beam. Comparing the performance of each of these designs, the geometry in Figure 6.3(c) is offered as the best, striking the best balance between radiation and impedance characteristics in a 7x7 finite array.

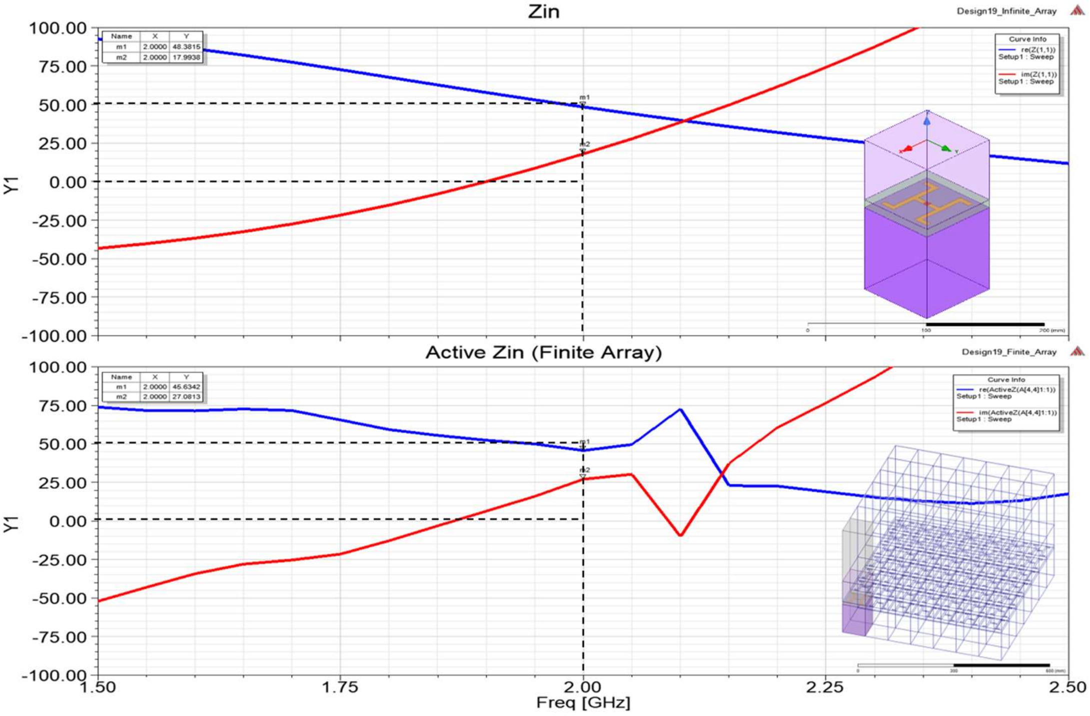

Figure 6.13. Input impedance of infinite array (top) and 7x7 planar array (bottom) of antenna elements with the geometry shown in Figure 6.3(c). Real impedance is shown in blue and imaginary impedance is shown in red, with the dashed line showing target values at 2 GHz.

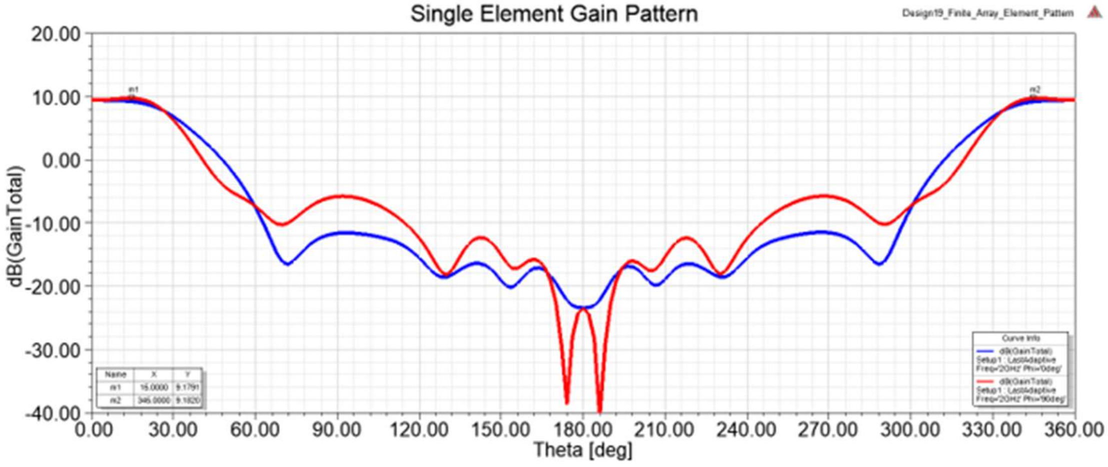

Figure 6.14. Single element pattern of antenna geometry shown in Figure 6.3(c) embedded in an NZIM at 2 GHz.

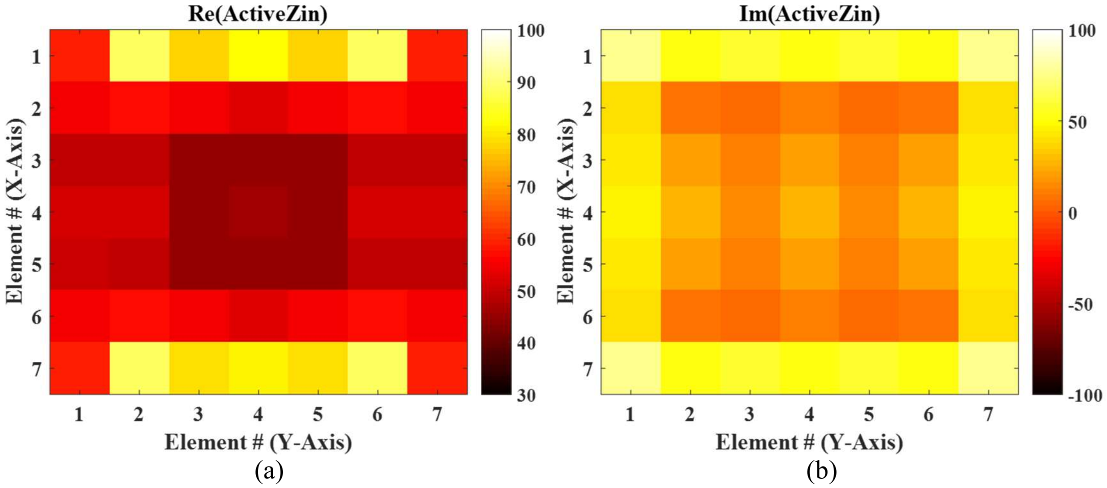

(a) (b)

Figure 6.15. Comparison of (a) real and (b) imaginary input impedances of 7x7 planar array for geometry shown in Figure 6.3(c).

Thus far, MOLACO has been applied to optimize planar MLA arrays embedded within an NZIM. Each design was simulated in PFEBI and validated in HFSS, and their radiation patterns and impedance characteristics were examined in both infinite and finite array settings. In the remainder of the chapter, application of MOLACO is considered in the optical regime, where metals can no longer be modeled as PECs, and are much closer to their plasma frequency, introducing unwanted absorption. Materials in this regime are much more dispersive than in the microwave regime and must be modeled accordingly. Under these constraints, inverse design of optical antennas is performed, and their application in phase-gradient metasurfaces will be considered.

6.2 Optical Antenna Design

Recently, optical antennas based on the generalized Snell's law of refraction shown in equation (28) have become of great interest for a wide variety of metamaterial applications, including phase gradient metasurfaces [91]-[93], wave control and conversion [94], and optical vortex beams [95].

$$\sin(\theta_t)n_t - \sin(\theta_i)n_i = \frac{\lambda}{2\pi}\nabla\Phi \tag{28}$$

These designs typically require a high reflection or transmission and a 2π phase range to efficiently scatter energy. Examples of existing metasurfaces are shown in Figure 6.16:

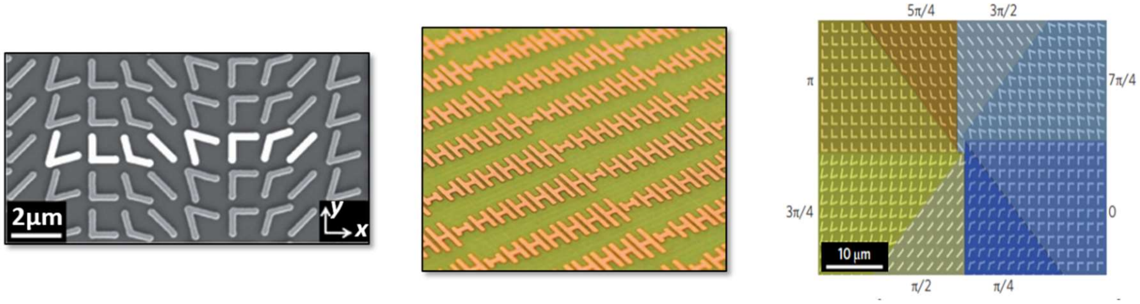

(a) (b) (c)

Figure 6.16. Comparison of (a) phase-gradient metasurface [91], (b) propagating to surface wave converter [94], and (c) optical vortex beam [95]. Figures reprinted by permission from Springer Customer Service Centre GmbH: Springer Nature [91] © 2014.

While many planar designs exist, limited work has been done on their 3D counterparts [96], despite a wide variety of existing 3D nanofabrication techniques, such as Focused Electron Beam Induced Deposition (FEBID) [97], Single-Step Electron Beam, Lithography [98], Direct Laser Writing with Electroless Plating [99], and Nanoimprint Lithography [100] shown in Figure 6.17. In this section, a 3D metallodielectric metamaterial unit cell based on Sandia National Laboratories' Membrane Projection Lithography (MPL) technology [101], [102] is extensively examined. Examples of these cavities are given in Figure 6.18.

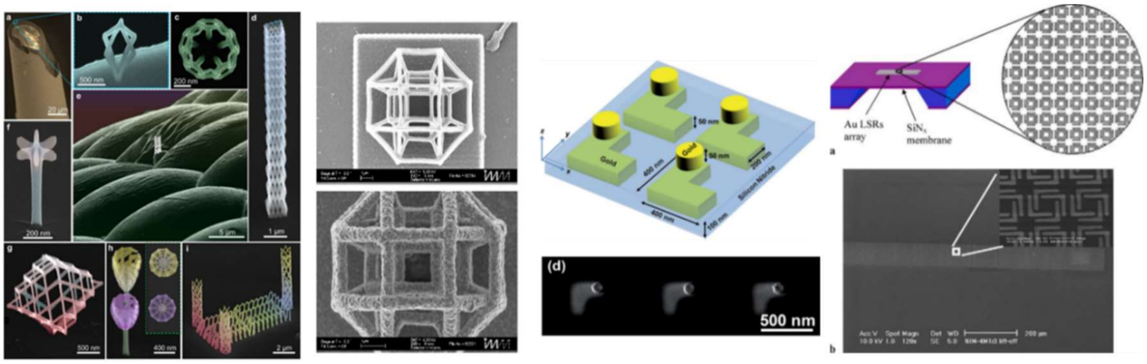

(a) (b) (c) (d)

Figure 6.17. Comparison of various 3D nanofabrication techniques, including (a) Focused Electron Beam Induced Deposition (FEBID) reprinted with permission from [97] © 2016 American Chemical Society, (b) Direct Laser Writing with Electroless Plating [99], (c) Single-Step Electron Beam Lithography [98], and (d) Nanoimprint Lithography, reprinted by permission from Springer Customer Service Centre GmbH: Springer Nature [100] © 2007.

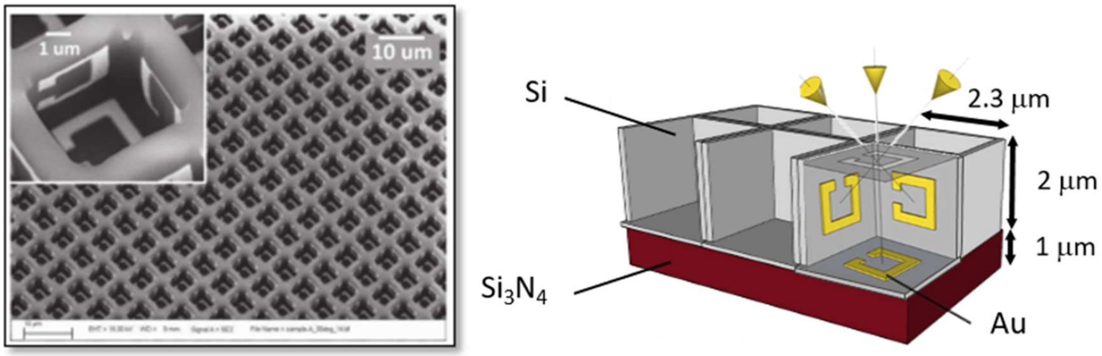

(a) (b)

Figure 6.18. SEM image of Split Ring Resonators (SRRs) arranged inside a cavity based on Sandia National Laboratories' Membrane Projection Lithography (MPL) fabrication technique reprinted with permission from Wiley: Advanced Materials [102] © 2010.

Unlike the RF regime, where metals can be approximated as PECs, the high frequencies used in the optical regime cause metals to behave differently. The regime of interest in this application is the MWIR range corresponding to wavelengths between 5-8 μm, and optimizations are performed using dispersive material properties experimentally characterized by Sandia National Laboratories for gold (Au), silicon (Si) and silicon nitride (Si_3N_4). As 3D nanofabrication techniques continue to evolve, the MOLACO algorithm can be applied to optimize designs or perform a directed parametric study of the design space, revealing valuable insight to the capabilities and limitations in fabrication methods.

6.2.1 Pareto Locus Based Search

As previously mentioned, the two primary objectives for the proposed optical antennas are to maximize transmission while maintaining phase diversity. Traditional approaches to discover these have usually started with a parametric study of a canonical structure with some known performance characteristics [93]-[95][103]-[105]. In this case, an inverse design process is utilized, where an unintuitive structure will be generated based on known manufacturing constraints of the MPL process using variations of the MOLACO algorithm to satisfy specific performance characteristics. Since multi-objective approaches inherently explore trade-offs between objectives, they have limited use in this scenario, since we are interested in maximizing transmission and phase range as opposed to exploring trade-offs between the two. Alternatively, it is possible (albeit time consuming and redundant) to run individual optimizations to find geometries that satisfy specific phase options. Instead, an alternative approach is proposed, where a single optimization can be used to generate a wide variety of geometries for a pre-defined number of phase options.

The proposed approach is a single-objective optimization of the transmission amplitude using the transmitted phase as a discriminator, which can be achieved using the concept of ε-boxes, found in other evolutionary algorithms, such as Borg [72]. The ε-dominance approach is typically performed in lieu of the FNDS method mentioned in Section 3.1. Since phases are wrapped between values of 0 and 2π, it makes sense to visualize the phase with a polar plot, where the radial component represents the transmission amplitude, and the angular component represents the transmitted phase. Thus, unlike traditional implementations of ε-boxes, which are based on Cartesian space, this implementation utilizes ε-sectors, based on Polar coordinates. Instead of maximizing or minimizing solutions within all ε-boxes, we maximize only the radial component in each of the pre-defined ε-sectors, ensuring a minimum number of search vectors corresponding to the number of targeted phase options. A comparison of the search behavior of traditional multi-objective optimization using a FNDS versus the proposed Pareto locus search is given in Figure 6.19. In the traditional FNDS approach, a trade-off between transmission and phase is made to form the Pareto set, which results in a skewed Pareto set of phase options, and solutions which have minimal transmission. On the other hand, the Pareto locus search forces search vectors to travel centrifugally, such that transmission is always maximized in each of the uniformly spaced phase sectors, whose size is pre-determined according to a specific application. In the example given, six phase sectors of 60° are used, which are radially sub-divided by concentric circles into transmission segments of 20%.

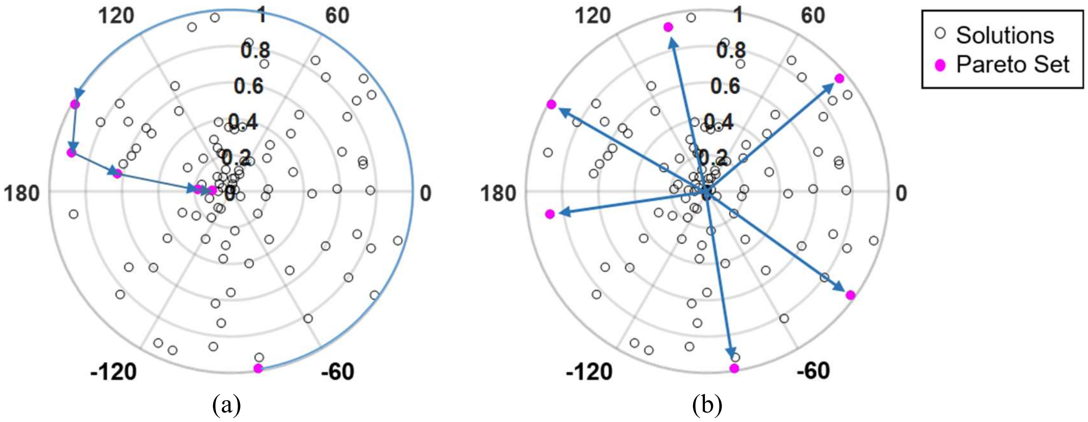

Figure 6.19. Example of (a) traditional multi-objective search pattern versus (b) ε-sector based search pattern.

6.2.2 Characterization of Membrane Projection Lithography Unit Cell

A simple analysis of the proposed MPL unit cell lattice without any gold evaporations shows a peak transmission at 5.5μm, which is taken as the target wavelength, assuming an incident s-polarized (or TE) plane wave. Figure 6.20 also shows degradation of the response if a film of silicon remains unetched from the silicon nitride substrate represented by the dashed line, suggesting the high refractive index (n = 3.42) of even a thin layer of silicon degrades transmission. While it is best to ensure a complete etch in the manufacturing process, both cases are considered in this section.

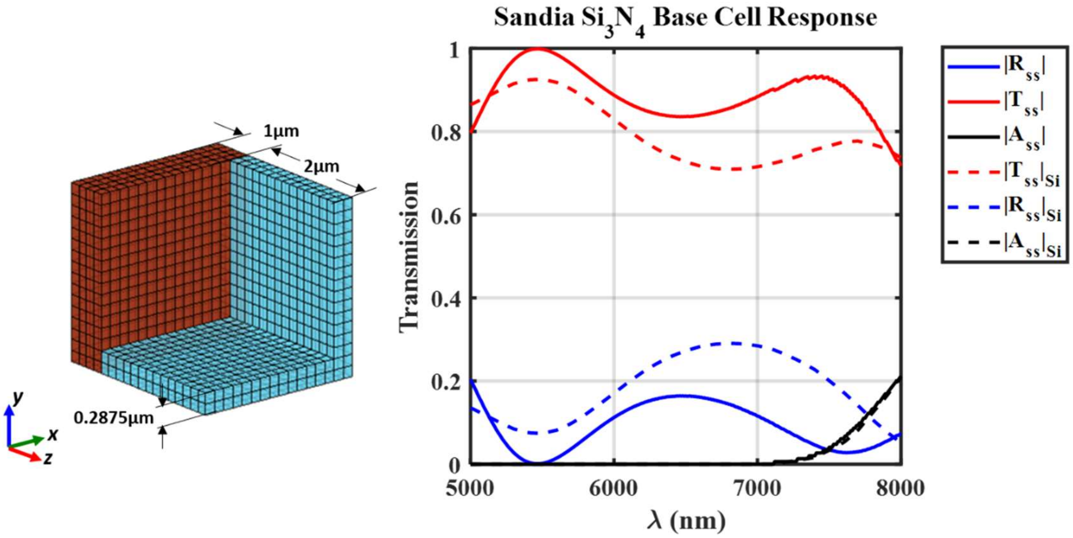

Figure 6.20. MWIR spectral response of periodic MPL unit cell without Au evaporations, consisting of a Silicon (Si) lattice (light blue) above a Silicon Nitride (Si_3N_4) substrate. Solid line assumes a pure Si3N4 substrate, whereas dotted line assumes an incomplete etching process resulting in a thin Si film remaining above substrate, which significantly degrades performance.

6.2.3 Optimization of Unit Cell

Given the baseline performance of the unit cell shown in the previous section, a variety of strategies of the MOLACO algorithm are applied to search the design space for

3D metallodielectric structures that are highly transmissive and offer a variety of transmitted phases over a relatively wide field of view. Although a large number of metallodielectric structures tend to be absorptive in nature, the depth of the MPL-based unit cell structure allows Au evaporations to take advantage of the additional surface area to advance or delay incident waveforms without too much blockage or absorption, yielding a diverse range of phases and high transmission.

First, design permutations that are closest to manufacturable are considered, beginning with orthogonal evaporation of a single membrane pattern. Since MPL can perform multiple evaporations using a single membrane, one topology that can be explored is the evaporation of the membrane pattern on one or more cavity walls. For a cavity with five walls, a single membrane stencil can have up to 32 possible combinations of orthogonal evaporations using this approach. Each of these configurations can be considered an operator on the meander geometry, and since each wall can be treated as a discrete variable that is either "on" or "off," optimization of these operators can be done using the MGA driven MOLACO. Alternatively, population-based adaptation can be performed as well, as will be shown later, with nearly identical results. In each case, the convention for designating wall evaporations will be given by a five-bit binary string representing the north, east, south, west, and back walls respectively. Using the MGA approach, over a period of 151.6 hours, a total of 116,586 designs are explored using this approach, with the archive of results plotted in Figure 6.21 according to transmissivity and transmitted phase. A clear peak exists surrounding a transmitted phase value of zero degrees, which coincides with the natural behavior of the cavity. Thus, at $\lambda = 5.5$ μm, the majority of designs based on orthogonal MPL evaporations retain the same response as the natural cavity, with varying amounts of absorption due to the Au traces. It is evident that while high transmission is possible, a very limited phase range is available for these regions, which is generally insufficient for many phase gradient metasurface designs.

As previously mentioned, the same analysis can also be done with population-adaptive operators. However, since a minimum population size is enforced to encourage continued exploration of all operators, one downside to a population-adaptive approach is the evaluation of fewer designs overall, since it is possible to exhaust each operator's contributing solutions. To better illustrate this, consider the example of a bit string of [0 0 0 0 0], corresponding to the first operator type. This operator always results in a single solution, since it is equivalent to the base unit cell (*i.e.* no Au evaporations on any walls). Thus, using population-adaptive operators, the algorithm will immediately discover and evaluate this solution, and for the remainder of the optimization, will restore a fixed portion of the population size to the same base unit cell solution, preventing exploration of other

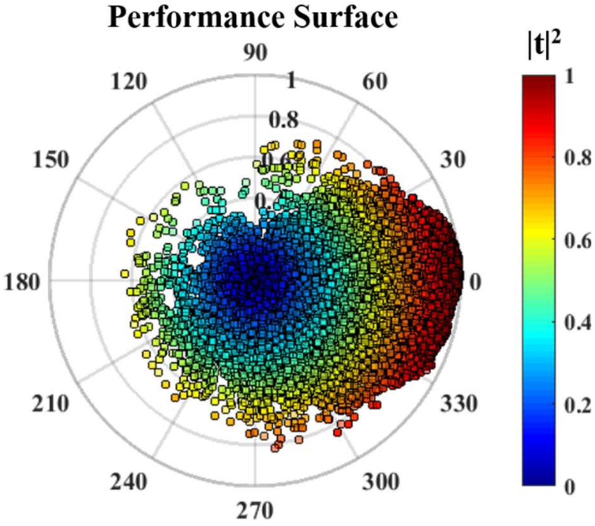

Figure 6.21. Performance surface of a variety of orthogonally projected membranes based on a Macro-GA.

designs that have yet to be explored. For clarity, a side by side comparison of the performance surfaces of a population adaptive scheme and auto-adaptive MGA is given in Cartesian coordinates in Figure 6.22. These optimizations are based on the worst-case design at the base unit cell's transmission minimum at a wavelength of λ = 6.5 μm, and assuming a thin film of silicon exists above the silicon nitride due to an incomplete etching process. It is evident that the peak transmission shifts to a different phase value, which intuitively makes sense, since the target wavelength has been increased, and a thin layer of silicon has been assumed above the substrate. Moreover, although the base unit cell has a near 80% s-polarized transmission efficiency at 6.5 μm, optimized designs are capable of exceeding this limitation. Additionally, both the population-adaptive and MGA adaptive approaches result in similar performance surfaces, and this information can be post-processed according to operator (or mask) type. For example, it is possible to identify which cavity walls significantly impact transmission and phase diversity when Au traces occupy them, providing useful insight into design rules, and driving improvements in manufacturing methods.

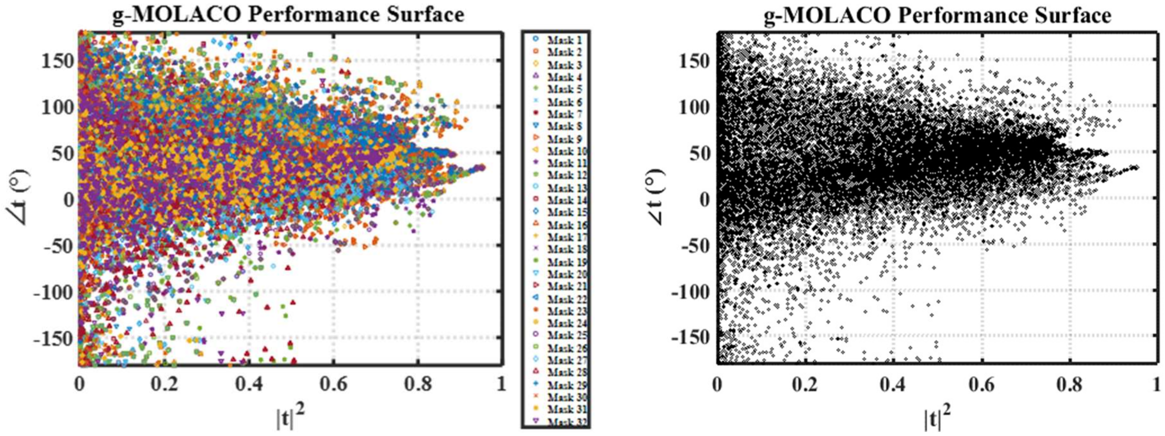

(a) (b)

Figure 6.22. Performance surfaces explored using (a) 32 population-adaptive operators, and (b) a Macro-GA.

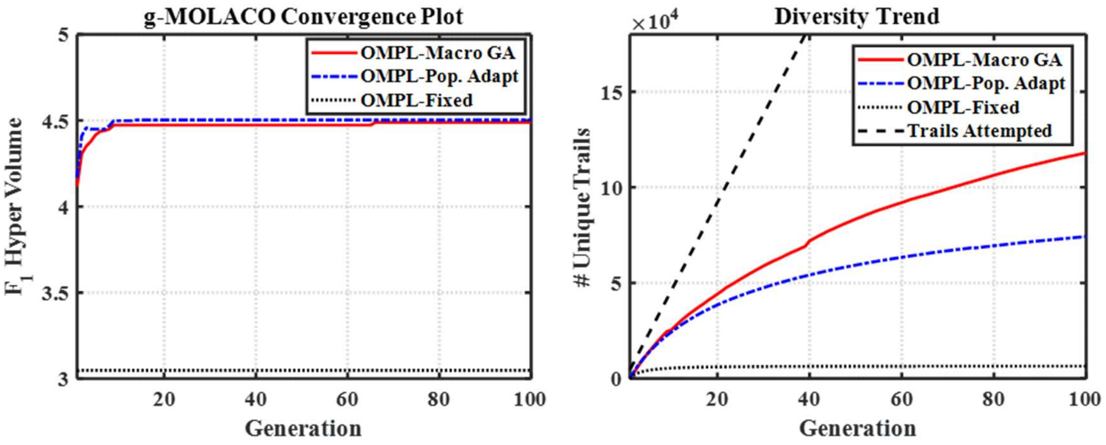

(a) (b)

Figure 6.23. Comparison of (a) convergence behavior of fixed projection, population-adaptive and MGA-adaptive approaches according to Pareto set transmission quality, and (b) diversity trend of all three approaches.

From Figure 6.23(a), it can be seen that for a large population size (P = 768) and generations (G = 100), the convergence behavior of both the population-adaptive and MGA optimizations are comparable, however, it is expected that the auto-adaptive MGA will outperform the population-based adaptive operators as the number of combinatorial variables increases significantly, and exploring every possibility with a population adaptive approach becomes more cumbersome and inefficient. Another advantage of using an MGA paired with MOLACO is that a smaller population size can be used; that is, as the number of operators increases for the population adaptive strategy, the size of the sub-populations committed to each operator must increase proportionally in order to ensure it is explored. In the MGA case, the entire population is adapted each generation towards having traits that have been the most successful thus far. In Figure 6.23(b), it is also obvious that an MGA-based approach yields far more unique solutions (over 118,517 trails) as compared to the population-adaptive approach (74,470 trails) and a fixed optimization, assuming a single operator (6,526 trails). However, these numbers still pale in comparison to the total number of geometries attempted (over 460,800, given six colonies of 768 ants over 100 generations). Since the imposed operators still tend to restrict designs to a fixed "cone" of phases, and there is plenty of room to enhance solution diversity, design constraints are further relaxed to enhance search efficiency and improve the phase diversity.

Rather than restricting the gold evaporations to 5x5 meander grids on orthogonal walls, two other scenarios are considered: increasing the resolution of the meander grid and performing projections at arbitrary incidence angles into the cavity. Examples of these designs, and performance contours of the entire history of solutions explored are shown in Figure 6.24, followed by a comparison of their diversity trends shown in Figure 6.25. First, based on available resources, it should be noted that the orthogonal MPL optimization was performed across three colonies, each parallelized across 24 cores, whereas the arbitrary MPL optimization used six colonies, each parallelized across 12 cores. However, comparing their relative efficiency based on number of unique solutions found (91.151% in the orthogonal MPL case, and 96.6923% in the arbitrary MPL case) shows that multiplying the meander area by a factor of four and allowing a single projection to occur at arbitrary incidence angles significantly opens the design space. Still, the Pareto contour of transmission and phase remain relatively narrow and centered around the nominal transmitted phase for $\lambda = 5.5$ μm. This suggests that orthogonal and single arbitrary MPL projections do not provide adequate phase diversity for use with metasurface designs for anomalous light refraction. To further increase the degrees of freedom, a new graph is adopted to represent the meander space. Under these topologies, the entire surface area of

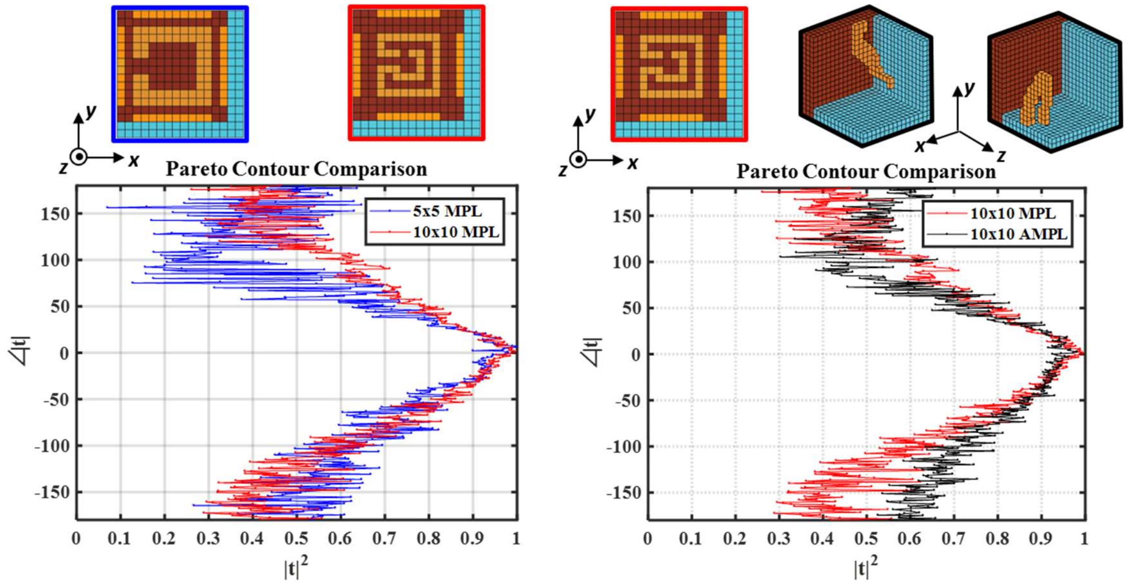

(a) (b)

Figure 6.24. Plot of Pareto contours for (a) 5x5 vs. 10x10 meander grids using orthogonal projections, and designs using (b) orthogonal MPL vs. Arbitrary MPL (AMPL). Example geometries are color coded above each plot.

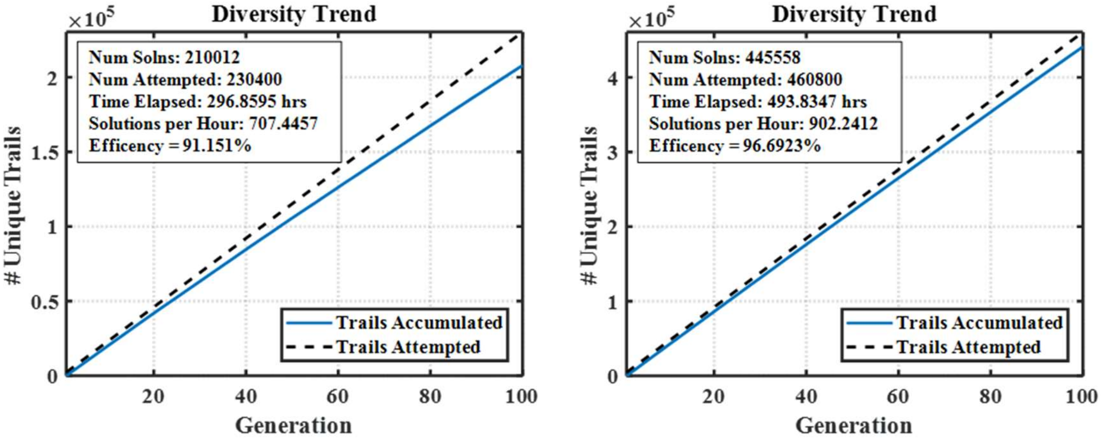

(a) (b)

Figure 6.25. Diversity plot of 10x10 (a) Orthogonal MPL and (b) Arbitrary MPL with respect to the total number of trails attempted in each case, showing significantly improved efficiency.

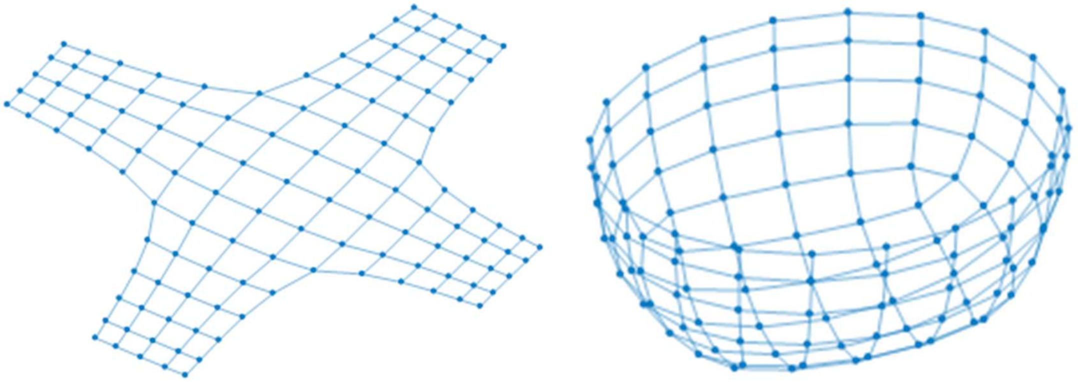
(a) (b)

Figure 6.26. Abstract representation of meander space using generalized graphs, including (a) folded and (b) fused cube net structures to represent the inside walls of the MPL-based cavity.

the cavity is made available using either a "folded" or "fused" cube net, as in Figure 6.26. In the case of the folded cube net graph, the walls of the unit cell cavity are connected with the surface of the substrate, but not one another. Alternatively, the fused cube net allows uninhibited meandering between all walls of the cavity. Re-optimizing the unit cell across four colonies simultaneously parallelized across 24 cores using the folded net graph yields a considerable improvement in phase range, as shown in Figure 6.27. While the peak transmission drops to near 90%, this is still highly transmissive for a metallodielectric structure operating in the MWIR regime. It should be noted that the initial exploration of the folded net structure assumes a graph with 125 nodes, with each wall consisting of a 5x5 grid, which explains the reduced evaluation efficiency relative to the 10x10 orthogonal MPL and arbitrary MPL cases. However, a folded net with a 5x5 wall still represents a 71% increase in efficiency (over 199,640 unique solutions evaluated) as compared to the 5x5 orthogonal MPL case, which only netted 116,584 unique solutions, even with two additional colonies. Most importantly, a wider phase range is achieved, opening up the possibility of phase gradient metasurface designs in the MWIR regime.

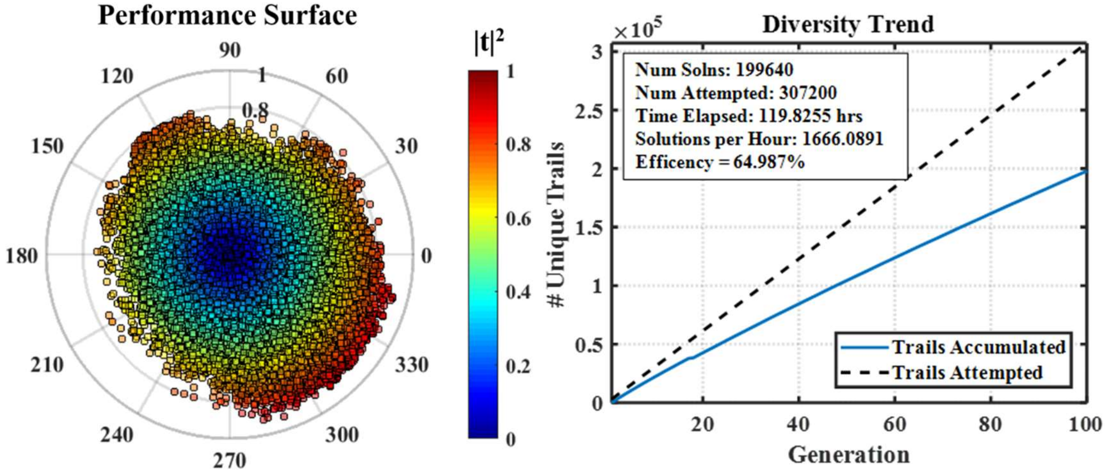

(a) (b)

Figure 6.27. Performance surface of MPL geometries optimized using a (a) folded net graph, and (b) corresponding diversity metrics of search.

Since optimization according to a folded net graph greatly enhance the unit cell's performance in both transmission and phase, the next step is to optimize a unit cell for maximum transmission and wide field of view, which is a known characteristic of 3D structures, based on previous work shown with FSSs. To exploit this, the fitness function is modified to include incidence angle information, according to equations (29) and (30):

$$T_{fit} = \frac{\min(T_{ss})}{\left(1+\Delta T_{ss}\right)} - \Psi_{correct} \tag{29}$$

$$\Psi_{correct} = \frac{\Delta\left[\angle T_{ss}\right]}{2\pi} \tag{30}$$

where angle dependence is assumed and the Δ operator represents the dynamic range of the s-polarized transmissivity and transmission phase as a function of incidence angle for all evaluated angles θ. In this case, angles of incidence of $\theta = 0°$, ±10°, ±20°, and ±30° are considered, and the corresponding performance surface is given in Figure 6.28. The design space closely mimics the shape of the previous optimization, however, gives insight into designs which are most tolerant of fluctuations in incidence angle. The best design is taken

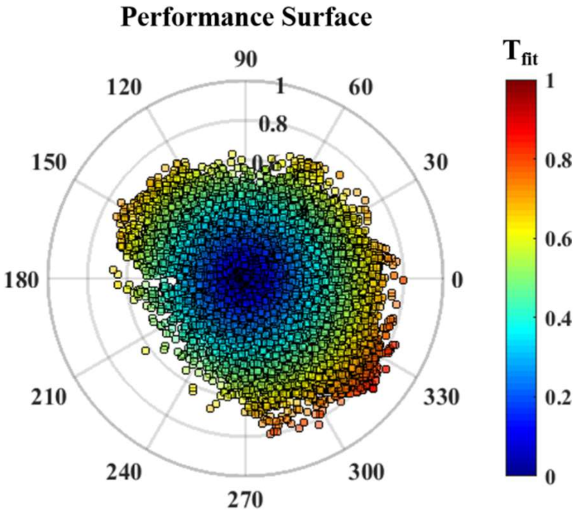

Figure 6.28. Performance surface of folded net geometry optimized for field of view.

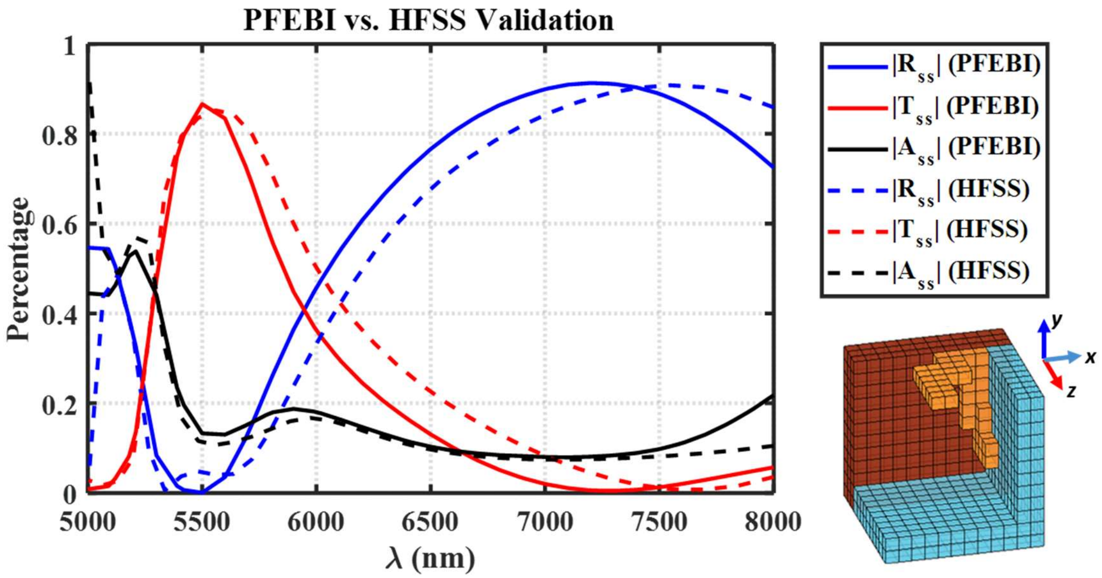

Figure 6.29. Comparison of proposed unit cell in PFEBI and HFSS in the MWIR spectrum, showing excellent agreement near the target wavelength, where the PFEBI design is uniformly meshed.

from the design space and its response and geometry are plotted in Figure 6.29 across the MWIR spectrum using both PFEBI and HFSS. While the design matches HFSS very well near and below the solution wavelength, there is a clear discrepancy at higher wavelengths, which is consistent with the fact that this implementation of PFEBI employs cubic mesh elements of a fixed size, based on the target wavelength. Although a fine mesh can easily be adopted, a coarse mesh grid enables a rapid characterization of the design space to provide insight into the capabilities and limitations of the design. As a frame of reference, the fixed mesh allowed for over 199,640 unique designs to be evaluated in under 120 hours. Exploring the same number of unique designs using HFSS in a similarly parallelized configuration would take approximately 5.3 months—nearly 32 times slower than with the selected solver PFEBI. The s-polarized transmission and phases for the proposed design are validated in HFSS and given in Figure 6.30 with respect to incidence angle. It can be seen that the peak performance of the proposed design occurs closer to 5.6 μm, with an average transmission of 82.5% ± 2.5%, and transmitted phase of approximately -30°. This

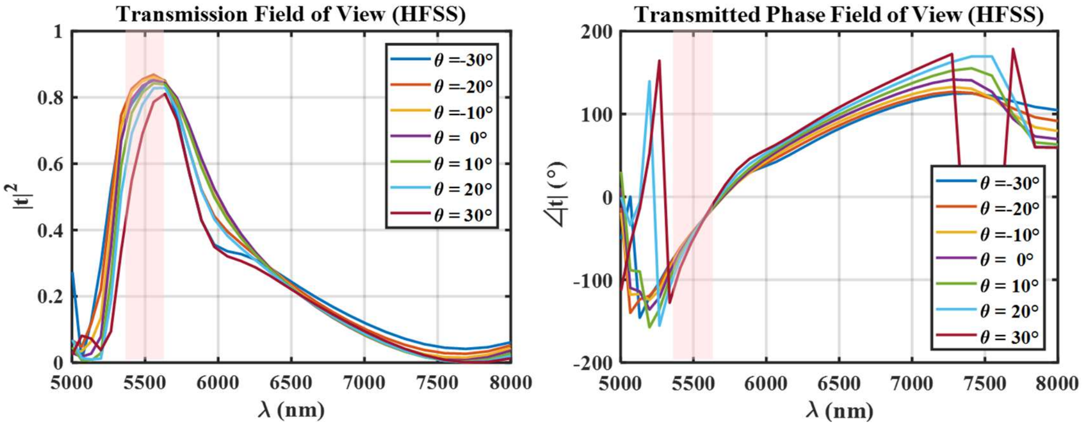

(a) (b)

Figure 6.30. Comparison of s-polarized (a) transmissivity and (b) s-polarized transmission phase, with highlighted region corresponding to target wavelength.

is an important discovery and can potentially be used for metasurface designs with wide fields of view, if a sufficient number of designs with several phase options and wide fields of view can be discovered.

Based on preliminary work in modeling and exploring the MPL design space, Sandia National Laboratories manufactured some MPL samples with a bulk silicon substrate and provided SEM imagery of these cavities, shown in Figure 6.31. Based on this sample fabrication, our model is refined to elongate the cavity depth to 2.7 μm and include a slight flaring effect at the base of the cavity. The dome-shaped bubble centered at the base of the cavity is an air pocket, formed between the substrate and cavity filling, which is etched away later. As a result of this deviation, the natural resonance of the structure is modified. The performance of this "deep dish" cavity without any gold traces is re-characterized and given in Figure 6.32, showing a transmission peak near 5.3 μm, which is chosen to be the new target wavelength for optimization. Based on previous work, use of a Silicon Nitride substrate ($\varepsilon_r = 11.7$) enhances transmission characteristics, and new

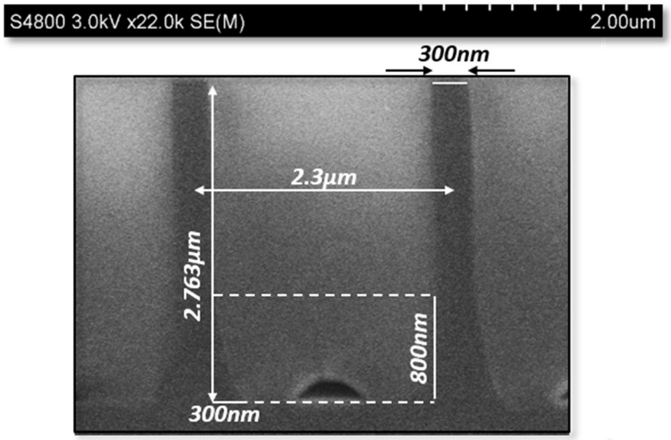

Figure 6.31. SEM cross section of prototype MPL cavity using bulk Silicon substrate, courtesy of Sandia National Laboratories, with approximate annotations of cavity dimensions.

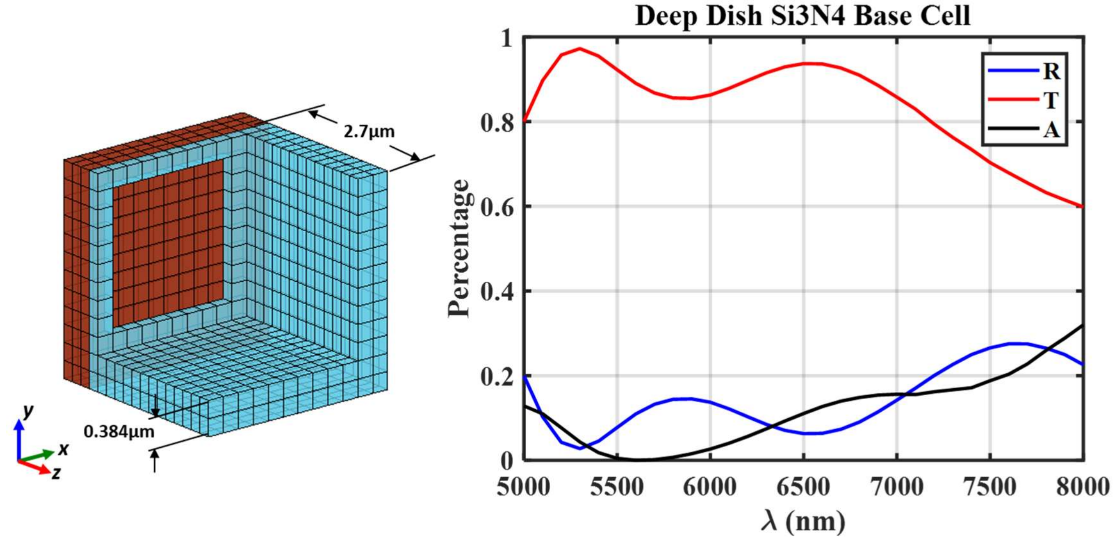

Figure 6.32. MWIR spectral response of periodic "deep dish" MPL cavity without Au evaporations, consisting of a Silicon (Si) lattice on a 1µm Silicon Nitride (Si_3N_4) substrate.

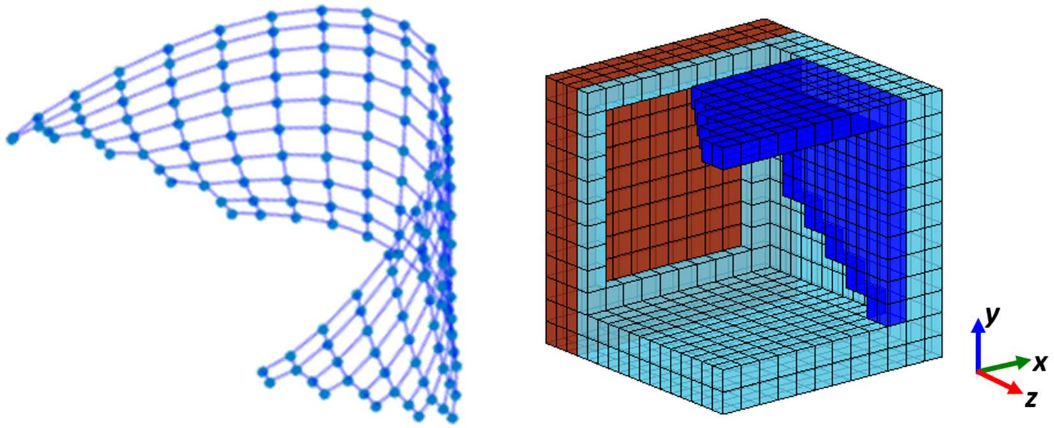

(a) (b)

Figure 6.33. Visualization of (a) graph topology of meander space, (b) projected onto cavity.

fabrication rules are developed for multiple wall, simultaneous evaporation designs. These newly formed designs rules are used to refine the graph structure, shown in Figure 6.33, which corresponds to the cavity regions which are easily accessible by multi-wall evaporation processes. Since the working region of the meander is further confined, a larger grid resolution is used to increase the number of accessible designs. The increased resolution is expected to be compatible with available E-beam lithography methods used to pattern the evaporating membrane. Finally, the new structure is once again optimized for field of view. The resulting design space and diversity trend are given in Figure 6.34, and the best design is validated in HFSS and given in Figure 6.35, with the FOV performance provided in Figure 6.36. The design with the highest performance metrics resembles a symmetrically curved dipole element and exhibits less than 2% fluctuation in s-polarized transmission of light at 5.3 μm, and less than ± 5° shift in transmitted phase for incidence angles up to θ = ±30°. Variations of this design can further be made to enhance its transmission bandwidth as well as transmitting wavelength, depending on the desired application, as well as the capabilities of the MPL fabrication process. Although a greater transmission bandwidth is achieved with the elongated 2.7 μm cavity, the increase in performance comes at a slight degradation in phase field of view as compared to the original 2 μm cavity design.

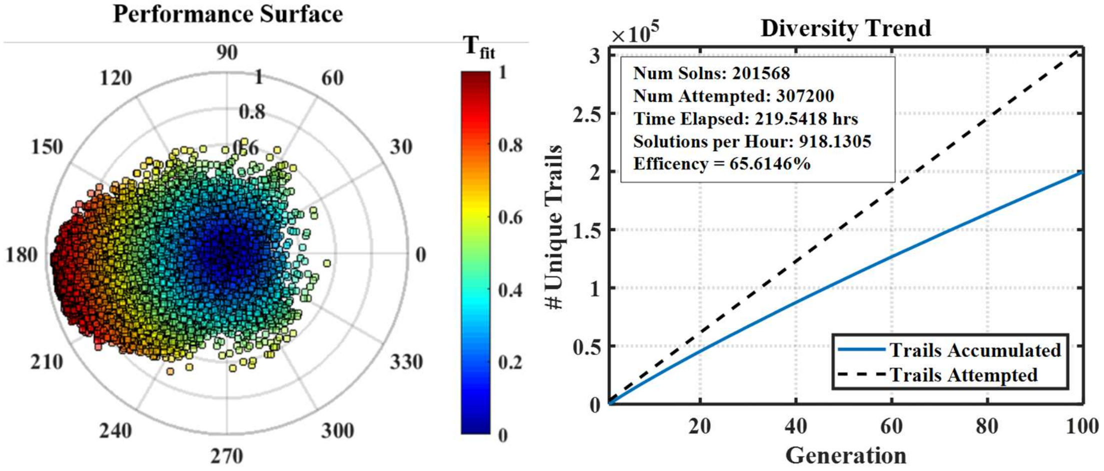

(a) (b)

Figure 6.34. Performance surface of deep dish MPL geometries optimized using a (a) partial net graph, and (b) corresponding diversity metrics of search.

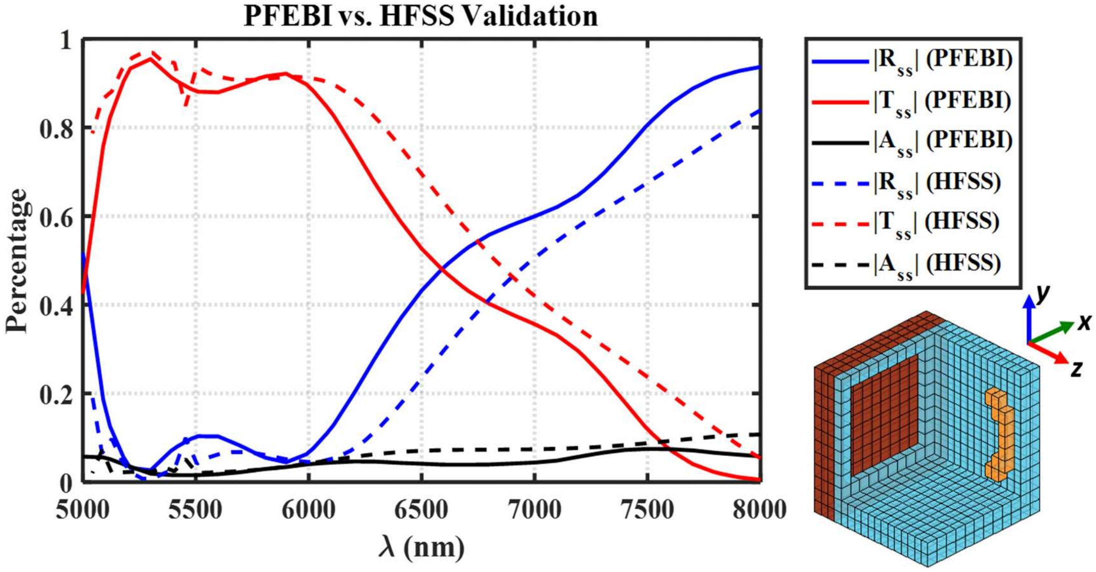

Figure 6.35. Comparison of proposed deep dish unit cell in PFEBI and HFSS in the MWIR spectrum, showing excellent agreement near the target wavelength, where the PFEBI design is uniformly meshed.

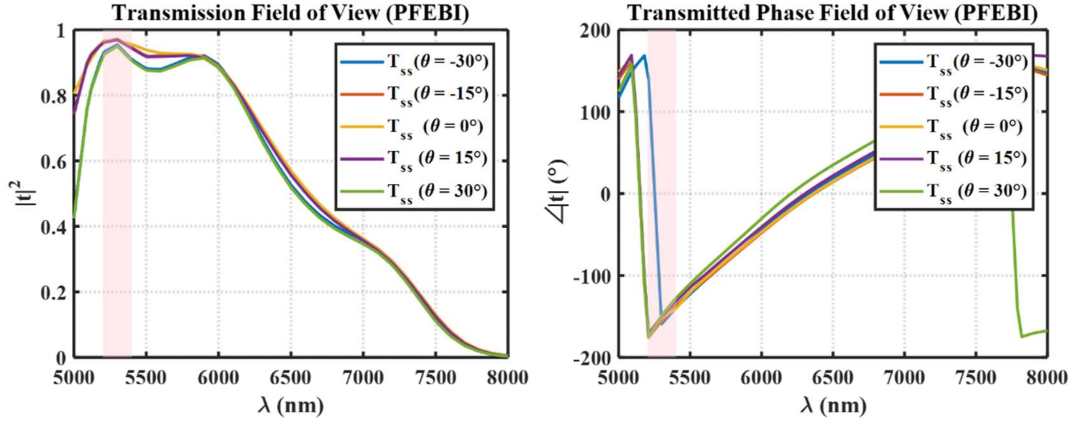

(a) (b)

Figure 6.36. Comparison of s-polarized (a) transmissivity and (b) s-polarized transmission phase, with highlighted region corresponding to target wavelength.

6.2.4 Design Space Analysis

Since design performance metrics are archived to mitigate redundancies in MOLACO, an added benefit of the rapid characterization of the metamaterial element design space is the compilation of a large amount of designs and their performance metrics.

Additional analysis on the design space can be performed to provide more insight into correlations between Au content and placement to transmission and phase. An overall appreciation of this can be gathered from Figure 6.37(a), based on 199,640 results gathered from the folded net optimization, where it is evident that the plasmonic behavior of the gold material provides an improved range of phase ranges, at the cost of transmission.

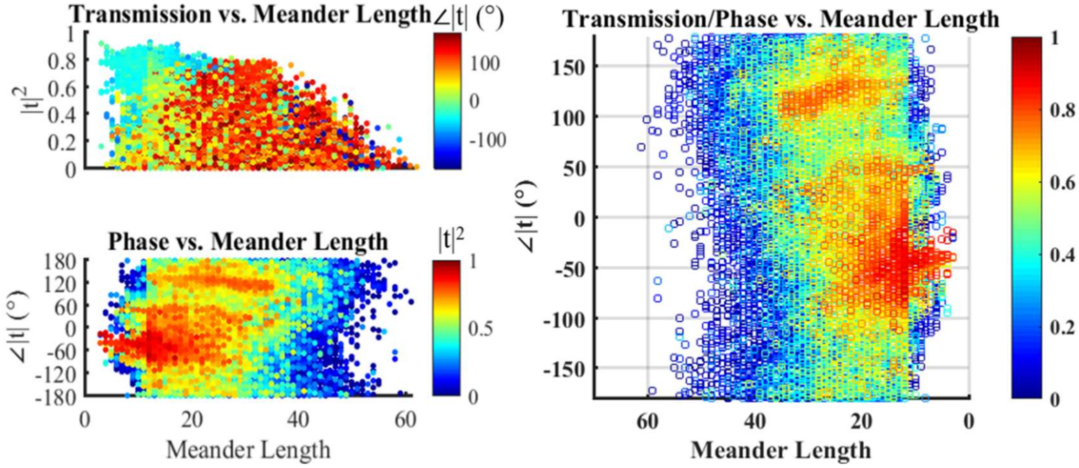

(a) (b)

Figure 6.37. A comparison of (a) transmission and phase vs. meander length, and (b) performance surface. Note that horizontal axis is reversed such that the peak transmission solutions can be visible.

A closer inspection of the gold content by cavity wall is given in Figure 6.38, which captures the relation between transmission and phase for all designs according to their concentration on each cavity wall. Each wall is permitted a 5x5 meander grid; thus, the maximum number of components occupying any wall is 25, however, a buffer is enforced between meanders, such that they are not allowed to neighbor one another to form a thickened trace. Since the incident field is polarized in the *y*-plane, the east and west walls shown in Figure 6.38(b) and (d) best highlight the advantage of increased gold content as it relates to transmission and phase. The more gold located on the east or west cavity walls

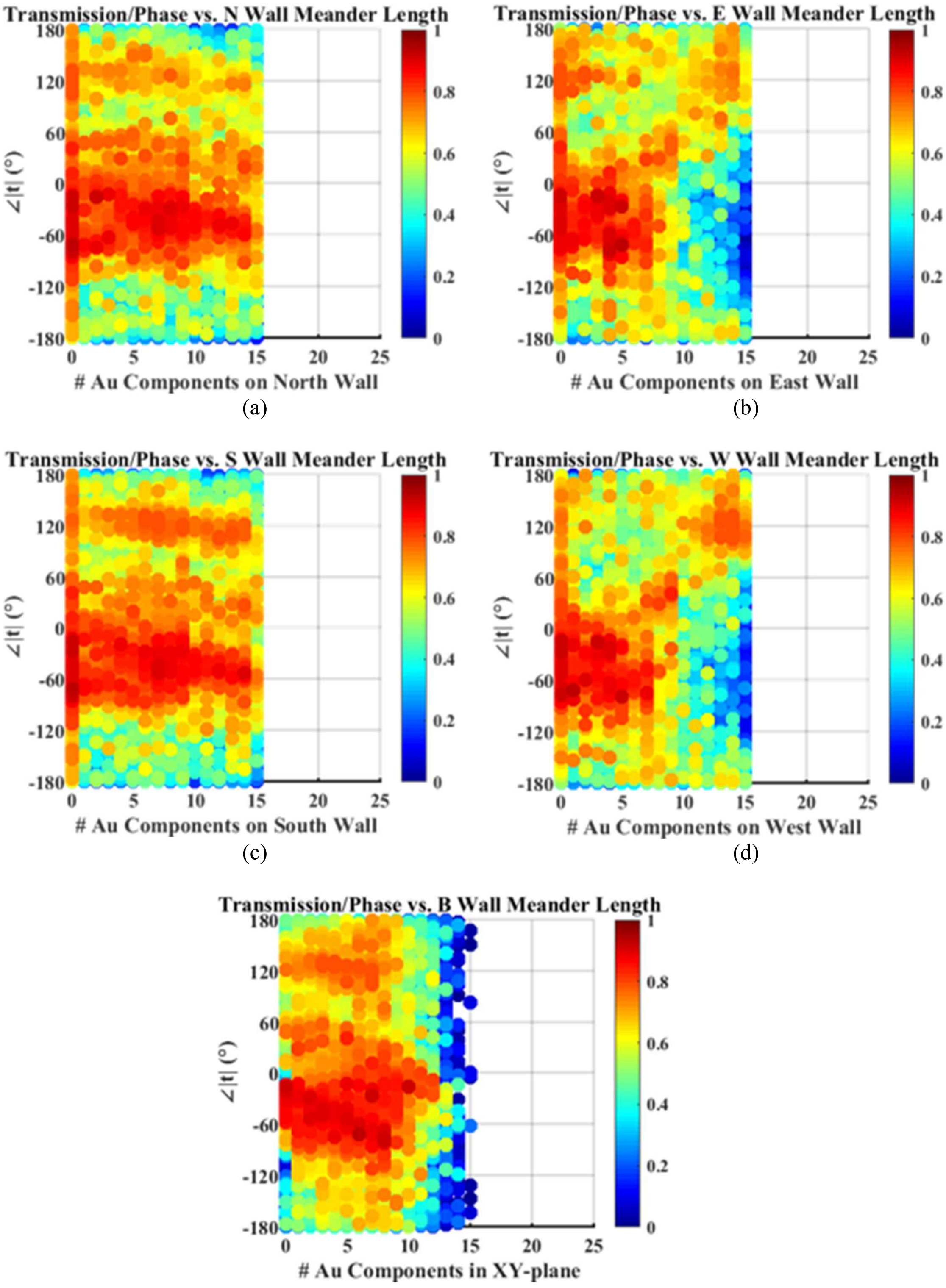

(a)

(b)

(c)

(d)

(e)

Figure 6.38. A comparison of transmission and phase vs. meander length, of all folded net designs, based on concentration of gold on (a) North, (b) East, (c) South, (d) West, and (e) Bottom cavity walls.

directly correlates to an increase in phase range, whereas even designs with no gold concentration on the north or south walls, as seen in Figure 6.38(a) and (c), are still able to achieve high transmission and a wide phase range. The bottom wall depicted in Figure 6.38(e) suggests that excess concentrations of gold in the *xy*-plane corresponds to "blockage" of incident waves, drastically reducing transmission. Based on these insights, a method for designing inhomogeneous metasurfaces based on optimized folded cube net structures will be introduced in the next section.

In the following section, an inverse design technique is used to leverage the 2 μm cavity results shown in this section to form a theoretical phase-gradient metasurface supercell design that demonstrates anomalous refraction of s-polarized light at MWIR. Inter-element coupling is discussed and two methods to mitigate these effects are demonstrated using MOLACO. In addition, discussion of an alternative approach to supercell design is offered through application of MOLACO's multi-ant modeling technique. Realizing these designs ultimately hinges on a precision fabrication method and is currently being explored in collaboration with Sandia National Laboratories.

6.3 Optimization of Phase Gradient Metasurfaces

Based on the library of unit cells identified by the MOLACO algorithm in the previous section, it is theoretically possible to reconstruct an inhomogeneous metasurface to induce anomalous refraction of incident light waves. This can be done by post-processing the archive of designs according to the desired unit cell characteristics, that meet the conditions of the metasurface. As an example, the simple case of a phase gradient metasurface, consisting of an inhomogeneous arrangement of unit cells, is considered. It will be demonstrated that an infinite arrangement of a collection of unit cells, referred to as a "supercell," can be used to generate anomalous refraction of incident light at a fixed angle. To minimize the size of the supercell and degrees of freedom, a three-element supercell will be considered. This reduces the potential for variation in unit cell performance, as well as potential coupling issues that will arise in the final unit cell design. In this case, to satisfy refraction at a fixed angle, each element must maintain a constant phase shift of 2π/3 or 120° from its neighbor.

6.3.1 Supercell Construction

An ideal supercell has equal amplitude and a constant phase shift between elements spanning a 2π phase range. To construct a supercell of elements that satisfy these conditions, a cross section of the performance surface containing solutions equal in amplitude and phase separation, is taken as illustrated in Figure 6.39 below:

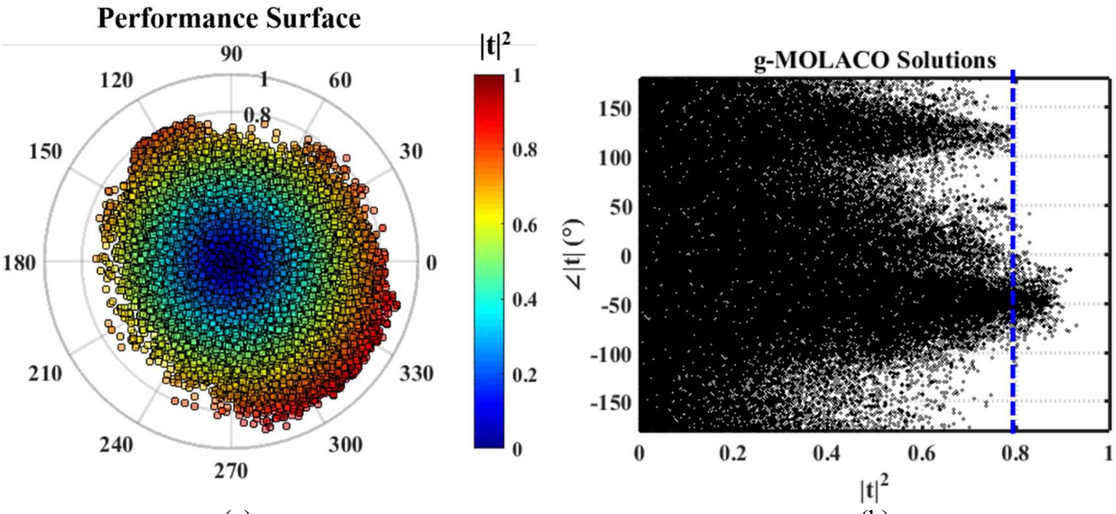

(a) (b)

Figure 6.39. Performance surface of MPL designs using a folded net graph in (a) polar form and (b) cartesian form, with the blue dashed line representing a cross section of elements taken as candidates for a phase-gradient supercell.

Alternatively, it is also possible to mix and match unit cells at the user's discretion to create other interesting behaviors, depending on the desired application. For phase gradient metasurface applications, once a collection of elements is generated, a simple linear fit can be performed across each unit cell from the cross section of available designs to identify candidate elements for the supercell design. An example of a three-element supercell formed from a linear fit of this candidate pool is given in Figure 6.40. A plot of the field

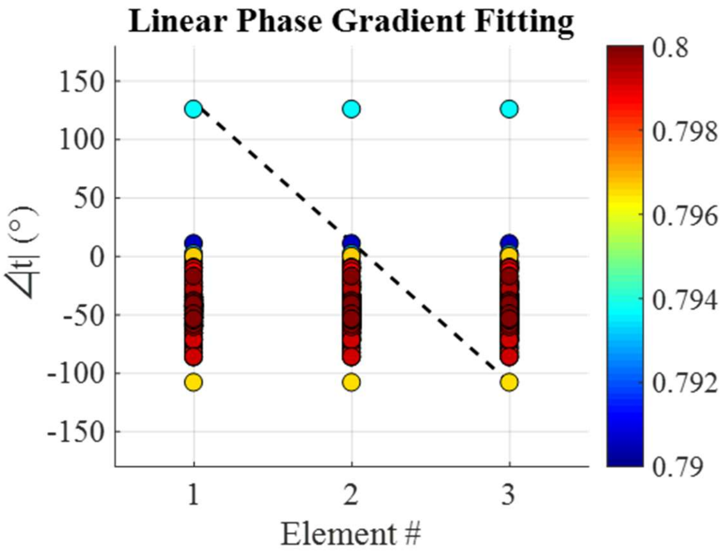

(a)

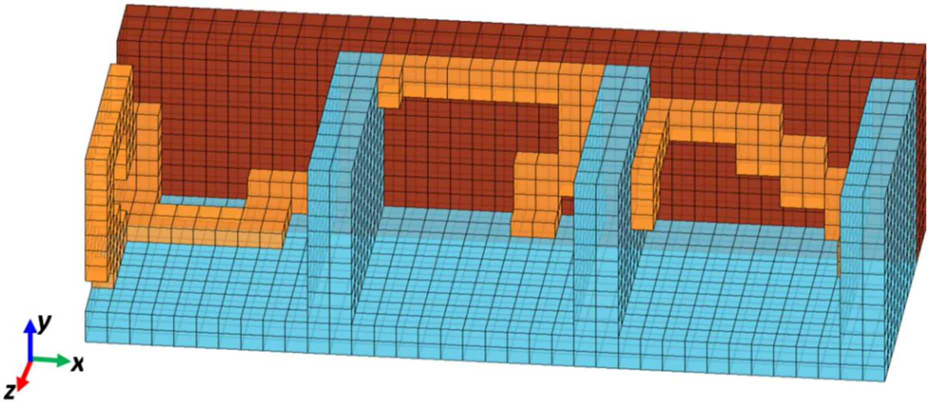

(b)

Figure 6.40. Selection of individual elements for a supercell based on (a) linear fit of 120° phase gradient, resulting in a (b) three-element supercell.

distribution of the proposed three element supercell is given in Figure 6.41, along with analytically generated fields based on both equivalent and ideal Huygen's sources, clearly showing that the supercell does not perform as intended. Closer inspection of the fields in the individual elements versus the fields in the supercell element shows striking differences, as seen in Figure 6.42, explaining their inability to induce anomalous refraction of an incident uniform plane wave. To further quantify this effect, the effective Huygen's source values can be retrieved using a least-squares fit of the simulated fields to the fields generated by the three-element supercell based on a superposition of many cylindrical Huygen sources, as seen in Figure 6.43. It is evident that anomalous refraction does not occur as a result of detuned amplitude and phase values of the individual optical antenna elements.

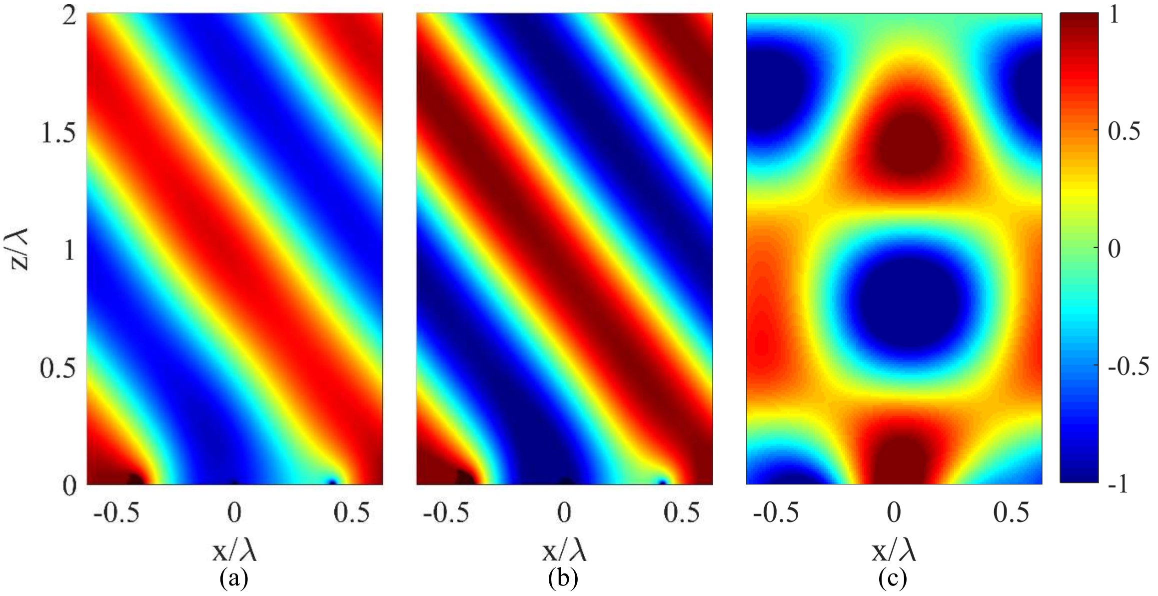

Figure 6.41. Comparison of field plots for (a) equivalent PFEBI transmission and phases (self-coupling), (b) ideal Huygen's sources (no coupling), and (c) three-element supercell (supercell coupling).

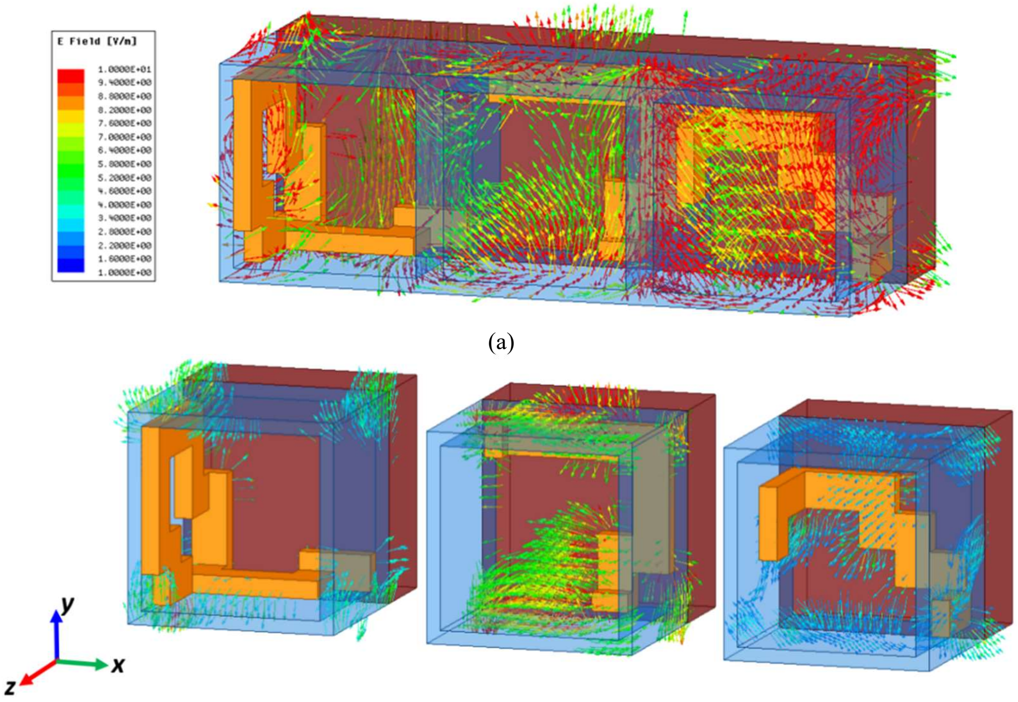

(a)

(b)

Figure 6.42. Comparison of differences in field distribution within (a) three-element supercell, and (b) individual supercell elements in infinitely periodic environment.

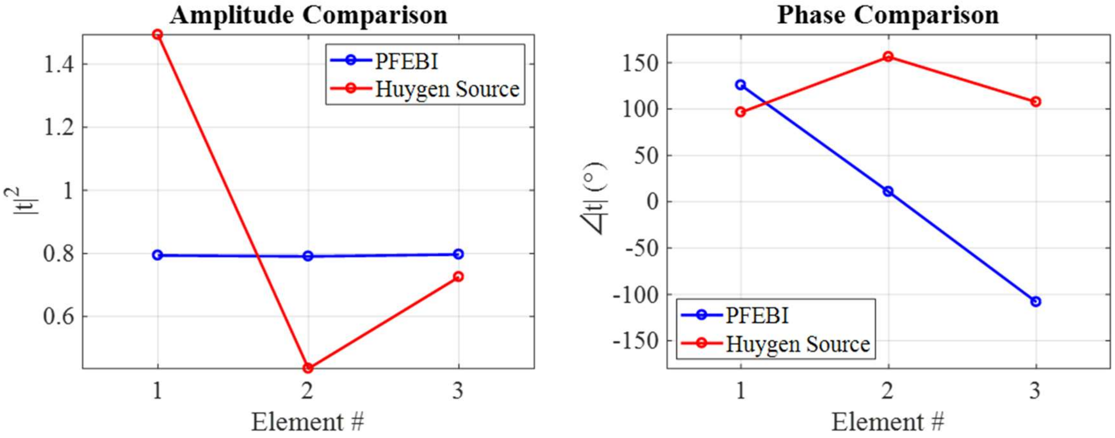

(a)

(b)

Figure 6.43. Comparison of expected and effective (a) amplitudes and (b) phases of individual elements based on extraction of effective Huygen's sources.

Plotting the vector fields of the three-element supercell shown in Figure 6.40(b) reveals a few important factors that must be considered. First, since the results were generated in a coarsely meshed full wave solver to approximate a wide range of designs in a short amount of time, the individual elements must be meshed finer and re-characterized. Second, even designs that have been validated and satisfy the proper transmission magnitudes and phases may not work well in a supercell environment. This is because when the unit cells are optimized, they are assumed to be in an infinitely periodic environment with identical elements in every direction, however, in the inhomogeneous supercell case, unit cells are only identically aligned in the plane of polarization. This either gives rise to or eliminates coupling effects from the single element, as seen in Figure 6.42, effectively detuning the structure. Since it is impossible to efficiently predict coupling effects in advance during optimization of individual elements, a more methodical approach must be taken to refine and postprocess the optimized library of unit cells, or re-optimization with intelligent constraints for coupling reduction. Each approach will be addressed in the following section.

6.3.2 Coupling Reduction Techniques

Since unit cells were optimized in an infinitely periodic, and therefore, homogeneous surface setting, simply combining unit cells is not enough to produce desired results, as evidenced in the previous section. The most obvious approach that can be employed to reduce coupling leverages the multi-ant modeling capabilities of MOLACO. Since individual elements optimized in an infinite environment only account for self-coupling effects, by optimizing an entire supercell, the mutual coupling effects between different elements can be incorporated into the optimization. In this case, rather than maximizing the transmission and phase of the individual elements, the fields of the transmitted waves are considered instead. The key disadvantage to this approach is that it is computationally intensive, as supercell designs are often many lambda in size, and requires an accurate means of representing a large amount of field data. After individual ants are formed into supercells, the design is evaluated and a planar cut of the field distribution is retrieved. Using the retrieved fields, the equivalent Huygen's source are extracted through a least-squares fit and compared to the ideal amplitude and phase values. The difference between the equivalent and ideal Huygen's sources can be used to form the basis of the cost function, which is scalarized and inverted into a fitness function compatible with MOLACO. A flowchart of the multi-ant optimization procedure is given in Figure 6.44.

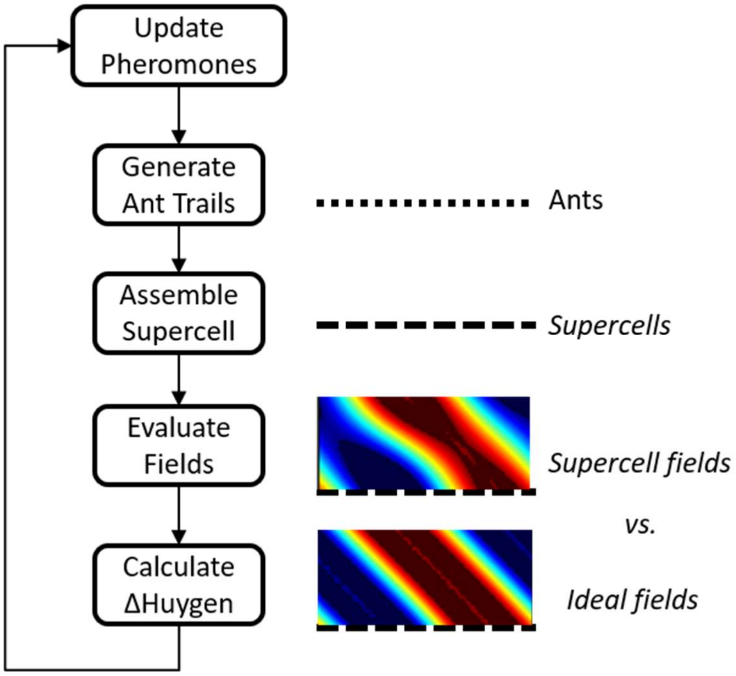

Figure 6.44. Simplified flowchart of multi ant modeling.

Alternatively, two methods that are much less computationally intensive are proposed to mitigate the effects of coupling during supercell construction:

1. Selection of supercell elements to minimize element-to-element interaction.
2. Re-optimization of unit cell structure using a mask to mitigate coupling regions.

In the first approach, designs can be post-processed to strictly identify geometries which are unlikely to couple to one another in the transverse plane. For example, designs can be individually optimized for geometries which are restricted to only one half of the unit cell and satisfy a 120° phase separation yields the candidates shown in Figure 6.45. Another advantage of having a library of unit cells is that in phase gradient metasurface applications, only the relative (and not absolute) transmitted phase values between elements is necessary, making a larger range of design candidates available.

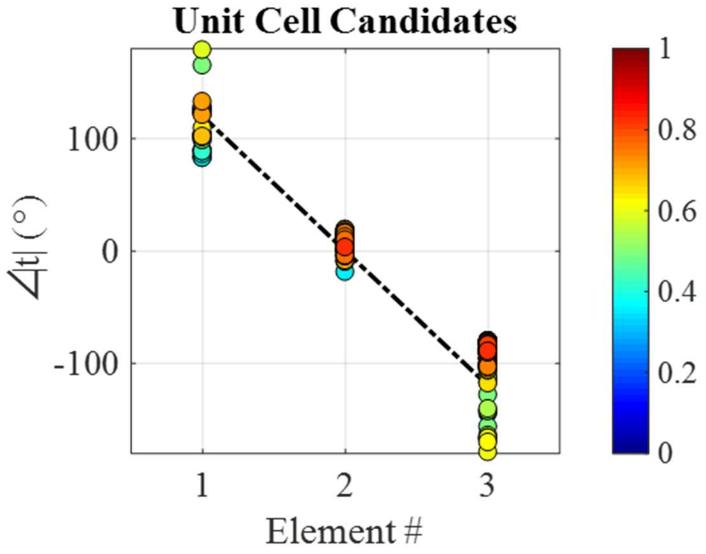

Figure 6.45. COMSOL validated performance of unit cells optimized with a full net graph with near 120° phase separation, and post-processed such that gold geometries are restricted to half of the unit cell.

From these designs, a new “de-coupled” supercell geometry is selected, as shown in Figure 6.46. A comparison of this geometry to that of Figure 6.40 shows that the majority of the element structure is maximally spaced from its neighbor. The performance of this supercell is evaluated according to its refracted fields, as simulated in COMSOL. This field distribution is shown in Figure 6.47 in wavelengths beyond the supercell, along with a comparison of the equivalent amplitudes and phases of the individual unit cells and extracted Huygen’s sources using a least-squares fit of the simulated fields. The non-uniformity in the refracted wave in Figure 6.47(a) is due to the reduced amplitude of the second element, and a 70° phase deviation of the first element, shown in Figure 6.47(b)-(c), as a result of coupling between elements, however, the steered angle is still consistent with a refracted angle of approximately 53°.

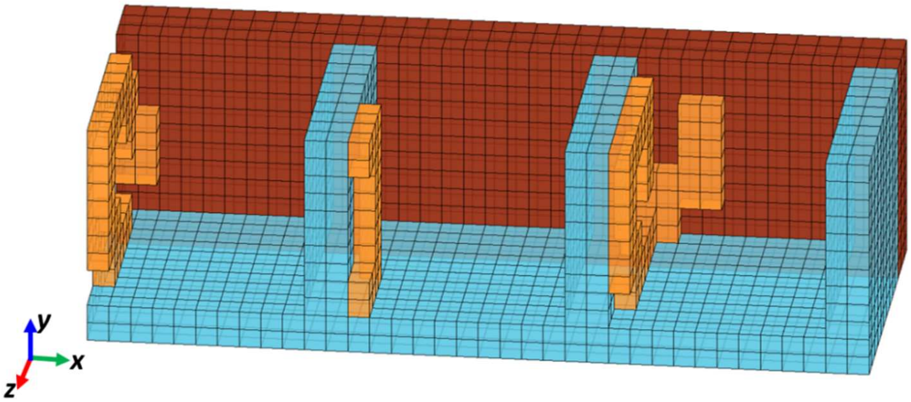

Figure 6.46. Supercell geometry of unit cell designs optimized using a full folded net graph, and post-processed to mitigate coupling between neighboring elements.

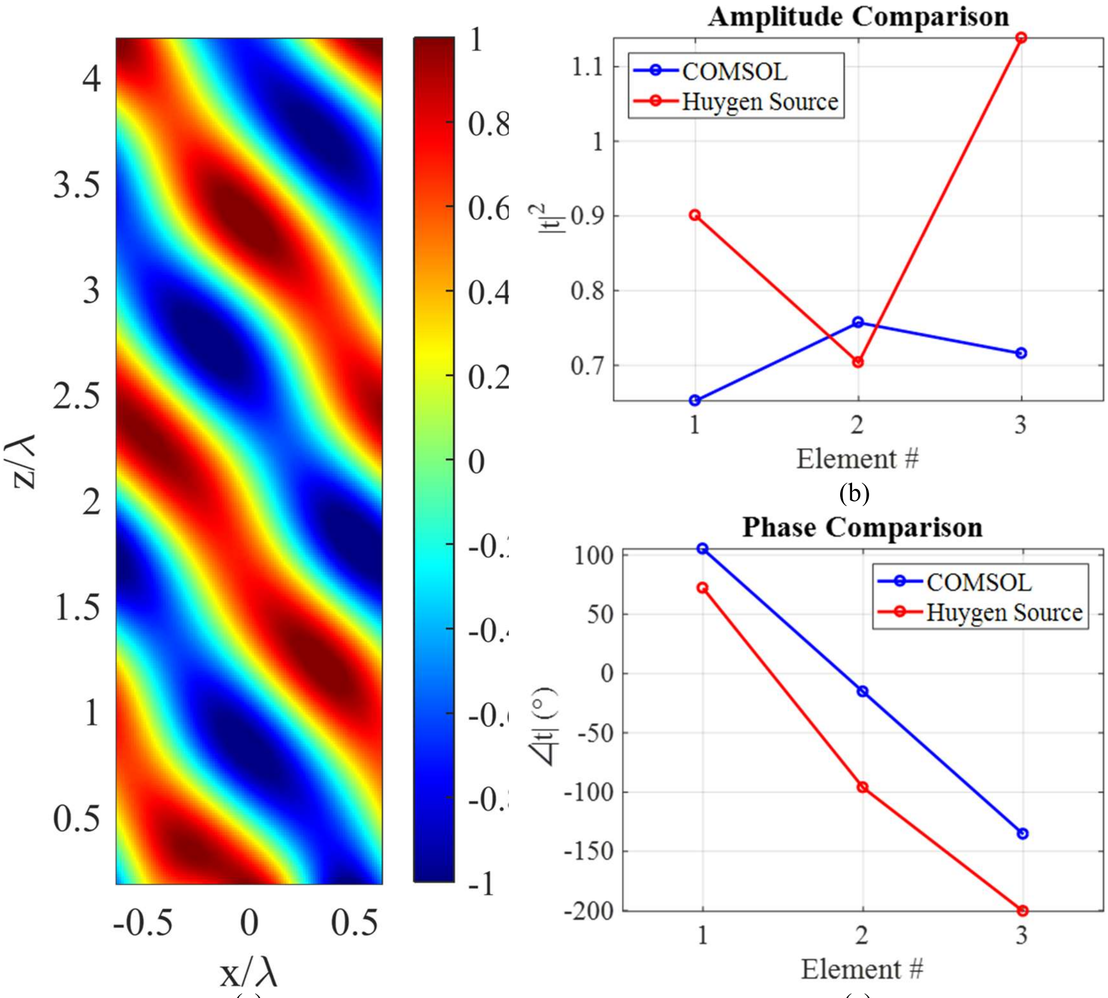

(a) (b) (c)

Figure 6.47. Plot of (a) refracted fields of post-processed full net supercell geometry along with equivalent Huygen's (b) amplitudes, and (c) phases.

The second approach to coupling mitigation involves re-optimization of the unit cell structures with an updated graph in MOLACO. In the original optimization, a folded net geometry was applied and no masking was used, since it was desirable to characterize the design space and discover new designs and their capabilities. Based on the characterized design space, and coupling effects of assembled supercells, a topology which maximally separates gold evaporations from adjacent elements is applied to reduce coupling. The optimized results and corresponding mask are shown in Figure 6.48, showing a distribution of highly transmissive designs with a variety of phases comparable to that of the original folded net topology, with a guaranteed λ/5 spacing in between neighboring gold elements, mitigating coupling effects. Once again, three candidate elements are selected from Figure 6.49 and placed into the supercell configuration.

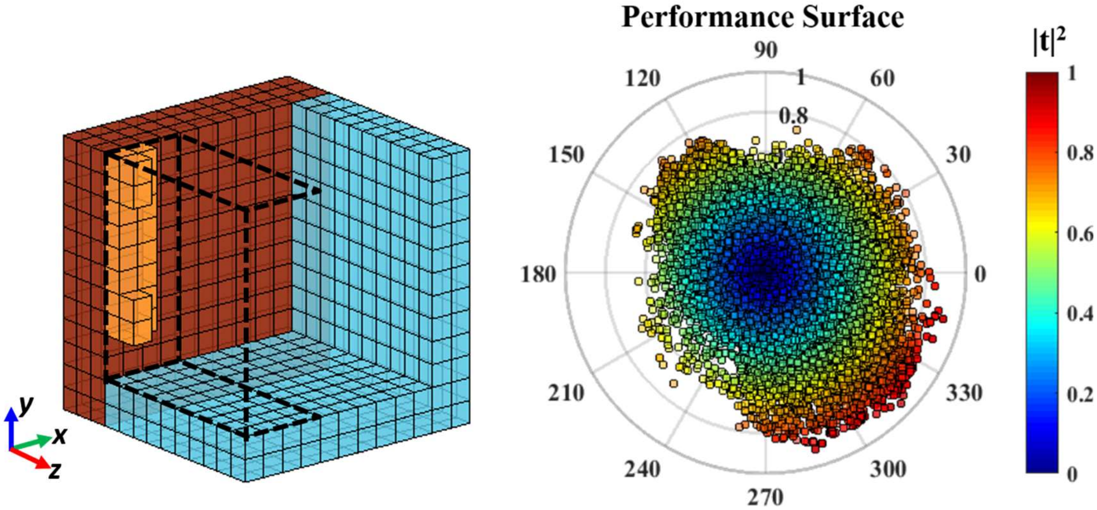

(a) (b)

Figure 6.48. Example geometry showing (a) restricted region corresponding to mask (dashed lines), and (b) associated performance surface based on MOLACO optimization.

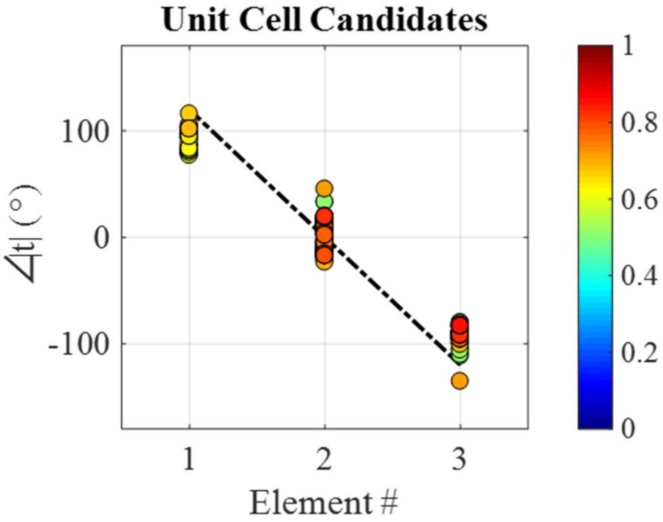

Figure 6.49. COMSOL performance of candidate elements optimized with a half net graph.

The geometry of the selected elements and their corresponding field distribution are shown in Figure 6.50 and Figure 6.51 respectively. It is evident that a more uniform refracted wave can be achieved, which also agrees well with a refraction angle of 53°. Although Figure 6.51(b) and (c) indicate some amplitude variation due to coupling, the average phase separation of elements is 111.1°, which is very close to the target phase deviation of 120° and significantly contributes to the uniformity of the refracted wave. Thus, whether by post-processing or re-optimization, use of generalized graphs allow MOLACO to not only explore and characterize design spaces based on existing fabrication methods; it also enables mitigation of unwanted coupling, which is a significant issue in supercell design that is often overlooked.

In this Chapter, alternative applications of the MOLACO algorithm have been showcased, including several advanced techniques such as use of generalized meander graphs, population-adaptive operators, auto-adaptive MGA, and a theoretical application of multi ant architecture. These techniques have been applied to a variety of problems, including impedance matching of MLAs, optimization of individual metamaterial unit cells for wide fields of view, and inverse design of metasurfaces using candidate unit cell designs with a wide range of performances. In addition to the different applications, MOLACO has also been used in a variety of ways, including characterization of new design spaces to refine fabrication methods by identifying design capabilities and limitations, as well as enabling big data analysis of design spaces to provide insight and intuition into a variety of design topologies.

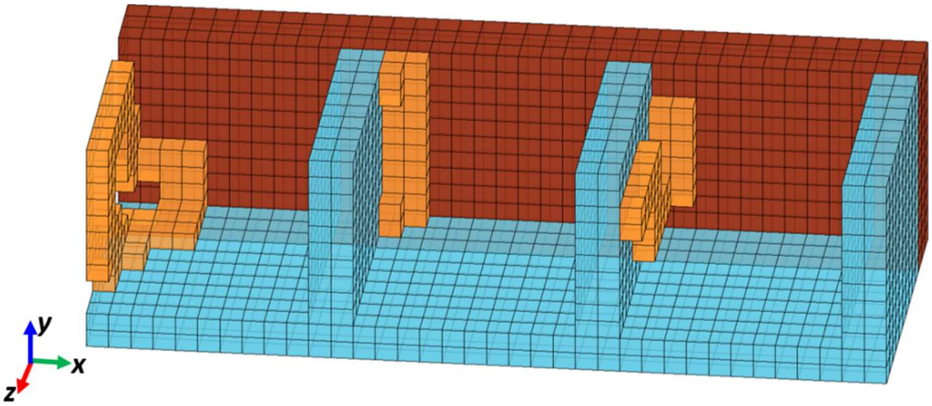

Figure 6.50. Supercell geometry of unit cell designs optimized using a half net graph to mitigate coupling between neighboring elements.

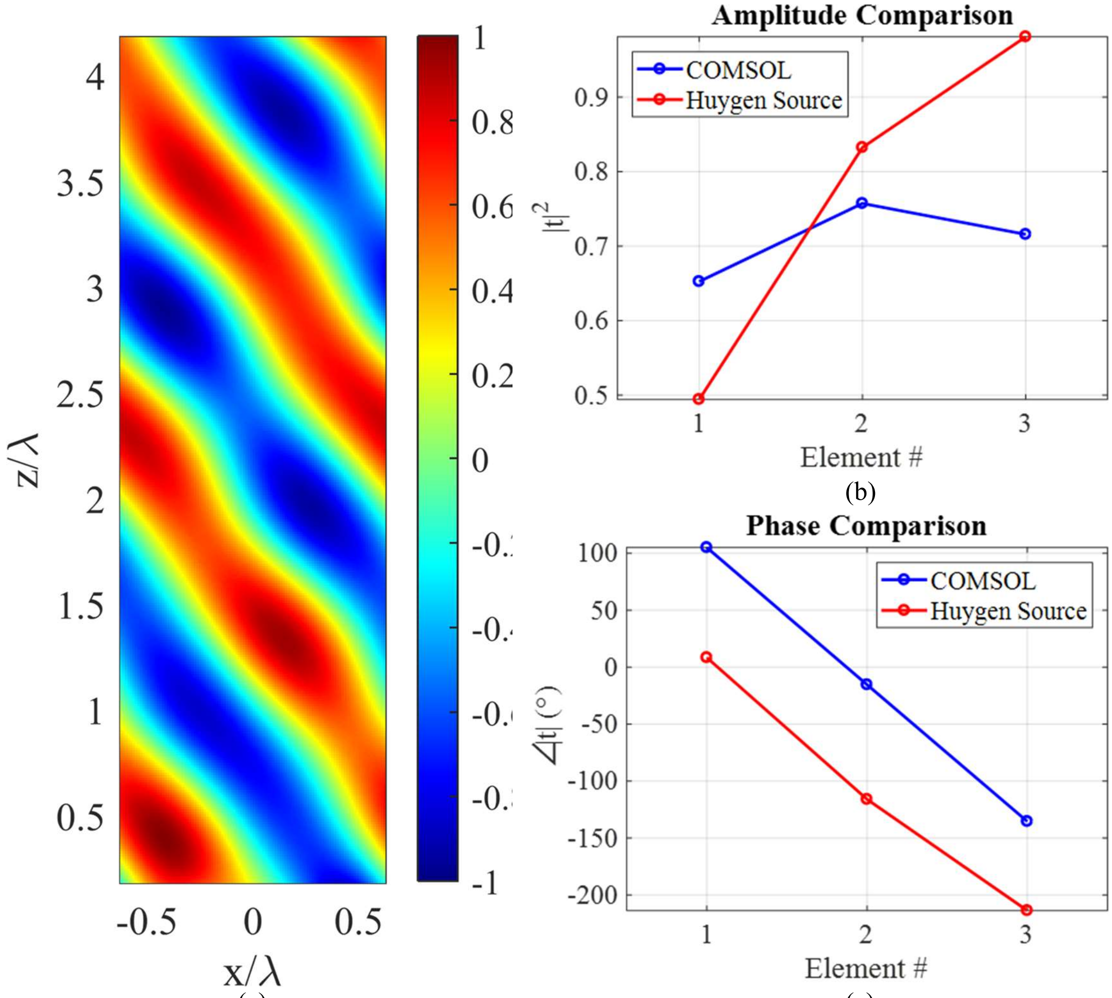

(a)

(b)

(c)

Figure 6.51. Plot of (a) refracted fields of half folded net supercell geometry along with equivalent Huygen's (b) amplitudes, and (c) phases.

Chapter 7

Conclusions

7.1 Significant Contributions

7.1.1 Generalized MOLACO Algorithm

A new combinatorial optimization algorithm, known as MOLACO based on a traditional implementation of MMAS has been introduced in this work. Traditional ACO approaches are preferred over other discrete optimization algorithms such as GA and PSO because they guarantee solutions with contiguous components, which are essential for manufacturability in three-dimensional designs. Unlike its predecessors, MOLACO does not assume that all ants behave in a uniform manner; instead, ants are assumed to have a diverse range of behaviors ranging from lazy to hyperactive. This key distinction drastically improves solution diversity by including non-space-filling as well as space-filling solutions, resulting in a more effective global optimization tool, especially for three-dimensional topology optimization. Additionally, MOLACO can also leverage population-based adaptation of solutions to a discrete set of topologies (masks) or meander operators. Furthermore, combining MOLACO with a MGA allows it to become fully auto-adaptive, which allows for large-scale combinatorial optimization problems as well as *in situ* parameter optimization, which is not possible under traditional ACO implementations. Finally, a theoretical multi-ant modeling method has also been proposed, and can be applied to problems in which it is desirable to have multiple meandered components, such as multi-element FSS or supercell design. Multiple examples of electromagnetic designs optimized by MOLACO have been presented, including novel 3D FSS, metamaterial and metasurface designs, as well as impedance matched meander line dipoles, however, the algorithm is not limited to only topology optimization. MOLACO can be applied to any problem which can be represented in graph form, including artificial intelligence, social networking and routing problems, to name a few.

7.1.2 Novel FSS Designs

A variety of unintuitive 3D FSS designs have been presented in Chapter 4, including polarization and angle independent stop-pass filters, as well as circularly polarized FSSs with a near-grazing FOV. Furthermore, a method for fabricating and experimentally characterizing small and large-scale arrays of optimized elements has been proposed in Chapter 5 using 3D printing and metallization techniques, as well as waveguide, free space and focused beam measurement methods. The proposed fabrication and metallization methods result in low-cost, lightweight 3D FSS elements that are electrically thin, and can be made conformal to surfaces with radii of curvature larger than a wavelength. The resulting elements are contiguous 3D geometries that have minimal alignment or registration requirements as compared to multi-layered designs, while achieving higher performance over a wide range of incidence angles.

7.1.3 Antenna Optimization

One popular application of traditional ACO in electromagnetics is the optimization of MLAs. In traditional ACO schemes, generated geometries fill the entire user-defined meander grid, which is excellent for miniaturization, however, the algorithm needs to be executed numerous times to satisfy a variety of grid sizes. With MOLACO, a single high-resolution grid can be used, alongside several discrete (or MGA-adaptive) masks. This allows a variety of geometry types to be explored in a single optimization, providing additional diversity in final designs, and alleviating the issue of over-meandered or space filled designs, which may not be desirable. An example of impedance matching meander line dipole elements embedded in a NZIM was demonstrated in Chapter 6.

7.1.4 Novel Metasurface Designs

In addition to optimization of RF designs, generalization of the MOLACO algorithm using graph-based topologies also extended the capability of the algorithm to any problem which can be represented by a graph and modeled by a computationally efficient solver. As an example, transmissive 3D metallodielectric metamaterials based on Sandia National Laboratories' MPL nanofabrication technique were optimized for the MWIR regimes in Chapter 6. Since metals are very lossy in the optical regime, most transmissive metamaterial designs leverage all-dielectric elements to maximize transmission. Unfortunately, all-dielectric designs offer a limited range of transmitted phases, which are necessary for many metasurface applications. By leveraging the expanded surface area of three-dimensional unit cell elements, it was demonstrated that unintuitive 3D metamaterial geometries that are highly transmissive and offer a wide field of view are not mutually exclusive with metallodielectric structures, as many thought they once were. Moreover, a new design methodology for metasurface design was introduced by substituting traditional FNDS approaches with a Pareto locus search mechanism, enabling discovery of a wide range of designs that are highly transmissive and span a variety of transmitted phase values in a single optimization. An example of this design procedure was applied to a phase gradient metasurface design, which demonstrated anomalous refraction. Effects of coupling between individually optimized unit cell elements were explored and quantified, and methods for coupling reduction using the generalized graph features of MOLACO were also successfully demonstrated—a crucial concern that is typically overlooked in the literature.

7.2 Future Work

7.2.1 Improved Adaptive Optimization Techniques

Under the population-adaptive and MGA-adaptive implementations of MOLACO, solutions are adaptively optimized over time to a discrete sets of masks or operators. Under each mask type, geometries are confined to a fixed set of colony boundaries, however, it is also possible to develop methods that expand the colony, or evolve it over time, rather than maintaining a fixed set of types. This would provide a significant increase to the types of topologies that can be achieved, and can come in the form of updating the nodes in a graph over time according to a performance metric. One approach to doing this is by applying the MGA to optimize nodes in the existing, pre-defined graph. Although GAs was originally abandoned in favor of an ACO-based algorithm due their propensity for generating fractured solutions, by activating or deactivating the nodes of each graph using a binary GA bit string, wire segments can remain contiguous, since ants can only travel between interconnected nodes, thereby mitigating the shortfalls of GA in topology optimization. The challenge with evolving nodes of a graph to either be eligible or not for meandering is that many island nodes would have no effect on the performance of solutions, which can introduce a significant amount of ambiguity to the evolution algorithm, potentially deteriorating it into a random search. Rather than manipulate a fixed graph, a more interesting mechanic would be a method to grow or truncate existing nodes, based on some problem-specific fitness metric. Although both these approaches are feasible, more studies must be performed using to determine their effectiveness in solving a variety of problems.

Alternately, for spatial geometries, another way to adapt the optimization would include automatic progressing from a coarse to a fine mesh. In theory, this allows for a faster optimization, however, would require an intelligent method to determine convergence and stagnation. This can be challenging for multi-objective optimization due to minor changes in Pareto sets that cause a fluctuation in the hypervolume indicator, although this can be alleviated by empirically establishing a hypervolume tolerance to determine convergence. Alternatively, since MOLACO is a combinatorial optimization approach, some estimation or prediction can be made based on the pre-determined graph size and the archiving mechanism can be leveraged to model a cumulative distribution function to determine the percentage of solutions that are either recurring, or have already been achieved, as a feedback mechanism.

7.2.2 Enhancements and Alternatives to Multi-Agent Ant Modeling

The proposed MOLACO algorithm is capable of creating single monolithic structures which are conducive to additive manufacturing, however, can be limited in resonant characteristics, which is the likely culprit for narrowband responses of the optimized FSSs shown in Chapter 4. In order to enhance resonant behaviors, additional resonant interactions must be introduced to the existing geometries. In addition to the multi-agent ant models introduced in Chapter 3, in which geometries are based on a set of *n* ants, rather than of a single ant, there are other possible approaches to implement this via path branching or complementary layered single-ant structures.

Branching can be thought of as either spawning offspring ants which travel a short distance off of the main path, or as a stochastic space colonizing approach, such as a fractal tree or Bezier surface generator, where a set of random points are generated which force a meander to gravitate towards them. For example, a GA can be used to generate random gravity points, which attract the meander tree by enhancing the probability of travel towards the point by a gravity factor, which is inversely proportional to the proximity of the meander to the gravity point. The set of gravity points used to manipulate the solution is then evolved according to standard GA approaches.

Alternatively, complementary layered single-ant structures would use traditional MOLACO techniques to establish a set of optimal single-ant meandered designs. Once these solutions appear converged (or after a fixed number of iterations), the best set of solutions forms the new foundation, over which additional layers are grown using the baseline meander as a mask. In this manner, a new ant is introduced to the geometry, allowing for coupling between the two meanders, and the potential for creating cavities and other resonant interactions. This process repeats for *m* layers and the best solution sets are reported to the user at the conclusion. While the layering approach explicitly builds on designs in the z-direction, increasing thickness, another technique can also utilize colony decomposition to break the colony into subsections in which ants are individually meandered. In this approach, ants are completely confined to their respective subsections and cannot travel between adjacent decomposed regions, each forming a 3D puzzle piece. The challenge with both of these approaches is that while they are likely to introduce additional coupling in a semi-controlled manner, the resulting designs will ultimately consist of non-contiguous fragments, potentially introducing alignment errors and additional manufacturing complexity.

7.2.3 Multi-Objective Weighting Methods

While single and bi-objective problems are easily adopted under the existing MOLACO framework, in order to optimize a large number of objectives, it is necessary to properly weight the pheromones of ant trails according to each objective throughout the search. Currently, a generational weight distribution is applied, in which ants are highly sensitized to pheromones for one objective early in the optimization, and gradually become more sensitive to the second objective as the procedure evolves. Ensuring ants detect pheromones associated with each objective with a different sensitivity ensures that the Pareto surface or search space can be more thoroughly mapped, resulting in a better range of solutions for the end user. Although previous MOACO implementations weight pheromones within each colony, since each ant within the colony has a unique fatigue behavior in MOLACO, doing so would require an exponentially large swarm of ants in each colony, such that they would be representative of a diverse range of both objective weights and fatigues. Alternatively, it may be possible to adapt fatigue within colonies while still ensuring equal distribution of pheromone weighting, or other approaches can be considered for weighting more than two objectives, under the generational objective weighting scheme.

One way of thinking of the distribution of objective weights, or pheromone receptor sensitivities is by modeling a *k*-simplex, where the number of vertices represents the number of objectives under consideration. In the example below, a three-objective simplex is considered.

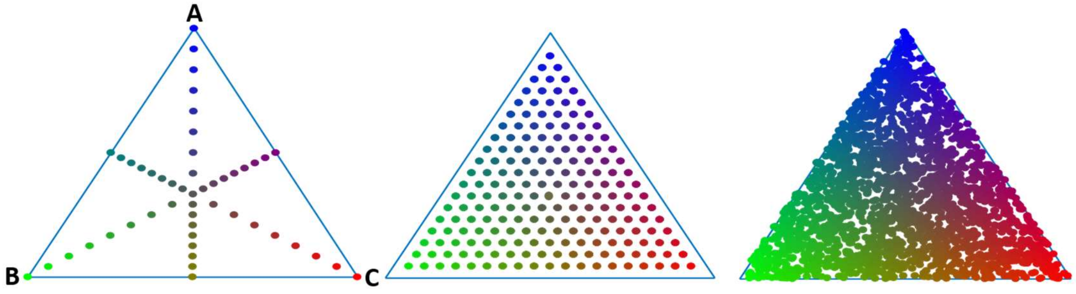

(a) (b) (c)

Figure 7.1. Three-dimensional simplexes with vertices representing objectives and points representing distribution of pheromone sensitivity throughout optimization using (a) goal programming, (b) uniform design, and (c) uniformly distributed random sampling.

Each point in the simplex space results in a different weighting or preference of an ant to a particular objective. For example, if the objective weights for a particular ant reside at the green vertex (*B*), then the ant will more heavily weight the pheromones associated with that objective, and is more likely to generate designs which perform will with respect to objective *B*. However, in order to reveal the Pareto surface of the design space, searches must be performed with respect to all objectives, and therefore it is necessary to use a variety of objective weights. Thus, the problem of tuning pheromone sensitivities can be simplified into a sampling problem of the simplex space. In Figure 7.1(a), a goal-programming approach [106] is taken, in which weights vary in sets, such that the weight of each objective increase or decreases proportionately with other objectives. Alternatively, if the number of goal-programmed weights is insufficient, a uniform design approach [107] can be taken, as shown in Figure 7.1(b), although this can be more computationally intensive, especially with a large number of objectives, since it requires computing all permutations of weight sets of high cardinality. Finally, a sampling procedure based on uniformly distributed random values can also be performed, as seen in Figure 7.1(c). This method is least computationally intensive and with a sufficient number of points, can adequately approximate the solution space. The best solution will depend on the landscape of the performance surface, however, another approach may be to adapt the weights over time, incorporating restart procedures based on the hypervolume of the Pareto surface. Nonetheless, more studies need to be performed in order to evaluate the effectiveness of these methods for a variety of problems.

Bibliography

[1] B. A. Munk, Frequency Selective Surfaces Theory and Design. New York: Wiley-Interscience, 2000, pp. 25, 36.

[2] G. Bharti, K. R. Jha, G. Singh, and R. Jyoti, “Angular Stable, Dual-Polarized and Multiband Modified Circular Ring Frequency Selective Surface,” *Frequenz*, vol. 69, no. 5-6, pp. 199-206, Apr. 2014.

[3] J. H. Choi, J. S. Sun, and T. Itoh, “An Alternative Technique in Designing a Low-Profile Two-Pole Bandpass Frequency Selective Surface (FSS) Using Aperture Coupling Interlayer,” in *Proc. IEEE MTT-S*, Seattle, WA, 2013, pp.1-3.

[4] S. Baisakhiya, R. Sivasamy, M. Kanagasabai, and S. Periaswamy, “Novel Compact UWB Frequency Selective Surface for Angular and Polarization Independent Operation,” *Progress in Electromagn. Research Lett.*, vol. 40, pp. 71-79, May 2013.

[5] F. C. G. S. Segundo, A. L. P. S. Campos, and A. G. Neto, “A Design Proposal for Ultrawide Band Frequency Selective Surface,” *J. Microw., Optoelectronics and Electromagn. Appl.*, vol. 12, no. 2, pp. 398-409, Dec. 2013.

[6] S. I. Sohail and M. Z. M. Jenu, “Dual-Layer Frequency Selective Surface for Wide Stop-Band Applications,” in *Proc. IEEE-APS*, Vancouver, Canada, 2015, p. 1270-1.

[7] Chatterjee and S. K. Parui, “A Dual Layer Frequency Selective Surface Reflector for Wideband Applications,” *J. Radioengineering*, vol. 25, no. 1, pp. 67-72, Apr. 2016.

[8] K. Payne, J. H. Choi, M. A. Ali, and C. M. Wu, "Highly-selective Miniaturized First-order Low-profile Dual-band Frequency Selective Surface," in *Proc. IEEE-APSURSI*, Fajardo, Puerto Rico, 2016, pp. 955-956.

[9] Li and Z. Shen, “Synthesis of Quasi-Elliptic Bandpass Frequency-Selective Surface Using Cascaded Loop Arrays,” *IEEE Trans. Antennas Propag.*, vol. 61, no. 6, pp. 3053-3059, Jun. 2013.

[10] K. Rashid and Z. Shen, “An Overview of Three-Dimensional Frequency-Selective Structures,” *IEEE Antennas Propag. Mag.*, vol. 56, no. 3, pp. 43-67, Jun. 2014.

[11] E. A. Parker and A. N. A. El Sheikh, "Convoluted Array Elements and Reduced Size Unit Cells for Frequency-selective Surfaces," in *Inst. Elect. Eng. Proceedings-H*, vol. 138, no. 1, pp. 19-22, Feb. 1991.

[12] L. P. S. Campos, E. E. C. de Oliveira, and P. H. F. Silva, "Miniaturization of Frequency Selective Surfaces Using Fractal Koch Curves," *Microwave Opt. Tech. Lett.*, vol. 51, no. 8, pp. 1983-1986, Aug. 2009.

[13] B. Brito, L. M. Araújo, A. G. D'Assunção, and R. H. C. Maniçoba, "A Minkowski Fractal Frequency Selective Surface with High Angular Stability," in *Proc. SBMO/IEEE MTT-S IMOC*, Rio de Janeiro, Brazil, 2013, pp. 1-4.

[14] Y. Li, L. Li, Y. Zhang, and C. Zhao, "Design and Synthesis of Multilayer Frequency Selective Surface Based on Antenna-Filter-Antenna Using Minkowski Fractal Structures," *IEEE Trans Antennas Propag.*, vol. 63, no. 1, pp. 133-141, Jan. 2015.

[15] L. Nóbrega, M. R. da Silva, P. H. F. Silva, A. G. D'Assunção, and G. L. Siqueira, "Simple, Compact, and Multiband Frequency Selective Surfaces Using Dissimilar Sierpinski Fractal Elements," *Int. J. Antennas Propag.*, vol. 2015, Article 614780, pp. 1-5.

[16] M. R. da Silva, C. L. Nóbrega, P. H. F. Silva, and A. G. D'Assunção, "Stable and Compact Multiband Frequency Selective Surfaces with Peano Pre-fractal Configurations," *IET Microwaves, Antennas Propag.*, vol. 7, no. 7, pp. 543-551, Mar. 2013.

[17] H. Yang, S. Gong, P. Zhang, F. Zha, and J. Ling, "A Novel Miniaturized Frequency Selective Surface with Excellent Center Frequency Stability," *Microwave Opt. Technol. Lett.*, vol. 51, no. 10, pp. 2513-2516, Oct. 2009.

[18] X. Hu, X. Zhou, L. Wu, L. Zhou, and W. Yin, "A Miniaturized Dual-Band Frequency Selective Surface (FSS) with Closed Loop and its Complementary Pattern," *IEEE Antennas Wireless Propag. Lett.*, vol. 8, no., pp. 1374-1377, Jan. 2010.

[19] W. Li, G. Yang, T. Zhang, Q. Wu, J. Hua, M. Chen, and X. Gu, "A Novel Miniaturized Band-Pass Frequency Selective Surface," in *Proc. IEEE-GSMM*, Harbin, China, 2012, pp. 245-248.

[20] M. Yan, S. Qu, J. Wang, J. Zhang, H. Zhou, H. Chen, and L. Zheng, "A Miniaturized Dual-Band FSS with Stable Resonance Frequencies of 2.4 GHz/5 GHz for WLAN Applications," *IEEE Antennas Wireless Propag. Lett.*, vol. 13, pp. 895-898, Apr. 2014.

[21] R. Sivasamy and M. Kanagasabai, "A Novel Dual-Band Angular Independent FSS with Closely Spaced Frequency Response," *IEEE Microw. Wireless Compon. Lett.*, vol. 25, no. 5, pp. 298-300, May 2015.

[22] A. Dewani, S. G. O'Keefe, D. V. Thiel, and A. Galehdar, "Miniaturised Meandered Square Frequency Selective Surface on a Thin Flexible Dielectric with Selective Transmission," *Flexible Printed Electronics*, vol. 1, no. 2, pp. 1-9, Apr. 2016.

[23] N. Liu, X. Sheng, and J. Fan, "A Compact Miniaturized Frequency Selective Surface with Stable Resonant Frequency," *Progress in Electromagn. Research Lett.*, vol. 62, pp. 17-22, Aug. 2016.

[24] R. Wu, H. Zhang, Z. Xu, Z. Yang, and Y. Lin, "A Novel Miniaturized Frequency Selective Surface with Stable Performance," in *Proc. PIERS*, Guangzhou, China, 2014, pp. 1647-1650.

[25] Park, Y. Jeong, J. Yook, I. Hong, H. Chun, Y. B. Park, and Y. Kim, "Registration Sensitivity Study of Double-layer FSS Design for Radome," in *Proc. IEEE-iWAT*, Seoul, Korea, 2015, pp. 342-344.

[26] Li and Z. Shen, "Miniaturized Bandstop Frequency-Selective Structure Using Stepped-Impedance Resonators," *IEEE Antennas Wireless Propag. Lett.*, vol. 11, pp. 1112-1115, Sep. 2012.

[27] K. Rashid, Z. Shen, and B. Li, "An Elliptical Bandpass Frequency Selective Structure Based on Microstrip Lines," *IEEE Trans. Antennas Propag.*, vol. 60, no. 10, pp. 4661-4669, Oct. 2012.

[28] Li and Z. Shen, "Angular-stable and Polarization-independent Frequency Selective Structure with High Selectivity," *Appl. Physics Lett.*, vol. 103, no. 171607, pp. 1-4, 2013.

[29] A. Omar and Z. Shen, "Multiband High-Order Bandstop 3-D Frequency-Selective Surfaces," *IEEE Trans. Antennas Propag.* vol. 64, no. 6, pp. 2217-2226, Jun. 2016.

[30] R. Mittra and C. Pelletti, "Three-Dimensional FSS Elements with Wide Frequency and Angular Responses," in *Proc. IEEE APS*, Chicago, IL, 2012, pp. 1-2.

[31] Sanz-Izquierdo and E. A. Parker, "3-D Printing of Elements in Frequency Selective Arrays," *IEEE Trans. Antennas Propag.*, vol. 62, no. 12, pp. 6060-6066, Dec. 2014.

[32] Sanz-Izquierdo and E. A. Parker, "3D Printed FSS Arrays for Long Wavelength Applications," in *Proc. EuCAP*, The Hague, Netherlands, 2014, pp. 2382-2386.

[33] W. Tang, J. Zhu, C. Wang, J. Ge, Z. Yu and W. Zhuang, "Waveguide 3-D FSSs by 3-D printing technique," in *Proc. 2016 Int. Conf. Electromagn. Adv. Appl.* (ICEAA), Cairns, QLD, 2016, pp. 675-678.

[34] J. v. Hagen, D. H. Werner, and R. Mittra, “Polarization-Selective Surfaces Composed of Trefoil Knot Elements,” *Microw. Opt. Technol. Lett.*, vol. 21, no. 3, pp. 170-173, May 1999.

[35] D. Sjoberg, and A. Ericcson, “A Multi Layer Meander Line Circular Polarization Selective Structure (MLML-CPSS),” in *Proc. 8th Eur. Conf. Antennas Propag. (EuCAP 2014)*, pp. 464-468.

[36] H. I. Lopez, “New Circular Polarization Selective Surface Concepts Based on the Pierrot Cell Using Printed Circuit Technology,” M.S. thesis, Electrical Engineering, University of Montreal, Montreal, 2013.

[37] F. Khosravi, “Applications of Frequency Selective Surfaces in Polarization Control of Antennas,” M.S. thesis, Electrical and Computer Engineering, University of Alberta, Alberta, Canada, 2014.

[38] M. Mutlu, A. E. Akosman, A. E. Serebryannikov, and E. Ozbay, “Asymmetric Chiral Metamaterial Circular Polarizer Based on Four U-shaped Split Ring Resonators,” *Optics Lett.*, vol. 36, no. 9, pp. 1653-1655, May 2011.

[39] W. Zhang, J. Li, and L. Wang, “Broadband Circular Polarizer Based on Multilayer Gradual Frequency Selective Surfaces,” *Int. J. Antennas and Propag.*, vol. 2016, no. 4928109, pp. 1-5, Aug. 2016.

[40] M. Biscarini, G. M. Sardi, E. Martini, F. Caminita, and S. Maci, “A Simple Broadband FSS Polarizer,” in *Proc. 7th Eur. Conf. Antennas Propag.* (EuCAP 2013).

[41] I. Sohail, Y. Ranga, K. P. Esselle, and S. G. Hay, “A Linear to Circular Polarization Converter Based on Jerusalem-Cross Frequency Selective Surface,” in *Proc. 7th Eur. Conf. Antennas Propag.* (EuCAP 2013).

[42] S. M. A. M. H. Abadi, and N. Behdad, “Wideband Linear-to-Circular Polarization Converters Based on Miniaturized-Element Frequency Selective Surfaces,” *IEEE Trans. Antennas Propag.*, vol. 64, no. 2, pp. 525-534, Feb. 2016.

[43] J. Bornemann, “Computer-Aided Design of Multilayered Dielectric Frequency-Selective Surfaces for Circularly Polarized Millimeter-Wave Applications,” *IEEE Trans. Antennas Propag.*, vol. 41, no. 11, pp. 1588-1591, Nov. 1993.

[44] X. J. Zhong, L. Chen, Y. Shi, and X. W. Shi, “A Dual-Frequency Single Layer Circularly Polarized Reflectarray with Frequency Selective Surface Backing,” *Progress in Electromagn. Research C*, vol. 51, pp. 87-93, 2014.

[45] R. Orr, V. Fusco, D. Zelenchuk, G. Goussetis, E. Saenz, M. Simeoni, and L. S. Drioloi, “Circular Polarization Frequency Selective Surface Operating in Ku and

Ka Band," *IEEE Trans. Antennas Propag.*, vol. 63, no. 11, pp. 5194-5197, Nov. 2015.

[46] S. Genovesi, R. Mittra, A. Monorchio, and G. Manara, "Particle Swarm Optimization for the Design of Frequency Selective Surfaces," *IEEE Antennas Wireless Propag. Lett.*, vol. 5, pp. 277-279, Apr. 2006.

[47] Egemen and M. Kuzuoglu, "Design of the Square Loop Frequency Selective Surfaces with Particle Swarm Optimization via the Equivalent Circuit Model," *Radioengineering*, vol. 18, no. 12, pp. 95-102, Jun. 2009.

[48] J. A. Bossard, D. H. Werner, T. S. Mayer, and R. P Drupp, "A Novel Design Methodology for Reconfigurable Frequency Selective Surfaces Using Genetic Algorithms," *IEEE Trans. Antennas Propag.*, vol. 53, no. 4, pp. 1390-1400, Apr. 2005.

[49] S. C. Bucuci, A. Dumitrascu, A. Danisor, S. Berescu, and R. D. Tamas, "Optimization of Meander Line Radiators for Frequency Selective Surfaces by Using Genetic Algorithm," in *Proc. SPIE*, vol. 9258, Constanta, Romania, 2015, pp. 1-6.

[50] Z. Bayraktar, M. D. Gregory, X. Wang, and D. H. Werner, "A Versatile Design Strategy for Thin Composite Planar Double-Sided High-Impedance Surfaces," *IEEE Trans. Antennas Propag.*, vol. 60, no. 6, pp. 2770-2780, Jun. 2012.

[51] J. Kern, D. H. Werner, A. Monorchio, L. Lanuzza, and M. J. Wilhelm, "The Design Synthesis of Multi-band Artificial Magnetic Conductors Using High Impedance Frequency Selective Surfaces," *IEEE Trans. Antennas Propag., Special Issue on Artificial Magnetic Conductors, Soft/Hard Surfaces, and other Complex Surfaces*, vol. 53, no. 1, pp. 8-17, Jan. 2005.

[52] J. H. Barton, C. R. Garcia, E. A. Berry, R. Salas, and R. C. Rumpf, "3-D Printed All-Dielectric Frequency Selective Surface with Large Bandwidth and Field of View," *IEEE Trans. Antennas Propag.*, vol. 63, no. 3, pp. 1032-1039, Mar. 2015.

[53] R. Eberhart and J. Kennedy, "A new optimizer using particle swarm theory," in *Proc. Sixth Int. Symp. Micro Mach. Human Sci.*, Nagoya, 1995, pp. 39-43.

[54] J. Kennedy and R. C. Eberhart, "A Discrete Binary Version of the Particle Swarm Algorithm," *IEEE Int. Conf. Syst., Man, Cybern., Comput. Cybern. Simulation*, Orlando, FL, 1997, pp. 4104-4108, vol. 5.

[55] M. Dorigo, V. Maniezzo, and A. Colorni, “Ant System: Optimization by a Colony of Cooperating Agents,” *IEEE Trans. Syst., Man, Cybern.*, vol. 26, no. 1, pp. 29-41, Feb. 1996.

[56] M. Dorigo and K. Socha, “An Introduction to Ant Colony Optimization,” in Handbook of Approximation Algorithms and Metaheuristics, T. F. Gonzalez, Ed. Boca Raton, FL, USA: Chapman & Hall/CRC, 2007, pp. 26-1.

[57] T. Stützle and H. H. Hoos, “MAX-MIN Ant System,” *Future Generation Computer Systems*, vol. 16, pp. 889-914, Jun. 2000.

[58] E. Mariano and E. Morales, “MOAQ an Ant-Q Algorithm for Multiple Objective Optimization Problems,” in *Proc. GECCO*, Orlando, FL, 1999, pp. 894-901.

[59] S. Iredi, D. Merkle, and M. Middendorf, “Bi-Criterion Optimization with Multi Colony Ant Algorithms,” Lecture Notes in Computer Science, vol. 1993, E. Zitzler, K. Deb, L. Thiele, C. C. Coello, and D. Corne, Ed. Berlin, Germany: Springer-Verlag, 2001, pp. 359-372.

[60] M. López-Ibánez, “Multi-Objective Ant Colony Optimization,” M.S. Thesis, Dept. Comp. Sci., Univ. of Granada, Granada, Spain, 2004.

[61] M. Coleman, E. J. Rothwell, and J. E. Ross, “Investigation of Simulated Annealing, Ant-Colony Optimization, and Genetic Algorithms for Self-Structuring Antennas,” *IEEE Trans. Antennas Propag.*, vol. 52, no. 4, pp. 1007-1014, Apr. 2004.

[62] Lewis, G. Weis, M. Randall, A. Galehdar, and D. Thiel, "Optimising Efficiency and Gain of Small Meander Line RFID Antennas Using Ant Colony System," *IEEE Cong. Evol. Comp.*, Trondheim, Norway, 2009, pp. 1486-1492.

[63] Galehdar, D. V. Thiel, A. Lewis, and M. Randall, "Multiobjective Optimization for Small Meander Wire Dipole Antennas in a Fixed Area Using Ant Colony System," *Int. J. RF and Microw. Comput.-Aided Eng.*, vol. 19, no. 5, pp. 1-7, Sep. 2009.

[64] Kaur and Y. Kumar, "Optimization of Meander Line Antenna Using ACO Technique," *Int. J. Recent Innov. Trends Comput. Commun.*, vol. 1, no. 10, pp. 761-766, Oct. 2013.

[65] A. Mantilla-Gaviria, A. Diaz-Morcillo, and J. V. Balbastre-Tejedor, “An Ant Colony Optimization Algorithm for Microwave Corrugated Filters Design,” *J. Comput. Eng.*, vol. 2013, no. 942126, pp. 1-8, Jun. 2013.

[66] Rajo-Iglesias and O. Quevedo-Teruel, “Linear Array Synthesis Using an Ant-Colony-Optimization-Based Algorithm,” *IEEE Ant. Propag. Mag.*, vol. 49, no. 2, pp. 70-79, Apr. 2007.

[67] S. Goss, S. Aron, J. L. Deneubourg, and J. M. Pasteels, “Self-organized Shortcuts in the Argentine Ant,” *Sci. Nature*, vol. 76, no. 12, pp. 579-581, Dec. 1989.

[68] Charbonneau and A. Dornhaus, “When Doing Nothing is Something. How Task Allocation Strategies Compromise Between Flexibility, Efficiency and Inactive Agents,” *J. Bioeconomics*, vol. 3, no. 3, pp. 217-242, Aug. 2015.

[69] Hasegawa, Y. Ishii, K. Tada, K. Kobayashi, and J. Yoshimura, “Lazy Workers are Necessary for Long-term Sustainability in Insect Societies,” *J. Scientific Reports*, vol. 6, Article no. 20846, Feb. 2016.

[70] Y. Sueoka, K. Nakayama, M. Ishikawa, Y. Sugimoto, and K. Ouska, “On Heterogeneity in Foraging by Ant-Like Colony: How Local Affects Global and Vice Versa,” in *Lecture Notes in Computer Science*, vol. 9882, M. Dorigo, M. Birattari, X. Li, M. López-Ibánez, K. Ohkura, C. Pinciroli and T. Stützle, Ed. Brussels, Belgium: Springer, 2016, pp. 249-256.

[71] K. Deb, A. Pratap, S. Agarwal and T. Meyarivan, “A Fast and Elitist Multiobjective Genetic Algorithm: NSGA-II,” *IEEE Trans. Evol. Comput.*, vol. 6, no. 2, pp. 182-197, Apr. 2002.

[72] Hadka and P. Reed, “Borg: An Auto-Adaptive Many-Objective Evolutionary Computing Framework,” *Evol. Comput.*, vol. 21, no. 2, pp. 231-259, May 2013.

[73] Z. Lee, S. Su, C. Chuang, and K. Liu, “Genetic algorithm with ant colony optimization (GA-ACO) for multiple sequence alignment,” *Applied Soft Computing,* vol. 8, no. 2008), pp. 55-78, Jan. 2008.

[74] J. B. Q. Zuliani, M. W. Cohen, L. d. S. Batista, and F. G. Guimarães, “Multi-objective topology optimization with ant colony optimization and Genetic Algorithms,” *Computer-Aided Design & Applications,* vol. 12, no. 6, 674-682, Apr. 2015.

[75] C. A. Balanis, Advanced Engineering Electromagnetics. New York: Wiley, 1989, p. 135.

[76] M. Al-Joumayly and N. Behdad, “A New Technique for Design of Low-Profile, Second-Order, Bandpass Frequency Selective Surfaces,” *IEEE Trans Antennas Propag.*, vol. 57, no. 2, pp. 452-459, Feb. 2009.

[77] R. C. Rumpf, J. Pazos, C. R. Garcia, L. Ochoa, and R. Wicker, "3D Printed Lattices with Spatially Variant Self-Collimation," *Progress in Electromagn. Research*, vol. 139, pp. 1-14, 2013.

[78] M. Liang, W. Ng, K. Chang, K. Gbele, M. E. Gehm, and H. Xin, "A 3D Luneburg Lens Antenna Fabricated by Polymer Jetting Rapid Prototyping," *IEEE Trans Antennas Propag.*, vol. 62, no. 4, pp. 1799-1807, Apr. 2014.

[79] P. I. Deffenbaugh, R. C. Rumpf, and K. C. Church, "Broadband Microwave Frequency Characterization of 3-D Printed Materials," *IEEE Trans. Compon. Packag. Manuf. Technol.*, vol. 3, no. 12, pp. 2147-2155, Dec. 2013.

[80] M. D. Gregory, J. A. Easum, and D. H. Werner, "A Wideband Axially Symmetric Antenna Design Fabricated with Additive and Subtractive Methods," presented at the *2016 IEEE Int. Symp. Antennas & Propag. USNC/URSI Nat. Radio Sci. Meeting*, June 26 - July 1, 2016, Fajardo, Puerto Rico.

[81] T. Oi, K. Shinyama and S. Fujita, "Electrical Properties of Heat-Treated Polylactic Acid," *Electr. Eng. Japan*, vol. 180, no. 1, pp. 1-8, 2012.

[82] M. T. Jilani et al, "A Brief Review of Measuring Techniques for Characterization of Dielectric Materials," *ITEE J.*, vol. 1, no. 1, pp. 1-5, 2012.

[83] P. A. Bernard and J. M. Gautray, "Measurement of Dielectric Constant Using a Microstrip Ring Resonator," *IEEE Trans. Microw. Theory and Techn.*, vol. 39, pp. 592-595, 1991.

[84] K. Saeed, M. F. Shafique, M. B. Byrne, and I. C. Hunter, "Planar Microwave Sensors for Complex Permittivity Characterization of Materials and Their Applications," in *Applied Measurement Systems*, 2nd ed., M. Z. Haq, Ed. Rijeka, Croatia: InTech, 2012, ch. 15, pp. 319-350.

[85] W. Hakki and P. D. Coleman, "A Dielectric Resonator Method of Measuring Inductive Capacities in the Millimeter Range," *IRE Trans. Microw. Theory Techn.*, pp. 402-410, 1960.

[86] A. M. Nicolson, and G. F. Ross, "Measurement of the Intrinsic Properties of Materials by Time Domain Techniques," *IEEE Trans. Instrum. Meas*., vol. IM-19, pp. 377-382, Nov. 1970.

[87] J. W. Schultz, J. G. Maloney, K. Cummings-Maloney, R. B. Schultz, J. G. Calzada, and B. C. Foos, "A Comparison of Material Measurement Accuracy of RF Spot Probes to a Lens-Based Focused Beam System," in *Proc. 2014 Antenna Meas. Techn. Assoc.*, Tucson, AZ, 2014, pp. 1-6.

[88] A. Ishikawa, T. Kato, N. Takeyasu, K. Fujimori, and K. Tsuruta, "Selective electroless plating of 3D-printed plastic structures for three-dimensional microwave metamaterials," *Appl. Phys. Lett.*, vol. 111, no. 183102, pp. 1-4, Nov. 2017.

[89] B. Riddle, J. Baker-Jarvis, and J. Krupka, "Complex Permittivity Measurements of Common Plastics Over Variable Temperatures," *IEEE. Trans. Microw. Theory Techn.*, vol. 51, no. 3, pp. 727-733, Mar. 2003.

[90] J. W. Schultz, *Focused Beam Methods*, Atlanta, GA, USA: Printed by CreateSpace, 2012, pp. 14-15.

[91] N. Yu, and F. Capasso, "Flat optics with designer metasurfaces," *Nature Mater.*, vol. 13, pp. 139-150, Jan. 2014.

[92] P. Genevet, F. Capasso, F. Aieta, M. Khorasaninejad, and R. Devlin, "Recent advances in planar optics: from plasmonic to dielectric metasurfaces," *Optica,* vol. 4, no. 1, pp. 139-152, Jan. 2017.

[93] S. Sun, K. Yang, C. Wang, T. Juan, W. T. Chen, C. Y. Liao, Q. He, S. Xiao, W. Kung, G. Guo, L. Zhou, and D. P. Tsai, "High-Efficiency Broadband Anomalous Reflection by Gradient Meta-Surfaces," *Nano Lett.*, vol. 12, no. 12, pp. 6223-6229, Nov. 2012.

[94] S. Sun, Q. He, S. Xiao, Q. Xu, X. Li, and L. Zhou, "Gradient-index meta-surfaces as a bridge linking propagating waves and surface waves," Nature Mat., vol. 11, pp. 426-431, Apr. 2012.

[95] P. Genevet, N. Yu, F. Aieta, J. Lin, M. A. Kats, R. Blanchard, M. O. Scully, Z. Gaburro, and F. Capasso, "Ultra-thin plasmonic optical vortex plate based on phase discontinuities," *Appl. Phys. Lett.*, vol. 100, no. 8, 013101-1-013101-3, Jan. 2012.

[96] C. M. Soukoulis, and M. Wegener, "Past achievements and future challenges in the development of three-dimensional photonic metamaterials," *Nature Photonics*, vol. 5, pp. 523-530, Jul. 2011.

[97] R. Winkler, F. Schmidt, U. Haselmann, J. D. Fowlkes, B. B. Lewis, G. Kothleitner, P. D. Rack, and H. Plank, "Direct-Write 3D Nanoprinting of Plasmonic Structures," *ACS Appl. Mater. Interfaces*, vol. 2017, no. 9, pp. 8233-8240, Nov. 2016.

[98] E. S. P. Leong, J. Deng, E. H. Khoo, S. Wu, W. K. Phua, and Y. J. Liu, "Fabrication of suspended, three-dimensional chiral plasmonic nanostructures with single-step electron-beam lithography," *RSC Adv.*, vol. 2015, no. 5, 96366-96371, Nov. 2015.

[99] A. Radke, T. Gissibl, T. Klotzbucher, P. V. Braun, and H. Giessen, “Three-Dimensional Bichiral Plasmonic Crystals Fabricated by Direct Laser Writing and Electroless Silver Plating,” *Adv. Mater.*, vol. 2011, no. 23, pp. 3018-3021, Apr. 2011.

[100] W. Wu, E. Kim, E. Ponizovskaya, Y. Liu, Z. Yu, N. Fang, Y. R. Shen, A. M. Bratkovsky, W. Tong, C. Sun, X. Zhang, S. Y. Wang, and R. S. Williams, “Optical metamaterials at near and mid-IR range fabricated by nanoimprint lithography,” *Appl. Phys. A*, vol. 87, no. 2, pp. 143-150, Feb. 2007.

[101] D. B. Burckel, J. R. Wendt, G. A. Ten Eyck, A. R. Ellis, I. Brener and M. B. Sinclair, “Fabrication of 3D Metamaterial Resonators Using Self-Aligned Membrane Projection Lithography,” *Adv. Mater.*, vol. 22, pp. 3171-3175, Jun. 2010**.**

[102] D. B. Burckel, J. R. Wendt, G. A. Ten Eyck, J. C. Ginn, A. R. Ellis, I. Brener, and M. B. Sinclair, “Micrometer-Scale Cubic Unit Cell 3D Metamaterial Layers,” *Adv. Mater.*, vol. 2010, no. 22, pp. 5053-5057, Oct. 2010.

[103] N. Kundtz, and D. R. Smith, “Extreme-angle broadband metamaterial lens,” *Nature Mater.*, vol. 9, pp. 129-132, Feb. 2010.

[104] A. Pors, M. G. Nielsen, R. L. Eriksen, and S. I. Bozhevolnyi, “Broadband Focusing Flat Mirrors Based on Plasmonic Gradient Metasurfaces,” *Nano Lett.* vol. 13, no. 2, pp. 829-834, Jan. 2013.

[105] X. Hu, and X. Wei, “Metallic metasurface for high efficiency optical phase control in transmission mode,” *Optics Express*, vol. 25, no. 13, pp. 15208-15215, Jun. 2017.

[106] D. Jones and T. Merhdad, “Advanced Topics in Goal Programming Formulation,” in *Practical Goal Programming*, Springer-Verlag, Berlin, 2010, Ch. 4, Sec. 4.5, pp. 70-72.

[107] Y. Leung, and Y. Wang, "Multiobjective Programming using Uniform Design and Genetic Algorithm," *IEEE Trans. Syst. Man. Cybern. C,* pl. Rev., vol. 30, no. 3, pp. 293-304, Aug 2000.

VITA
Danny Z. Zhu
danny.z.zhu@gmail.com

EDUCATION

Ph. D.	Pennsylvania State University, University Park, PA	Aug 2018
M.S.	Rochester Institute of Technology, Rochester, NY	May 2007
B.S.	Rochester Institute of Technology, Rochester, NY	May 2007

EXPERIENCE

Research Assistant, CEARL, University Park, PA	2015-Pres
Brigade Executive Officer, 501st MI Brigade, Seoul, Republic of Korea	2014-2015
Company Commander, 524th MI Battalion, Seoul, Republic of Korea	2013-2014
Battalion Plans Officer, 524th MI Battalion, Seoul, Republic of Korea	2012-2013
Intelligence Officer, 75th Ranger Regiment, Fort Benning, Georgia	2010-2012
Platoon Leader, 224th MI Battalion, Hunter Army Airfield, Georgia	2008-2010

PUBLICATIONS

D. Z. Zhu, E. B. Whiting, S. D. Campbell, and D. H. Werner, “Inverse Design of Phase-Gradient Metasurfaces using Three-dimensional Metallodielectric Structures Optimized with a Generalized Lazy Ant Colony Algorithm,” (to be submitted to Optica).

D. Z. Zhu, M. D. Gregory, P. L. Werner, and D. H. Werner, “Fabrication and Characterization of Multi-Band Polarization Independent 3D Frequency Selective Structures with Ultra-Wide Fields of View,” (submitted to IEEE TAP).

S. D. Campbell, D. Z. Zhu, E. B. Whiting, J. Nagar, D. H. Werner, and P. L. Werner, "Advanced multi-objective and surrogate-assisted optimization of topologically-diverse metasurface architectures," SPIE OPTICS+PHOTONICS, Metamaterials, Metadevices 2018, August 19 - August 23, 2018, San Diego, USA.

D. Z. Zhu, P. L. Werner, and D. H. Werner, "Multi-Objective Lazy Ant Colony Optimization for Frequency Selective Surface Design," in *Proc. 2018 IEEE Int. Symp. Antennas Propag. USNC-URSI Radio Sci. Meeting*, July 8-13, 2018, Boston, MA, USA (accepted).

S. D. Campbell, D. Z. Zhu, J. Nagar, R. P. Jenkins, J. A. Easum, D. H. Werner, and P. L. Werner, “Inverse Design of Engineered Materials for Extreme Optical Devices,” presented at *2018 Int. ACES Symp.*, March 24-29, 2018, Denver, CO, USA.

D. Z. Zhu, M. D. Gregory, P. L. Werner, and D. H. Werner, "Design, Optimization and Experimental Characterization of Frequency Selective Structures and Metamaterials Comprised of 3D Elements," presented at *20th Annu. Directed Energy Sci. and Technol. Symp.*, February 26 – March 2, 2018, Oxnard, CA, USA.

M. D. Gregory, J. A. Bossard, Z. C. P. O. Morgan, C. S. Cicero, J. A. Easum, J. D. Binion, D. Z. Zhu, C. P. Scarborough, P. L. Werner, D. H. Werner, S. Griffiths, M. Ketner, and J. Pompeii, "A Low Cost and Highly Efficient Metamaterial Reflector Antenna," *IEEE Trans. Antennas Propag.*, March, 2018, vol. 66, no. 3, pp. 1545-1548.

D. Z. Zhu, P. L. Werner, and D. H. Werner, "Design and Optimization of 3D Frequency Selective Surfaces Based on a Multi-Objective Lazy Ant Colony Optimization Algorithm," *IEEE Trans. Antennas Propag.*, December 2017, vol. 65, no. 12, pp. 7137 - 7149.

M. D. Gregory, J. D. Binion, D. Z. Zhu, J. A. Easum, P. L. Werner, D. H. Werner, C. S. Scarborough, S. Griffiths and J. Pompeii, "High Power Metasurface Reflectarray Antennas Using Switched Shorted Circular Elements", in *Proc. 2017 IEEE Int. Symp. Antennas Propag. USNC-URSI Radio Sci. Meeting,* July 9-14, 2017, San Diego, California, USA.

M. D. Gregory, J. A. Bossard, Z. C. P. O. Morgan, C. S. Cicero, J. A. Easum, J. D. Binion, D. Z. Zhu, C. P. Scarborough, P. L. Werner, D. H. Werner, S. Griffiths, and M. Ketner , "Metamaterials for High Power Reflectarray Design," in *Proc. 2016 ACES Conf.,* March 13-17, 2016, Honolulu, Hawaii, USA.